Fig. 68 shows the profiles of ion thermal diffusivity coefficient ($\chi_{\rm i}$), electron thermal diffusivity coefficient ($\chi_{\rm e}$), hydrogenic diffusivity coefficient ($D_{\rm H}$) and impurity diffusivity coefficient ($D_{\rm Z}$) as functions of normalized minor radius at 3,600 sec for ITER standard H-mode scenario (same time with Fig. 65). It can be seen that all diffusivities for the simulations using the dynamic boundary density model are higher than those using the static boundary density model. Contributions for ion thermal and impurity diffusivity coefficients as functions of normalized minor radius from the simulations using the static and dynamic boundary density models for ITER standard H-mode scenario are shown in Fig. 69. It can be seen that for $\chi_{\rm i}$, the ITG and TEM contributions provide the largest contribution in most region of the plasma, except closed to the plasma centre in which the neoclassical transport is dominant. This is similar observed in previous ITER simulations [180, 184, 193-195]. For the impurity transport, the kinetic-ballooning term provides the largest contribution in most region of the plasma, except closed to the plasma edge, in which the ITG and TEM contribution becomes the largest. It is worth mentioning that the resistive ballooning contribution is rather small everywhere in the plasma.

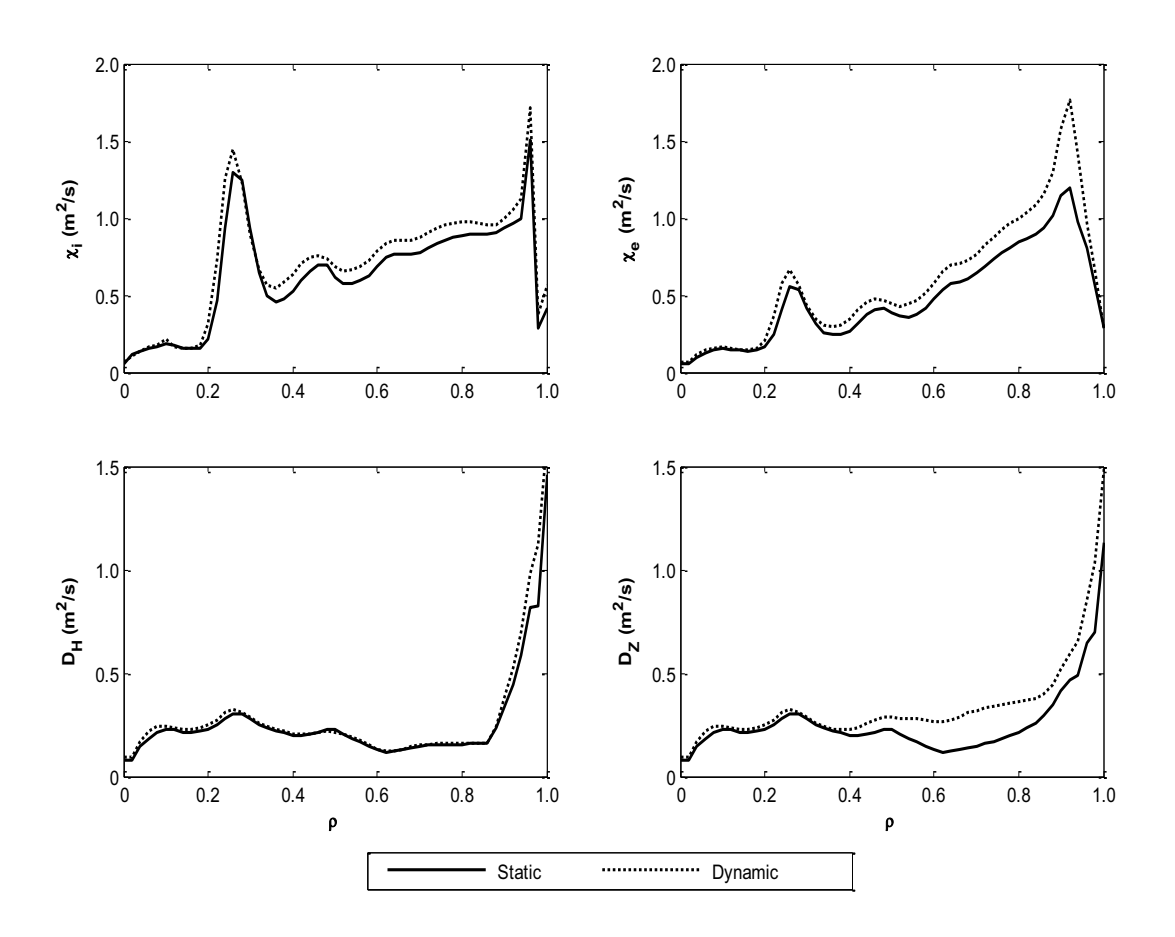


Figure. 68 Profiles of ion thermal diffusion coefficient (χ_i), electron thermal diffusion coefficient(χ_e), hydrogenic particle diffusion coefficient (D_H) and impurity particle diffusion coefficient (D_Z) as functions of normalized minor radius at time 3,600 sec are shown. These simulations are carried out using the static and dynamic boundary density models for ITER standard H-mode scenario.

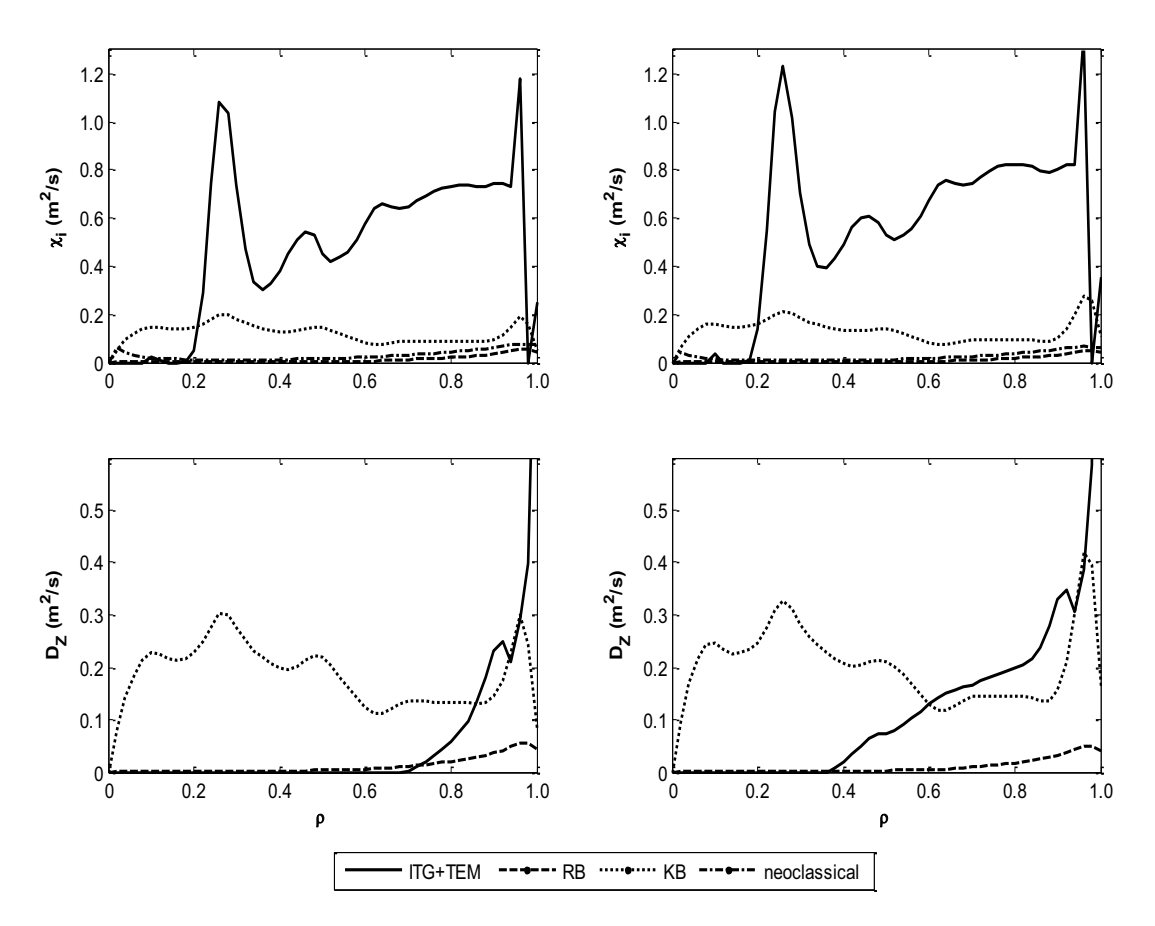


Figure. 69 Contributing terms of ion thermal diffusion coefficient (χ_i) and impurity particle diffusion coefficient (D_z) as functions of normalized minor radius at time 3,600 sec are shown. These simulations are carried out by using ITER standard H-mode scenario with static (left panel) and dynamic (right panel) boundary density models.

Fig. 70 shows the impurity content of beryllium and helium as functions of time from 3,000 sec to 3,600 sec for simulations with standard *H*-mode and steady state scenarios. For both scenarios, it can be seen that the simulation results of impurity density in steady state using the static boundary density model predicted the impurity density that is higher than that using the dynamic boundary density model. The summary of averaged central and total

densities for deuterium, tritium, beryllium, and helium are shown in Table 33. It can be seen that the static density boundary model yields lower central and total densities for deuterium and tritium, but higher central and total densities for beryllium and helium density compared to those with the dynamic density boundary model. This trend is observed in the simulations of both scenarios for ITER. The behaviors of the boundary densities can explain the behaviors of the profiles previously observed in Figs. 66 and 67.

Table 33 Summary of plasma properties at the time of 3,600 sec obtained from simulations using MMM95 core transport model coupled with two different boundary density models (static boundary density model and dynamic boundary density model) for ITER standard type I ELMy *H*-mode and steady state scenario.

Parameters	Type I EI	My <i>H</i> -mode	Steady state		
rarameters	Static model	Dynamic model	Static model	Dynamic model	
$n_{D,0}(\times 10^{19} m^{-3})$	4.058	4.692	2.998	3.637	
$n_{T,0}(\times 10^{19} m^{-3})$	3.237	3.657	2.533	3.229	
$n_{He,0}(\times 10^{19} m^{-3})$	0.814	0.465	0.601	0.071	
$n_{Be,0}(\times 10^{19} m^{-3})$	0.252	0.056	0.132	0.034	
$n_{D,total}(\times 10^{22} particles)$	3.440	3.801	2.461	3.087	
$n_{T,total}(\times 10^{22} particles)$	2.811	3.335	2.233	2.809	
$n_{He,total}(\times 10^{22} particles)$	0.530	0.279	0.488	0.046	
$n_{Be,total}(\times 10^{22} particles)$	0.144	0.039	0.101	0.027	

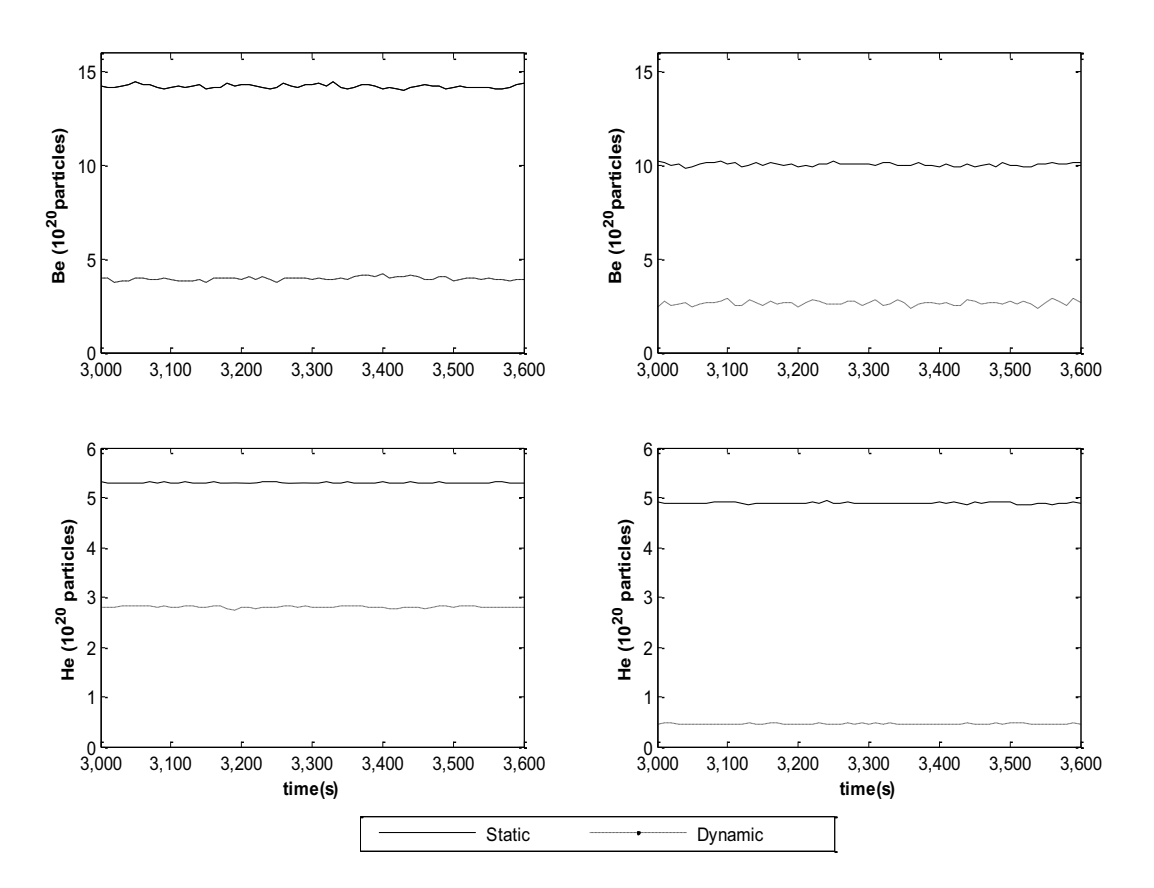


Figure. 70 Densities of beryllium (*Be*) and helium (*He*) as functions of time during 3,000 to 3,600 sec are shown. These simulations are carried out by using ITER standard *H*-mode (left panels) and steady state (right panels) scenarios with static and dynamic models.

Fig. 71 shows the time evolution of effective charge ($Z_{\rm eff}$) at different normalized minor radii (ρ = 0.00, 0.25, 0.50, 0.75, and 1.00) during 3,000 to 3,600 sec. It can be seen that the effective charge in the simulations using the static boundary density model is around 1.4; while the effective charge in the simulations using the dynamic boundary density model is much lower, about 1.1. The effective charge with the dynamic boundary model is quite low. It can also be seen that the effective charge in the simulations for standard type I ELMy H-mode tends to be higher than that for steady state.

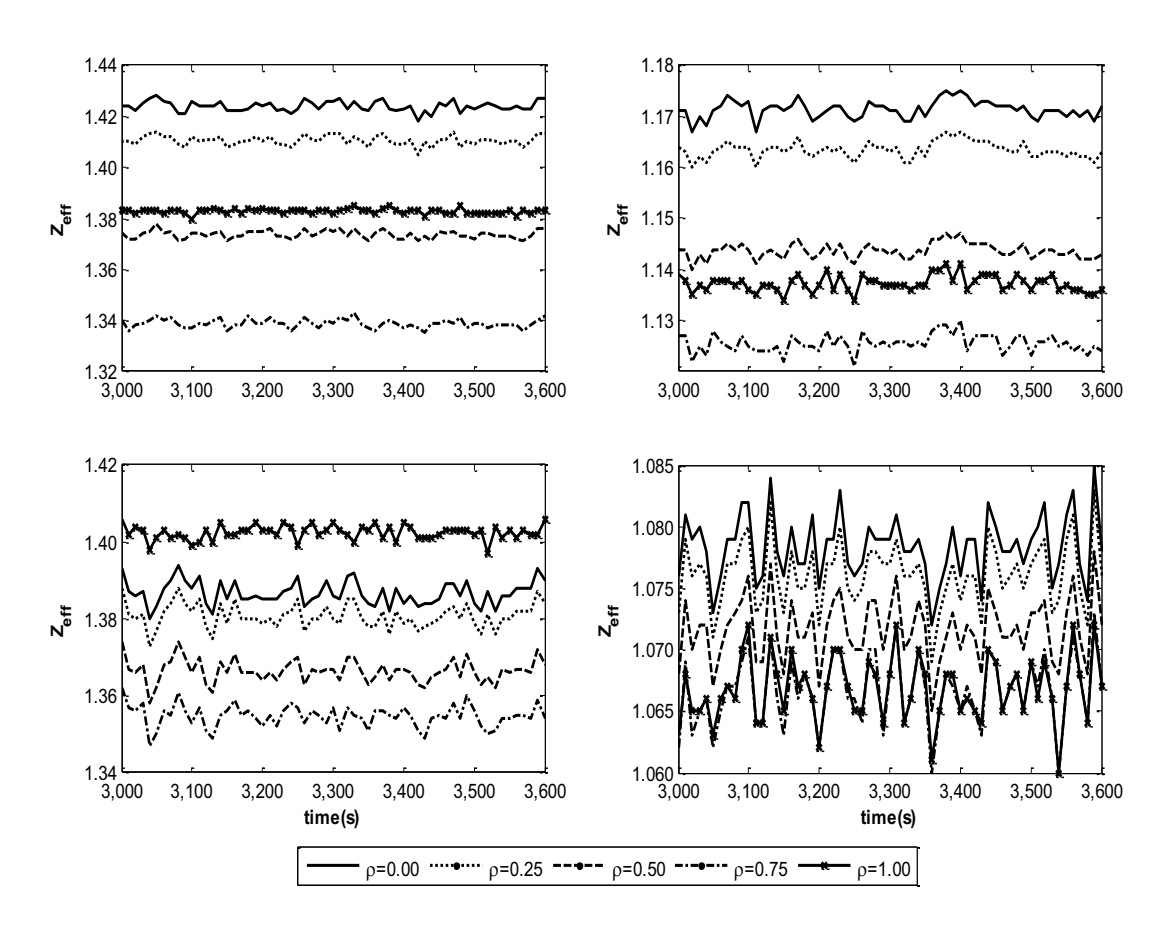


Figure. 71 Time evolutions of effective charge ($Z_{\it eff}$) with ρ of 0.00, 0.25, 0.50, 0.75 and 1.0 during 3,000 to 3,600 sec are shown. These simulations are carried out by using ITER standard H-mode with static model (top left), ITER standard H-mode with dynamic model (top right), steady state with static model (bottom left) and steady state with dynamic model (bottom right).

4. Sensitivity Study

In this section, the parametric sensitivity of BALDUR simulations is investigated using the dynamic boundary density model. The effects of pedestal temperature ($T_{\rm ped}$), pedestal density ($n_{\rm ped}$), line averaged density (\overline{n}_i) and impurity influx on the impurity behaviours in ITER plasmas are investigated in this section.

4.1 Variation of pedestal temperature

In this study, the simulations of ITER plasmas with standard type I ELMy H-mode and steady state scenarios are carried out using different values of pedestal temperature (T_{ped} = 3.0, 4.0 and 5.0 keV). It is found that the plasma reaches the quasi steady state in all simulations. The densities of beryllium and helium in the simulations for both the standard

type I ELMy *H*-mode and steady state scenarios are shown in Fig. 72. It can be seen that the density for both beryllium and helium decreases with the increasing of pedestal temperature. The averaged central and total densities for deuterium, tritium, beryllium and helium during the time from 3,000 sec to 3,600 sec for ITER standard type I ELMy *H*-mode scenario are summarized in Table 34. For the ITER standard type I ELMy *H*-mode scenario, it can be seen that the total beryllium particles decrease about 58% and 75% as the pedestal temperature increases from 3 keV to 4 keV and to 5 keV, respectively. For the total helium particles, it decreases from 17% and 20% as the pedestal temperature increases from 3 keV to 4 keV and 5 keV, respectively. On the other hand, the total deuterium and tritium particles increase with the increase of pedestal temperature. Note that the similar trend is observed for the ITER steady state scenario. It is also found that the impurity transport increases as the pedestal temperature increases, especially near the plasma edge. Each contributions of impurity diffusivity are shown in Fig. 73 for each pedestal temperature. It can be seen that the contribution from ITG&TEM modes increases with the increasing temperature. On the other hand, the contribution from RB and KB modes decreases.

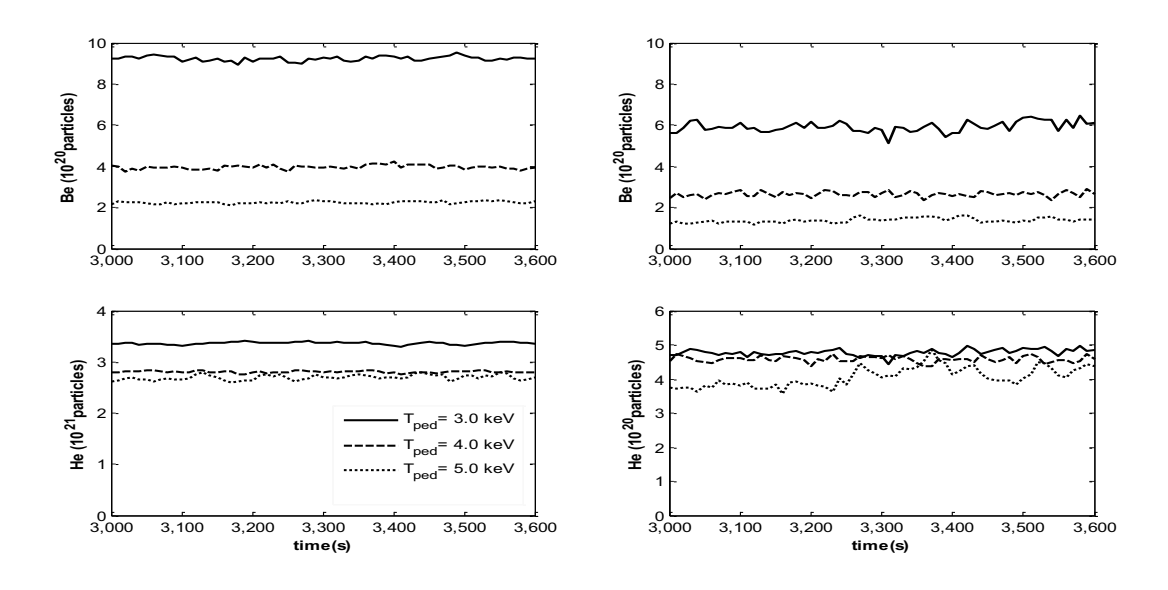


Figure. 72 Densities of beryllium (*Be*) and helium (*He*) as functions of time during 3,000 to 3,600 sec are shown. These simulations are carried out by using dynamic boundary density model for ITER standard *H*-mode (left panel) and steady state (right panel) scenarios. The pedestal temperature is varied to be 3.0, 4.0 and 5.0 keV.

Table 34 Averaged deuterium, tritium, beryllium and helium densities during the time from 3,000 sec to 3,600 sec are summarized for different pedestal temperatures. The simulations are carried out for type I ELMy *H*-mode scenario.

T	Deuterium		Tritium		Beryllium		Helium	
1 ped	Center	Total	Center	Total	Center	Total	Center	Total
(keV)	(×10 ¹⁹ m ⁻³)	(×10 ²² pts.)	(×10 ¹⁹ m ⁻³)	(×10 ²² pts.)	(×10 ¹⁹ m ⁻³)	(×10 ²² pts.)	(×10 ¹⁹ m ⁻³)	(×10 ²² pts.)
3.0	4.638	3.708	3.264	3.092	0.132	0.092	0.546	0.336
4.0	4.692	3.801	3.657	3.335	0.056	0.039	0.465	0.279
5.0	4.507	3.977	3.930	3.525	0.031	0.023	0.439	0.270

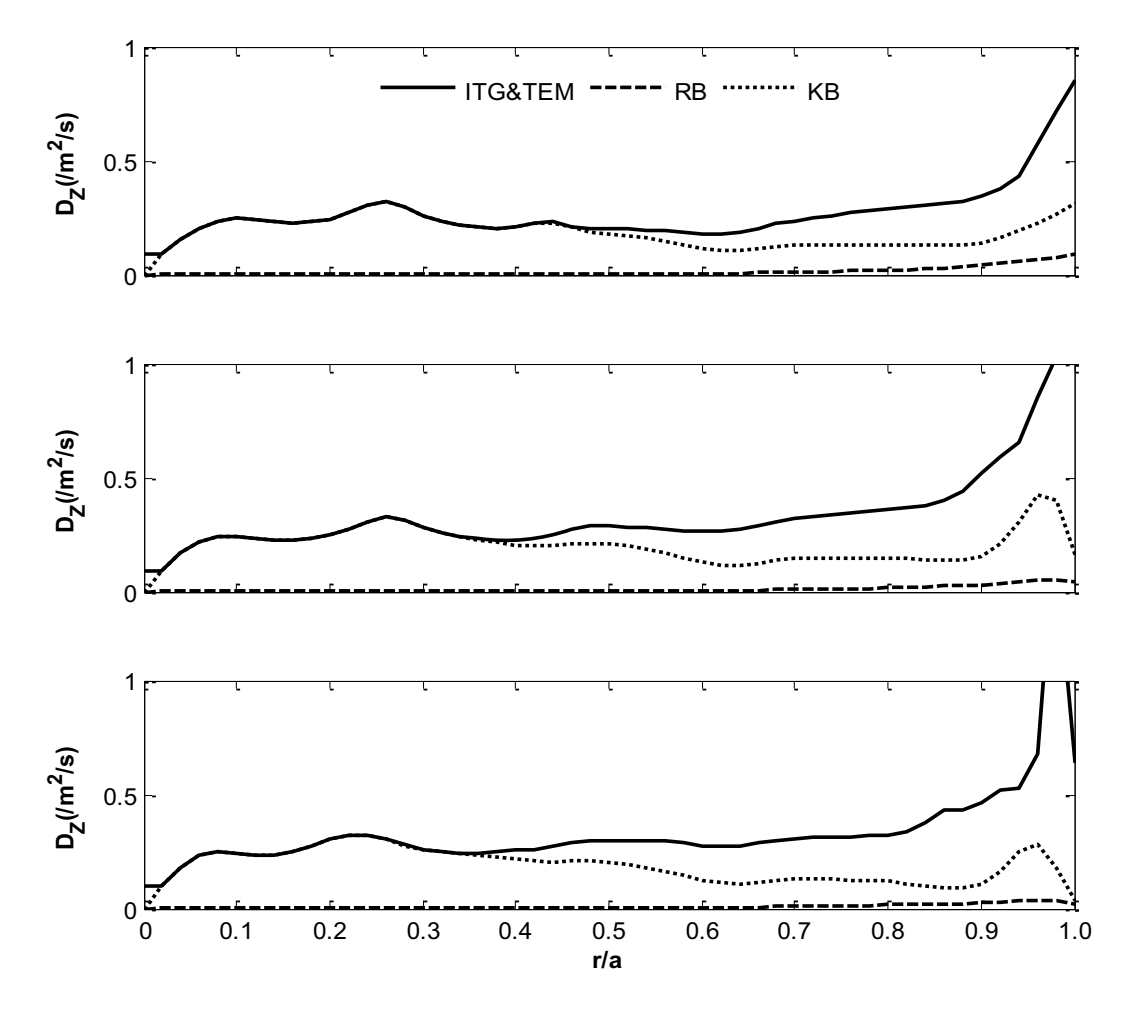


Figure. 73 Contributing terms of impurity particle diffusion coefficient ($D_{\rm Z}$) are plotted as a function of normalized minor radius at time 3,600 sec for different pedestal temperature: 3 keV (top panel), 4 keV (middle panel) and 5 keV (bottom panel). These simulations are carried out by using ITER standard H-mode scenario with the dynamic boundary density models.

4.2 Variation of density constant

In this study, the simulations of ITER plasmas with standard type I ELMy H-mode and steady state scenarios are carried out using different values of the density constant (0.51, 0.61 and 0.71). Note that lower density constant results in lower pedestal density. It is found that the densities of beryllium and helium in the simulations for both the standard type I ELMy H-mode and steady state scenarios decrease as the density constant decreases, shown in Fig. 74. The averaged central and total densities for deuterium, tritium, beryllium and helium during the time from 3,000 sec to 3,600 sec for ITER standard type I ELMy Hmode scenario are summarized in Table 35. For the ITER standard type I ELMy H-mode scenario, it can be seen that the total beryllium particles decrease about 70% and 89% as the density constant decreases from 0.71 to 0.61 and 0.51, respectively. For the total helium particles, it decreases from 61% and 78% as the density constant decreases from 0.71 to 0.61 and 0.51, respectively. Similarly, the total deuterium and tritium particles decrease with the decrease of the density constant. Note that the similar trend is observed for the ITER steady state scenario. It is also found that the impurity transport decreases as the pedestal density increases, especially near the plasma edge. Each contributions of impurity diffusivity are shown in Fig. 75 for each density constant. It can be seen that the contribution from each mode changes slightly with increasing density constant. However, no clear trend is observed

Table 35 Averaged deuterium, tritium, beryllium and helium densities during the time from 3,000 sec to 3,600 sec are summarized for different density constants. The simulations are carried out for type I ELMy *H*-mode scenario.

22	Deuterium		Tritium		Beryllium		Helium	
n _{ped} 19 -3	Center	Total	Center	Total	Center	Total	Center	Total
(×10 m)	$(\times 10^{19} m^{-3})$	(×10 ²² pts.)	$(\times 10^{19} m^{-3})$	(×10 ²² pts.)	$(\times 10^{19} m^{-3})$	(×10 ²² pts.)	$(\times 10^{19} m^{-3})$	(×10 ²² pts.)
0.51	4.437	3.798	4.043	3.826	0.013	0.009	0.216	0.108
0.61	5.346	4.735	4.399	3.725	0.024	0.018	0.030	0.157
0.71	4.692	3.801	3.657	3.335	0.056	0.039	0.465	0.279

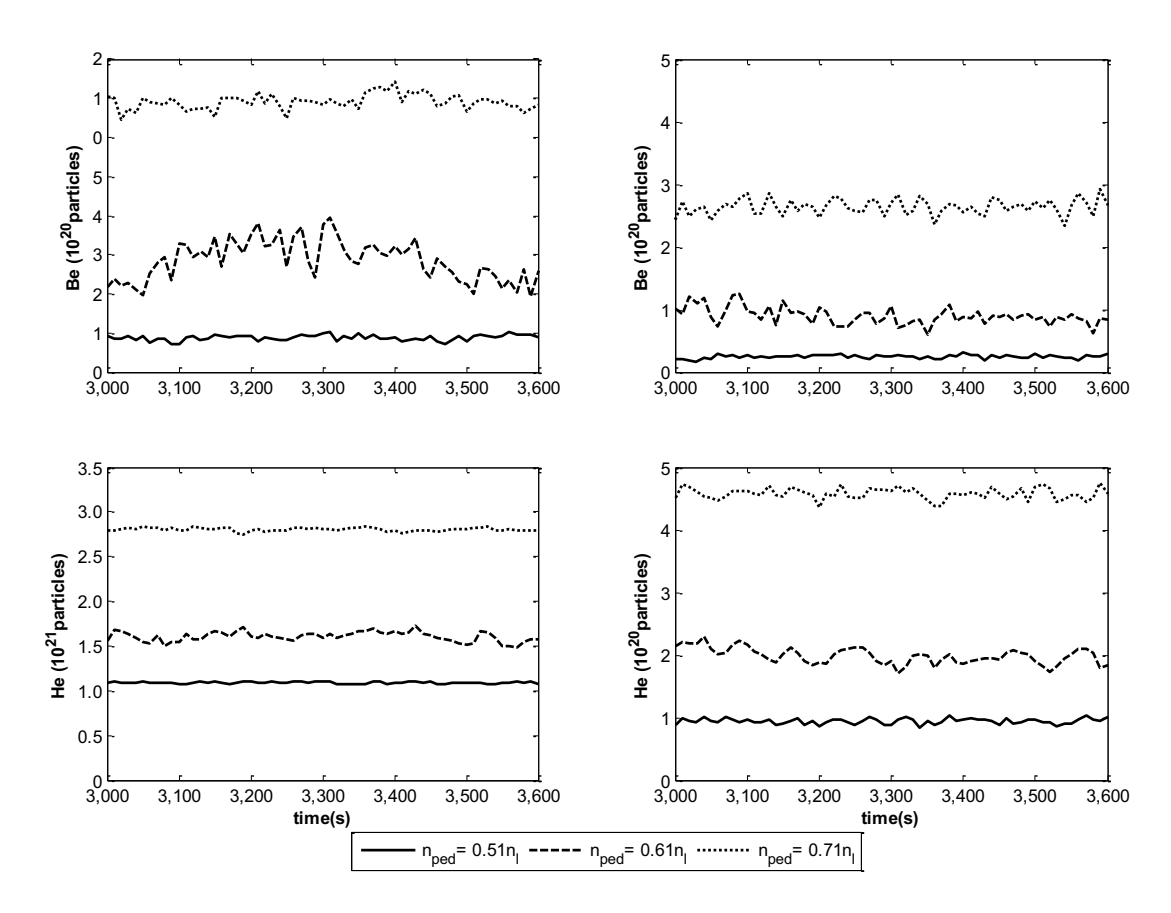


Figure. 74 Densities of beryllium (Be) and helium (He) as functions of time during 3,000 to 3,600 sec are shown. These simulations are carried out by using dynamic ITER standard H-mode (left panels) and dynamic steady state (right panels) scenarios with $n_{\rm ped}$ of $0.51n_{\rm l}$, $0.61n_{\rm l}$ and $0.71n_{\rm l}$ m⁻³.

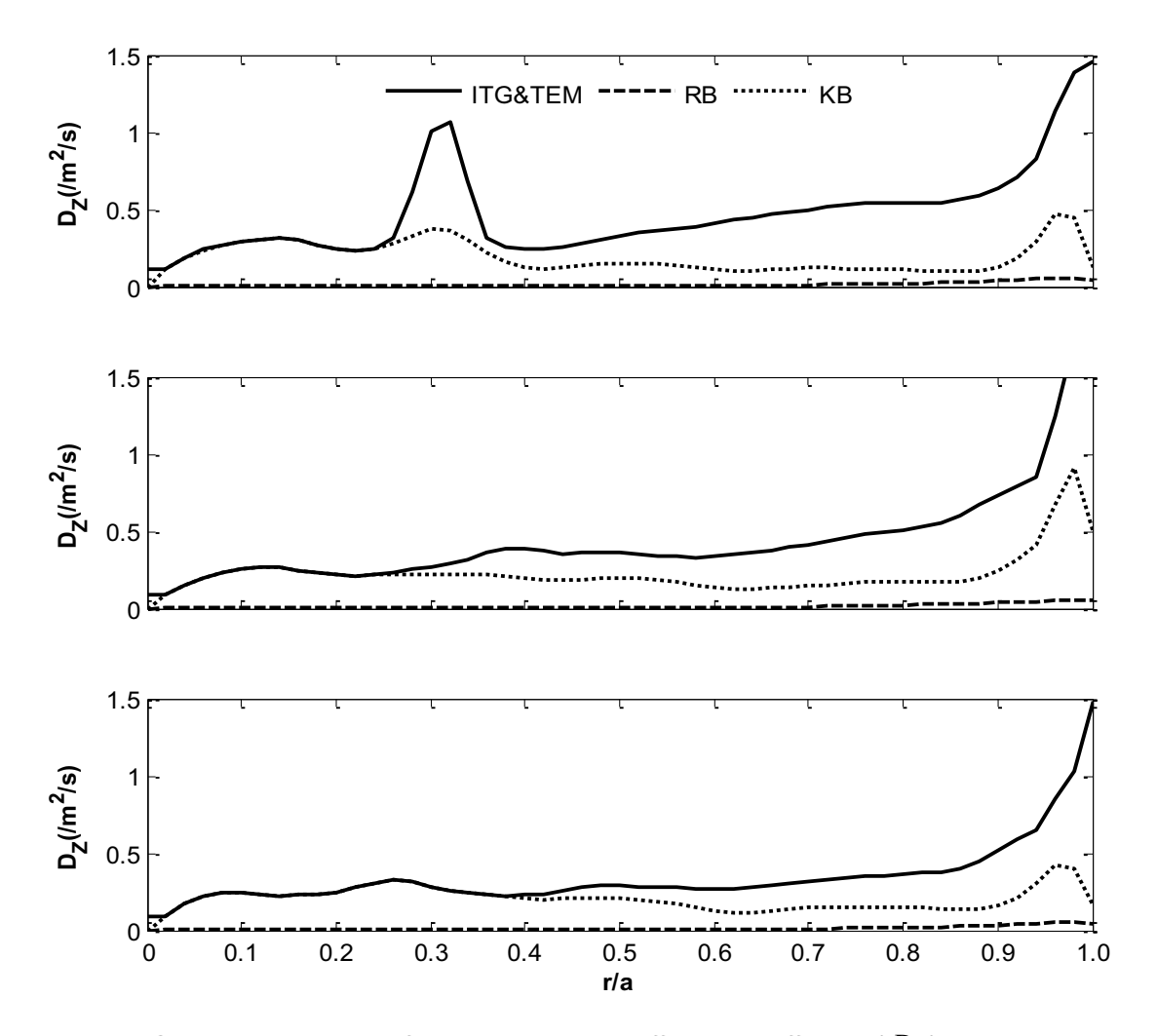


Figure. 75 Contributing terms of impurity particle diffusion coefficient ($D_{\rm Z}$) are plotted as a function of normalized minor radius at time 3,600 sec for different pedestal density: $0.51n_{\rm I}$ (top panel), $0.61n_{\rm I}$ (middle panel) and $0.71n_{\rm I}$ m⁻³(bottom panel). These simulations are carried out by using ITER standard H-mode scenario with the dynamic boundary density models.

4.3 Variation of line averaged electron density

Impurity transport depends on a number of factors such as plasma temperature, lineaveraged density and the nature of impurity species. Since line-averaged density can be easily monitored and controlled in actual tokamak operation, it would be interesting to find if impurity density in steady state can be enhanced or hindered, *i.e.* controlled, merely by varying the plasma density. The line-averaged density of 1.0×10^{20} m⁻³ is used for the simulations of standard type I ELMy *H*-mode scenario in section 3. In this section, simulations are carried out using \overline{n}_l of 0.8×10^{20} , 1.0×10^{20} and 1.2×10^{20} m⁻³. It is found that

the densities of beryllium and helium in the simulations for both the standard type I ELMy *H*-mode and steady state scenarios decrease as the density constant decreases, shown in Fig. 76. The averaged central and total densities for deuterium, tritium, beryllium and helium during the time from 3,000 sec to 3,600 sec for ITER standard type I ELMy *H*-mode scenario are summarized in Table 36. For the ITER standard type I ELMy *H*-mode scenario, it can be seen that the total beryllium particles decrease about 26% and 48% as the line average density increases from 0.8x10²⁰, 1.0x10²⁰ and 1.2x10²⁰ m⁻³, respectively. For the total helium particles, it decreases from 26% and 61% as the density constant increases from 0.8x10²⁰, 1.0x10²⁰ and 1.2x10²⁰ m⁻³, respectively. Similarly, the total deuterium and tritium particles increase with the increase of line average density. Note that the similar trend is observed for the ITER steady state scenario. It is also found that the impurity transport increases as the line average density increases, especially near the plasma edge. Each contributions of impurity diffusivity are shown in Fig. 77 for each line average density. It can be seen that the contributions from KB modes increases with the increasing line average density.

Table 36 Averaged deuterium, tritium, beryllium and helium densities during the time from 3,000 sec to 3,600 sec are summarized for different line averaged densities. The simulations are carried out for type I ELMy *H*-mode scenario.

		Deuterium		Tritium		Beryllium		Helium	
	(m^{-3})	Center	Total	Center	Total	Center	Total	Center	Total
		$(\times 10^{19} m^{-3})$	(×10 ²² pts.)	$(\times 10^{19} m^{-3})$	(×10 ²² pts.)	(×10 ¹⁹ m ⁻³)	(×10 ²² pts.)	$(\times 10^{19} m^{-3})$	(×10 ²² pts.)
	0.8	3.318	3.194	2.464	2.537	0.041	0.031	0.334	0.206
	1.0	4.692	3.801	3.657	3.335	0.056	0.039	0.465	0.279
	1.2	6.071	4.690	4.778	3.938	0.066	0.046	0.570	0.332

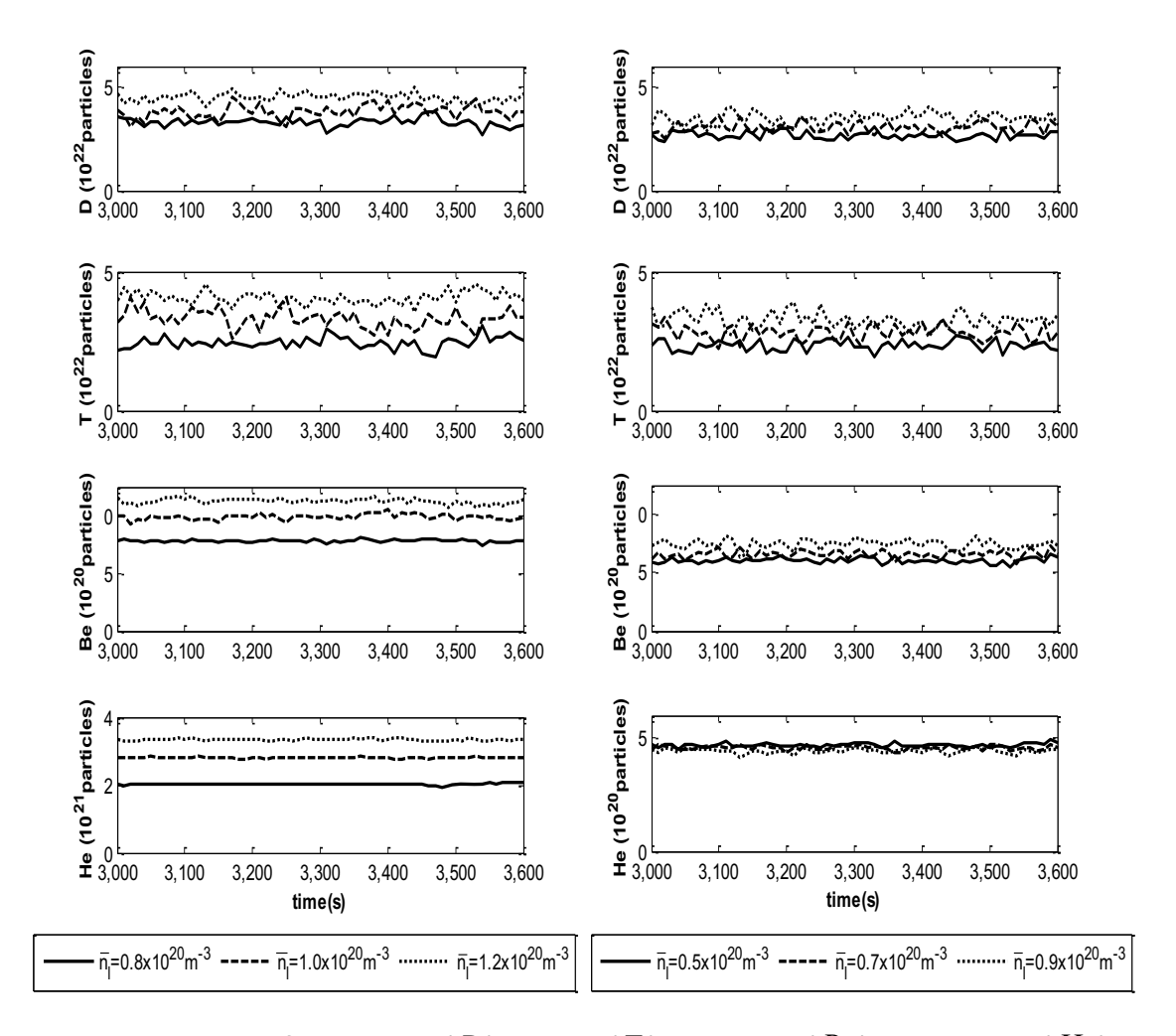


Figure. 76 Densities of deuterium (D), tritium (T), beryllium (Be) and helium (He) as functions of time during 3,000 to 3,600 sec are shown. These simulations are carried out by using dynamic ITER standard H-mode (left panels) with \overline{n}_l of 0.8×10^{20} , 1.0×10^{20} and 1.2×10^{20} m⁻³, and dynamic steady state (right panels) with \overline{n}_l of 0.5×10^{20} , 0.7×10^{20} and 0.9×10^{20} m⁻³.

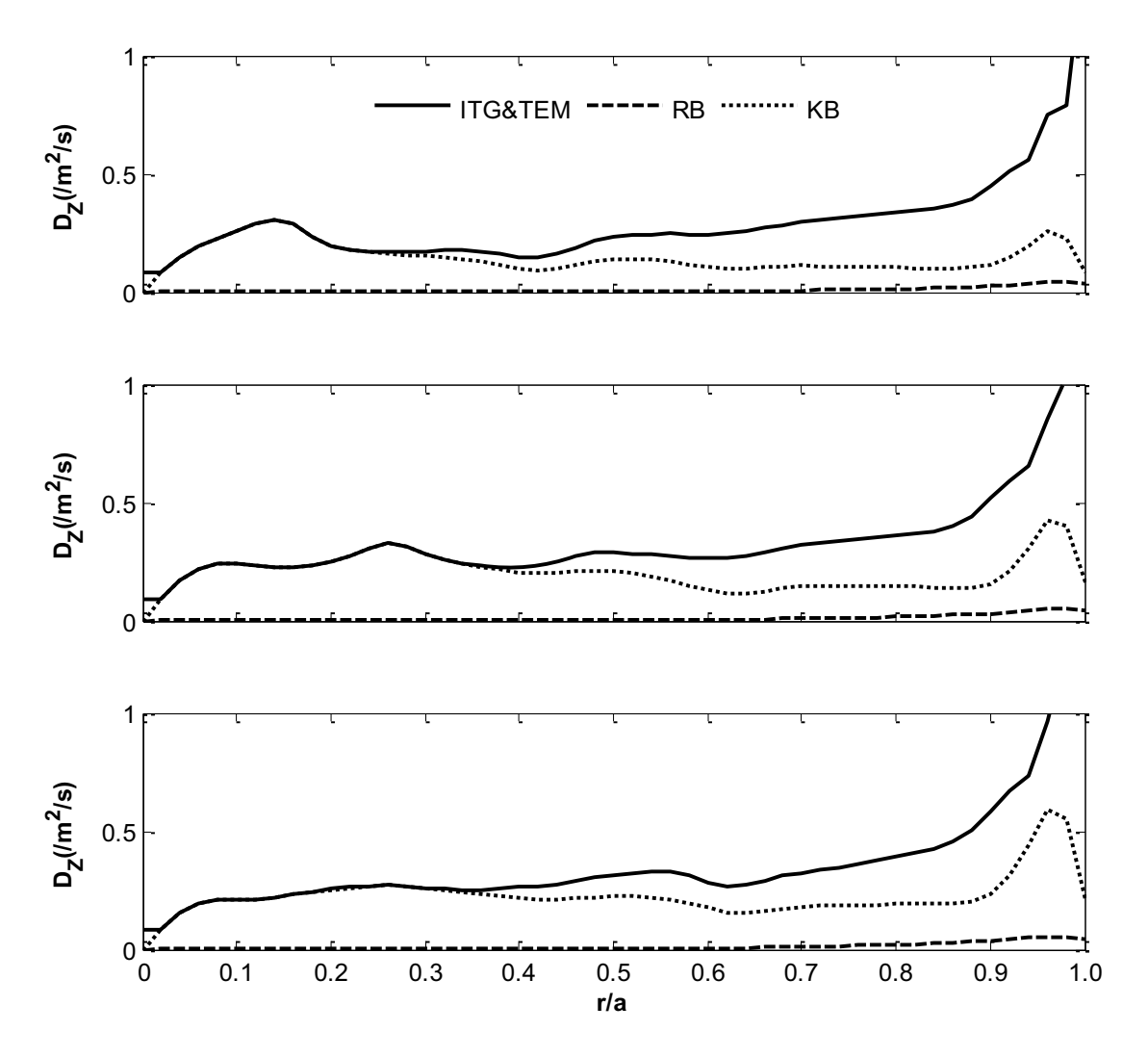


Figure. 77 Contributing terms of impurity particle diffusion coefficient ($D_{\rm Z}$) are plotted as a function of normalized minor radius at time 3,600 sec for different pedestal density: \overline{n}_l of 0.8×10^{20} (top panel), 1.0×10^{20} (middle panel) and 1.2×10^{20} m⁻³ (bottom panel). These simulations are carried out by using ITER standard *H*-mode scenario with the dynamic boundary density model.

4.4 Variation of impurity influx

In the BALDUR simulations, the impurity from outside of the main plasma, such as from SOL region, and the nuclear fusion reactions are the main impurity sources. In all of the previous simulations, a constant beryllium influx of 1.0×10^{11} particle/cm².sec is used. To investigate the sensitivity of the impurity influx, the impurity influx is varied to be 1.0×10^{11} particle/cm².sec, 1.0×10^{12} particle/cm².sec, and 1.0×10^{13} particle/cm².sec. It is found that the plasma temperature and density reach the quasi steady state in all simulations. The evolution

of deuterium, tritium, beryllium and helium in the simulations for the standard type I ELMy *H*-mode are shown in Fig.78. It can be seen that the density in steady state for both beryllium tends to increase slightly with the increasing of impurity influx; while the density of other species reminds almost the same. It is also found that there is no significant change in the impurity transport as the impurity influx increases.

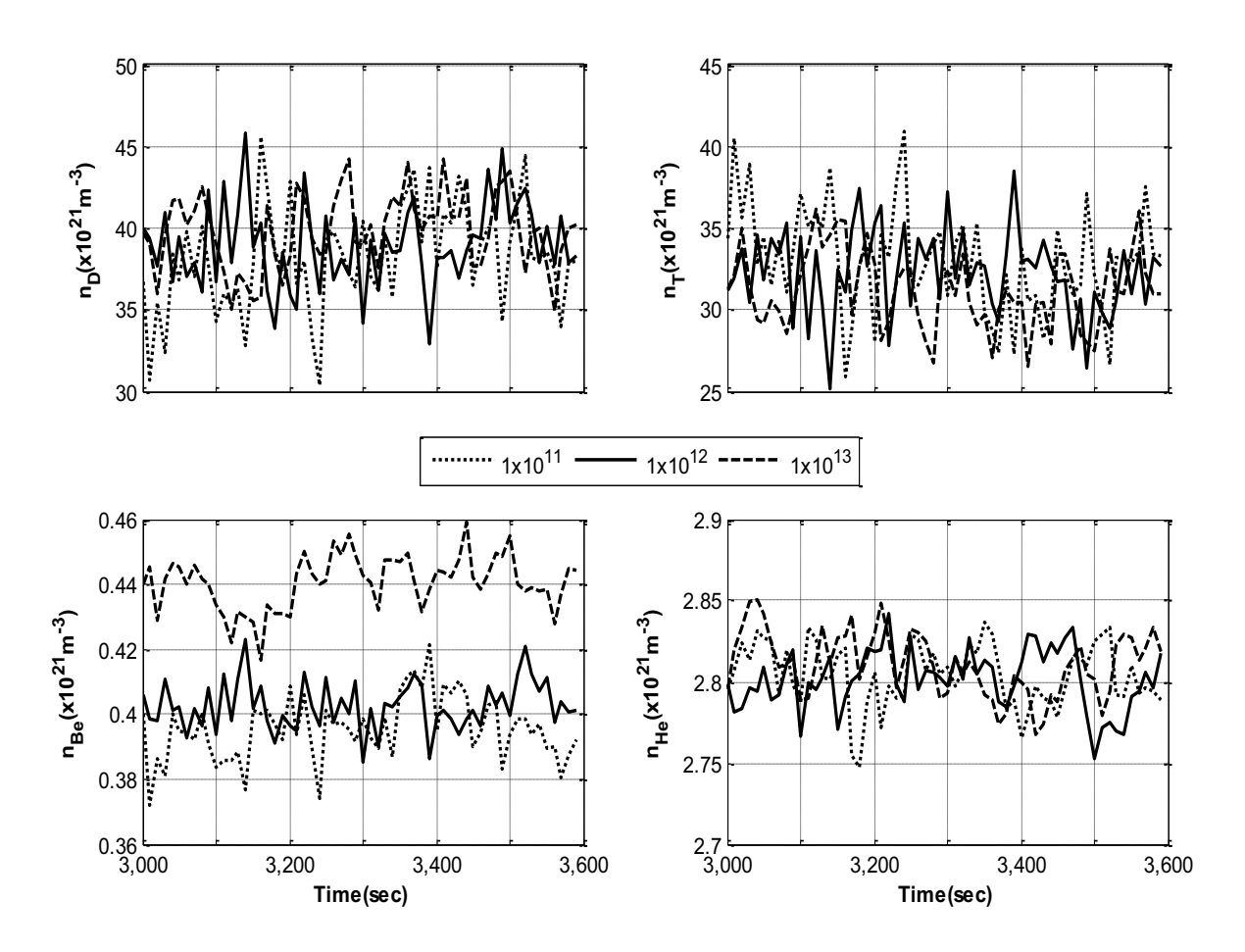


Figure. 78 Densities of deuterium (D), tritium (T), beryllium (Be) and helium (He) as functions of time during 3,000 to 3,600 sec are shown. These simulations are carried out by using dynamic ITER standard H-mode with impurity influx of 1.0×10^{11} particle/cm².sec, 1.0×10^{12} particle/cm².sec, and 1.0×10^{13} particle/cm².sec.

5. Summary

In this work, the behaviors of impurity behaviors in standard *H*-mode and steady state scenarios are investigated via simulation using the 1.5D BALDUR integrated predictive modelling code. The impurity species considered are a combination of helium and beryllium. The simulations are carried out using MMM95 core transport model, coupled with NCLASS neoclassical model and different boundary models (static and dynamic boundary models). It is found that ion and electron temperatures, as well as ion, electron, deuterium, tritium, helium and beryllium densities reach quasi-steady state values and all parameters are not much different between the two boundary models. However, the impurity density in steady state and the edge effective charge are significantly different in the two models. In the parametric sensitivity analysis, the pedestal temperature, pedestal density, line averaged density, and impurity influx are investigated. All three parameters are observed to influence impurity behaviors.

References

- [1] H. Zohm, Plasma. Phys. Control. **38**, 105-128 (1996)
- [2] G. Bateman et al, Phys. Plasmas 5, 1793 (1998)
- [3] D. Hannum *et al*, Phys. Plasmas **8**, 964 (2001)
- [4] J. G. Cordey, Nucl. Fusion43, 670–674 (2003)
- [5] J.E. Kinsey, Nucl. Fusion43, 1845–1854 (2003)
- [6] T. Onjun, Ph. D. Thesis, Lehigh University, 2004.
- [7] J.Rapp et al, Proceedings of the 22nd IAEA Fusion Energy Conference, Geneva, Switzerland (13th-18th October (2008)
- [8] T. Onjun *et al*, Phys. Plasmas**9**, 5018 (2002)
- [9] J. G. Cordey et al, Nucl. Fusion 39, 301-307 (1999)
- [10] D. McDonald et al, Nucl. Fusion 47, 147 (2007)
- [11] ITER Physics Basis, Nucl. Fusion47, (2007)
- [12] R. J. Goldston, Plasma Phys. Control. Fusion 26 no. 1A,87 (1984)
- [13] N. A. Uckan, Workshop on Physics Issues for FIRE, May 1–3, 2000, Princeton, NJ.
- [14] T. Onjun et al, Phys. Plasmas **8**,975 (2001)
- [15] J. Freidberg, Plasma Physics and Fusion Energy, Cambridge Univ. Press, Cambridge, 2007.
- [16] W. M. Stacey, Fusion Plasma Physics Weinheim; Chichester: Wiley-VCH; John Wiley, distributor 2005.
- [17] J. Wesson, Tokamaks, 3rd Edition, Clarendon Press, Oxford, 2004.
- [18] D. Boucher et al, Nucl. Fusion40, 1955 (2000)
- [19] Wagner F. et al 1982 Physical Review Letters 49(19) 1408
- [20] Connor J. W. and Wilson H. R. 2000 Plasma Physics and Controlled Fusion 42 R1-R74
- [21] Singer C. E. et al 1988 Computer Physics Communications 49 (2) 275-398
- [22] Honda M. and Fukuyama A. 2006 Nuclear Fusion 46 580-593
- [23] Cenacchi G. and Taroni A. 1988 JET-IR 88
- [24] Pereverzev G. and Yushmanov P. N. 2002 Max-Planck Institut fur Plasmaphysik IPP 5/98
- [25] Basiuk V. et al 2003 Nuclear Fusion 43 822
- [26] Kinsey J. E. et al 2002 Physics of Plasmas 9(5) 1676
- [27] Bateman G. et al 1998 Physics of Plasmas 5 1793

- [28] Bateman G. et al 2003 Plasma Physics and Controlled Fusion 45 (11) 1939-1960
- [29] Kinsey J. E. et al 2003 Nuclear Fusion 43 (12) 1845
- [30] Onjun T. et al 2001 Physics of Plasmas 8 975
- [31] Hannum D. et al 2001 Physics of Plasmas 8 964
- [32] Biglari H. et al 1990 Physics of Fluids B: Plasma Physics 2 (1) 1-4
- [33] Gohil P. 2006 Comptes Rendus Physique 7 (6) 606-621
- [34] Boedo J. et al 2000 Nuclear Fusion 40 1397
- [35] Oost G. V. et al 2003 Plasma Physics and Controlled Fusion 45 1-23
- [36] Pankin A. Y. et al 2005 Plasma Physics and Controlled Fusion (3) 483
- [37] Pacher G. W. and et al. 2004 Plasma Physics and Controlled Fusion 46 (5A) A257
- [38] Onjun T. et al 2002 Physics of Plasmas 9 5018-5030
- [39] Onjun T. et al 2004 Physics of Plasmas 11 1469
- [40] Parail V. et al 2003 Plasma Physics Reports 29 (7) 539-544
- [41] Lönnroth J. S. and et al. 2004 Plasma Physics and Controlled Fusion 46 (8) 1197
- [42] Lönnroth J. S. and et al. 2004 Plasma Physics and Controlled Fusion 46 (5) 767
- [43] Doyle E. J. et al 2007 Nuclear Fusion 47 (6) S18
- [44] Yoshizawa A. et al, Plasma and fluid turbulence: theory and modelling. (Institute of Physics Publishing, Bristol, 2003).
- [45] Waltz R. E. et al 1997 Physics of Plasmas 4 (7) 2482
- [46] Itoh K. and et al. 1994 Plasma Physics and Controlled Fusion 36 (1) 123
- [47] Itoh K. and et al. 1998 Plasma Physics and Controlled Fusion 40 (5) 661
- [48] Itoh S. I. et al 1994 Physical Review Letters 72 (8) 1200
- [49] Figarella C. F. et al 2003 Physical Review Letters 90 (1) 015002
- [50] Zolotukhin O. V. et al, in 28th EPS Confer. on Contr. Fusion and Plasma Phys. (Funchal, Portugal, 2001), Vol. 25A, pp. 677-680.
- [51] Sugihara M. et al, in 28th EPS Conf. on Contr. Fusion and Plasma Phys. (Funchal, Portugal, 2001), Vol. 25A, pp. 629-632.
- [52] Kessel C. et al 1994 Physical Review Letters 72 (8) 1212
- [53] Diamond P. H. et al 1997 Physical Review Letters 78 (8) 1472
- [54] Sugihara M. and et al. 2000 Nuclear Fusion 40 (10) 1743
- [55] Hahm T. S. and Diamond P. H. 1987 Physics of Fluids 30 (1) 133-143
- [56] Pacher G. W. et al 2003 Nuclear Fusion 43 188-195

- [57] Janeschitz G. and et al. 2002 Plasma Physics and Controlled Fusion 44 (5A) A459
- [58] Onjun T. and Pianroj Y. 2009 Nuclear Fusion 49 075003
- [59] Tala T. J. J. et al 2001 Plasma Physics and Controlled Fusion 43 507-523
- [60] Chang C. S. and Hinton F. L. 1986 Physics of Fluids 29 (10) 3314-3316
- [61] Boucher D. et al 2000 Nuclear Fusion 40 (12) 1955
- [62] Shimomura Y. et al, presented at the IAEA Fusion Energy Conference, Sorrento, Italy, 2000 (unpublished).
- [63] Cordey J. G. and et al. 1999 Nuclear Fusion 39 (3) 301
- [64] Lingertat J. et al 1999 Journal of Nuclear Materials 266-269 124-130
- [65] Onjun T., "PEDESTAL model." http://w3.pppl.gov/NTCC/PEDESTAL
- [66] Burrell K. H. 1997 Physics of Plasmas 4 1499
- [67] Boucher D. et al 2000 Nuclear Fusion 40 (12) 1955
- [68] Aymar R et al., 2002 Plasma Phys. Control. Fusion 44 519
- [69] Hubbard A, 2000 Plasma Phys. Control. Fusion 42 A15
- [70] Connor J W et al., 2004 Nucl. Fusion 44 R1
- [71] Burrell K H, 1994 Plasma Phys. Control. Fusion 36 A291
- [72] Burrell K H., 1997 Phys. Plasmas 4 1499
- [73] Tala T et al., 2007 Plasma Phys. Control. Fusion 49 B291
- [74] Rozhansky V et al., 2002 Nucl. Fusion 42 1110
- [75] Rogister A L et al., 2002 Nucl. Fusion 42 1144
- [76] Eriksson A et al., 2007 Plasma Phys. Control. Fusion 49 1931
- [77] Tala T. et al., 2009 Phys. Rev. Lett. 102 075001
- [78] Solomon W. et al., 2008 Phys. Rev. Lett. 101 065004
- [79] Onjun T et al., 2002 Phys. Plasmas 9 5018
- [80] Sugihara M et al., 2000 Nucl. Fusion **40** 1743
- [81] Tala T et al., 2001 Plasma Phys. Control. Fusion 43 507
- [82] Tala T et al., 2002 Plasma Phys. Control. Fusion 44 A495
- [83] Parail V V et al., 1999 Nucl. Fusion 39 429
- [84] Parail V V, 2002 Plasma Phys. Control. Fusion 44 A63
- [85] Tala T et al., 2005 Nucl. Fusion **45** 1027
- [86] Tala T et al., 2006 Nucl. Fusion 46 548

- [87] Kessel C E et al. in Fusion Energy 2006 (Proc. 21st Int. Conf. Chengdu, 2006) (Vienna: IAEA) CD-ROM file IT/P1-7 and http://www-naweb.iaea.org/napc/physics/FEC/FEC2006/html/index.htm
- [88] Singer C E et al., 1988 Comput. Phys. Commun. 49 399
- [89] Onjun T and Pianroj Y 2009 Nucl. Fusion **49** 075003
- [90] Hannum D et al., 2001 Phys. Plasmas 8 964
- [91] Onjun T et al., 2001 Phys. Plasmas 8 975
- [92] Erba M et al., 1997 Plasma Phys. Control. Fusion 39 261
- [93] Taroni A et al., 1994 Plasma Phys. Control. Fusion 36 1629
- [94] Erba M et al., 1995 Plasma Phys. Control. Fusion 37 124
- [95] Erba M et al., 1998 Plasma Phys. Control. Fusion 38 1013
- [96] Pankin A Y et al., 2005 Plasma Phys. Control Fusion 47 483
- [97] Zhu P et al., 2000 Phys. Plasmas **7** 2898
- [98] Kritz A H et al., 2004 Comput. Phys. Comm., 164, 108 (HUhttp://w3.pppl.gov/NTCCUH)
- [99] Connor J, 1998 Plasma Phys. Control. Fusion 40 191
- [100] Bateman G et al., 2003 Plasma Phys. Control. Fusion 45 1939
- [101] Boucher et al., 2000 Nucl. Fusion 40 1955
- [102] Aymar R et al., 2002 Plasma Phys. Control. Fusion 44 519
- [103] Hubbard A, 2000 Plasma Phys. Control. Fusion 42 A15
- [104] Connor J W et al., 2004 Nucl. Fusion 44 R1
- [105] Bateman G et al., 2003 Plasma Phys. Control. Fusion 45 1939
- [106] Onjun T et al., 2005 Phys. Plasmas 12 082513
- [107] Onjun T et al., 2008 J. of Physics: Conference Series 123 012034
- [108] Tharasrisuthi K *et al.*, 2008 Thammasat International Journal of Science and Tech. **13**45
- [109] Picha R *et al.*, 2008 Proc. 35th EPS Conf on Plasma Physics, Hersonissos 9-13 June 2008
- [110] Halpern, F.D. et al., 2008, Phys. Plasmas 15 062505
- [111] Budny, R.V. et al., 2008 Nucl. Fusion 48 075005
- [112] Roach C M et al., 2008 Nucl. Fusion 48 125001
- [113] Hannum D et al., 2001 Phys. Plasmas 8 964
- [114] Onjun T et al., 2001 Phys. Plasmas 8 975

- [115] Sugihara M et al., 2003 Plasma Phys. Control. Fusion 45 L55
- [116] Zhu P et al., 2000 Phys. Plasmas 7 2898
- [117] Tala T J J et al., 2001 Plasma Phys. Control. Fusion 43 507
- [118] Kinsey J E et al., 2005 Phys. Plasmas 12 052503
- [119] Parail V V et al., 1999 Nucl. Fusion 38 429
- [120] Parail V V, 2002 Plasma Phys. Control. Fusion 44 A63
- [121] Tala T J J et al., 2002 Plasma Phys. Control. Fusion 44 A495
- [122] Tala T V V et al., 2005 Nucl. Fusion 45 1027
- [123] Tala T et al., 2006 Nucl. Fusion 46 548
- [124] Onjun T et al., 2002 Phys. Plasmas 9 5018
- [125] Sugihara M et al., 2000 Nucl. Fusion 40 1743
- [126] Osborne T H et al. 1999 Journal of Nuclear Materials 266-269 131
- [127] Kritz A et al., 2004 Comput. Phys. Comm., 164, 108; http://w3.pppl.gov/NTCC
- [128] Singer C E et al., 1988 Comput. Phys. Commun. 49 399
- [129] Onjun T et al., 2008 J. of Physics: Conference Series 123 012014
- [130] Shimomura Y et al., 2000 Proc. 18th IAEA Conf. (Sorrento, Italy)
- [131] Houlberg W A et al., 1997 Phys. Plasmas 4 3231
- [132] Porcelli F et al., 1996 Plasma Phys. Control. Fusion 38 2163
- [133] Bateman G et al., 2006 Phys. Plasmas 13 072505
- [134] Kessel C E et al. 2006 Proc. 21st Fusion Energy Conference (Chengdu, China, 2006)
 Nucl. Fusion (Vienna: IAEA) Paper IT/P1-7
- [135] Onjun T et al., 2004 Phys. Plasmas 11 1469
- [136] Aymar R, Barabaschi P, Shimomura Y (2002) The ITER design *Plasma Phys. Control.*Fusion **44** 519
- [137] Tala T, Garbet X and JET EFDA contributors (2006) Physics of Internal Transport Barriers. C. R. Physique **7** 622
- [138] Nakamura H, Dietz J and Ladd P (1996) Gas and pellet fuelling in ITER Vacuum 47 969
- [139] Kuteev B V (1999) Pellet-injection-based technologies for fusion reactors *Tech. Phys.*44 1058
- [140] Yang Y, Bao Y, Jiangang L, *et al.*, (1999) Pellet injection research on the HT-6M and HT-7 tokamaks *Nucl. fusion* **39** 1871

- [141] Pegourie B (2007) Review: Pellet injection experiments and modelling *Plas. Phys. Cont. Fusion* **49** R87
- [142] Belonohy E, Kardaun O.J.W.F, Fehér T, et al., (2008) A high field side pellet penetration depth scaling derived for ASDEX Upgrade *Nucl. Fusion* **48** 065009
- [143] Gohil P, Evans T.E, Ferron J.R, et al., (2006) Control of plasma profiles in DIII-D discharges *Plas. Phys. Cont. Fusion* **48** A45
- [144] Rozhansky V, Senichenkov I, Veselova I, et al., (2004) Mass deposition after pellet injection into a tokamak *Plas. Phys. Cont. Fusion* **46** 575
- [145] Baylor L R, Geraud A, Houlberg W.A, et al., (1997) An international pellet ablation database Nucl. Fusion 37 445
- [146] Lengyel L L, Schneider R, Kardaun O.J.W.E, et al., (2008) Pellet Plasma Interaction: an Analysis of Pellet Injection Experiments by Means of a Multi-Dimensional MHD Pellet Code Contrib. Plasma. Phys. 48 623
- [147] Milora S L, Houlberg W A, Lengyel L L, et al., (1995) Pellet fuelling Nucl. Fusion 35
- [148] Wisitsorasak A and Onjun T (2009) Submitted to Nucl. Fusion
- [149] Garzotti L, et al., (2004) In the proc. of the 31st EPS Conference on Plasma Phys., London, ECA 28G P-1.147
- [150] Frigione D, et al., (2003) In the proc. of the 30th EPS Conference on Controlled Fusion and Plasma Phys., St. Petersburg, ECA 27A P-2.91
- [151] Garzotti L, et al., (2003) In the proc. of the 30th EPS Conference on Controlled Fusion and Plasma Phys., St. Petersburg, ECA 27A P-2.92
- [152] Higashiyama Y, Yamazaki K, Garcia J, et al., (2008) Internal Transport Barrier Formation and Pellet Injection Simulation in Helical and Tokamak Reactors Plasma Fusion Res. 3 S1048
- [153] Milora S L (1983) Oak Ridge National Laboratory Report: New algorithm for computing the ablation of hydrogenic pellets in hot plasmas ORNL/TM-861631
- [154] Tala T J J, Parail V V, Becoulet A, et al., (2002) Comparison of theory-based and semiempirical transport modelling in JET plasmas with ITBs Plasma Phys. Control. Fusion 44 A495
- [155] Onjun T, Bateman G, Kritz AH, et al., (2002) Models for the pedestal temperature at the edge of *H*-mode tokamak plasmas *Physics of Plasmas* **9** 5018

- [156] Sugihara M, Igitkhanov Yu, Janeschitz G, et al., (2000) A model for H mode pedestal width scaling using the International Pedestal Database *Nucl. Fusion* **40** 1743
- [157] Singer C E, Post D.E, Mikkelsen D. R, et al., (1988) Baldur: A one-dimensional plasma transport code Comput. Phys. Commun. 49 399
- [158] Hannum D, Bateman G, Kinsey J, et al., (2001) Comparison of high-mode predictive simulations using Mixed Bohm/gyro-Bohm and Multi-Mode MMM95 transport models Physics of Plasmas 8 964
- [159] Onjun T, Bateman G, Kritz AH, et al., (2001) Comparison of low confinement mode transport simulations using the mixed Bohm/gyro-Bohm and the Multi-Mode-95 transport model *Physics of Plasmas* **8** 975
- [160] Milora S L and Foster C A (1978) IEEE Transactions on Plasma Science 6 578
- [161] Houlberg W A, Attenberger S.E, Baylor L.R, et al., (1992) Pellet penetration experiments on JET *Nucl. Fusion* **32** 1951
- [162] Tala T J J, Heikkinen J.A, Parail V.V, et al., (2001) ITB formation in terms of $\omega_{\text{E}\times\text{B}}$ flow shear and magnetic shear s on JET Plas. Phys. Cont. Fusion 36 507
- [163] Erba M, Cherubini A, Parail VV, et al., (1997) Development of a non-local model for tokamak heat transport in L-mode, H-mode and transient regimes Plasma Phys. Control. Fusion 39 261
- [164] Taroni A, Erba M, Springmann E, et al., (1994) Global and local energy confinement properties of simple transport coefficients of the Bohm type Plasma Phys. Control. Fusion **36** 1629
- [165] Erba M, Parail V, Springmann E, et al., (1995) Extension of a Bohm model for L-mode electron heat transport to ion heat transport and to the ohmic regime Plas. Phys. Cont. Fusion 37 1249
- [166] Erba M, Aniel T, Basiuk V, et al., (1998) Validation of a new mixed Bohm/gyro-Bohm model for electron and ion heat transport against the ITER, Tore Supra and START database discharges Plasma Phys. Control. Fusion 38 1013
- [167] Pankin A Y,Voitsekhovitch I, Bateman G, et al., (2005) Combined model for the *H*-mode pedestal and ELMs *Plasma Phys. Control Fusion* **47** 483
- [168] Zhu P, Bateman G, Kritz AH, et al., (2000) Predictive transport simulations of internal transport barriers using the Multi-Mode model *Phys. Plasmas* **7** 2898
- [169] Chatthong B and Onjun T (2009) Prepared for submission in Nucl. Fusion

- [170] Onjun, T, Tharasrisuthi K, Pankin AY, et al., (2008) Projected performance of ITER based on different theoretical based pedestal temperature models J. of Physics: Conference Series 123 012034
- [171] Sugihara M, Mukhovatov V, Polevoiet A, et al., (2003) Scaling of H-mode edge pedestal pressure for a Type-I ELM regime in tokamaks Plasma Phys. Control. Fusion 45 L55
- [172] Bateman G, Onjun T, Kritz AH (2003) Integrated predictive modelling simulations of burning plasma experiment designs *Plasma Phys. Control. Fusion* **45** 1939
- [173] Aymar R, Barabaschi P, Shimomura Y (2002) The ITER design Plasma Phys. Control. Fusion **44** 519
- [174] Fulop T and Weiland J (2006) Impurity transport in ITER-like plasma Phys. Plasmas. **13** 112504.
- [175] Post, D. and S. Cohen, ITER Physics, 1990. ITER Physics Group and IAEA.
- [176] Yamada, I., et al., (2008) Transport analysis of high-Z impurity with MHD effects in tokamak system. Proceedings of ITC 18 P1-27 242
- [177] Davis, J.W. and A.A. Haasz (1997) Impurity release from low-Z materials under light particle bombardment J. of Nucl. Mater 241 37
- [178] Hogan, J (1997) Helium transport and exhaust experiments in tokamaks J. of Nucl. Mater 241 68
- [179] Burbaumer H, Kamelander G, Sigmar D.J, et al. (1999) Helium Oscillations in Burning Tokamaks Fusion Tech 35 280
- [180] Onjun, T. and Y. Pianroj (2009) Simulations of ITER with combined effects of internal and edge transport barriers Nucl. Fusion 49 075003
- [181] Leekhaphan, P. and T. Onjun, sumitted to Thammasat International Journal of Science and Technology.
- [182] Parail V, Belo P, Boerner P, et al. (2009) Intergrated modelling of ITER reference scenarios Nucl. Fusion 49 075030
- [183] Singer C E, Post D.E, Mikkelsen D. R, et al. (1988) Baldur: A one-dimensional plasma transport code Comput. Phys. Commun. **49** 399
- [184] Hannum D, Bateman G, Kinsey J, et al. (2001) Comparison of high-mode predictive simulations using Mixed Bohm/gyro-Bohm and Multi-Mode MMM95 transport models Physics of Plasmas 8 964

- [185] Onjun T, Bateman G, Kritz AH, et al. (2001) Comparison of low confinement mode transport simulations using the mixed Bohm/gyro-Bohm and the Multi-Mode-95 transport model Physics of Plasmas **8** 975
- [186] Nordman, H., J. Weiland, and A. Jarmen (1990) Nucl. Fusion 30 983
- [187] Weiland J and Hirose A (1992) Electromagnetic and kinetic effects on the ion temperature gradient mode Nucl. Fusion **32** 151
- [188] Nilsson J. and Weiland J (1994) Fluid model for general collisionality and magnetic curvature Nucl. Fusion **34** 803
- [189] Kinsey J.E, Bateman G, Arnold H.K, et al. (1996) Comparison of two resistive ballooning mode models in transport simulations Phys. Plasmas **3** 561
- [190] Guzdar, P.N, Drake J.F, McCarthy D, et al. (1993) Three-dimensional fluid simulations of the nonlinear drift-resistive ballooning modes in tokamak edge plasmas Phys. Fluids B 5 3712
- [191] Bateman G, Arnold H.K, Kinsey J.E, et al. (1998) Predicting temperature and density profiles in tokamaks Phys. Plasmas **5** 1793
- [192] Houlberg WA, Shaing KC, Hirshman SP, et al. (1997) Bootstrap current and neoclassical transport in tokamaks of arbitrary collisionality and aspect ratio Physics of Plasmas 4 3231
- [193] Bateman G, Onjun T, Kritz AH (2003) Integrated predictive modelling simulations of burning plasma experiment designs Plasma Phys. Control. Fusion **45** 1939
- [194] Onjun T, Bateman G, Kritz AH, et al. (2005) Magnetohydrodynamic-calibrated edgelocalized mode model in simulations of International Thermonuclear Experimental Reactor, Physics of Plasmas 12 082513
- [195] Onjun T, Tharasrisuthi K, and Onjun O (2008) Projected performance of international thermonuclear experimental reactor Tokamak based on different pedestal width scalings J. of Physics: Conference Series **123** 012034

งานวิจัยในโครงการนี้ได้ตีพิมพ์ในวารสารวิชาการระดับนานาชาติดังนี้

- 1. Pianroj Y and **Onjun T**, "Pedestal transport model based on suppression of anomalous transport using $\omega_{E\times B}$ flow shear and magnetic shear," submitted to *Nuclear Fusion*
- 2. Leekhaphan P, and **Onjun T**, "Pellet Injection into H-mode ITER Plasma with the Presence of Internal Transport Barriers (2011); **37(4)**, 321-337 (IF = 0.584)
- 3. Wisitsorasak A, and **Onjun T**, "Impacts of Pellets Injected from the Low Field Side on Plasma in ITER," Plasma Physics Reports (2011); **37(1)**, 1-18 (IF = 0.584)
- Pianroj Y, Chuchinda C, Leekhaphan P, and Onjun T, "Behaviors of Impurity in ITER
 Plasma with Standard Type I ELMy H-mode and Steady State Scenarios," Plasma
 Physics Reports (2010); 36(10), 827 (IF = 0.584)
- Chatthong B, Onjun T, and Singhsomroje W, "Model for toroidal velocity in H-mode plasmas in the presence of internal transport barriers," *Nuclear Fusion* (2010); 50: 064009 (IF = 4.27)
- 6. **Onjun T**, "ITER Performance Study with the Presence of Internal Transport Barrier,"

 Journal of Plasma and Fusion Research Series (2009); 8: 347
- 7. **Onjun T** and Pianroj Y, "Simulations of ITER with combined effects of internal and edge transport barriers," *Nuclear Fusion* (2009); **49**: 075003 (IF = 4.27)

งานวิจัยในโครงการนี้ได้ตีพิมพ์ในวารสารวิชาการระดับชาติดังนี้

- 1. Leekhaphan P and **Onjun T**, "Impurity Transport and Helium Accumulation in ITER" Thammasat International Journal of Science and Technology (2010); **15**(3), 47-68
- 2. **Onjun T** "The Effects of E_rxB Flow Shear Profile on the Formation of Internal Transport Barrier in ITER" Thammasat International Journal of Science and Technology (2009); **14(3)**, 14

ได้ตีพิมพ์เป็น Proceeding ของการประชุมวิชาการระดับนานาชาติดังนี้

- 1. Chatthong B, **Onjun T**, *et al.*, "Simulations of ITB *H*-Mode Tokamak Plasmas with Predictive Toroidal Velocity Model" in *Proc.* 1st TSME International Conference on Mechanical Engineering, 20-22 October, 2010, Ubon Ratchathani, Thailand
- Klaywitthaphat P, Onjun T, et al., "Simulation of ITER plasma during pellet injection" in Proc. 1st TSME International Conference on Mechanical Engineering, 20-22 October, 2010, Ubon Ratchathani, Thailand
- 3. Pianroj Y, **Onjun T**, *et al.*, "Preliminary results of core-edge simulations of *H*-mode tokamak plasmas using BALDUR and TASK codes" in *Proc.* 1st TSME International Conference on Mechanical Engineering, 20-22 October, 2010, Ubon Ratchathani, Thailand
- Klaywitthaphat P, Onjun T, et al., "Scaling of Density Peaking for Plasma with Pellet Injection," in Proc. 23nd IAEA Fusion Energy Conf., 11-16 October 2010 Daejon, Rep. of Korea
- 5. Pianroj Y, Chatthong B, **Onjun T**, *et al.*, "Core-edge simulations of *H*-mode tokamak plasma using BALDUR and TASK codes," in *Proc. 23nd IAEA Fusion Energy Conf.*, 11-16 October 2010, Daejon, Rep. of Korea
- 6. Chuchinda C, **Onjun T**, *et al.*, "Impurity behaviours in ITER plasmas with standard type I ELMy *H*-mode before and after heating phase," in *Proc. 37th EPS Conference on Plasma Phys.*, 21 25 June 2010, Dublin, Ireland, (P1.1052)
- 7. Chatthong B, **Onjun T**, *et al.*, "Comparison of Toroidal Velocity Models Using Integrated Predictive Modeling Code in ITB *H*-Mode Plasma," in *Proc. 37th EPS Conference on Plasma Phys.*, 21 25 June 2010, Dublin, Ireland, (P1.1079)
- 8. Siriwitpreecha A, **Onjun T**, *et al.*, "Development of dynamic boundary density models with hydrogenic and impurity densities in *H*-mode scenarios," in *Proc. 37th EPS Conference on Plasma Phys.*, 21 25 June 2010, Dublin, Ireland, (P2.153)
- 9. Klaywittaphat P, **Onjun T**, *et al.*, "Simulations of ITER plasma during pellet injection," in *Proc. 37th EPS Conference on Plasma Phys.*, 21 25 June 2010, Dublin, Ireland, (P5.158)

ภาคผนวก

Pedestal transport model based on suppression of anomalous transport using $\omega_{E\times B}$ flow shear and magnetic shear

Y. Pianroj and T. Onjun

School of Manufacturing Systems and Mechanical Engineering, Sirindhorn International Institute of Technology, Thammasat University, Pathum Thani, 12121, Thailand

E-mail: thawatchai@siit.tu.ac.th

Abstract. A model for describing a pedestal transport in H-mode tokamak plasmas is developed and tested in BALDUR integrated predictive modelling code. The transport model is calculated based on the suppression of an anomalous core transport due to the $\omega_{E\times B}$ flow shear and magnetic shear. The radial electric field for the $\omega_{E \times B}$ flow shear is estimated using a complete force balance, which includes the pressure gradient term, toroidal velocity term, and poloidal velocity component term. Because of the reduction of transport in the pedestal region, the pedestal can be formed and evolved. In this work, an anomalous transport is computed using a semi-empirical Mixed Bohm/gyro-Bohm transport model. The BALDUR code with both core and pedestal transport is used to simulate a time evolution of plasma current, ion and electron temperature, and particle and impurity density profiles for 10 DIII-D tokamaks in various H-mode plasma scenarios (i.e. gyro-radius scan, density scan, power scan, and elongation scan). It is found that the formation of the pedestal can be seen in all simulations, in which the L-H transition behaviours are consistent with the L-H transition power threshold and bifurcation models. Moreover, both values at the top of the pedestal and the pedestal width for ion and electron temperatures and particle and impurity densities are all in the ranges expected for the experimental data and are also in the agreement with several existing pedestal scaling (i.e. flow and magnetic shear stabilization with scaling, normalized poloidal beta width scaling, and neutral penetration width scaling). To quantify the agreement between the simulated core-edge profiles and the corresponding experiment, several statistical analysis techniques, including RMS and offset, are carried out. It is found that the simulated profiles yield an agreement with experimental data in the ranges from 7.45% to 17.39% for density and temperature, respectively, which is slightly worse than those using experimental data at the top of the pedestal as boundary conditions. In addition, a cross comparison technique is used to confirm the predictive capability of the model by using a comparison with 12 JET H-mode discharges. It shows that the predicted plasma profiles yield satisfactory agreement.

Keywords: Plasma, Tokamak, Fusion, Pedestal, H-mode, ITER

1. Introduction

After the discovery of a new operation regime called the "High confinement mode" (*H*-mode) [1] in 1982, this regime has been commonly operated in many experiments from different tokamak around the world due to the significantly increase of plasma temperature and density, and energy confinement time. The enhancement of plasma performance mainly results from the formation of transport barrier at the edge of the plasmas, usually referred as the edge transport barrier (ETB) or "pedestal".

Typically, the energy content in an H-mode discharge is approximately twice the energy contained in an L-mode discharge, for the similar plasma with the same input power [2]. Advanced computer codes are developed to improve understanding of the physical processes and the interrelationships between those physical processes that occur in tokamak H-mode plasma experiments,. The integrated predictive modelling codes, such as BALDUR [3], TASK/TR [4], JETTO [5], ASTRA [6] and CRONOS [7], have played an important role in carrying out simulations in order to predict the time evolution of plasma current, temperature, and density profiles. In fact, many of the simulations carried out with these integrated predictive modelling codes normally make use of boundary conditions usually been taken at the top of the pedestal from experimental data. As a result, it limits predictive capability of the codes, especially for the prediction of future experiments like ITER. For example, in Refs. [8-13], the evolution of the core plasma profiles in H-mode conditions was carried out using boundary conditions taken from experimental data at the top of the pedestal. It was found that their predictions depend sensitively on the choice of the pedestal conditions used. This indicates the need for reliable method for predicting boundary conditions of the integrated predictive modelling in order to advance the predictive capability, which is essential in designing future experiments for existing and future tokamaks.

One of reliable theoretical based approach for predicting a pedestal is to apply the concept of the reduction of a pedestal transport, which can be occurred due to a stabilization or decorrelation of microturbulence in the edge plasma. The stabilization mechanisms, which can suppress turbulent modes, have to take into an account for the different dynamical behaviors of the various species in the plasma. The first candidate for edge turbulence stabilization is the stabilization by the $\omega_{E\times B}$ flow shear. The $\omega_{E\times B}$ flow shear can suppress turbulence by linear stabilization of turbulent modes, and in particular by non-linear decorrelation of turbulence vortices [14-16], thereby reducing transport by acting on both the amplitude of the fluctuations and the phase between them [17]. The second candidate is the magnetic shear stabilization, which is reduced only in the region where the magnetic shear exceeds its threshold. In the past, the $\omega_{E\times B}$ flow shear and the turbulence correlation time were used to suppress the ion and electron thermal diffusivity carried out by the multimode core transport model. This work was done and it was implemented in the ASTRA code by A.Y.Pankin et al [18]. In Ref.[18], the suppression functions for ion and electron transports are extended to the Multi Mode core transport Model (MMM) to describe the pedestal formation. But the density and impurity transports are not suppressed. Similar work was carried out by G. W. Pacher et al [19] by implementing the suppression function which consists of two stabilization candidate terms into ASTRA code. The pedestal formation was also studied using JETTO code [20-24], in which anomalous transport is assumed to be completely suppressed in the pedestal region. However, the pedestal width is predicted using some scalings. In this work, the anomalous core transport model, Mixed Bohm/gyro-Bohm (Mixed B/gB), is extended for describing the transport in the pedestal region. The anomalous transport is suppressed by both $\omega_{E\times B}$ flow shear and magnetic shear in every channel of transport coefficients: electron thermal diffusivity, ion thermal diffusivity, hydrogenic mass diffusivity and impurity mass diffusivity. As a result, the pedestal can be formed.

This paper is organized as follows: the extension of anomalous core transport model for the pedestal transport will be described in section 2. In section 3, the calibration and the sensitivity of coefficient C_x and the simulation results for standard H-mode will be validated by statistical comparisons with the experimental data from DIII-D tokamak. The final section is the conclusion.

2. Modeling of pedestal formation

The aim of this modelling is to develop a model for a self-formation of the pedestal and the detailed structure of the pedestal including the pedestal width and height for the plasma density (both hydrogen and impurity) and temperature (both ion and electron). This modelling inevitably requires the full

integration of core and edge plasmas since the two regions have a great deal of interactions. One of the many difficulties is that there exist various physical mechanisms with different time scales, which takes place in both regions. For example, the pedestal structure evolves on a transport time scale. However, during this evolution, magnetohydrodynamic (MHD) phenomena with very short time scales occur, as from type-I edge localized modes (ELMs) [25]. The occurrence of an MHD event (ELM) burst produces a significant pulsed flow of particles and energy onto the divertor target, diminishing the edge pressure gradients in the process. Thus, this modelling has not yet clearly developed. In recent studies, A. Yoshizawa et al. [26] started to derive the turbulent suppression by $\omega_{E\times B}$ flow shear with the turbulent transport coefficient, which was suggested by Ref. [27]. It is composed of the liner growth rate in the absence of flow shear, the $\omega_{E\times B}$ flow shear, the shear of diamagnetic flow, and the damping rate of a representative beat mode, then treated in the case of selfsustaining turbulence. The thermal diffusivity has been derived for Current Diffusive Interchange Mode (CDIM) [28] in toroidal geometry such as Current Diffusive Ballooning Mode (CDBM) turbulence. Finally, the toroidal flow in tokamaks varies in the poloidal direction if a hot ion component exists. This poloidal dependence suppresses nonlinear turbulence [29], so the turbulence transport coefficient for Ion Temperature Gradient (ITG) mode, which is suppressed by $\omega_{E\times B}$ flow shear, is expressed in Eq.1:

$$\chi_{turb} \propto \frac{1}{1 + (\omega_{E \times R}/\gamma)^h}$$
(1)

where, γ is the instability growth rate in the absence of flow shear and h is an index. The index is given as h = 2 [28, 30] and $h = \frac{2}{3}$ [14]. Moreover, Figarella *et al* [31] used a suppression form in Eq.2 that the anomalous transport is caused by the resistive pressure-gradient with difference indexes.

$$f(\omega_{E\times B}) \sim \frac{1}{1 + (\tau_{co}\omega_{E\times B})^h} \tag{2}$$

where, τ_{c_0} is the correlation time of the fluctuations for the case without flow. A appropriate transport suppression function (f_s) due to $\omega_{E\times B}$ flow shearing rate together with the reduction of turbulence growth rate [18, 32, 33] is represented in the first term. However, the $E\times B$ flow shear alone produces pedestals which are appreciably lower than those experimentally obtained. Therefore, an additional magnetic shear stabilization also reduces the geodesic curvature drive of micro-instabilities, such as ITG, TEM, and high n ballooning modes [34, 35], as well as the stabilizing magnetic shear effect, is related to ITG thermal diffusivity [36] and the number of high radial ITG modes [37]. Hence, the second term of suppression function has magnetic shear stabilization in the form $s^{-1.8}$ [38, 39],or the transport is reduced only in the region where the magnetic shear exceeds the threshold. In this work, the threshold is set to be equal to 0.5, which is similar to the numerical value in Ref. [19]. Thus, the suppression function used in this work can be written as follows:

$$f_{S_x} = \frac{1}{1 + C_x \left(\frac{\omega_{E \times B}}{\gamma_{ITG}}\right)^2} \times \frac{1}{\max(1, (s - 0.5)^2)}$$
(3)

where, C_x is the optimization coefficient for each transport channels $\gamma_{\rm ITG}$ is the liner ion temperature gradient (ITG) growth rate, and s is the magnetic shear. Note that the value of C_x used is chosen to optimize the plasma profiles from simulations and corresponding experimental data. The methods that are used to find these coefficients are described in the next section. Therefore, by using the suppression function, every channel of transport is suppressed. The suppression of ion thermal diffusivity (χ_{e_s}), suppression of hydrogenic particle diffusivity (D_{H_s}) and suppression of impurity particle diffusivity (D_{Z_s}), are given by Eq.4-7.

$$\chi_{i_S} = \chi_i \times f_{S_{ion}} \tag{4}$$

$$\chi_{e_s} = \chi_e \times f_{Selectron} \tag{5}$$

$$\chi_{e_s} = \chi_e \times f_{s_{electron}}$$

$$D_{H_s} = D_H \times f_{s_{Hydrogenic}}$$
(5)
(6)

$$D_{z_{\rm S}} = D_{\rm z} \times f_{s_{imnurity}} \tag{7}$$

Moreover, the anomalous core transport is described using the Mixed B/gB transport model. The Mixed B/gB transport model can be expressed as follows [40]:

$$\chi_{\rm e} = 1.0\chi_{\rm gB} + 2.0\chi_{\rm B} \tag{8}$$

$$\chi_{\rm i} = 0.5\chi_{\rm gR} + 4.0\chi_{\rm R} + \chi_{\rm neo} \tag{9}$$

$$D_{\rm H} = [0.3 + 0.7\rho] \frac{\chi_{\rm e} \chi_{\rm i}}{\chi_{\rm o} + \chi_{\rm i}} \tag{10}$$

$$\chi_{i} = 0.5\chi_{gB} + 4.0\chi_{B} + \chi_{neo}$$

$$D_{H} = [0.3 + 0.7\rho] \frac{\chi_{e}\chi_{i}}{\chi_{e} + \chi_{i}}$$

$$D_{z} = [0.3 + 0.7\rho] \frac{\chi_{e}\chi_{i}}{\chi_{e} + \chi_{i}}$$
(10)

where,

$$\chi_{\rm gB} = 5 \times 10^{-6} \sqrt{T_{\rm e}} \left| \frac{\nabla T_{\rm e}}{B_{\rm A}^2} \right| \tag{12}$$

$$\chi_{gB} = 5 \times 10^{-6} \sqrt{T_e} \left| \frac{\nabla T_e}{B_{\phi}^2} \right|$$

$$\chi_B = 4 \times 10^{-5} R \left| \frac{\nabla (n_e T_e)}{n_e B_{\phi}} \right| q^2 \left(\frac{T_{e,0.8} - T_{e,1.0}}{T_{e,1.0}} \right)$$
(12)

where, $\chi_{\rm e}$ is the electron diffusivity, $\chi_{\rm i}$ is the ion diffusivity, D_H is the particle diffusivity, D_Z is the impurity diffusivity, $\chi_{\rm gB}$ is the gyro-Bohm contribution, $\chi_{\rm B}$ is Bohm contribution, ρ is normalized minor radius, T_e is the electron temperature in keV, B_{ϕ} is the toroidal magnetic field, R is the major radius, n_e is the local electron density, q is the safety factor, s is the magnetic shear, $\omega_{E\times B}$ is the flow shearing rate, and γ_{ITG} is the linear ion temperature gradient (ITG) growth rate, estimated as v_{ti}/R [41], in which v_{ti} is the ion thermal velocity. In this work, the Chang-Hinton neoclassical transport models [42] that includes finite inverse aspect ratio effects, whereas this model that explicitly deals with impurities. Some dilution effects (effective charge (Z_{eff}) is not equal to 1), have been incorporated into the other models. These corrections seem to be limited to values of Z_{eff} close to unity. It is crucial to mention that in this work, the effect of ELMs is not included. The pedestal is allowed to grow and limited by the transport properties. The constant C_x is chosen to adjust the agreement. In some ways, one can think that the constant C_x somewhat includes the ELMs effect.

3. Calibration for the coefficients C_x

The BALDUR code with the pedestal transport model based on the extension of anomalous core transport model with $\omega_{E\times R}$ flow shear and magnetic shear effects described in section 2 are used to carry out core-edge simulations of 10 DIII-D H-mode discharges obtained from the International Profile Database [43]. These experimental data can be classified into four pairs of H-mode plasma scans and their major plasma parameters are listed in Table 1. The plasma scans considered include plasma power scans (77557 and 77559), density scans (81321 and 81329), elongation scans (81499 and 81507), and gyro-radius scans (82205 and 82788). In this work, the boundary conditions for the core-edge simulations are taken to be a fixed value at the separatrix, in which it is assumed that the separatrix temperature is 10 eV and the separatrix density is $1 \times 10^{17} \,\mathrm{m}^{-3}$ in all simulations. Note that it was found that a choice of separatrix temperature and density does not affect the simulation results.

In this pedestal transport model, the coefficients (C_x) of ion and electron thermal transports and hydrogenic and impurity transports in Eq.3 can be adjusted. These coefficients are used to optimize the agreement between the simulations and their corresponding experimental data. In this work, four possible choices of agreement are considered. The first choice is to minimise agreement of the whole plasma profiles between simulations and experimental data. The second method is to minimise agreement of the edge region profiles (for example, from $\rho = 0.9$ to $\rho = 1.0$) between simulations and experimental data. The third choice is to minimize agreement of the value at top of the pedestal temperature. The last choice is to minimize agreement of the value at top of the pedestal density. The agreement between simulations and experiment can be quantified in term of the root-average-square (RMS) deviation or the root-average-square error (RMSE), which are used in the previous works by [13] and [20], respectively. The RMS and RMSE are defined as follows:

RMS(%) =
$$\sqrt{\frac{1}{N} \sum_{i=1}^{N} \left(\frac{X_{sim_i} - X_{exp_i}}{X_{exp_0}} \right)^2} \times 100$$
 (14)

RMSE(%) =
$$\sqrt{\frac{1}{N-1} \sum_{j=1}^{N} (\ln(X_{\exp_j}) - \ln(X_{\sin y_j}))^2}$$
 (15)

where, X_{exp_i} is the i^{th} data point of the experimental profile, X_{sim_i} is the corresponding data point of the simulation profile, and X_{exp_0} is the maximum data point of the experimental profile of X as a function of radius, which has N total number of data points.

Figure 1 shows the average RMSs from different optimization choices when different values of the coefficient (C_x) is varied. In each panel, the coefficient of electron thermal transport (top-left), ion thermal transport (top-right), particle transport (bottom-left), and impurity transport (bottom-right) is varied one at the time while other coefficients are held fixed. It can be seen that the average of RMS(%) separates into two groups. The first group is the results from whole plasma profiles or the edge region profiles comparison. For this group, the average of RMS is calculated by Eq. 14 (RMSE%). Another group is the comparison of value at top of pedestal temperature or pedestal density. In this group, the average of RMS is calculated by Eq. 15 (RMSE%), which picks up only one data point at the top pedestal of 10 DIII-D discharges. Nevertheless, the optimization point of the coefficients by difference methods occur at almost the same point, in which the exact values are summarized in Table 2. For simplicity, the set of C_x used in the rest of this paper are based on the optimization using 10% of edge data.

The impacts of the value of coefficients on the prediction of plasma profiles are shown in Fig.2 for DIII-D discharge 82205. It depicts the set of coefficients C_x that is used in this work, the set of coefficients C_x that is less than ten times of C_x (0.1 C_x), and the set of coefficients C_x that is more than five times of $(5.0C_x)$. It is shown that the set of coefficients C_x , which is used in this work, presents the best fit to the experimental data for both thermal and density. When the set of $0.1C_x$ is applied, it affects the electron and ion temperature to be underpredict the experimental data; because, the pedestal is not formed steeply, so the core region is lower than that shows in the experimental data. In the case of electron and deuterium density, it is not quite difference from the experimental data. On the other hand, when the set of $5.0C_x$ is applied to the simulation, it affects to the electron and ion temperature to be overpredict the experimental data. Because, the pedestal height and width are extremely overpredict the experimental data, so the simulation inside the core region badly overpredicts.

The simulation results carried out by the core-edge model of BALDUR code with 10% edge area method of the optimization coefficients set (C_x) is validated with ten DIII-D experimental data by using statistical analysis which is the results of RMS and offset are presented in Figs.3 and 4. Note that the offset is defined as below.

offset(%) =
$$\frac{1}{N} \sum_{i=1}^{N} \left(\frac{X_{sim_i} - X_{exp_i}}{X_{exp_0}} \right) \times 100$$
 (16)

when the offset is positive, it can be indicated that the simulated profile is systematically higher than the experimental profile and negative if the simulated profile is systematically lower than the experimental profile. In these figures, the RMS of the electron temperature ranges from 6.31% to 28.18% in which the average value is 13.48%; as well as, the offsets of electron temperature are mostly positive, indicating that simulation overpredict the experimental data. Moreover, in the case of ion temperature, the RMS ranges from 5.73% to 29.49% and the average value of RMS is 17.39%, also the offsets are mostly negative. This indicates that the simulation data underpredict the experimental data in this case. For electron density, the RMS ranges from 3.08% to 13.38% and the average value of RMS is 7.45, also the offsets are mostly negative, indicating that simulation underpredict the experimental data. Finally, the RMS of the deuterium temperature ranges from 4.73% to 18.55% and the average value is 12.41%; as well as, the offsets of deuterium density are mostly positive, indicating that simulation overpredict the experimental data. Fig. 5 shows the comparison of electron temperature, ion temperature, electron density and deuterium density profiles as a function of minor radius obtained from simulations and experimental data for DIII-D discharges in the gyro-radius scan. It can be seen that all simulated profiles are in the range of experimental data. This agreement occurs in both core and pedestal region. The mechanism that is used to stabilize the anomalous transport for triggering an edge transport barrier can be seen by the suppression function that is shown in Fig.6 (discharge 82205 low ρ^*). This function is composed of two terms which suppressed the turbulent transport. The first term is shear, in which the $E \times B$ flow velocity likely plays a role to reduce the turbulent transport. It can be seen that the suppression function is inactive at the normalized minor radius (r/a) = 0.9-1.0. The effect of $E \times B$ flow shear stabilization is considered to be important in allowing transport barrier formation. To demonstrate this effect appropriately, the radial electric field (E_r) shows greater strength near the edge area (at normalized minor radius 0.9). Thus, the radial electric field will affect the $\omega_{E\times B}$ flow shear that is depicted in Eq.17 [44].

$$\omega_{E \times B} = \frac{(RB_{\theta})^2}{B_{\phi}} \left(\frac{\partial}{\partial \psi}\right) \frac{E_r}{RB_{\theta}} \tag{17}$$

where, R is the major radius, B_{θ} is the poloidal magnetic field, and B_{ϕ} is the toroidal magnetic field. The $\omega_{E\times B}$ flow shear calculated by the predictive modelling codes is shown in Fig.6, and shows the same trend as the radial electric field pattern where the magnitude is very strong at the plasma edge. The last term, the magnetic shear also plays a key role in facilitating entry into enhanced confinement or low magnetic shear acts to reduce turbulence growth rates [25, 27]. Thus, the magnetic shear profiles are also shown in Fig.6. The magnetic shear profiles increases swiftly at r/a = 0.6-1.0. Therefore, the inverse of maximum function between 1.0 to $(s - 0.5)^2$ of this term works to suppress the plasma edge area, too.

4. Simulation results and discussions

4.1 Comparison for L-H transition with power threshold model

The nuclear fusion performance of tokamak plasmas can be significantly improved after achieving H-mode regime. It is widely observed in experiments from various tokamaks that a transition from L-mode to H-mode (L-H transition) requires adequate auxiliary heating power. To demonstrate this plasma behavior, two discharges as the gyro-radius scan are considered. In these discharges, the neutral beam injection (NBI) power is applied at 1.5 sec with the power of 6.3 MW for the low ρ^* discharge and 3.3 MW for the high ρ^* discharge, as shown in Fig.7. It can be seen that the simulated

plasmas in both simulations can illustrate an *L-H* transition, indicating by an enhancement of plasma density and plasma stored energy. Both electron density (both at the center and on average) and plasma stored energy rise rapidly after the auxiliary heating is turned on. Note that the rise of density and energy indicates a better plasma confinement. The *L-H* transition observed is in agreement with the prediction from *L-H* power threshold model that plasma can make an *L-H* transition when heating power exceeds power threshold. Note that the power threshold for the transition from *L*-mode to *H*-mode expresses in the following empirical expression [45]:

$$P_{L-H}[MW] = 2.84 M_{AMU}^{-1} B_T^{0.82} n_{e,20}^{-0.58} R^{1.00} a^{0.81}$$
(18)

where M_{AMU} is the ion mass, B_{T} is the toroidal magnetic field, $n_{\text{e},20}$ is the electron density, R is the major radius, and a is the minor radius. Beside, this agreement for L-H transition between simulations and the power threshold model can be seen in all simulations for this work.

4.2 Comparison for L-H transition with Bifurcation model

The physics of L-H transition is related to an abrupt change of the edge plasma stability. A bifurcation in the particle and energy confinement properties based on the basic assumptions that the edge turbulence is suppressed by $E \times B$ flow, and the radial ion pressure gradient is approximately balanced by the radial electric field [46]. Recently, M. A. Malkov and P. H. Diamond [47] presented a simplify the bistable particle and energy transport model and its stationary solutions, which firstly suggested by Hinton and Staebler [46]. They found that a local bifurcation can occur under the condition that the ratio of the anomalous thermal diffusivity over the neoclassical thermal diffusivity is greater or equal the critical value 16/9. To confirm this concept, Fig. 8 shows the ratio of average anomalous thermal diffusivity ($\chi_{ano.avg}$) and average neoclassical thermal diffusivity ($\chi_{neo.avg}$), which carried out by BALDUR simulations. It is plotted by 10 DIII-D H-mode discharges at the diagnostic time. In this figure, the top and the bottom panels show the ratio of $\chi_{ano.avg}/\chi_{neo.avg}$ for ion and electron, respectively. This ratio of 10 DIII-D H-mode discharges at the diagnostic time exceeds than the critical value.

4.3 Prediction of pedestal width and pedestal top values

It was found in the previous pedestal width (Δ) studies that the pedestal width scalings have a range of results in various tokamaks. Some studies have found a scaling consistent with a pedestal width that is linearly proportional to the gyro-radius ($\Delta \propto \rho$) [48] or to the gyro-radius with some power ($\Delta \propto \rho^{\upsilon}$), with υ in the range of 1/2 to 2/3 [49]. Even though it is inconclusive about the exact power for this relationship between the pedestal width and the gyro-radius, it can be expected the pedestal to increase with the increasing gyro-radius. Consequently, the pedestal width in high ρ^* discharge should be wider than that for low ρ^* discharge. According to the International Pedestal Database (version 3.2), the pedestal width of electron temperature, the top pedestal value of electron temperature, and the top pedestal value of electron density for discharges 82205 (low ρ^*) and 82788 (high ρ^*) and the simulation results of two discharges are shown in Table 3. In this table, the simulation results that carried out by BALDUR show the powerful prediction because they have a same trend moreover a closer range when compared to the experimental data.

The next width scaling based on neutral particles penetration, which usually comes from the scrape-off-layer region. In this width scaling, the resulting width of the pedestal scales inversely proportional to the pedestal, that is $\Delta \propto 1/n_{ped}^{3/2}$ [20], where $n_{ped}=n_i$ is the pedestal density. Thus, the pedestal width of electron density in high n_e discharge should be narrow than that for low n_e discharge. The pedestal width of electron density, the top pedestal value of electron temperature, and the top pedestal

value of electron density from Database (ver. 3.2) for these 81321 (low n_e) and 81329 (high n_e) are shown in Table 3. It can be seen that the simulations yield similar trend and good agreement to the experiment. Nevertheless, in power scan discharges and κ scan discharges, these parameters are not shown the relation of the width scaling due to the MHD instability.

The capability of BALDUR core-edge models for predicting the pedestal width and pedestal height is investigated by comparing the prediction width and height to the experimental data and to the PEDESTAL model [50], which is a model to predict the pedestal temperature of type I ELMy H-mode plasma. The PEDESTAL model, which used in this work, composes of three theories motivated models. The first is based on magnetic and flow shear stabilization ($\Delta \propto \rho s^2$), the second is based on flow shear stabilization ($\Delta \propto \sqrt{\rho Rq}$), and the last is base on normalized poloidal pressure ($\Delta \propto \sqrt{\beta_{\theta}R}$). Fig. 9 shows the pedestal width (%) of electron temperature and electron density, also the top pedestal of electron temperature and electron density between simulation results and experimental results. The correlation coefficient (R^2) of BALDUR core-edge model is shown in this figure. It is found that, the top pedestal of electron density which carried out by BALDUR core-edge model shows the good correlation between simulation and experiment with $R^2 = 0.98$. However, other parameters in this figure are not captured by these four models; because, the data patterns are not located on the 45 degree line. Therefore, to quantify the comparison between the predictions of each model and experimental data, the root average square error (RMSE) is computed, like the previous work by T. Onjun [20], as shows in Eq.15. These results of pedestal comparison are summarized in Table 4. In this table, it shows the simulation results which carried out by BALDUR with core-edge model; it has a closer between simulation and experiment, because this model can produced the overall RMSE(%) lower than that produced by other models from the PEDESTAL model.

Fig.10 the radial profiles of the ion thermal diffusion coefficient (χ_i) , electron thermal diffusion coefficient (χ_e) , hydrogenic particle diffusion coefficient (D_H) , and impurity diffusion coefficient (D_Z) as functions of the normalized minor radius of the DIII-D device discharge 82205. On the left panel of this figure, it depicts the thermal and particle diffusivities, which the suppression function is excluded. A Bohm term is the dominant term in ion and electron thermal diffusivity channels and this term play a key role at the edge area (r/a=0.8). After implement the core-edge model, they show fluctuation in all terms of diffusivity coefficients; as well as, the total term of ion and electron thermal diffusivities are suppressed by the suppression function which are included to the integrated predictive modelling codes at the edge area from normalized minor radius (r/a)=0.9 to 1.0. That is the reason why the pedestal can be performed when the velocity shear becomes strong enough and the condition $\omega_{E\times B} > \gamma_{\text{ITG}_{\text{max}}}$ is satisfied.

4.4 Cross validation test

To confirm the predictive capability of the core-edge model based on the suppression of anomalous transport via $\omega_{E\times B}$ flow shear and magnetic shear. The "Cross Validation Test" method is employed. The BALDUR code is used to carry out core-edge simulation of 12 JET H-mode discharges get from the International Profile Database [51]. Some plasma parameters 12 JET H-mode discharges used in the test are listed in Table 5. The simulation profiles of electron temperature, ion temperature, electron density and deuterium density as a function of minor radius that compared to the JET experimental data discharge 35156 (low ρ^*) and 35157 (high ρ^*) are shown in Fig.11. In this figure, all temperature and density profiles fit well in the core region, but quite overpredict at the edge region, because the JET experimental data are not obviously depict the pedestal formation. Therefore, to measure the accuracy of the model by cross validation method, the summary of RMS and offset which are carried out by the integrated predictive modelling code of 12 JET H-mode discharges, the average of RMS and the average of offset are shown in Fig. 12. In this figure, the RMS average and the offset average

of electron temperature, ion temperature, electron density and deuterium density of 12 JET *H*-mode discharges deviate from the RMS average of 10 DIII-D *H*-mode discharges 6.90%, -0.25%, 7.74%, and 6.91%, respectively.

5. Conclusions

A theory-based model for predicting the pedestal transports in *H*-mode plasma is developed and implemented in the integrated predictive modelling code BALDUR. It is found that the simulations using BALDUR code with both core and pedestal transport models can reproduce experimental data. It yields the average RMS of electron temperature, ion temperature, electron density, and deuterium density in the case of DIII-D equal to 13.48%, 17.39%, 7.45%, and 12.41%, respectively. To confirm the accuracy of this model, it is used the cross validation method to test with 12 JET *H*-mode discharges. The results of the RMS average of electron temperature, ion temperature, electron density and deuterium density of 12 JET *H*-mode discharges deviate from the RMS average of 10 DIII-D *H*-mode discharges 6.90%, -0.25%, 7.74%, and 6.91%, respectively. Moreover, the simulation data show the prediction of *L-H* transition when heating power exceeds power threshold and the transition is confirmed by bistabel particle and energy transport model, the simulation of pedestal width and pedestal top values, which carried out by BALDUR core-edge model and the PEDESTAL model, are not capable to reach the experimental data. It is accepted in the case of the electron density pedestal top which carried out by BALDUR core-edge model, because this result shows the good correlation between simulation and experimental data with correlation coefficient 0.98.

Acknowledgments

This work is supported by the Commission on Higher Education (CHE) and the Thailand Research Fund (TRF) under Contract No RMU5180017, Thailand National Research University Project, and the Commission on Higher Education, Thailand, under the program "Strategic Scholarships for Frontier Research Network for the Ph.D. Program Thai Doctoral Degree".

References

- [1] Wagner F. et al 1982 Physical Review Letters **49(19)** 1408
- [2] Connor J. W. and Wilson H. R. 2000 Plasma Physics and Controlled Fusion 42 R1-R74
- [3] Singer C. E. et al 1988 Computer Physics Communications 49 (2) 275-398
- [4] Honda M. and Fukuyama A. 2006 Nuclear Fusion 46 580-593
- [5] Cenacchi G. and Taroni A. 1988 JET-IR 88
- [6] Pereverzev G. and Yushmanov P. N. 2002 Max-Planck Institut fur Plasmaphysik IPP 5/98
- [7] Basiuk V. et al 2003 Nuclear Fusion 43 822
- [8] Kinsey J. E. et al 2002 Physics of Plasmas 9(5) 1676
- [9] Bateman G. et al 1998 Physics of Plasmas 5 1793
- [10] Bateman G. et al 2003 Plasma Physics and Controlled Fusion 45 (11) 1939-1960
- [11] Kinsey J. E. et al 2003 Nuclear Fusion 43 (12) 1845
- [12] Onjun T. et al 2001 Physics of Plasmas 8 975
- [13] Hannum D. et al 2001 Physics of Plasmas 8 964
- [14] Biglari H. et al 1990 Physics of Fluids B: Plasma Physics 2 (1) 1-4
- [15] Gohil P. 2006 Comptes Rendus Physique 7 (6) 606-621
- [16] Boedo J. et al 2000 Nuclear Fusion 40 1397

- [17] Oost G. V. et al 2003 Plasma Physics and Controlled Fusion 45 1-23
- [18] Pankin A. Y. et al 2005 Plasma Physics and Controlled Fusion (3) 483
- [19] Pacher G. W. and et al. 2004 Plasma Physics and Controlled Fusion 46 (5A) A257
- [20] Onjun T. et al 2002 Physics of Plasmas 9 5018-5030
- [21] Onjun T. et al 2004 Physics of Plasmas 11 1469
- [22] Parail V. et al 2003 Plasma Physics Reports 29 (7) 539-544
- [23] Lönnroth J. S. and et al. 2004 Plasma Physics and Controlled Fusion 46 (8) 1197
- [24] Lönnroth J. S. and et al. 2004 Plasma Physics and Controlled Fusion 46 (5) 767
- [25] Doyle E. J. et al 2007 Nuclear Fusion 47 (6) S18
- [26] Yoshizawa A. *et al*, *Plasma and fluid turbulence : theory and modelling*. (Institute of Physics Publishing, Bristol, 2003).
- [27] Waltz R. E. et al 1997 Physics of Plasmas 4 (7) 2482
- [28] Itoh K. and et al. 1994 Plasma Physics and Controlled Fusion 36 (1) 123
- [29] Itoh K. and et al. 1998 Plasma Physics and Controlled Fusion 40 (5) 661
- [30] Itoh S. I. et al 1994 Physical Review Letters 72 (8) 1200
- [31] Figarella C. F. et al 2003 Physical Review Letters 90 (1) 015002
- [32] Zolotukhin O. V. et al, in 28th EPS Confer. on Contr. Fusion and Plasma Phys. (Funchal, Portugal, 2001), Vol. 25A, pp. 677-680.
- [33] Sugihara M. et al, in 28th EPS Conf. on Contr. Fusion and Plasma Phys. (Funchal, Portugal, 2001), Vol. 25A, pp. 629-632.
- [34] Kessel C. et al 1994 Physical Review Letters 72 (8) 1212
- [35] Diamond P. H. et al 1997 Physical Review Letters 78 (8) 1472
- [36] Sugihara M. and et al. 2000 *Nuclear Fusion* **40** (10) 1743
- [37] Hahm T. S. and Diamond P. H. 1987 Physics of Fluids 30 (1) 133-143
- [38] Pacher G. W. et al 2003 Nuclear Fusion 43 188-195
- [39] Janeschitz G. and et al. 2002 Plasma Physics and Controlled Fusion 44 (5A) A459
- [40] Onjun T. and Pianroj Y. 2009 Nuclear Fusion 49 075003
- [41] Tala T. J. J. et al 2001 Plasma Physics and Controlled Fusion 43 507-523
- [42] Chang C. S. and Hinton F. L. 1986 *Physics of Fluids* **29** (10) 3314-3316
- [43] Boucher D. et al 2000 Nuclear Fusion 40 (12) 1955
- [44] Burrell K. H. 1997 *Physics of Plasmas* **4** 1499
- [45] Shimomura Y. et al, presented at the IAEA Fusion Energy Conference, Sorrento, Italy, 2000 (unpublished).
- [46] Hinton F. L. and Staebler G. M. 1993 Physics of Fluids B: Plasma Physics 5 (4) 1281-1288
- [47] Malkov M. A. and Diamond P. H. 2008 Physics of Plasmas 15 (12) 122301
- [48] Cordey J. G. and et al. 1999 Nuclear Fusion 39 (3) 301
- [49] Lingertat J. et al 1999 Journal of Nuclear Materials 266-269 124-130
- [50] Onjun T., "PEDESTAL model." http://w3.pppl.gov/NTCC/PEDESTAL
- [51] Boucher D. et al 2000 Nuclear Fusion 40 (12) 1955

Table 1: Details of plasma parameters for each discharge.

Discharges	77557	77559	81321	81329	81499	81507	82205	82788	82188	82183
Type	Low	High	Low	High	Low κ	High	Low	High	-	-
	power	power	n_e	n_e		κ	$ ho^*$	$ ho^*$		
R(m)	1.68	1.69	1.69	1.70	1.69	1.61	1.69	1.68	1.69	1.69
<i>a</i> (m)	0.62	0.62	0.60	0.59	0.63	0.54	0.63	0.62	0.63	0.54
κ	1.85	1.84	1.83	1.83	1.68	1.95	1.71	1.67	1.65	1.91
δ	0.33	0.35	0.29	0.36	0.32	0.29	0.37	0.35	0.29	0.22
$B_T(T)$	1.99	1.99	1.98	1.94	1.91	1.91	1.87	0.94	1.57	1.57
$I_p(MA)$	1.00	1.00	1.00	1.00	1.35	1.34	1.34	0.66	1.33	1.33
$\overline{n_e}(10^{19}m^{-3})$	4.88	5.02	2.94	5.35	4.81	4.90	5.34	2.86	6.47	6.87
Z_{eff}	1.68	2.21	2.42	1.65	2.33	1.93	2.13	1.94	1.95	1.95
$P_{NB}(MW)$	4.78	13.23	3.49	8.34	5.74	5.71	5.86	3.25	3.92	3.92
Diagnostic time (sec)	2.70	2.70	3.90	3.80	4.00	3.80	3.66	3.54	3.78	3.78

Table 2: The set of coefficients C_x for each species that yields the optimized agreement between simulations and experimental data for three different optimization methods in BALDUR code.

Choice	Optimization Methods	C_i	C_e	C_H	C_z
1	Whole plasma profile	4.32×10^{3}	3.91×10^{3}	1.19×10^{2}	1.22×10^{2}
2	Edge area (10%)	3.89×10^{3}	3.98×10^{3}	1.28×10^{2}	1.21×10^{2}
3	Top of pedestal temperature	3.80×10^{3}	3.15×10^{3}	1.33×10^{2}	1.27×10^{2}
4	Top of pedestal density	3.90×10^{3}	4.05×10^{3}	1.55×10^{2}	1.34×10^{2}

Table 3: Summary of the pedestal width of electron density, the top pedestal of electron density, and the top pedestal of electron temperature that compare between experiment and simulation.

Parameters	Data	82205	82788	81321	81329
1 arameters	Data	(Low ρ^*)	(High ρ^*)	$(\text{Low } n_e)$	(High n_e)
An (cm)	Experiment	-	-	1.6	1.4
$\Delta n_e(cm)$	Simulation	-	-	2.0	1.3
n (m ⁻³)	Experiment	4.4×10^{19}	2.5×10^{19}	2.1×10^{19}	4.0×10^{19}
$n_{e,ped} (m^{-3})$	Simulation	4.4×10^{19}	2.2×10^{19}	2.2×10^{19}	3.9×10^{19}
AT (kaV)	Experiment	1.2	1.5	1	-
$\Delta T_e \text{ (keV)}$	Simulation	1.2	$\begin{array}{c ccccccccccccccccccccccccccccccccccc$	-	
T (kov)	Experiment	0.7	0.4	0.7	0.6
$T_{e,ped}$ (kev)	Simulation	1.1	0.3	0.7	0.6

Table 4: Summary of pedestal comparison.

			Mod	elling	
Paran	neters	Flow and	Flow shear	Normalized	BALDUR
1 aran	ileter 5	magnetic shear	stabilization	pedestal	(core-edge
		stabilization		pressure	model)
	$\Delta_{T_{m{e}}}$	88.47	82.67	21.34	25.96
DMC (0/)	$T_{e,ped}$	37.34	34.18	53.24	41.94
RMS (%)	Δ_{n_e}	-	-	-	36.21
	$n_{e,ped}$	47.43	45.76	45.99	6.62
	$\Delta_{T_{m{e}}}$	-83.02	-77.01	-15.23	-1.00
Offset (%)	$T_{e,ped}$	-4.10	0.00	38.03	-17.00
O11861 (70)	Δ_{n_e}	-	-	-	21.00
	$n_{e,ped}$	12.11	10.21	11.00	2.00

Table 5: Details of plasma parameters for 12 JET H-mode discharges.

Discharges	33131	33140	33465	34340	35156	35171	35174	37379	37718	37728	38407	38415
Tyma	Low	High	Identity		Low	High			Low	High	Low	High
Type	$ ho^*$	$ ho^*$		-	$ ho^*$	$ ho^*$	-	-	v^*	v^*	β	β
R(m)	2.94	2.93	2.87	2.88	2.87	2.88	2.87	2.91	2.94	2.92	2.91	2.88
<i>a</i> (m)	0.94	0.92	0.95	0.88	0.93	0.94	0.84	0.83	0.93	0.96	0.94	0.97
κ	1.70	1.56	1.55	1.66	1.56	1.58	1.56	1.62	1.58	1.64	1.60	1.55
δ	0.28	0.26	0.19	0.15	0.11	0.24	0.22	0.18	0.13	0.20	0.16	0.11
$B_T(T)$	3.13	1.77	1.10	2.16	2.17	1.09	1.08	1.05	2.11	2.71	1.59	1.84
$I_p(MA)$	2.83	1.61	1.04	2.03	2.05	1.01	1.02	1.00	1.97	2.57	1.47	1.67
$\overline{n_e}(10^{19}m^{-3})$	7.10	3.65	3.26	6.27	5.44	2.44	2.50	2.00	4.54	4.90	3.05	4.02
Z_{eff}	1.92	1.66	1.52	1.99	1.25	1.10	1.44	2.27	1.93	1.76	2.09	2.06
$P_{NB}(MW)$	18.0	5.80	2.77	2.00	8.60	2.91	3.00	4.70	9.70	13.3	5.60	15.7
Diagnostic time (sec)	55.69	56.50	63.76	56.37	55.85	65.00	64.38	63.38	55.38	58.12	57.40	56.61

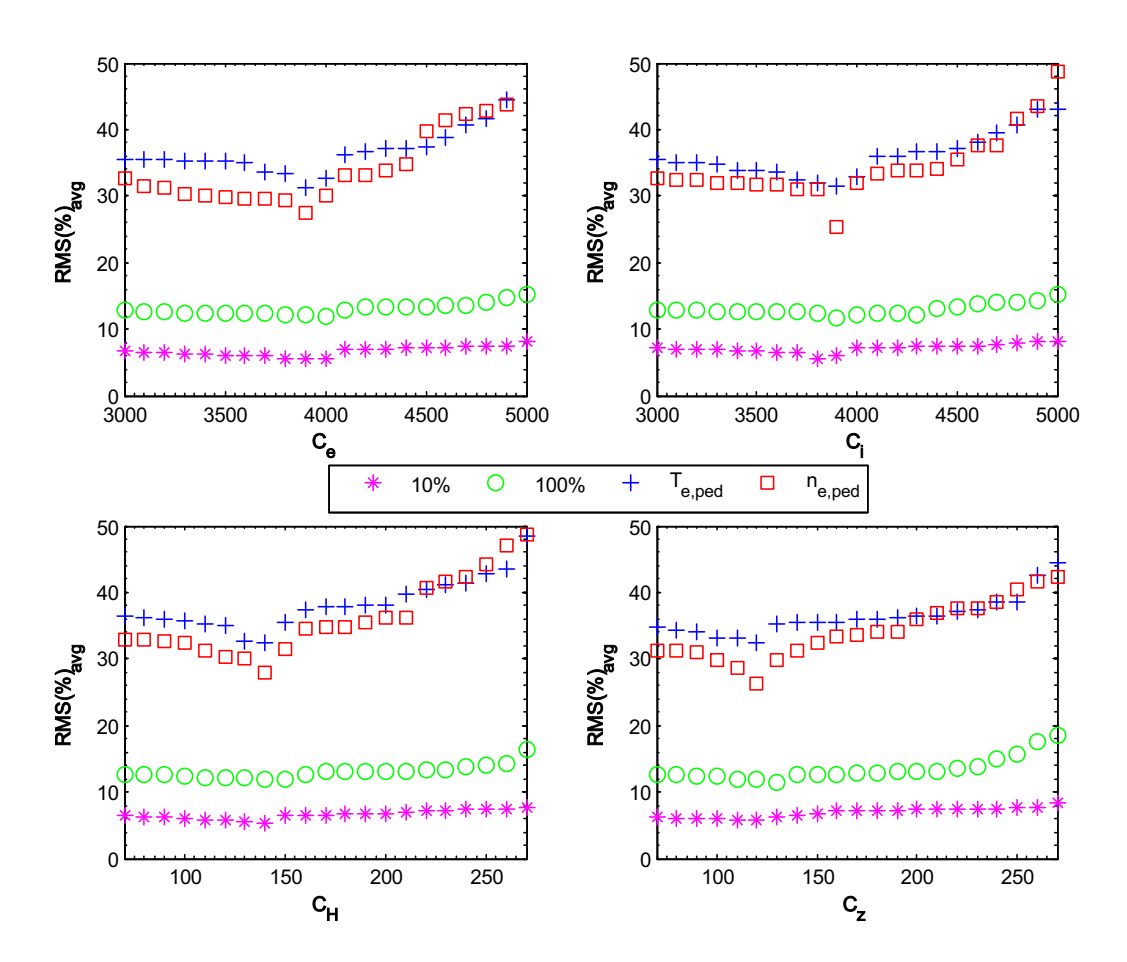


FIG.1: The average RMSs are shown as a function of coefficient $C_{x,i}$.

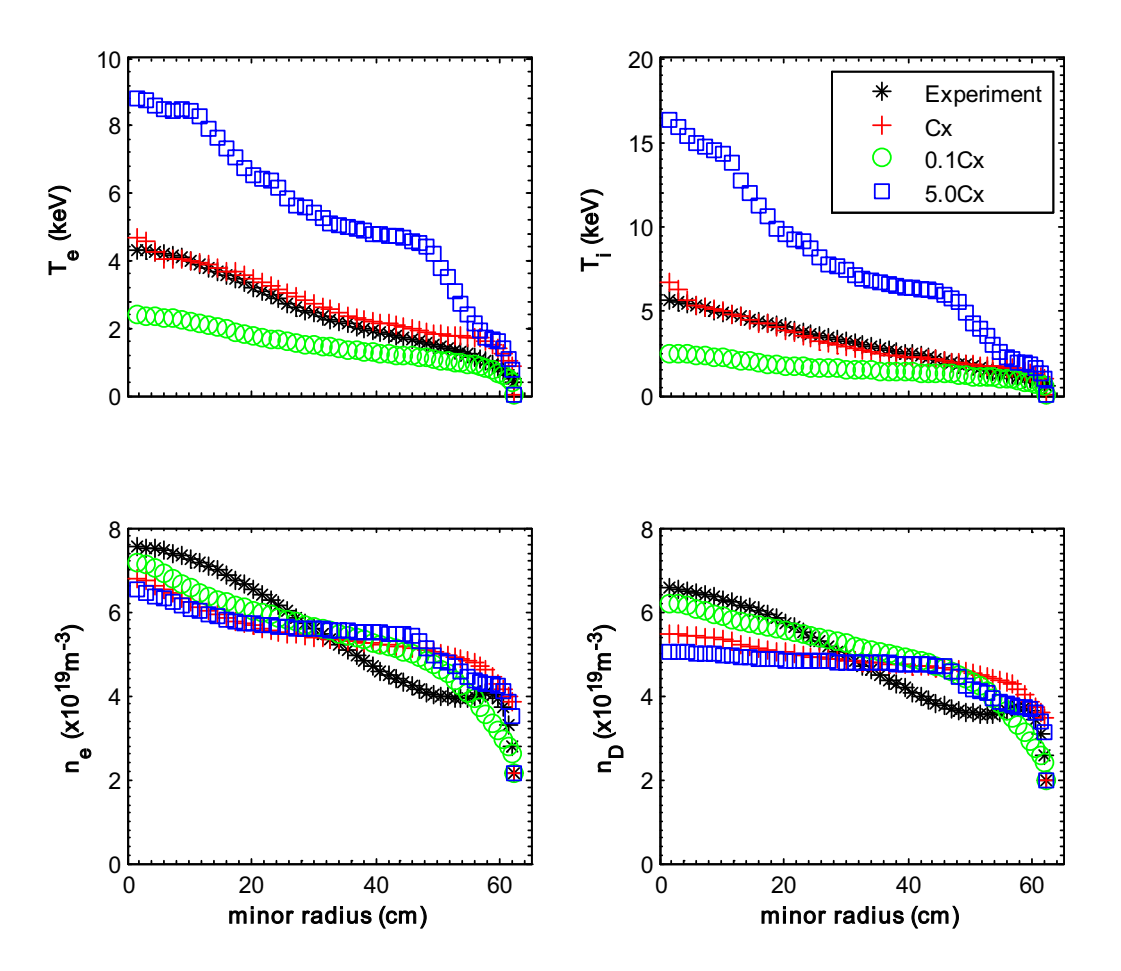


FIG.2: The profile of electron temperature, ion temperature, electron density, and deuterium density as a function of minor radius. The simulation results are carried out by BALDUR code for showing the calibration and sensitivity of coefficient C_x , which are compared to the DIII-D discharge 82205 at the diagnostic time.

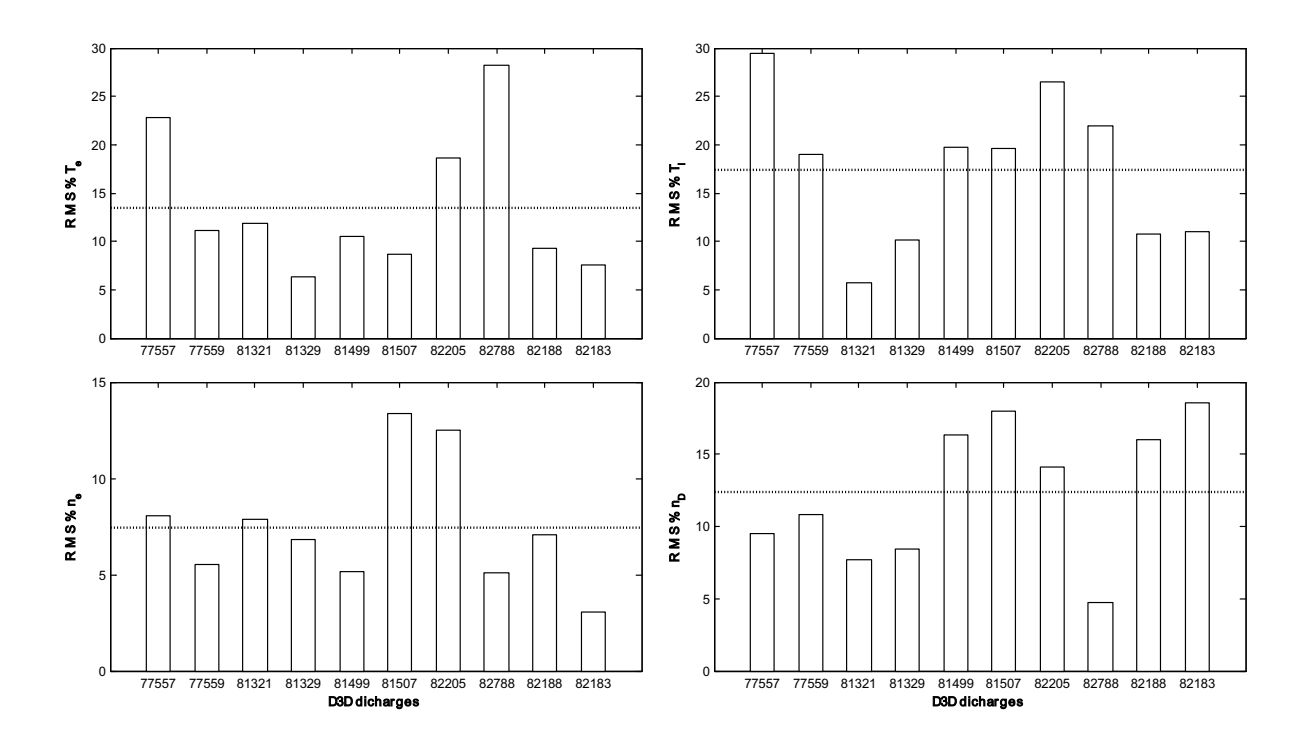


FIG.3: The root mean square (RMS%) for the electron temperature, ion temperature, electron density, and deuterium density profiles produced by simulation using the core-edge model from BALDUR code, compared with experimental data for 10 *H*-mode discharges (pedestal occurred), listed by DIII-D device and the average of RMS% in each profile is shown by dash line in each graph panel.

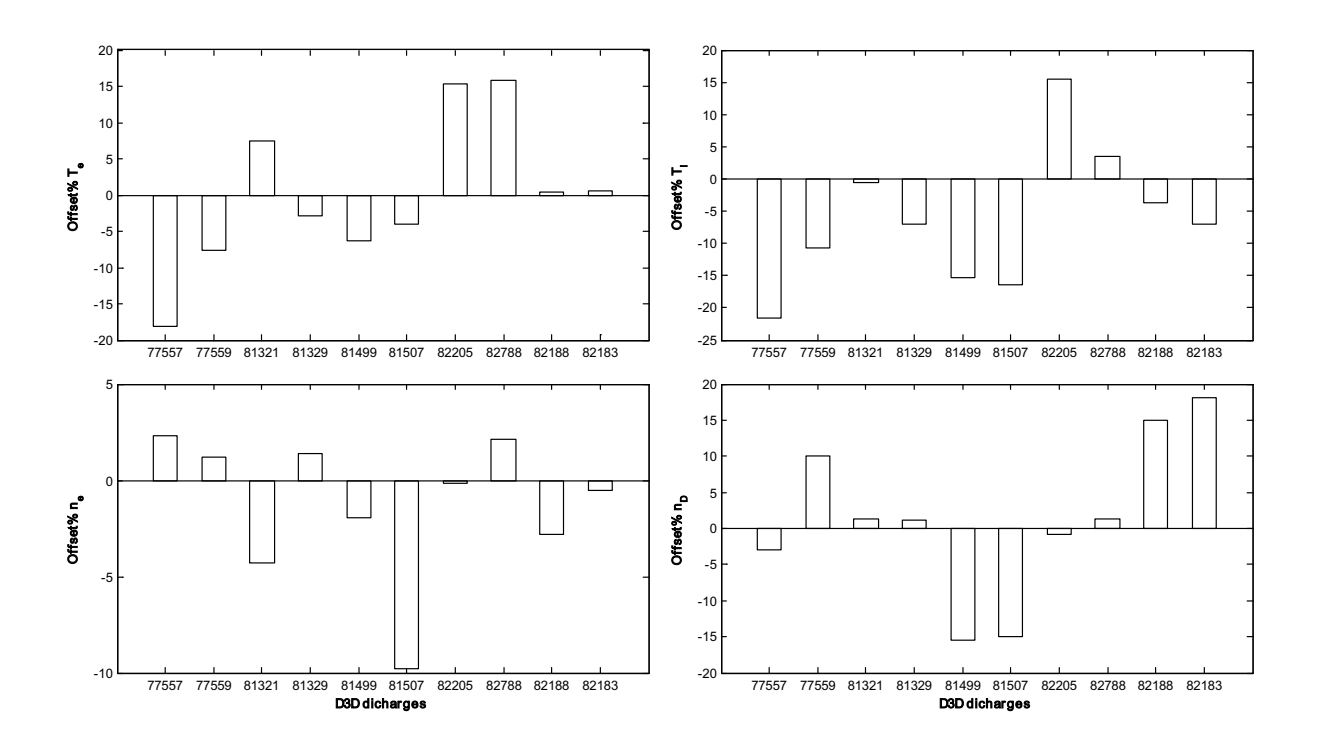


FIG.4: The Offset% for the ion temperature profiles produced by the simulation using the core-edge model from BALDUR code, compared with experimental data for 10 *H*-mode discharges (pedestal occurred), listed by DIII-D device.

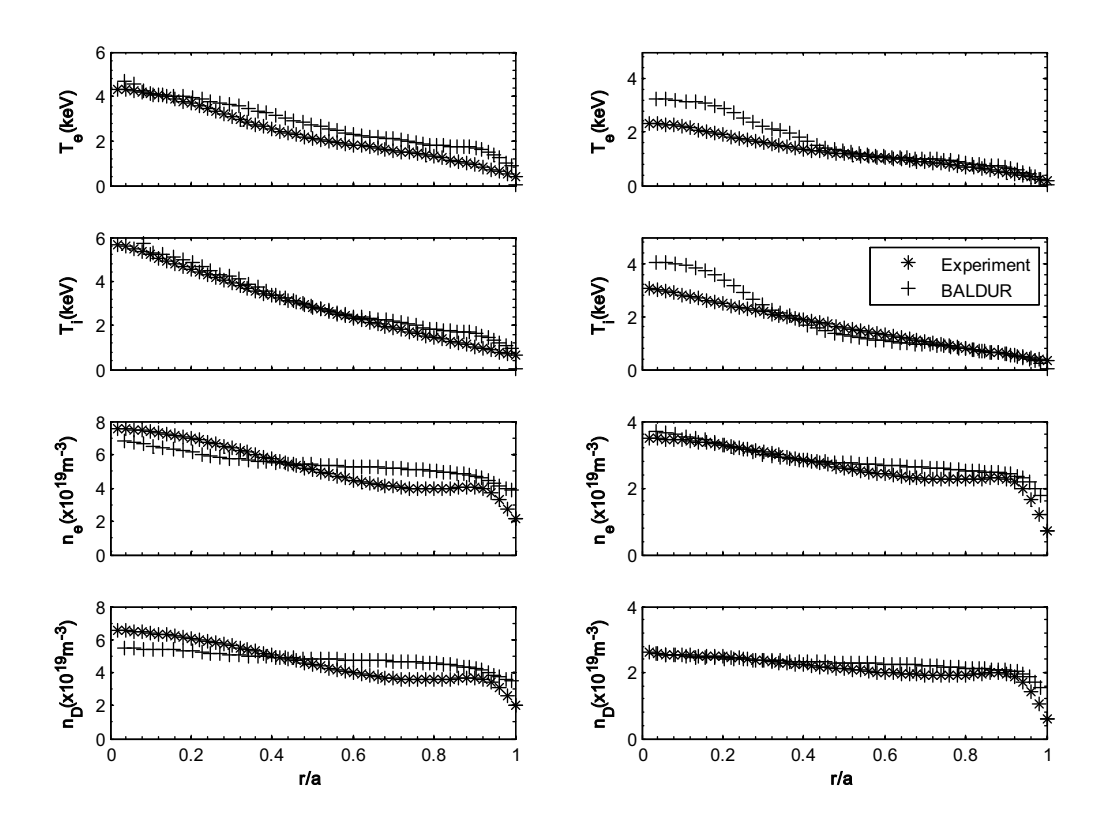


FIG.5: The profiles of electron temperature, ion temperature electron density and deuterium density as a function of minor radius. The simulation results are carried out by BALDUR with the core-edge transport model, compared to the DIII-D experimental data discharge 82205 (Low ρ^* ; Left panel) and 82788 (High ρ^* ; Right panel) at diagnostic time.

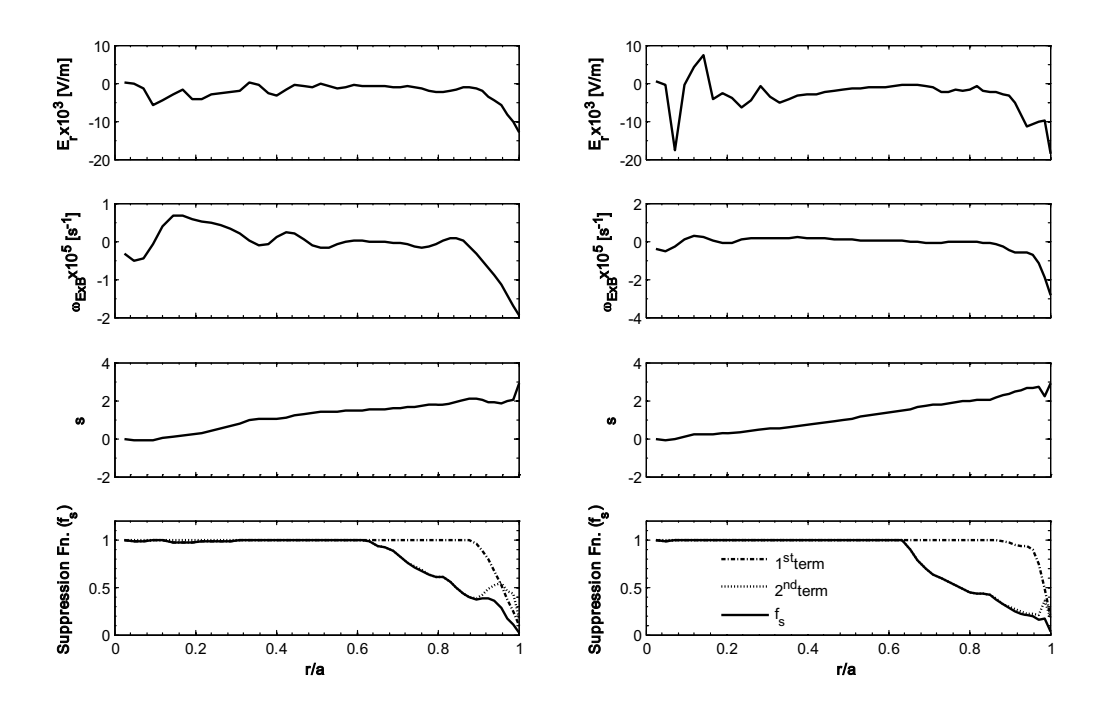


FIG.6: The radial electric field, $\omega_{E\times B}$ flow shear, magnetic shear and suppression function as a function of normalized minor radius, carried out by the predicted modelling code BALDUR. Left panel is DIII-D discharge 82205 and right panel is DIII-D discharge 82788 at diagnostic time.

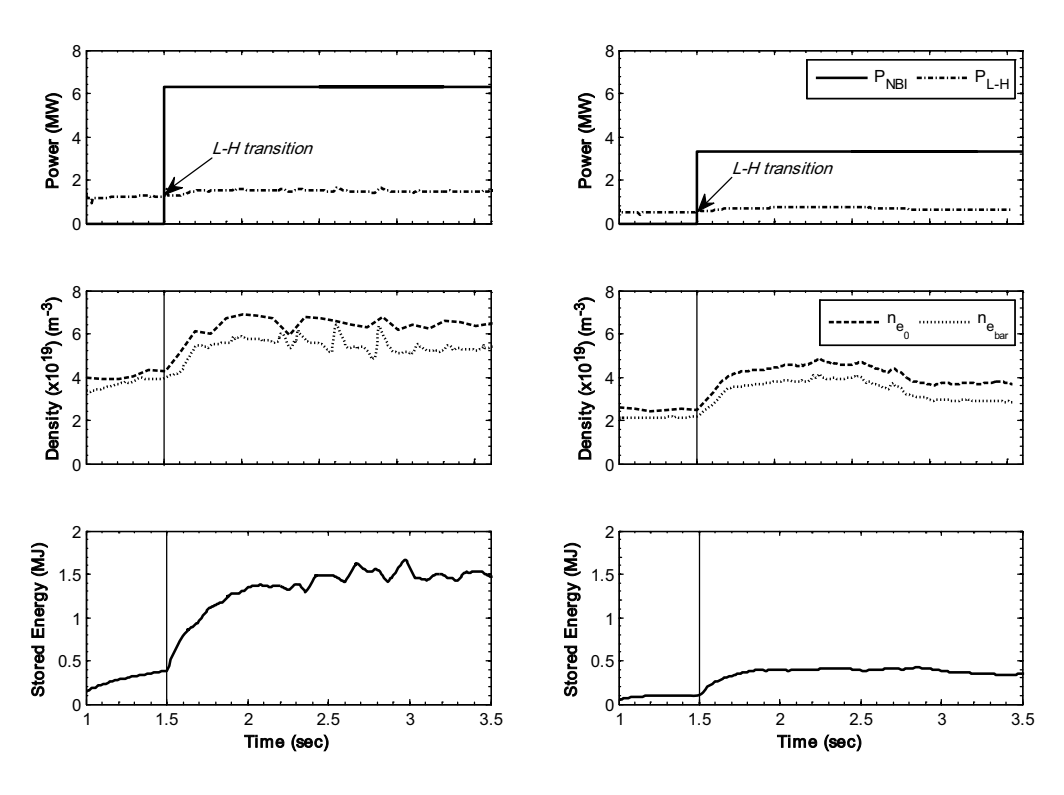


FIG.7: The NBI heating power (P_{NBI}), L-H transition threshold power (P_{L-H}), electrons density at the plasma core (n_{e_0}), electron line average density ($n_{e_{bar}}$) and plasma stored energy are plotted as a function of time. The left panels represent the low gyro-radius scan of DIII-D discharge 82205, and the right panels represent the high gyro-radius scan of DIII-D device discharge 82788.

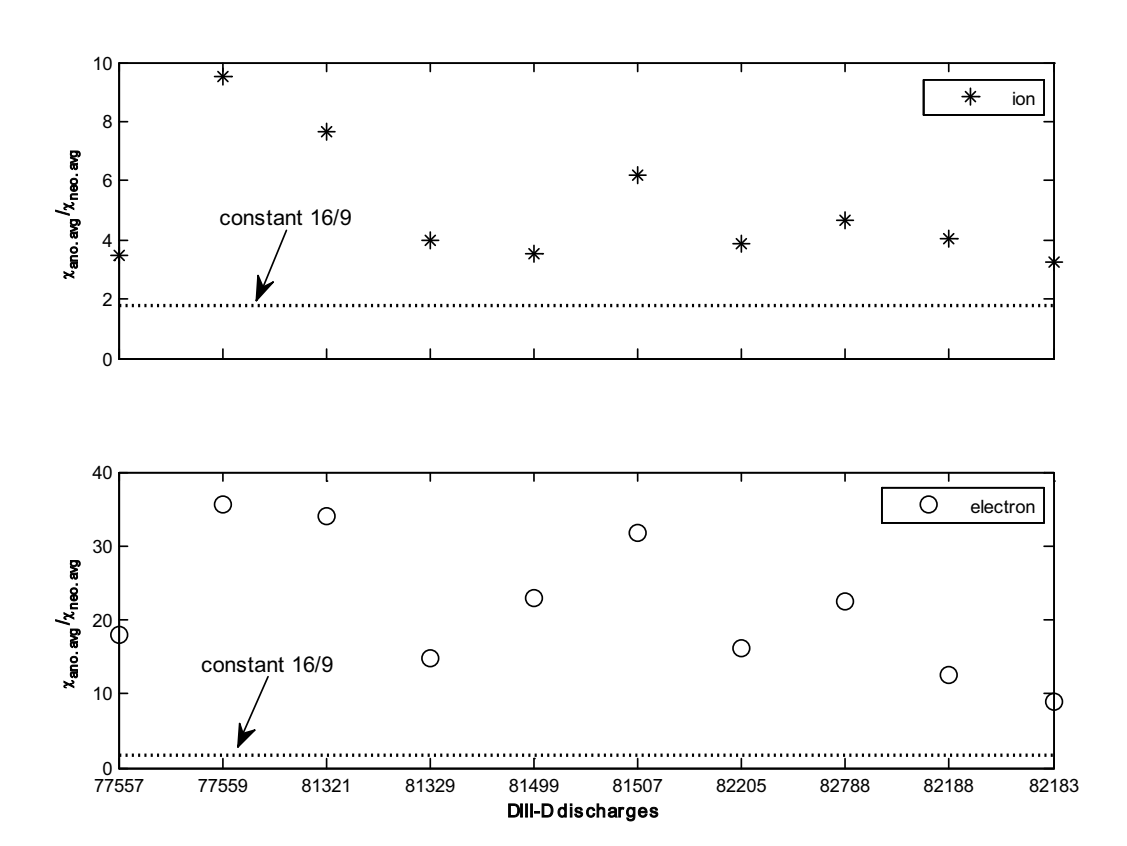


FIG.8: The ratio of average anomalous thermal diffusion coefficient ($\chi_{ano.avg}$) and average neoclassical thermal diffusion coefficient ($\chi_{neo.avg}$), which carried out by BALDUR simulations, is plotted by 10 DIII-D H-mode discharges at the diagnostic time.

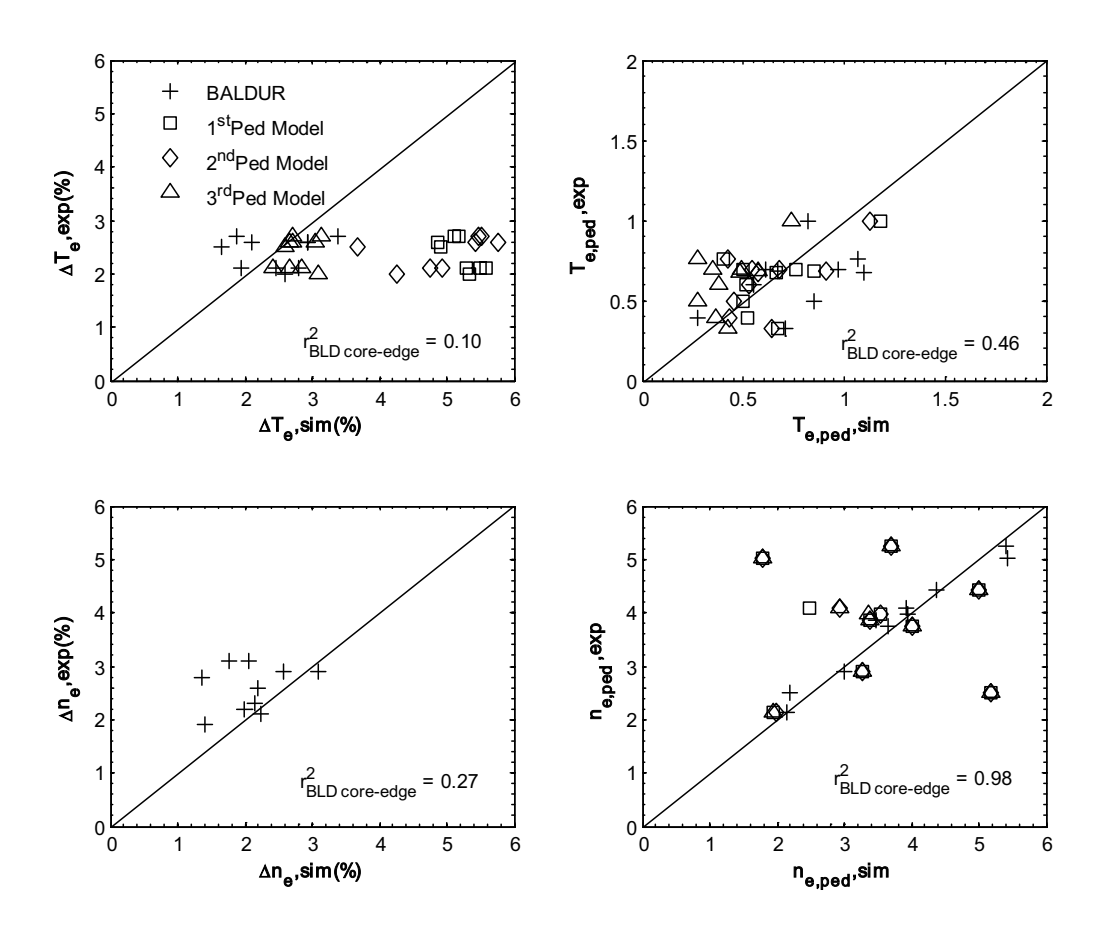


FIG.9: Plot for the percentage of pedestal width of electron temperature, and electron density predicted by the core-edge model of BALDUR code, and PEDESTAL model, compared with experimental data from 10 DIII-D *H*-mode discharges (left panel). The electron temperature and electron density at the top of pedestal predicted by the core-edge model of BALDUR code, and PEDESTAL model, compared with experimental data from 10 DIII-D *H*-mode discharges (right panel).

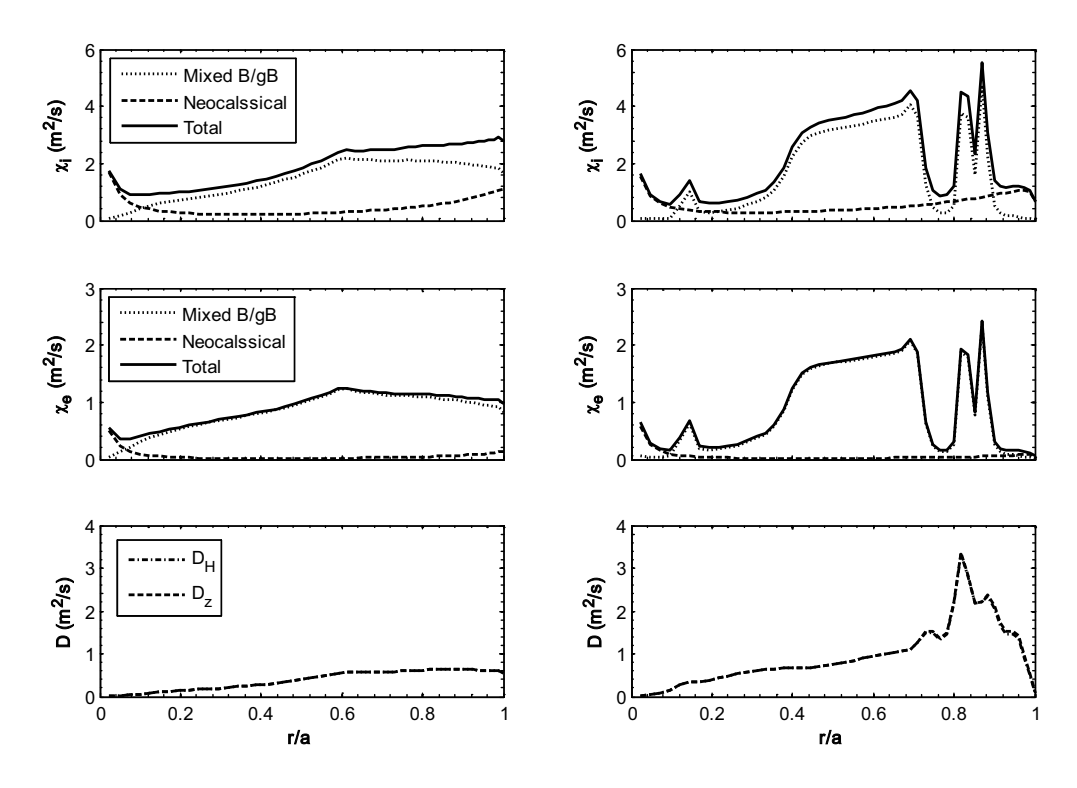


FIG.10: Radial profiles of the ion thermal diffusion coefficient (χ_i), electron thermal diffusion coefficient (χ_e), hydrogenic particle diffusion coefficient (D_H), and impurity diffusion coefficient (D_z) as functions of the normalized minor radius at the diagnostic time of the DIII-D device discharge 82205. On the left panels, all coefficients which carried out by BALDUR simulations are excluded the suppression function; nevertheless, on the right panels, they are included the suppression function.

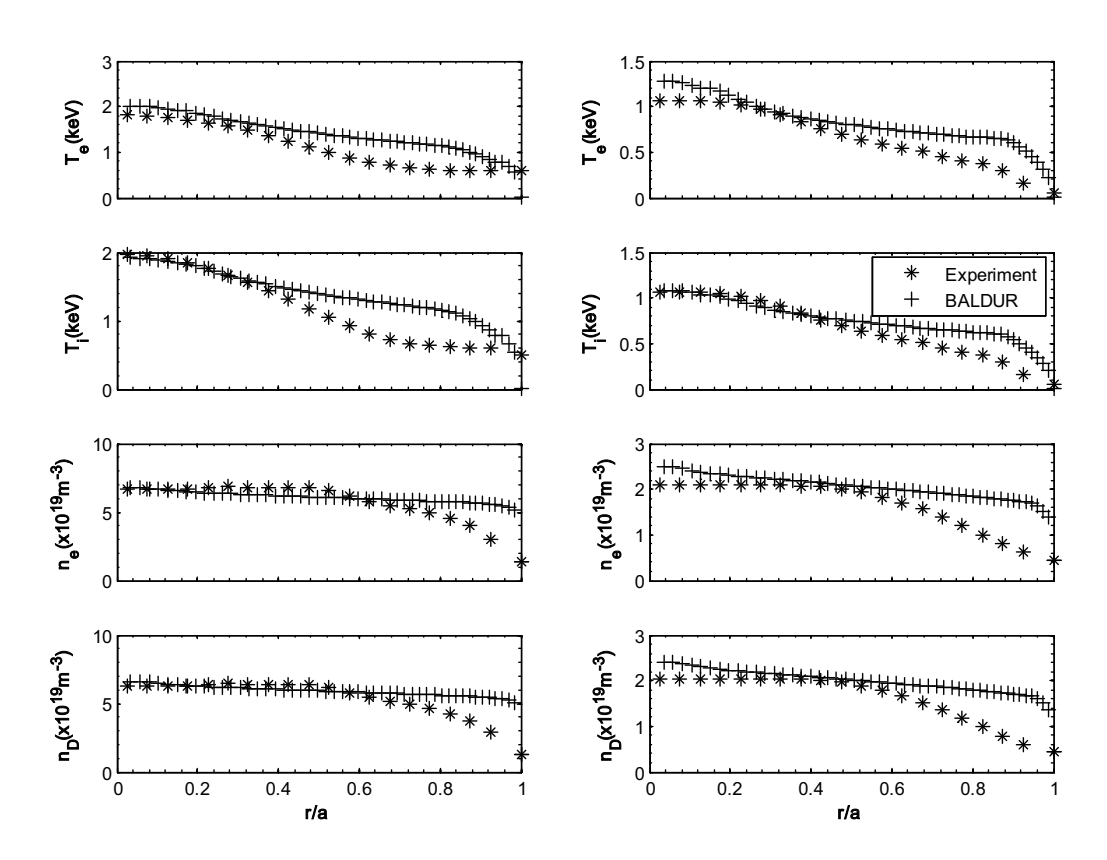


FIG.11: The profiles of electron temperature, ion temperature electron density and deuterium density as a function of minor radius. The simulation results are carried out by BALDUR with the core-edge transport model, compared to the JET experimental data discharge 35156 (Low ρ^* ; Left panel) and 35171 (High ρ^* ; Right panel) at diagnostic time.

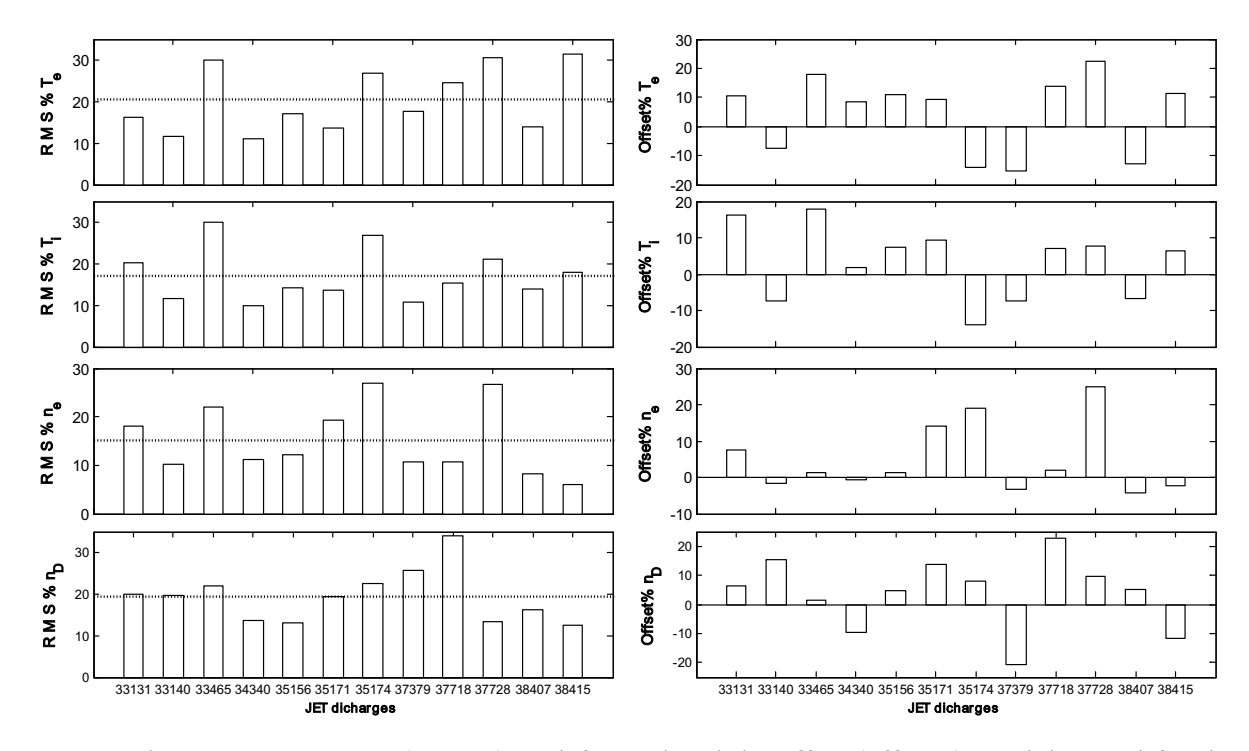


FIG.12: The root mean square (RMS%) on left panel and the offset (offset%) on right panel for the electron temperature, ion temperature, electron density, and deuterium density profiles produced by simulation using the core-edge model from BALDUR code, compared with experimental data for 12 *H*-mode discharges (pedestal occurred), listed by JET device and the average of RMS% in each profile is shown by dash line in each graph on left panel.

TOKAMAKS —

Behaviors of Impurity in ITER Plasma with Standard Type I ELMy H-Mode and Steady-State Scenarios¹

Y. Pianroj^a, C. Chuchinda^a, P. Leekhaphan^b, and T. Onjun^a

Abstract—Self-consistent simulations of impurity behaviors in ITER plasmas in standard Type I ELMy H-mode and steady-state scenarios are investigated using 1.5D BALDUR integrated predictive modeling code. In these simulations, the plasma core transports, including electron and ion thermal, hydrogenic and impurity transports, are predicted using a linear combination of anomalous and neoclassical transports. An anomalous transport is calculated using a theory-based Multimode (MMM95) model; while the neoclassical transport is calculated using NCLASS model. The temperature and density boundary conditions are described at the top of the pedestal. Two different models for hydrogenic and impurity boundary density conditions are considered. The first model is called a "static boundary density model," in which the hydrogenic and impurity densities at the boundary are fixed. For the second model, called a "dynamic boundary density model," the hydrogenic and impurity densities at the boundary are assumed to be a large fraction of its lineaveraged density. For simplicity, the pedestal temperature is assumed to be a constant in all simulations. The combination of a core transport model together with the boundary density models is used to simulate the time evolution of plasma current, temperature, and density profiles for ITER plasmas in standard type I ELMy H-mode and steady-state scenarios. As a result, the behaviors of impurity in ITER plasmas can be investigated. It is found in both ITER scenarios that the total amount of impurity, including beryllium and helium, in plasma core increases rapidly in early state and reaches a steady-state value. The level of impurity content in the steady state depends sensitively on the impurity boundary conditions. The effective charge at the edge is found to be about 1.4 and 1.1 using a static boundary density model and a dynamic boundary density model, respectively. It is also found that the hydrogenic and impurity transports in ITER plasmas for both scenarios is dominated by the kinetic ballooning modes, while the ITG and TEM modes provide the largest contributions for both thermal transports in most of region. In addition, a sensitivity study is carried out to investigate the impacts of pedestal temperature, pedestal density and line-averaged density on the impurity behaviors. It is found that increasing the pedestal temperature results in a reduction of the impurity content. On the other hand, increasing the pedestal density, line-averaged density or impurity influx result in an increase of the impurity content.

DOI: 10.1134/S1063780X10100016

1. INTRODUCTION

The concept of magnetically confined thermonuclear fusion using tokamaks has been an interest in scientists and engineers' community for a long period of time because of its potential to provide an environmentally-friendly and cheap energy source. However, scientific and technological feasibility of fusion energy has not yet been demonstrated. Therefore, an international project called the International Thermonuclear Experimental Reactor (ITER) [1] has been initiated. One of the most important concerns in ITER experiments is the behaviors of impurity, in particular the question of an impurity accumulation. It is known that the retention of the helium ash or alpha particles generated from D—T nuclear fusion reaction is inevitable.

The accumulation of impurity can result in severe problems, such as fuel dilution, enhancement of core radiation, and degradation of fusion performance [2]. As a result, it is crucial to investigate the impurity behaviors in the ITER plasmas, in particular the issue of impurity accumulation, to increase a possibility to use thermonuclear fusion for energy source of the future.

Impurity accumulation in the confinementenhanced H-mode plasma, as would be expected in ITER, has been anticipated. In fact, one of primary goals for ITER is to improve the understanding of helium accumulation and to develop a method for enhancement of helium exhaust [3]. Yamada et al. [4] studied the radial distribution of impurity in tokamak and helical system by using 1.5D transport code toroidal transport analysis linkage (TOTAL) to simulate the

¹ The article is published in the original.

high-Z impurity from the plasma facing component materials. It was found the critical level of impurity concentration in ITER equals to 4.0% for carbon, 0.1% for iron and 0.008% for tungsten with respect to electron density. Moreover impurity from low-Z materials, such as beryllium and carbon, under bombardment conditions characteristic of magnetic fusion experiment is reviewed in [5]. Several experiments were designed to investigate on this issue and have confirmed an affirmative observation [6]. A comprehensive review of experiments on helium accumulation and exhaust can be found in [6]. Various simulations of ITER cases have also been conducted to study an impurity accumulation in ITER, especially that of the helium ash. Burbaumer et al. [7] carried out simulations on ITER-like cases using 1.5D transport code and found that temperature and helium density reach steady-state values under an appropriate burn control system. Recent work by Onjun and Pianroj [8] also indicates quasi-steady-state density of helium, as well as that of carbon. A simple modeling of ITER impurity is also carried out by Leekhaphan and Onjun [9], which reports that the level of steady-state impurity content in ITER with type I ELMy H-mode scenario depends sensitively on the boundary conditions and transport. A more comprehensive integrated modeling of ITER reference scenarios can be found in [10], where various issues concerning ITER operations are addressed. However, impurity behavior studied in the paper focused on the accumulation of helium and beryllium in standard H-mode and steady-state scenario of ITER plasma.

The present study aims to predict, via self-consistent simulations, the plasma profiles, including current, temperature, and density for type I ELMy Hmode and steady-state ITER discharges. In these simulations, the plasma core transport is described using a combination of an anomalous and neoclassical transport. An anomalous transport is calculated using the theory-based multimode (MMM95) model; while the neoclassical transport is calculated using NCLASS model. In addition, the boundary conditions for temperature and density are described at the top of the pedestal. Two different models for hydrogenic and impurity boundary conditions are considered. The first model is called a static boundary model, in which the hydrogenic and impurity densities at the edge are fixed. Consequently, the edge effective charge is constant. In the second model, hydrogenic and impurity densities are assumed to be a large fraction of its lineaveraged density. As a result, the hydrogenic and impurity densities (as well as edge effective charge) are varied. For the pedestal temperature, it is assumed to be a constant. With these simulations, the behaviors of impurity in ITER plasmas can be studies. In addition, a parametric sensitivity study is carried out to determine the impacts of pedestal temperature, pedestal density, line-averaged density and impurity influx on

the impurity behaviors, mainly on the impurity transport and accumulation.

This paper is organized as follows: brief descriptions of relevant components of the BALDUR code, including the anomalous transport are given in Section 2; the prediction of ITER plasma profiles for standard type I ELMy H-mode and steady-state scenarios are presented and discussed in Section 3; sensitivity analysis is found in Section 4; and a summary is given in Section 5.

2. BALDUR INTEGRATED PREDICTIVE MODELING CODE

The BALDUR integrated predictive modeling code [11] is a 1.5-dimensional transport code designed to simulate a wide variety of plasma conditions in tokamaks. The BALDUR code follows the time evolution of electron and ion temperatures, charged particle densities, and the poloidal magnetic flux density as a function of magnetic flux surface. The shapes of the flux surfaces are determined by solving axisymmetric equilibrium force balance equations, given boundary conditions that may be changing with time. BALDUR provides a detailed and self-consistent treatment of neutral hydrogen and impurity transport, multi-species effects, several forms of auxiliary heating, fast alpha particles and fusion heating, plasma compression effects, ripple losses, and scrape-off layer. In addition, there are various options available to treat the axisymmetric effects of large scale instabilities such as sawtooth oscillations, saturated tearing modes, and high-n ballooning modes. Various physical processes incorporated in the code are: transport, plasma heating, helium influx, boundary conditions, plasma equilibrium shape and sawtooth oscillations. The models for each process are combined to self-consistently solve for plasma properties. BALDUR code predicts fusion heating and helium ash accumulation via the nuclear fusion rate, coupled with Fokker-Planck package used to calculate the slowing down of the spectrum of fast alpha particles on each flux surface. Also the fusion heating component of the BAL-DUR code calculates the production rate of thermal helium ions and the rate of the depletion of deuterium and tritium ions within the plasma core. The basic diffusion equations solved in BALDUR in Gaussian units are:

$$\begin{split} \frac{\partial n_a}{\partial t} &= -\frac{1}{r} \frac{\partial}{\partial r} (r \Gamma_a) + S_a, \quad a = 1, 2, l, h, \\ \frac{\partial E_j}{\partial t} &= -\frac{1}{r} \frac{\partial}{\partial r} (r q_j) + Q_j, \quad j = i, e, \\ \frac{\partial B_0}{\partial t} &= \frac{c^2}{4\pi} \frac{\partial}{\partial r} \left[\frac{\eta}{r} \frac{\partial (r B_0)}{\partial r} \right] - c \frac{\partial}{\partial r} (\eta J_{\text{beam}}), \end{split}$$

where n_a is the number density of species a, E_j is the energy density of thermal ions or of electrons, and B_{θ} is the magnetic field along the (poloidal) direction

Table 1. Notation used in this paper

Symbol	Unit	Description	Symbol	Unit	Description
χweiland	m ² /s	Weiland thermal diffusivity	$\overline{n}_{\mathrm{Be}}$	m^{-3}	Line-averaged density of Beryllium
χ_{RB}	m ² /s	Resistive ballooning thermal diffusivity	\overline{n}_l	m^{-3}	Line-averaged density
χ_{KB}	m ² /s	Kinetic ballooning thermal diffusivity	R	m	Major radius
χ_i	m ² /s	Ion thermal diffusivity	a	m	Minor radius
χ_e	m ² /s	Electron thermal diffusivity	I_p	MA	Plasma current
$D_{ m H}$	m^2/s	Particle diffusivity	B_T	T	Magnetic field
D_{Z}	m ² /s	Impurity diffusivity	κ ₉₅		Elongation
ρ		Normalized minor radius	δ_{95}		Triangularity
$n_{\rm D,ped}$	m^{-3}	Pedestal density of deuterium	$c_{ m D,imp}$		Deuterium constant multiplier
$n_{\rm T, ped}$	m^{-3}	Pedestal density of tritium	$c_{ m T,imp}$		Tritium constant multiplier
$n_{\mathrm{He,ped}}$	m^{-3}	Pedestal density of helium	$c_{ m He,imp}$		Helium constant multiplier
$n_{\mathrm{Be,ped}}$	m^{-3}	Pedestal density of beryllium	$c_{\mathrm{Be,imp}}$		Beryllium constant multiplier
$\overline{n}_{\mathrm{D}}$	m^{-3}	Line-averaged density of deuterium	$T_{\rm ped}$	keV	Pedestal temperature
$\overline{n}_{\mathrm{T}}$	m^{-3}	Line-averaged density of tritium	$n_{\rm ped}$	m^{-3}	Pedestal density
$\overline{n}_{\mathrm{He}}$	m^{-3}	Line-averaged density of helium	$Z_{ m eff}$		Effective charge

encircling the plasma column. More details of the code can be found in [11]. Simulation results obtained from BALDUR code have previously been compared with experimental data, yielding an overall agreement of approximately 10% average normalized rms deviation [12, 13].

2.1. Multimode Core Transport Model (MMM95)

In this work, the Multimode Model version 1995 (MMM95) is a combination of theory-motivated transport models used to predict plasma profiles in tokamaks. It consists of the Weliand model for the ion temperature gradient (ITG) and trapped electron modes (TEM) [14–16], the Guzdar–Drake model for drift-resistive ballooning modes [17, 18], and kinetic ballooning modes [19]. Usually, the Weiland model for ITG and TEM modes provides the largest contribution, followed by drift-resistive ballooning mode and kinetic ballooning mode, respectively. The Weiland model is derived by linearizing the fluid equations, with magnetic drifts for each plasma species. Eigenvalues and eigenvectors computed from these fluid equations are computed for a given Fourier harmonic of the perturbed variables. It is then used to compute a quasi-linear approximation for the thermal and helium transport fluxes. The Weiland model includes many different physical phenomena such as effects of trapped electrons, unequal ion and electron temperatures $(T_i \neq T_e)$ impurities, fast ions, finite β and collisions. The resistive ballooning model (χ_{RB}) in MMM95 transport model is based on the 1993 $\mathbf{E} \times \mathbf{B}$ drift-resistive ballooning mode model by Guzdar-Drake, in which the transport is proportional to the pressure gradient and collisionality. The contribution from the resistive ballooning model usually dominates the transport near the plasma edge. The kinetic ballooning model (χ_{KB}) is a semi-empirical model, which usually provides a small contribution to the total diffusivity throughout the plasma, except near the magnetic axis.

However, for the ITER cases in this work, it is found that the contribution from the kinetic ballooning model plays quite a significant role in the region near the plasma core up to a radius of 1.0 m. This model is an approximation to the first ballooning mode stability limit. All the anomalous transport contributions to the MMM95 transport model are multiplied by κ^{-4} since the models were originally derived for circular plasmas. The expressions of transport coefficients in MMM95 are

$$\chi_i = 0.8\chi_{i,\text{ITG\&TEM}} + \chi_{i,\text{RB}} + \chi_{i,\text{KB}}, \tag{1}$$

$$\chi_e = 0.8\chi_{e,\text{ITG\&TEM}} + \chi_{e,\text{RB}} + \chi_{e,\text{KB}}, \qquad (2)$$

$$D_{\rm H} = 0.8 D_{\rm H.ITG\&TEM} + D_{\rm H.RB} + D_{\rm H.KB},$$
 (3)

$$D_{\rm Z} = 0.8 D_{\rm Z,ITG\&TEM} + D_{\rm Z,RB} + D_{\rm Z,KB}.$$
 (4)

Note that the notation used in this paper can be found in Table 1.

2.2. NCLASS Module

The NCLASS module [20] calculates the neoclassical transport properties of multi-species axisymmetric plasma of arbitrary aspect ratio, geometry and collisionality. The neoclassical effects refer to the flows resulting from Coulomb collisions between particles

drifting in nonuniform magnetic and electric fields. This module determines a multifluid model for the parallel and radial force balance equations from which the neoclassical bootstrap current, parallel electrical resistivity, impurity and fuel ion radial particle transport, ion radial thermal transport and plasma poloidal rotation. It is designed to be called from a transport code that provides the plasma density and temperature profiles, as well as a number of flux-surface-averaged geometric quantities.

2.3. Boundary Density Model

It is known that source of each plasma species are different. For example, deuterium and tritium are from gas puffing or pellet injection. Helium mainly occurs from the fusion reactions inside the plasma core; while beryllium can be originated from the SOL or plasma wall. In this work, two simple treatments for boundary density are investigated. The first model is called a "static boundary density model," in which a fixed density is assumed as follows:

$$n_{\text{D,ped}} = 2.69 \times 10^{19} \text{ m}^{-3},$$

 $n_{\text{T,ped}} = 2.69 \times 10^{19} \text{ m}^{-3},$
 $n_{\text{He,ped}} = 5.68 \times 10^{18} \text{ m}^{-3},$
 $n_{\text{Be,ped}} = 1.42 \times 10^{18} \text{ m}^{-3}.$

In the calculation of density values above, it is assumed that the deuterium density is equal to the tritium density. In addition, the pedestal density of beryllium is assumed to be 2% of the electron density at the pedestal, and the effective charge is assumed to be 1.4. Also, the pedestal density is 71% of the line-averaged electron density, which is the boundary for density used in [21]. For the second model, it is called a "dynamic boundary density model." The hydrogenic and impurity density for each species is a large fraction of its line-averaged density. The pedestal density model is implemented to calculate each particle species, which show as Eqs. (5)—(8),

$$n_{\rm D.ped} = c_{\rm D} \overline{n}_{\rm D},\tag{5}$$

$$n_{\mathrm{T,ped}} = c_{\mathrm{T}} \overline{n}_{\mathrm{T}}, \tag{6}$$

$$n_{\text{He,ped}} = c_{\text{He}} \overline{n}_{\text{He}},$$
 (7)

$$n_{\text{Be,ped}} = c_{\text{Be}} \overline{n}_{\text{Be}},$$
 (8)

where c_x and \overline{n}_x are the density constants and lineaveraged density for each plasma species, respectively. For simplicity in this work, all density constants (c_D , c_T , c_{He} , and c_{Be}) are assumed to be constant with the value of 0.71, which is similar to the constant value for electron pedestal density proposed in [21]. Note that this constant value for electron pedestal density yielded agreement with experimental data about 12% rms deviation [21]. The comparison results for these

two density boundary models will be discussed in Section 3 and these density constants will be varied later in Section 4.2. It is worth mentioning that beryllium source in this work results from the impurity influx from outside main plasma. Also, the actual behaviors for those plasmas and impurities are complicated. In the common sense, the density constants (c_D , c_T , c_{He} , and c_{Be}) should be different. However, for simplicity in this work, they are assumed to be the same. However, even though the constants for each plasma species in the dynamic model are the same (at 0.71), the actual value of boundary can be different, depending its line average density. For the pedestal temperature, a fixed pedestal temperature of 4 keV is used and this value is varied in Section 4.1.

3. SIMULATION RESULTS AND DISCUSSION

Self-consistent simulations for ITER plasma are carried out using 1.5D BALDUR integrated predictive modeling code. Physical parameters are chosen to match those of type I ELMy H-mode ITER scenarios $(R = 6.2 \text{ m}, a = 2.0 \text{ m}, I_p = 15 \text{ mA}, B_T = 5.3 \text{ T}, \kappa_{95} =$ 1.7, $\delta_{95} = 0.33$, and $\overline{n}_l = 10^{20} \text{ m}^{-3}$) and steady-state scenarios (R = 6.2 m, a = 2.0 m, $I_p = 9 \text{ mA}$, $B_T = 5.3 \text{ T}$, $\kappa_{95} = 2.0$, $\delta_{95} = 0.5$, and $\bar{n}_l = 0.7 \times 10^{20} \, \text{m}^{-3}$). The time period that used in all simulations is 1 h (3600 s) for both standard H-mode and steady-state scenarios. The total auxiliary heating power used in the H-mode simulations in 40 MW, of which 33 MW comes from the NBI heating power and 7 MW comes from the RF heating power. In the steady-state simulations, the total auxiliary heating power is 53 MW, of which 33 MW comes from the NBI heating power and 20 MW comes from the RF heating power. The plasma current and density are slowly ramped up to their target values with in the first 100 s of the simulations. During the start-up phase, the plasma current was initially 3 MA, and it is slowly increased to the target value of 15 MA, in the case of standard H-mode. The same initial setup is used for the steady-state scenario, but the plasma current target is only 9 MA. It should be noted that several physical processes are not included in these simulations, such as ELM crashes and neoclassical tearing modes. Hence, the simulation results do not represent the complete ITER plasma dynamics. However, it is expected that these simulations include sufficient physics to describe the plasma when it reaches a quasi-steady state. For each simulation, anomalous transport is calculated using the theory-based MMM95 core transport model and the NCLASS neoclassical transport module. It is assumed in this work that there are only four plasma species considered: two working gas species (deuterium and tritium) and two impurity species (helium and beryllium). The boundary temperature conditions are provided at the top of the pedestal by fixing both the ion

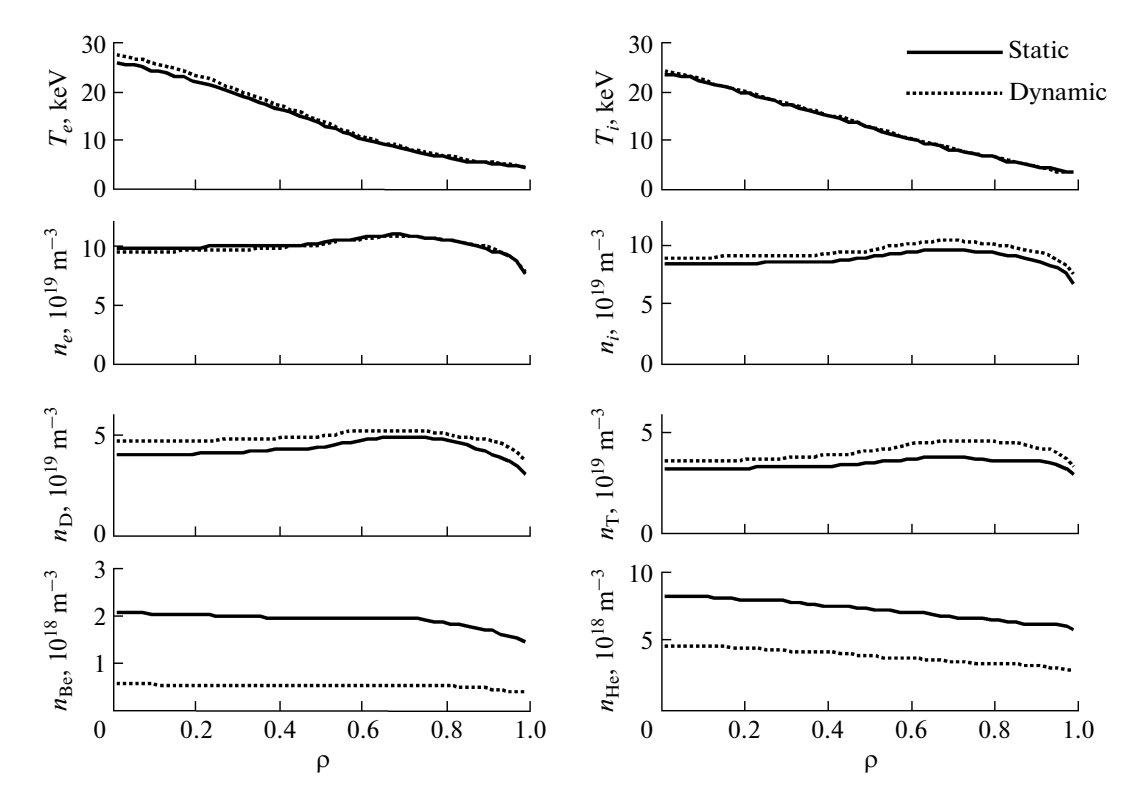


Fig. 1. Profiles of the ion and electron temperatures (T_e and T_i) and the ion, electron, deuterium, tritium, beryllium, and helium densities (n_e , n_i , n_D , n_T , n_{Be} , and n_{He}) as functions of the normalized minor radius at the time 3600 s. The simulations were carried out using the static and dynamic boundary density models for the ITER standard H-mode scenario.

and electron pedestal temperatures at 4.0 keV. For the plasma density, two different models for hydrogenic and impurity boundary conditions are considered. The first model is called a static boundary model, where the impurity density at the edge is fixed. In the second model, impurity density for each impurity species is a large fraction of its line-averaged density. It is assumed in this work that the impurity influx is 10^{11} particles/(cm² s). Note that the impurity influx will be varied to observe its impacts on the impurity behaviors in Section 4.4.

Figures 1 and 2 show the profiles of the electron temperature; ion temperature; and electron, deuterium, tritium, beryllium, and helium densities as functions of normalized minor radius at 3600 s for the simulations with type I ELMy H-mode and steady-state scenarios, respectively. Note that the plasma has already reached a steady state at this time. These results are shown for simulations using static and dynamic boundary density models. It can be seen that the predicted temperatures are quite similar for both simulations with different boundary models. However, the densities for hydrogenic and impurity species are noticeably different. The simulation with the static density boundary model yields lower deuterium and tritium profiles, but higher beryllium and helium den-

sity profiles compared to those with the dynamic density boundary model.

Figure 3 shows the profiles of ion thermal diffusivity coefficient (χ_i) , electron thermal diffusivity coefficient (χ_e) , hydrogenic diffusivity coefficient (D_H) and impurity diffusivity coefficient (D_7) as functions of normalized minor radius at 3600 s for ITER standard H-mode scenario (same time with Fig. 1). It can be seen that all diffusivities for the simulations using the dynamic boundary density model are higher than those using the static boundary density model. Contributions for ion thermal and impurity diffusivity coefficients as functions of normalized minor radius from the simulations using the static and dynamic boundary density models for ITER standard H-mode scenario are shown in Fig. 4. It can be seen that for γ_i , the ITG and TEM contributions provide the largest contribution in most region of the plasma, except closed to the plasma center in which the neoclassical transport is dominant. This is similar observed in previous ITER simulations [8, 12, 21-23]. For the impurity transport, the kinetic-ballooning term provides the largest contribution in most region of the plasma, except closed to the plasma edge, in which the ITG and TEM contribution becomes the largest. It is worth mentioning that the resistive ballooning contribution is rather small everywhere in the plasma.

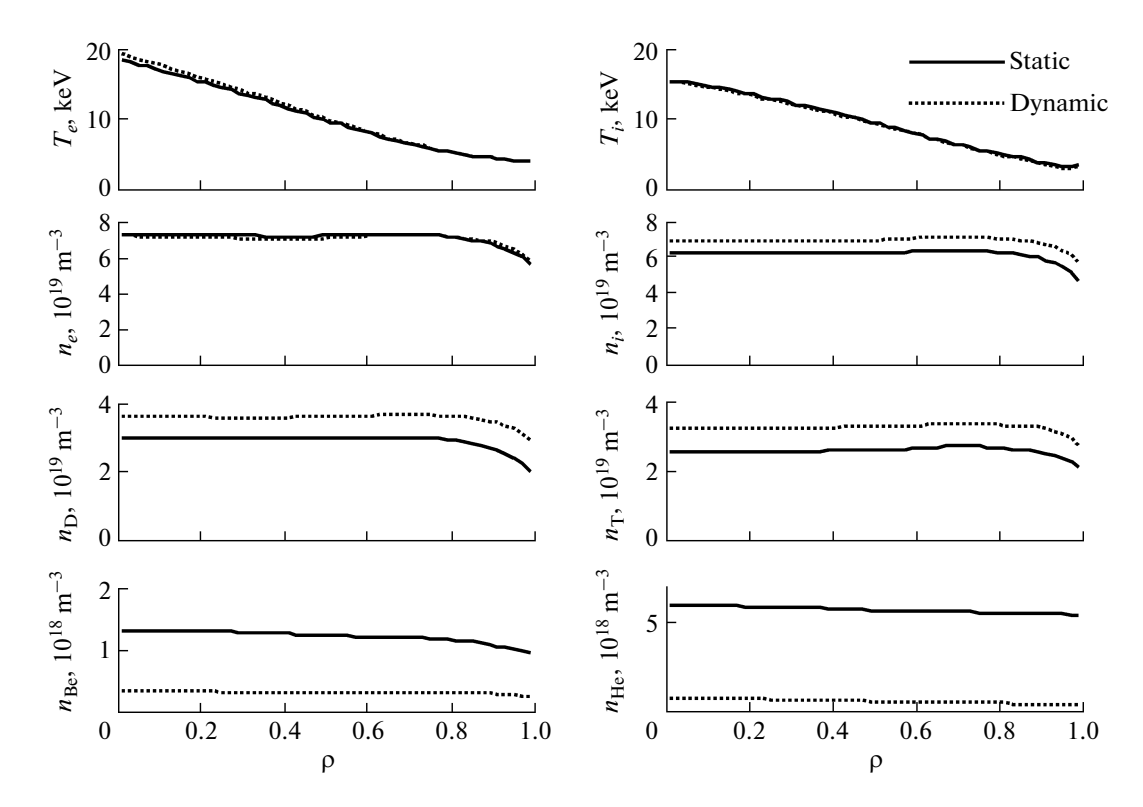


Fig. 2. Profiles of the ion and electron temperatures (T_e and T_i) and the ion, electron, deuterium, tritium, beryllium, and helium densities (n_e , n_i , n_D , n_T , n_{Be} , and n_{He}) as functions of the normalized minor radius at the time 3600 s. The simulations were carried out using the static and dynamic boundary density models for the ITER steady-state scenario.

Figure 5 shows the impurity content of beryllium and helium as functions of time from 3000 to 3600 s for simulations with standard H-mode and steady-state scenarios. For both scenarios, it can be seen that the simulation results of impurity density in steady state using the static boundary density model predicted the impurity density that is higher than that using the dynamic boundary density model. The summary of averaged central and total densities for deuterium, tritium, beryllium, and helium are shown in Table 2. It

can be seen that the static density boundary model yields lower central and total densities for deuterium and tritium, but higher central and total densities for beryllium and helium density compared to those with the dynamic density boundary model. This trend is observed in the simulations of both scenarios for ITER. The behaviors of the boundary densities can explain the behaviors of the profiles previously observed in Figs. 1 and 2.

Table 2. Summary of plasma properties at the time of 3600 s obtained from simulations using MMM95 core transport model coupled with two different boundary density models (static boundary density model and dynamic boundary density model) for ITER standard type I ELMy H-mode and steady state scenario

Parameters	Type I EL	My H-mode	Steady state			
Parameters	Static model	Dynamic model	Static model	Dynamic model		
$n_{\rm D.0}, \times 10^{19}{\rm m}^{-3}$	4.058	4.692	2.998	3.637		
$n_{\rm D,0}, \times 10^{19} \mathrm{m}^{-3}$ $n_{\rm T,0}, \times 10^{19} \mathrm{m}^{-3}$ $n_{\rm He,0}, \times 10^{19} \mathrm{m}^{-3}$	3.237	3.657	2.533	3.229		
$n_{\text{He.0}}, \times 10^{19} \text{m}^{-3}$	0.814	0.465	0.601	0.071		
$n_{\text{Be }0}, \times 10^{19} \text{m}^{-3}$	0.252	0.056	0.132	0.034		
$n_{\rm D,total}$, ×10 ²² particles	3.440	3.801	2.461	3.087		
$n_{\text{T,total}}, \times 10^{22} \text{ particles}$	2.811	3.335	2.233	2.809		
$n_{\rm He,total}$, ×10 ²² particles	0.530	0.279	0.488	0.046		
$n_{\rm Be,total}$, ×10 ²² particles	0.144	0.039	0.101	0.027		

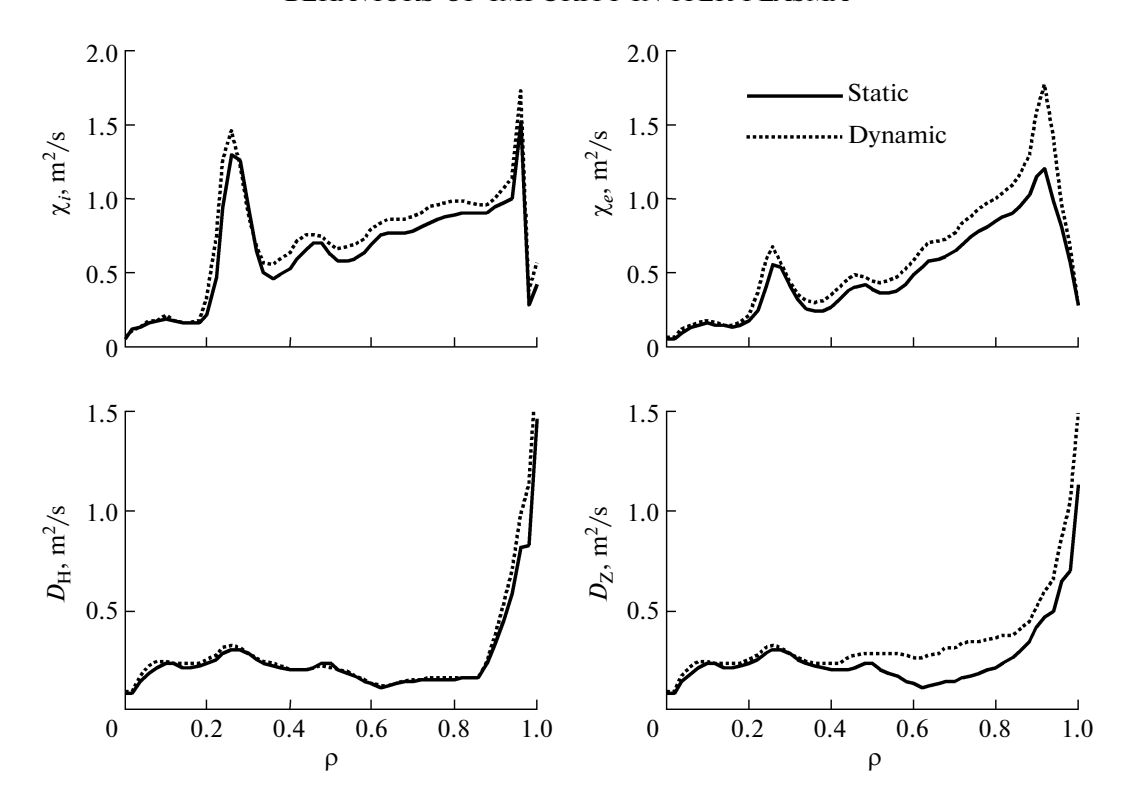


Fig. 3. Profiles of the ion thermal diffusion coefficient (χ_i), electron thermal diffusion coefficient (χ_e), hydrogenic particle diffusion coefficient (D_H), and impurity particle diffusion coefficient (D_Z) as functions of the normalized minor radius at the time 3600 s. The simulations were carried out using the static and dynamic boundary density models for the ITER standard H-mode scenario

Figure 6 shows the time evolution of effective charge ($Z_{\rm eff}$) at different normalized minor radii ($\rho = 0.00, 0.25, 0.50, 0.75,$ and 1.00) during 3000 to 3600 s. It can be seen that the effective charge in the simulations using the static boundary density model is around 1.4; while the effective charge in the simulations using the dynamic boundary density model is much lower, about 1.1. The effective charge with the dynamic boundary model is quite low. It can also be seen that the effective charge in the simulations for standard type I ELMy H-mode tends to be higher than that for steady state.

4. SENSITIVITY STUDY

In this section, the parametric sensitivity of BAL-DUR simulations is investigated using the dynamic boundary density model. The effects of pedestal temperature ($T_{\rm ped}$), pedestal density ($n_{\rm ped}$), line-averaged density (\overline{n}_l) and impurity influx on the impurity behaviors in ITER plasmas are investigated in this section.

4.1. Variation of the Pedestal Temperature

In this study, the simulations of ITER plasmas with standard type I ELMy H-mode and steady-state sce-

narios are carried out using different values of pedestal temperature ($T_{ped} = 3.0, 4.0, \text{ and } 5.0 \text{ keV}$). It is found that the plasma reaches the quasi-steady state in all simulations. The densities of beryllium and helium in the simulations for both the standard type I ELMy Hmode and steady-state scenarios are shown in Fig. 7. It can be seen that the density for both beryllium and helium decreases with the increasing of pedestal temperature. The averaged central and total densities for deuterium, tritium, beryllium and helium during the time from 3000 to 3600 s for ITER standard type I ELMy H-mode scenario are summarized in Table 3. For the ITER standard type I ELMy H-mode scenario, it can be seen that the total beryllium particles decrease about 58 and 75% as the pedestal temperature increases from 3 to 4 and 5 keV, respectively. For the total helium particles, it decreases from 17 and 20% as the pedestal temperature increases from 3 to 4 and 5 keV, respectively. On the other hand, the total deuterium and tritium particles increase with the increase of pedestal temperature. Note that the similar trend is observed for the ITER steady-state scenario. It is also found that the impurity transport increases as the pedestal temperature increases, especially near the plasma edge. Each contributions of impurity diffusivity are shown in Fig. 8 for each pedestal temperature. It can be seen that the contribution from ITG&TEM

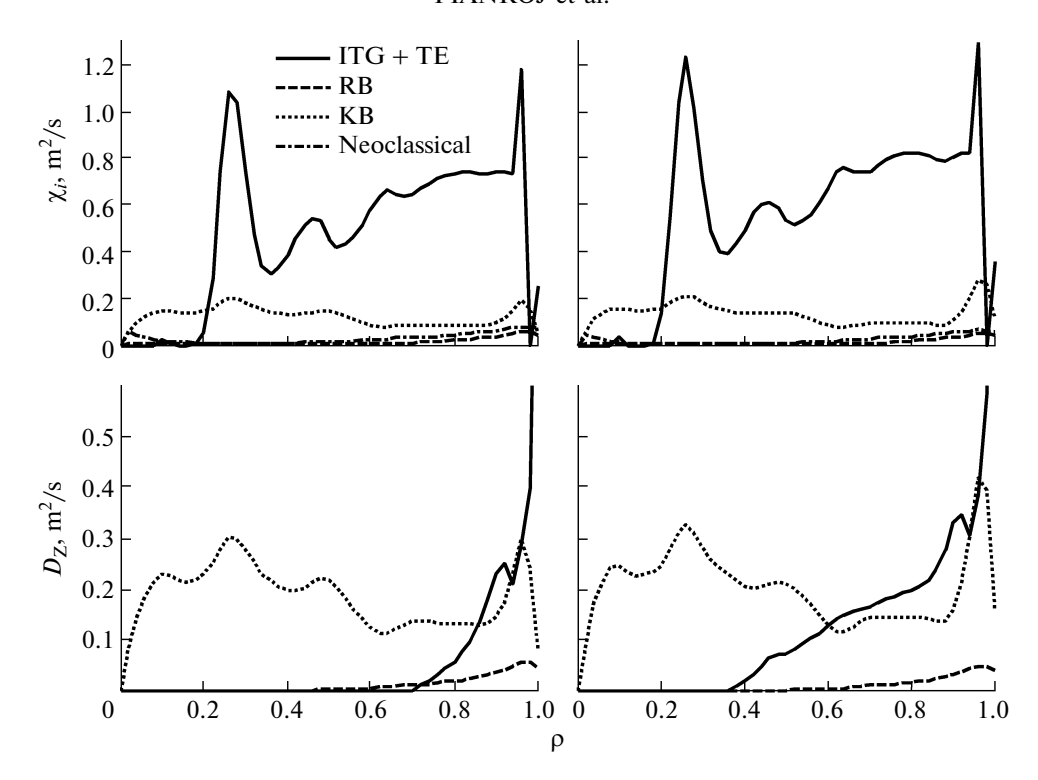


Fig. 4. Contributing terms of the ion thermal diffusion coefficient (χ_i) and impurity particle diffusion coefficient (D_Z) as functions of the normalized minor radius at the time 3600 s. The simulations were carried out by using the ITER standard H-mode scenario with static (left panel) and dynamic (right panel) boundary density models.

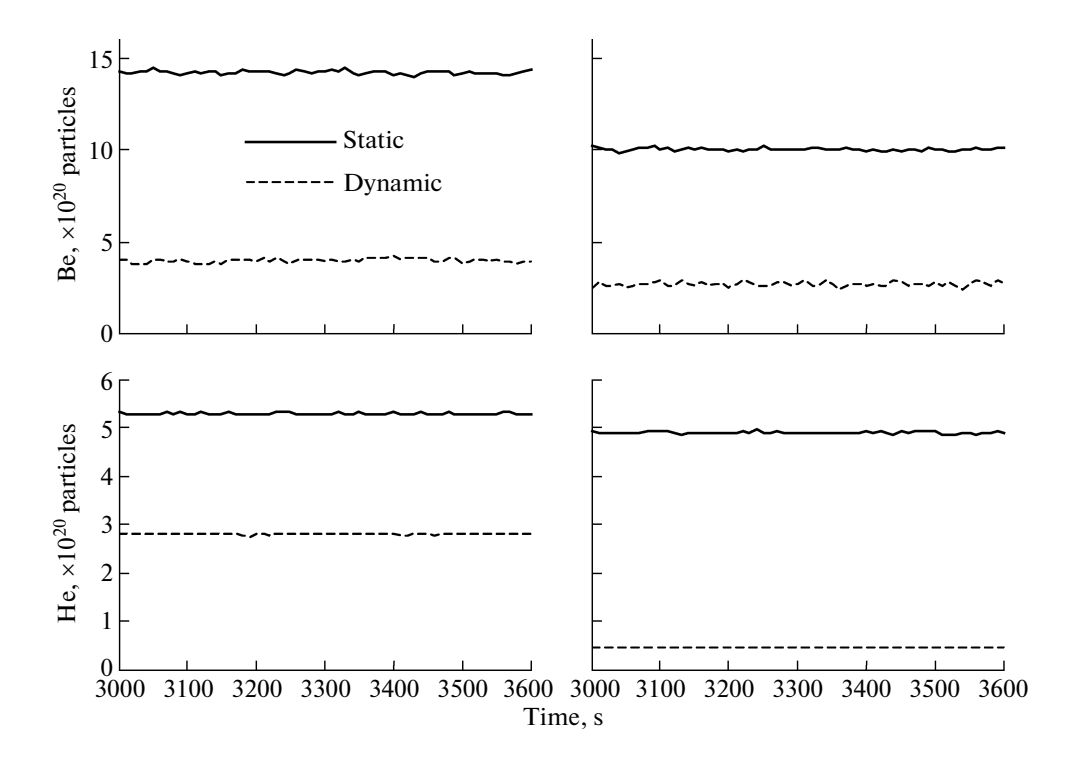


Fig. 5. Densities of beryllium (Be) and helium (He) as functions of time during 3000 to 3600 s. The simulations were carried out by using the ITER standard H-mode (left panels) and steady state (right panels) scenarios with static and dynamic models.

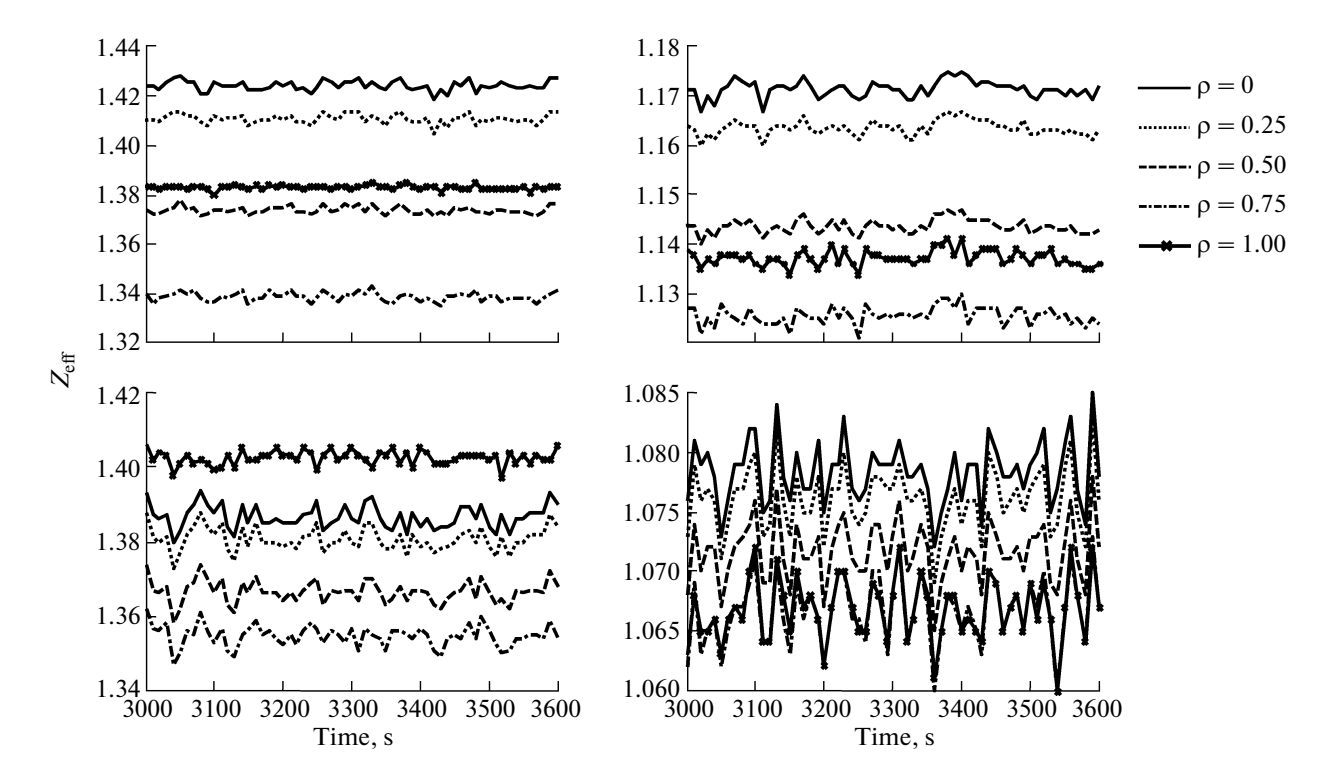


Fig. 6. Time evolutions of the effective charge ($Z_{\rm eff}$) with ρ of 0.00, 0.25, 0.50, 0.75, and 1.0 during 3000 to 3600 s. The simulations were carried out by using the ITER standard H-mode with static model (top left), ITER standard H-mode with dynamic model (top right), steady-state with static model (bottom left) and steady-state with dynamic model (bottom right).

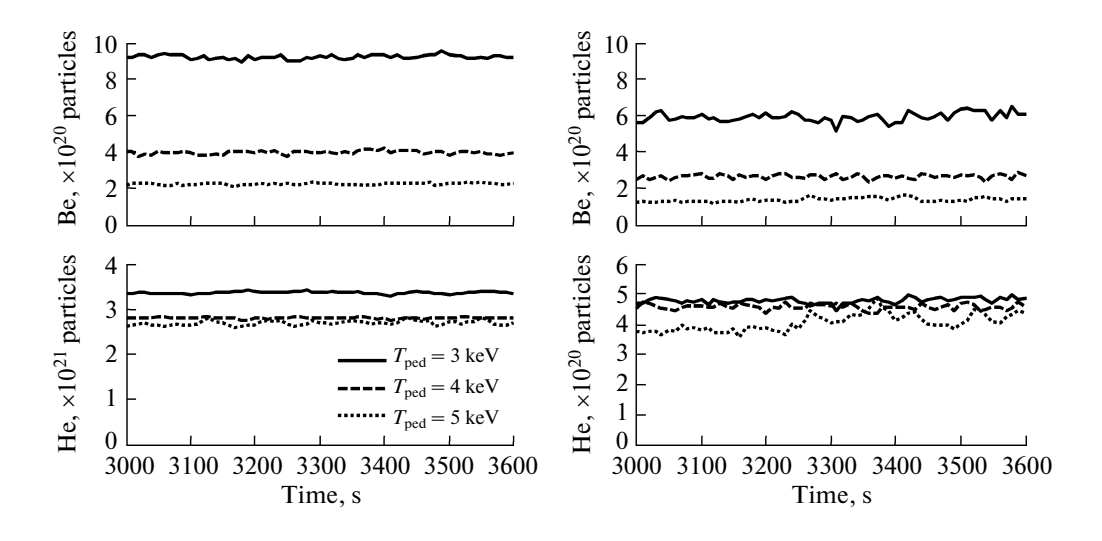


Fig. 7. Densities of beryllium (Be) and helium (He) as functions of time during 3000 to 3600 s. The simulations were carried out by using dynamic boundary density model for the ITER standard H-mode (left panel) and steady-state (right panel) scenarios. The pedestal temperatures are 3.0, 4.0, and 5.0 keV.

modes increases with the increasing temperature. On the other hand, the contribution from resistive ballooning (RB) and kinetic ballooning (KB) modes decreases.

4.2. Variation of the Density Constant

In this study, the simulations of ITER plasmas with standard type I ELMy H-mode and steady-state scenarios are carried out using different values of the den-

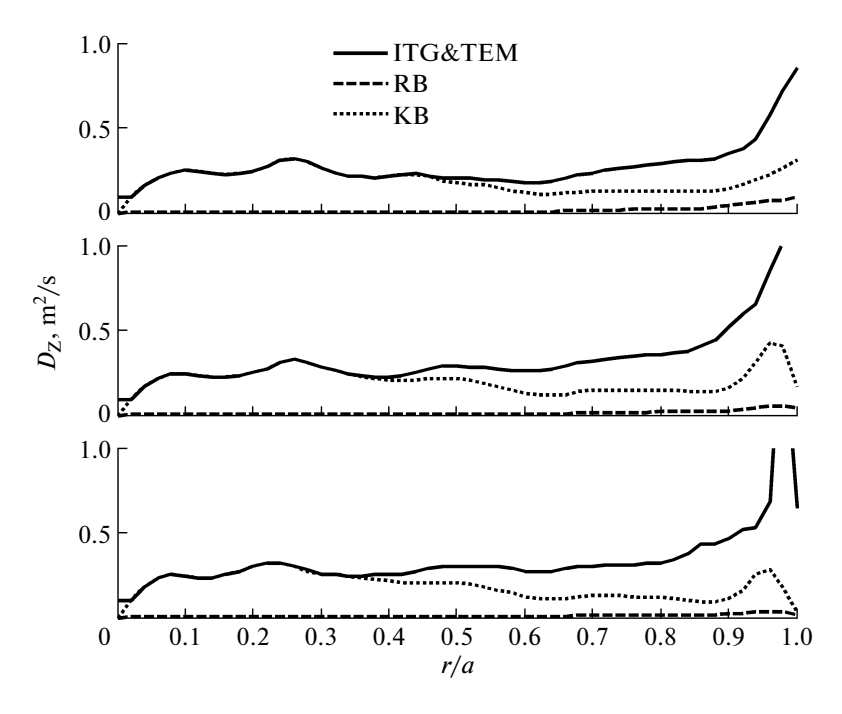


Fig. 8. Contributing terms of impurity particle diffusion coefficient (D_Z) are plotted as a function of normalized minor radius at time 3600 s for different pedestal temperatures: 3 (top panel), 4 (middle panel), and 5 keV (bottom panel). The simulations were carried out by using the ITER standard H-mode scenario with the dynamic boundary density models.

sity constant (0.51, 0.61 and 0.71). Note that lower density constant results in lower pedestal density. It is found that the densities of beryllium and helium in the simulations for both the standard type I ELMy Hmode and steady-state scenarios decrease as the density constant decreases, shown in Fig. 9. The averaged central and total densities for deuterium, tritium, beryllium and helium during the time from 3000 to 3600 s for ITER standard type I ELMy H-mode scenario are summarized in Table 4. For the ITER standard type I ELMy H-mode scenario, it can be seen that the total beryllium particles decrease about 70 and 89% as the density constant decreases from 0.71 to 0.61 and 0.51, respectively. For the total helium particles, it decreases from 61 and 78% as the density constant decreases from 0.71 to 0.61 and 0.51, respectively. Similarly, the total deuterium and tritium particles decrease with the decrease of the density constant.

Note that the similar trend is observed for the ITER steady-state scenario. It is also found that the impurity transport decreases as the pedestal density increases, especially near the plasma edge. Each contributions of impurity diffusivity are shown in Fig. 10 for each density constant. It can be seen that the contribution from each mode changes slightly with increasing density constant. However, no clear trend is observed.

4.3. Variation of the Line-Averaged Electron Density

Impurity transport depends on a number of factors such as plasma temperature, line-averaged density and the nature of impurity species. Since line-averaged density can be easily monitored and controlled in actual tokamak operation, it would be interesting to find if impurity density in steady state can be enhanced or hindered, i.e., controlled, merely by varying the

Table 3. Averaged deuterium, tritium, beryllium, and helium densities during the time from 3000 to 3600 s are summarized for different pedestal temperatures (the simulations are carried out for type I ELMy H-mode scenario)

$T_{\rm red}$, keV	Deuterium		Tritium		Bery	llium	Helium		
	Center (×10 ¹⁹ m ⁻³)	Total (×10 ²² pts.)	Center (×10 ¹⁹ m ⁻³)	Total (×10 ²² pts.)	Center (×10 ¹⁹ m ⁻³)	Total (×10 ²² pts.)	Center (×10 ¹⁹ m ⁻³)	Total (×10 ²² pts.)	
3.0	4.638	3.708	3.264	3.092	0.132	0.092	0.546	0.336	
4.0	4.692	3.801	3.657	3.335	0.056	0.039	0.465	0.279	
5.0	4.507	3.977	3.930	3.525	0.031	0.023	0.439	0.270	

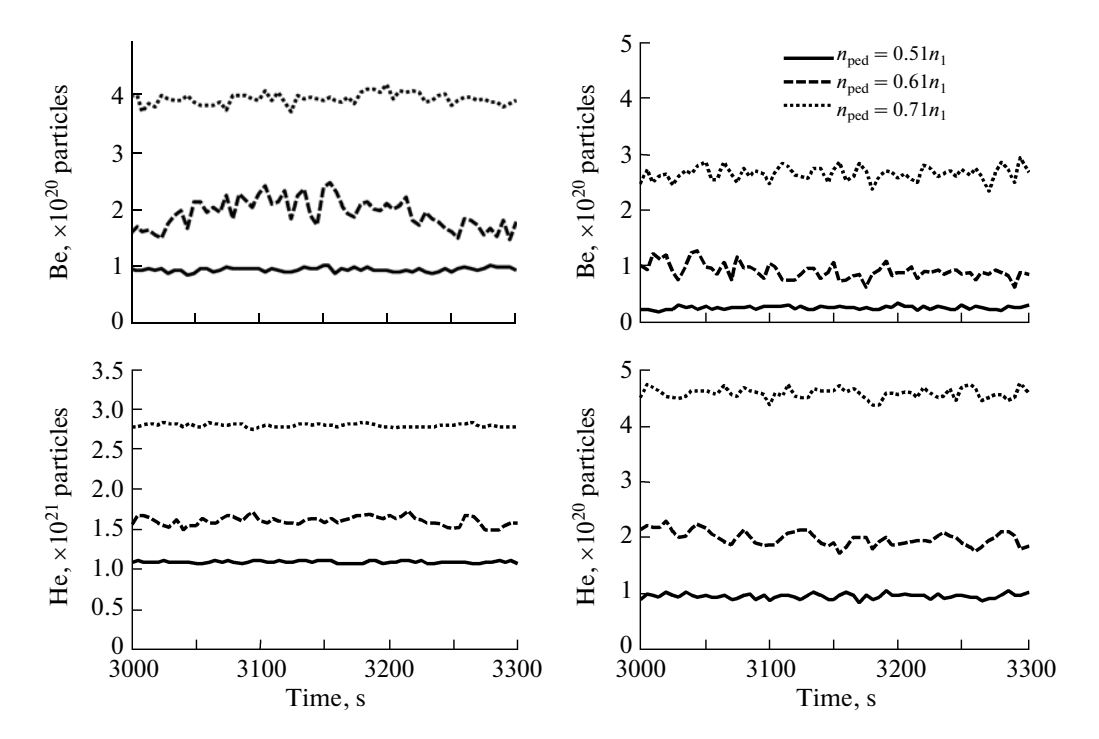


Fig. 9. Densities of beryllium (Be) and helium (He) as functions of time during 3000 to 3600 s. The simulations were carried out by using the dynamic ITER standard H-mode (left panels) and dynamic steady-state (right panels) scenarios with $n_{\text{ped}} = 0.51n_{l}$, $0.61n_{l}$, and $0.71n_{l}$.

plasma density. The line-averaged density of 10^{20} m⁻³ is used for the simulations of standard type I ELMy H-mode scenario in Section 3. In this section, simulations are carried out using \bar{n}_l of 0.8×10^{20} , 10^{20} , and 1.2×10^{20} m⁻³. It is found that the densities of beryllium and helium in the simulations for both the standard type I ELMy H-mode and steady-state scenarios decrease as the density constant decreases, shown in Fig. 11. The averaged central and total densities for deuterium, tritium, beryllium and helium during the time from 3000 to 3600 s for ITER standard type I ELMy H-mode scenario are summarized in Table 4. For the ITER standard type I ELMy H-mode scenario, it can be seen that the total beryllium particles decrease about 26 and 48% as the line average density

increases from 0.8×10^{20} , 10^{20} , and 1.2×10^{20} m⁻³, respectively. For the total helium particles, it decreases from 26 and 61% as the density constant increases from 0.8×10^{20} , 10^{20} , and 1.2×10^{20} m⁻³, respectively. Similarly, the total deuterium and tritium particles increase with the increase of line average density. Note that the similar trend is observed for the ITER steady-state scenario. It is also found that the impurity transport increases as the line average density increases, especially near the plasma edge. Each contributions of impurity diffusivity are shown in Fig. 12 for each line average density. It can be seen that the contributions from KB modes increases with the increasing line average density.

Table 4. Averaged deuterium, tritium, beryllium, and helium densities during the time from 3000 to 3600 s are summarized for different density constants (the simulations are carried out for the type I ELMy H-mode scenario)

$n_{\rm red},$ $\times 10^{19} {\rm m}^{-3}$	Deuterium		Tritium		Bery	llium	Helium		
	Center (×10 ¹⁹ m ⁻³)	Total (×10 ²² pts.)	Center (×10 ¹⁹ m ⁻³)	Total (×10 ²² pts.)	Center (×10 ¹⁹ m ⁻³)	Total (×10 ²² pts.)	Center (×10 ¹⁹ m ⁻³)	Total (×10 ²² pts.)	
0.51	4.437	3.798	4.043	3.826	0.013	0.009	0.216	0.108	
0.61	5.346	4.735	4.399	3.725	0.024	0.018	0.030	0.157	
0.71	4.692	3.801	3.657	3.335	0.056	0.039	0.465	0.279	

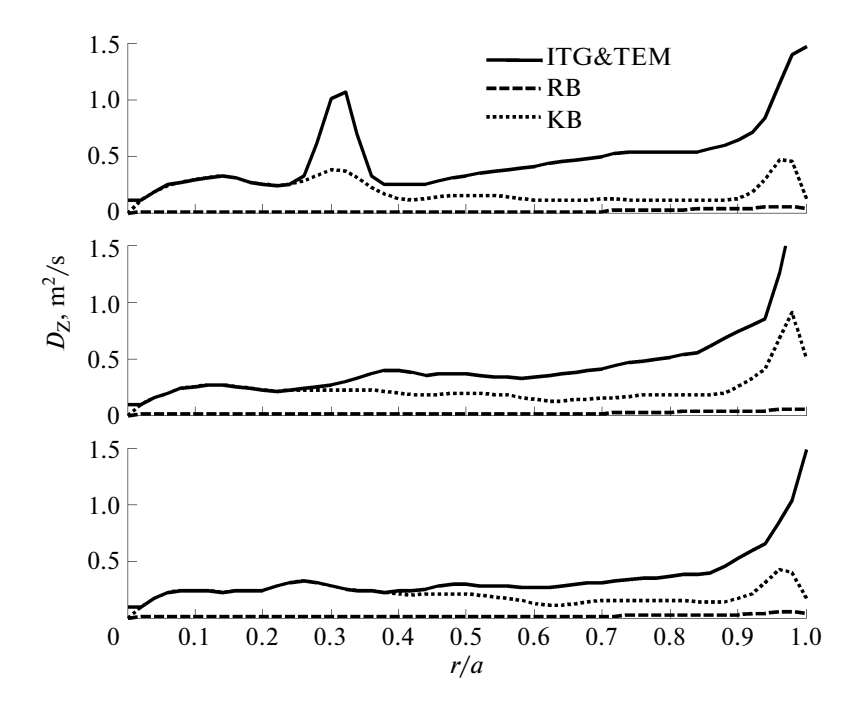


Fig. 10. Contributing terms of the impurity particle diffusion coefficient (D_Z) as functions of the normalized minor radius at the time 3600 s for different pedestal densities: $0.51n_I$ (top panel), $0.61n_I$ (middle panel), and $0.71n_I$ (bottom panel). The simulations were carried out by using the ITER standard H-mode scenario with the dynamic boundary density models.

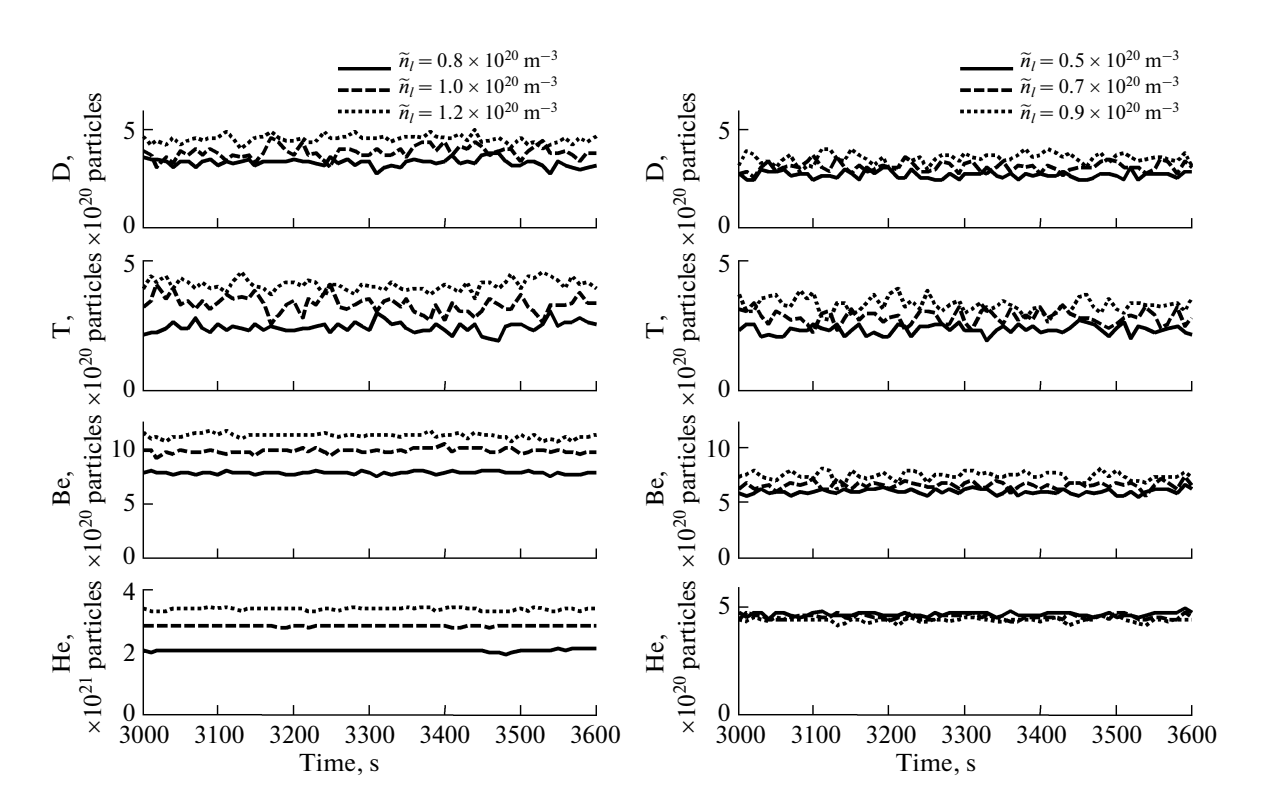


Fig. 11. Densities of deuterium (D), tritium (T), beryllium (Be) and helium (He) as functions of time during 3000 to 3600 s. The simulations were carried out by using the dynamic ITER standard H-mode (left panels) with $\bar{n}_l = 0.8 \times 10^{20}$, 10^{20} , and 1.2×10^{20} m⁻³ and dynamic steady state (right panels) with $\bar{n}_l = 0.5 \times 10^{20}$, 0.7×10^{20} , and 0.9×10^{20} m⁻³.

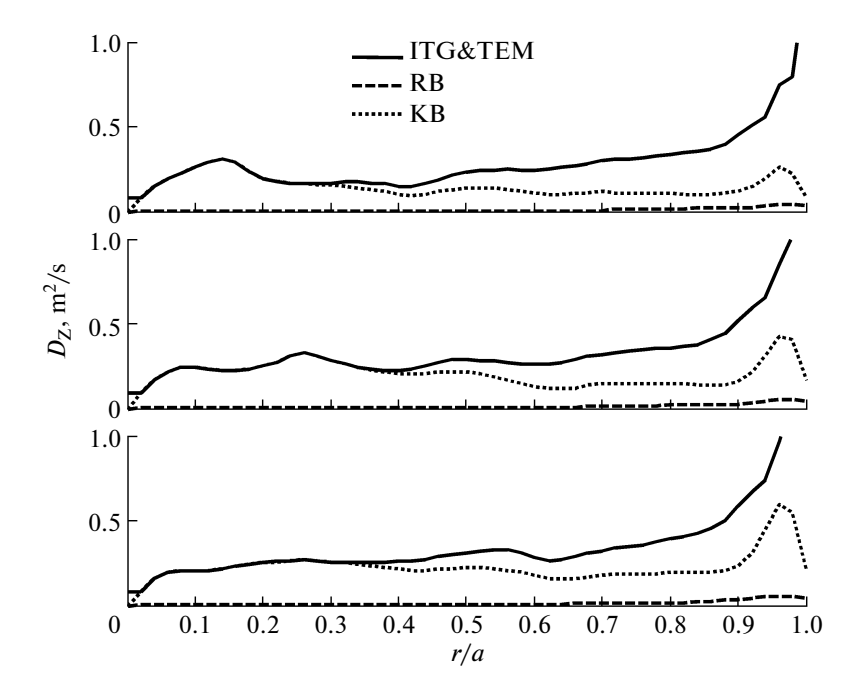


Fig. 12. Contributing terms of impurity particle diffusion coefficient (D_Z) as functions of the normalized minor radius at the time 3600 s for different pedestal densities: $\bar{n}_l = 0.8 \times 10^{20}$ (top panel), 10^{20} (middle panel), and 1.2×10^{20} m⁻³ (bottom panel). The simulations were carried out by using the ITER standard H-mode scenario with the dynamic boundary density model.

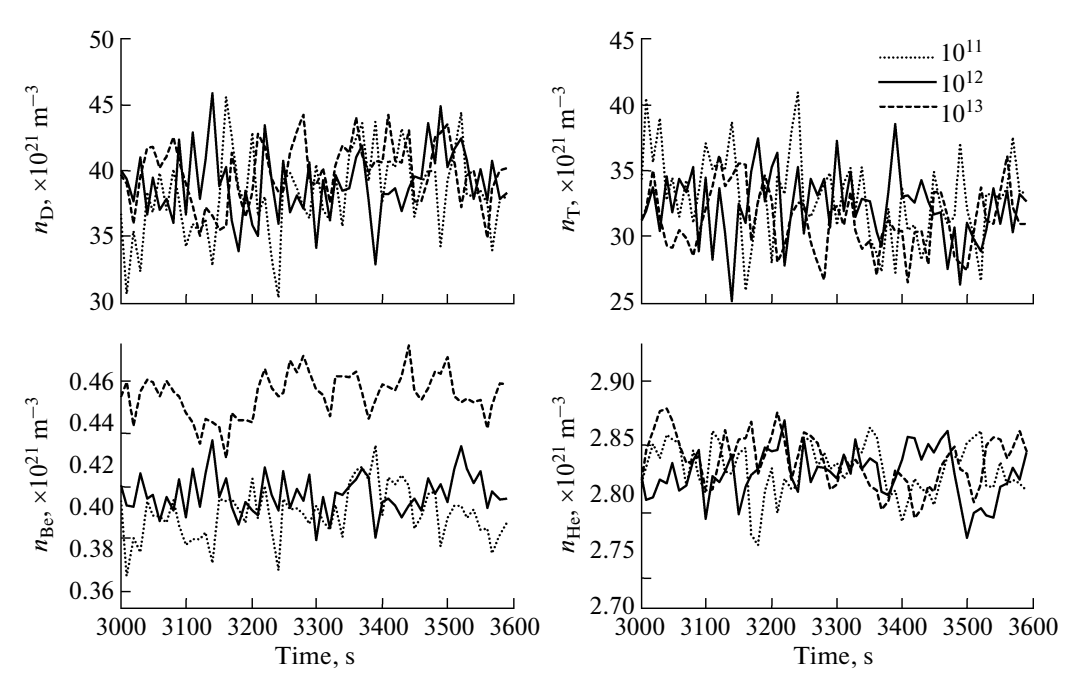


Fig. 13. Densities of deuterium (D), tritium (T), beryllium (Be), and helium (He) as functions of time during 3000 to 3600 s. The simulations were carried out by using the dynamic ITER standard H-mode with impurity influx of 10^{11} , 10^{12} , and 10^{13} particles/(cm² s).

4.4. Variation of the Impurity Influx

In the BALDUR simulations, the impurity from outside of the main plasma, such as from SOL region,

and the nuclear fusion reactions are the main impurity sources. In all of the previous simulations, a constant beryllium influx of 10^{11} particles/(cm² s) is used. To

	Deuterium		Tritium		Bery	llium	Helium		
	\overline{n}_l , m ⁻³	Center (×10 ¹⁹ m ⁻³)	Total (×10 ²² pts.)	Center (×10 ¹⁹ m ⁻³)	Total (×10 ²² pts.)	Center (×10 ¹⁹ m ⁻³)	Total (×10 ²² pts.)	Center (×10 ¹⁹ m ⁻³)	Total (×10 ²² pts.)
_	0.8	3.318	3.194	2.464	2.537	0.041	0.031	0.334	0.206
	1.0	4.692	3.801	3.657	3.335	0.056	0.039	0.465	0.279
	1.2	6.071	4.690	4.778	3.938	0.066	0.046	0.570	0.332

Table 5. Averaged deuterium, tritium, beryllium, and helium densities during the time from 3000 to 3600 s are summarized for different line averaged densities (the simulations are carried out for type I ELMy H-mode scenario)

investigate the sensitivity of the impurity influx, the impurity influx is varied to be 10^{11} , 10^{12} , and 10^{13} particles/(cm² s). It is found that the plasma temperature and density reach the quasi-steady state in all simulations. The evolution of deuterium, tritium, beryllium and helium in the simulations for the standard type I ELMy H-mode are shown in Fig. 13. It can be seen that the density in steady state for both beryllium tends to increase slightly with the increasing of impurity influx; while the density of other species reminds almost the same. It is also found that there is no significant change in the impurity transport as the impurity influx increases.

5. CONCLUSIONS

In this work, the behaviors of impurity in ITER in standard H-mode and steady-state scenarios are investigated via simulation using the 1.5D BALDUR integrated predictive modeling code. The impurity species considered are a combination of helium and beryllium. The simulations are carried out using MMM95 core transport model, coupled with NCLASS neoclassical model and different boundary models (static and dynamic boundary models). It is found that ion and electron temperatures, as well as ion, electron, deuterium, tritium, helium and beryllium densities reach quasi-steady-state values and all parameters are not much different between the two boundary models. However, the impurity density in steady state and the edge effective charge are significantly different in the two models. In the parametric sensitivity analysis, the pedestal temperature, pedestal density, line-averaged density, and impurity influx are investigated. All three parameters are observed to influence impurity behaviors.

ACKNOWLEDGMENTS

Authors thank Dr. R. Picha for discussions. This work was supported by Commission on Higher Education (CHE) and the Thailand Research Fund (TRF) under Contract No. RMU5180017. Mr. Y. Painroj thanks the Commission on Higher Education for supporting by grant fund under the program Strategic Scholarships for Frontier Research Network for the Ph.D. Program Thai Doctoral degree for this research.

REFERENCES

- 1. R. Aymar, P. Barabaschi, and Y. Shimomura, Plasma Phys. Controlled Fusion **44**, 519 (2002).
- T. Fulop and J. Weiland, Phys. Plasmas 13, 112504 (2006).
- 3. D. Post and S. Cohen, *ITER Physics* (ITER Physics Group and IAEA, Vienna, 1990).
- I. Yamada, K. Yamazaki, T. Oishi, et al., in *Proceedings* of the 18th International Toki Conference, Toki, 2008, p. 242.
- J. W. Davis and A. A. Haasz, J. Nucl. Mater. 241, 37 (1997).
- 6. J. Hogan, J. Nucl. Mater. **241**, 68 (1997).
- 7. H. Burbaumer, G. Kamelander, D. J. Sigmar, et al., Fusion Technol. **35**, 280 (1999).
- 8. T. Onjun and Y. Pianroj, Nucl. Fusion **49**, 075003 (2009).
- 9. P. Leekhaphan and T. Onjun, Thammasat Intern. J. Sci. Technol. **15** (3) (2010).
- V. Parail, P. Belo, P. Boerner, et al., Nucl. Fusion 49, 075 030 (2009).
- C. E. Singer, D. E. Post, D. R. Mikkelsen, et al., Comput. Phys. Commun. 49, 399 (1988).
- D. Hannum, G. Bateman, J. Kinsey, et al., Phys. Plasmas 8, 964 (2001).
- 13. T. Onjun, G. Bateman, A. H. Kritz, et al., Phys. Plasmas **8**, 975 (2001).
- H. Nordman, J. Weiland, and A. Jarmen, Nucl. Fusion 30, 983 (1990).
- 15. J. Weiland and A. Hirose, Nucl. Fusion 32, 151 (1992).
- 16. J. Nilsson and J. Weiland, Nucl. Fusion 34, 803 (1994).
- 17. J. E. Kinsey, G. Bateman, H. K. Arnold, et al., Phys. Plasmas 3, 561 (1996).
- 18. P. N. Guzdar, J. F. Drake, D. McCarthy, et al., Phys. Fluids B 5, 3712 (1993).
- 19. G. Bateman, H. K. Arnold, J. E. Kinsey, et al., Phys. Plasmas 5, 1793 (1998).
- W. A. Houlberg, K. C. Shaing, S. P. Hirshman, et al., Phys. Plasmas 4, 3231 (1997).
- 21. G. Bateman, T. Onjun, and A. H. Kritz, Plasma Phys. Controlled Fusion **45**, 1939 (2003).
- 22. T. Onjun, G. Bateman, A. H. Kritz, et al., Phys. Plasmas **12**, 082 513 (2005).
- 23. T. Onjun, K. Tharasrisuthi, and O. Onjun, J. Phys. Conf. Ser **123**, 012 034 (2008).



Home Search Collections Journals About Contact us My IOPscience

Model for toroidal velocity in H-mode plasmas in the presence of internal transport barriers

This article has been downloaded from IOPscience. Please scroll down to see the full text article.

2010 Nucl. Fusion 50 064009

(http://iopscience.iop.org/0029-5515/50/6/064009)

View the table of contents for this issue, or go to the journal homepage for more

Download details:

IP Address: 203.131.209.66

The article was downloaded on 18/06/2010 at 01:46

Please note that terms and conditions apply.

Model for toroidal velocity in H-mode plasmas in the presence of internal transport barriers

B. Chatthong¹, T. Onjun² and W. Singhsomroje¹

- ¹ Department of Physics, Faculty of Science, Mahidol University, Bangkok, Thailand
- ² School of Manufacturing Systems and Mechanical Engineering, Sirindhorn International Institute of Technology, Thammasat University, Pathum-Thani, Thailand

E-mail: thawatchai@siit.tu.ac.th

Received 12 October 2009, accepted for publication 6 May 2010 Published 28 May 2010 Online at stacks.iop.org/NF/50/064009

Abstract

A model for predicting toroidal velocity in H-mode plasmas in the presence of internal transport barriers (ITBs) is developed using an empirical approach. In this model, it is assumed that the toroidal velocity is directly proportional to the local ion temperature. This model is implemented in the BALDUR integrated predictive modelling code so that simulations of ITB plasmas can be carried out self-consistently. In these simulations, a combination of a semi-empirical mixed Bohm/gyro-Bohm (mixed B/gB) core transport model that includes ITB effects and NCLASS neoclassical transport is used to compute a core transport. The boundary is taken to be at the top of the pedestal, where the pedestal values are described using a theory-based pedestal model based on a combination of magnetic and flow shear stabilization pedestal width scaling and an infinite-*n* ballooning pressure gradient model. The combination of the mixed B/gB core transport model with ITB effects, together with the pedestal and the toroidal velocity models, is used to simulate the time evolution of plasma current, temperature and density profiles of 10 JET optimized shear discharges. It is found that the simulations can reproduce an ITB formation in these discharges. Statistical analyses including root mean square error (RMSE) and offset are used to quantify the agreement. It is found that the averaged RMSE and offset among these discharges are about 24.59% and -0.14%, respectively.

1

PACS numbers: 52.65.-y, 52.55.Fa, 52.25.Fi

1. Introduction

To produce significant fusion reactions inside a tokamak reactor, high plasma temperature and density, as well as a sufficient long energy confinement time, are needed. Since the high confinement mode (H-mode) plasmas in tokamaks generally provide high temperature and excellent energy confinement time, burning plasma experiments such as the ITER project [1] are designed to operate in the H-mode regime. It is known that the improved performance of H-mode results mainly from the formation of an edge transport barrier (ETB) [2], called the pedestal. The performance of an H-mode discharge can be further improved by the formation of a transport barrier inside the plasma, called an internal transport barrier (ITB) [3]. It is widely believed that $\omega_{E\times R}$ flow shear is one of the keys in the formation of ITB. Theoretically, the calculation of $\omega_{E\times B}$ flow shear requires the information of toroidal velocity. As a result, it is crucial to develop a model for predicting toroidal velocity in order to predict the ITB formation in H-mode plasmas.

The development of the $\omega_{E\times B}$ flow shear concept to describe the formation of ITBs in magnetic confinement devices is one of the breakthroughs in fusion plasma research [4,5]. It was originally developed to explain the plasma edge during L-H mode transition. Then, it was extended to explain further improvement of tokamak confinement with transport barriers in the core of a plasma which has low or negative magnetic shear [4]. It is found that the reduction of transport is associated with shear effects, in particular the velocity shear and magnetic shear [5]. Toroidal velocity is one of the terms used in the $\omega_{E\times B}$ flow shear calculation. There have been studies of momentum and velocity transport in the poloidal direction but not much has been done in the toroidal direction [6–9]. In general, one can expect the form of toroidal velocity in terms of plasma parameters such as plasma density, plasma current or torque. The exact calculation of toroidal velocity is complicated since it requires much detailed information. Several excellent works were carried out to investigate this issue, e.g. [10, 11]. However, currently there is no model to describe toroidal velocity in a simple fashion. In

Nucl. Fusion **50** (2010) 064009

B. Chatthong *et al*

this work, instead of using complicated approaches, a simple model for predicting toroidal velocity is proposed by assuming that toroidal velocity is a function of local ion temperature. Even though several important plasma parameters for toroidal velocity mentioned previously are not directly included in this model, one can see that those parameters are indirectly included through the calculation of ion temperature. It is worth noting that a theoretical base model should be developed as a next step in order to make a better prediction. We will leave this development for a future work.

In this paper, a simple model for predicting toroidal velocity is developed based on an empirical approach. Then, this simple toroidal velocity model is implemented in the 1.5D BALDUR integrated predictive modelling code so that they can be used together to self-consistently simulate the time evolution of plasma current, density and temperature profiles for ITB plasmas. In all simulations, the boundary conditions are expressed in terms of a pedestal model, in which the model developed in [12] is used. In that model, the pedestal temperature was predicted using the estimation of pedestal width based on magnetic and flow shear stabilization $(\Delta \propto \rho_i s^2)$ [13] and pedestal pressure gradient based on ballooning mode instability. The pedestal model was found to be in agreement with experimental data around 30% root mean square error (RMSE) [12]. It is widely accepted that theory-based transport models, such as GLF23, TGLF, CDBM, Weiland and MMM08, are among reliable choices for predicting anomalous core transport. However, a semiempirical mixed Bohm/gyro-Bohm (mixed B/gB) model has been widely used in core transport prediction as well. In addition, transport models such as GLF23, MMM08 and TGLF can predict the momentum transport, which can lead to toroidal velocity. In this work, a mixed B/gB core transport model which can include the ITB effects is used. This model was developed for JET plasmas. However, it is believed that it can be extended to the ITER plasma. The formation of ITB in this model is caused by a suppression of anomalous transport due to $\omega_{E\times B}$ flow shear and magnetic shear [14]. This model is successfully found to be in agreement with data from various JET experiments [14–19]. In BALDUR, the value of $\omega_{E\times B}$ can be calculated from the information of electric field, toroidal velocity (v_{tor}) and poloidal velocity. This paper focuses on the development of a simple model for predicting toroidal velocity. This model is developed using an empirical approach and it is in a similar form to that suggested in [20] in which the toroidal velocity is a function of local ion temperature. The model is tested by carrying out simulations of 10 JET optimized shear discharges obtained from the International Profile Database. It is known that these 10 JET optimized shear discharges are high quality discharges. However, with fast developing technology, numerous measurements have been improved. As a result, more recent optimized shear discharges can provide a better comparison.

The paper is organized as follows: an introduction to the BALDUR code is presented in section 2, along with the toroidal velocity model, the mixed B/gB model with ITB effects included and the ETB models; the simulations results and discussion are presented in section 3; and the summary is given in section 4.

2. The BALDUR code

This section introduces theories and models used in the calculation of plasma profiles; the BALDUR predictive modelling code is also introduced here. The 1.5D BALDUR integrated predictive modelling code [21] is a time-dependent one and a half-dimensional transport modelling code which is used to compute many physical quantities in tokamaks. The code computes the plasma profiles such as time evolution of electron density, electron and ion temperatures as in this paper. It can also be used to compute other physical quantities such as impurity and hydrogen densities, magnetic q and other gas densities [22].

The BALDUR code self-consistently computes these profiles by mixing many physical processes together in the form of modules including transport, plasma heating, particle flux, boundary conditions and sawtooth oscillations modules. It was found that the BALDUR code can yield simulations which are in agreement with experimental data. For example, in [23, 24], the BALDUR simulations with either the MMM95 transport model or the mixed B/gB transport model yielded an agreement of about 10% relative root mean square (RMS) deviation for both L-mode and H-mode plasmas.

2.1. The toroidal velocity model

In this work, an empirical approach for developing the toroidal velocity (v_{tor}) model is used. It is assumed that toroidal velocity is directly proportional to local ion temperature (T_i) , which appears as follows:

$$v_{\text{tor}} = CT_{i}. \tag{1}$$

Note that this function is similar to the form suggested in [20]. The correlation between these two parameters is demonstrated in figure 1 for four JET optimized shear discharges (40542, 40847, 53521 and 53537). Note that the notation used in this paper can be found in table 1. It is also worth mentioning that this is a simple model. It does not include the direct source of toroidal velocity such as the NBI torque. Also, the plasma conditions, such as plasma density and plasma current, are not included. However, those parameters can influence the toroidal velocity through ion temperature. As a result, one can expect that this toroidal velocity model is somewhat including those important plasma parameters as well.

The coefficient C in the expression for toroidal velocity is determined by calibrating the model for toroidal velocity against experimental data points for optimized shear H-mode plasmas, obtained from the International Profile Database. The value $C = 1.43 \times 10^4$ minimized the RMSE deviation (yielding approximately 40.5%) when the predicted pedestal temperature was compared with the 10 260 data points. As a result, the model for toroidal velocity appears as

$$v_{\text{tor}}[\text{m/s}] = 1.43 \times 10^4 T_{\text{i}} \text{ [keV]}.$$
 (2)

An estimate will now be made for the uncertainty in the toroidal velocity model. This estimate is motivated by the observation that the width of the distribution of any set of data points can be characterized by a standard deviation above and below the mean value. Approximately 34% of the data points lie between

Nucl. Fusion **50** (2010) 064009

B. Chatthong *et al*

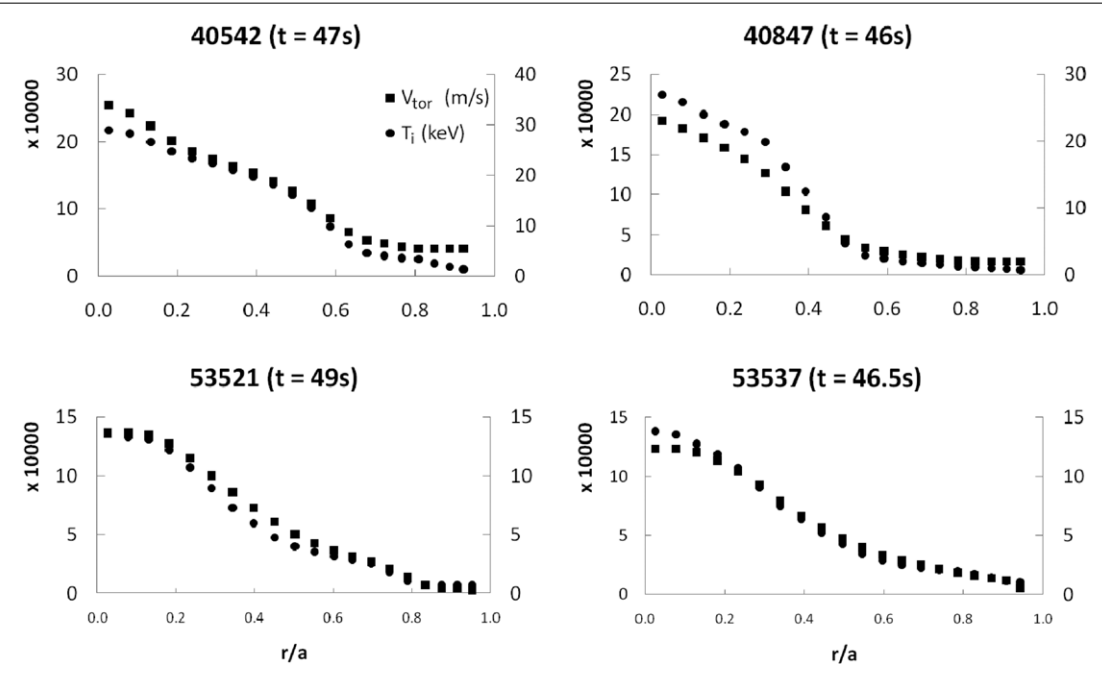


Figure 1. Experimental data for toroidal velocity and ion temperature are plotted as a function of minor radius for 40542 discharge at time = 47 s (top left), 40847 discharge at time = 46 s (top right), 53521 discharge at time = 49 s (bottom left) and 53537 discharge at time = 46.5 s (bottom right).

Table 1. Notation used in this paper.

Symbol	Unit	Description
$\omega_{E \times B}$	s^{-1}	Flow shearing rate
Δ	m	Pedestal width
$ ho_{ m i}$		Ion gyro-radius
S		Magnetic shear
$V_{ m tor}$	$\mathrm{m}\mathrm{s}^{-1}$	Toroidal velocity
$T_{\rm i}$	keV	Local ion temperature
R	m	Major radius
Χe	$m^2 s^{-1}$	Electron thermal diffusivity
$\chi_{\rm i}$	$m^2 s^{-1}$	Ion thermal diffusivity
χ_{gB}	$m^2 s^{-1}$	Gyro-Bohm contribution diffusivity
ХВ	$m^2 s^{-1}$	Bohm contribution diffusivity
D_{H}	$m^2 s^{-1}$	Particle diffusivity
D_{Z}	$m^2 s^{-1}$	Impurity diffusivity
ρ		Normalized minor radius
$T_{\rm e}$	keV	Local electron temperature
B_{T}	T	Toroidal magnetic field
γıtg	s^{-1}	ITG growth rate
$n_{\rm e}$	m^{-3}	Local electron density
q		Safety factor
v_{th}	$\mathrm{m}\mathrm{s}^{-1}$	Electron thermal velocity
$B_{ heta}$	T	Poloidal magnetic field
E_r	$N C^{-1}$	Radial electric field
Ψ	${ m Ncm^{-2}}$	Poloidal flux
p	${ m Nm^{-2}}$	Pressure
v_{θ}	$\mathrm{m}\mathrm{s}^{-1}$	Poloidal velocity
$n_{\rm i}$	m^{-3}	Local electron density
$T_{\rm ped}$	keV	Pedestal temperature
$n_{\rm ped}$	m^{-3}	Pedestal density
n_1	m^{-3}	Line average density
$\alpha_{\rm c}$		Normalized critical pressure gradient
δ		Triangularity
κ		Elongation
$A_{ m H}$	amu	Average hydrogenic mass
а	m	Minor radius
$I_{\rm p}$	MA	Plasma current

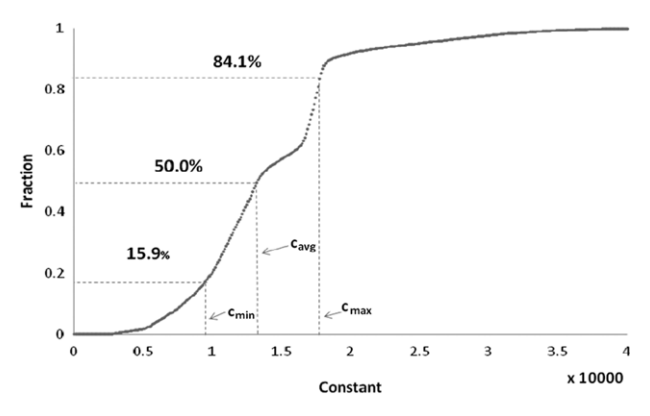


Figure 2. Fraction of experimental data points with toroidal velocity lower than the value predicted by equation (2) as a function of the coefficient C value. Points along the curve from left to right indicate one standard deviation below the model (with $C_{\min} = 0.93 \times 10^4$), the model (with $C = 1.43 \times 10^4$) and one standard deviation above the model (with $C_{\max} = 1.78 \times 10^4$).

the mean value and what will be referred to in this paper as 'one standard deviation' above, or 'one standard deviation below', the mean value. In the case of the toroidal velocity model with $C=1.43\times 10^4$ in equation (2), approximately half the data points lie below the model and half the data points lie above the model (as shown in figure 2). Hence, the model with $C=1.43\times 10^4$ lies at the mean value of the distribution. As the coefficient C is varied, the fraction of data points that lie above the model changes (as shown in figure 2). In order to estimate the range of variation needed to cover one standard deviation above and below the model for toroidal velocity, the coefficient C is swept through the range of values that covers 34% of the data points above and below the standard model. That is, if C is increased to 1.78×10^4 , it is found that

Nucl. Fusion 50 (2010) 064009	Chatth	ong et c	ıl
--------------------------------------	--------	----------	----

JET	Time (s)	R (m)	a (m)	I _p (MA)	$B_{\mathrm{T}}\left(\mathrm{T}\right)$	κ	δ	$n_1 (10^{19} \mathrm{m}^{-3})$
40542	47.0	2.93	0.94	3.22	3.49	1.64	0.35	2.41
40847	46.0	2.92	0.96	2.85	3.50	1.56	0.20	2.33
46123	46.5	2.89	0.98	2.50	2.54	1.52	0.17	2.24
46664	45.7	2.92	0.94	2.95	3.50	1.71	0.20	2.27
51599	46.0	2.89	0.96	2.21	2.64	1.66	0.23	1.90
51976	46.3	2.92	0.95	2.40	3.49	1.69	0.26	2.45
52009	21.6	3.01	0.88	2.49	2.70	1.72	0.47	7.30
53521	49.0	2.89	0.97	2.00	3.54	1.63	0.21	2.99
53532	46.5	2.89	0.96	2.22	2.64	1.67	0.23	2.52
53537	46.5	2.90	0.96	2.22	2.64	1.67	0.23	2.15

Table 2. Summary of plasma parameters for 10 JET optimized shear discharges at the diagnostic time.

34% of the data points lie between the standard model (with $C = 1.43 \times 10^4$) and this upper bound. If C is decreased to 0.93×10^4 , it is found that 34% of the data points lie between the standard model and this lower bound. This way of determining the models that lie 'one standard deviation' above and below the standard model makes no assumption about the distribution of the data points above and below the model. It is clear that the distribution of data points is not a symmetric function of C.

2.2. The ITB model

The physical mechanism of ITB formation has not yet been clearly identified. However, it is found that the suppression of core anomalous transport due to $\omega_{E\times B}$ flow shear and magnetic shear causes ITB formation [14,25]. The ITB formation and its dynamics are modelled through a semiempirical core transport model called mixed B/gB [15]. It was originally a local transport model with Bohm scaling which means the diffusivities are proportional to the gyro-radius times the thermal velocity. These transport diffusivities are also functions of plasma parameters such as magnetic q and profile shapes. So in the simulations, all parameters are fixed while the gyro-radius is changed according to plasma dimensions. The Bohm model was first derived for electron transport for the JET tokamak [26]. Then, it was modified to additionally describe ion transport [27] and a new term called gyro-Bohm was added in order to simulate results from both smaller and larger sized tokamaks [28]. Gyro-Bohm scaling essentially means the diffusivities are proportional to the square of the gyro-radius times the thermal velocity divided by the plasma major radius [22]. Usually, the Bohm term dominates over most of the plasma. The gyro-Bohm term contributes mainly in the deep core of the plasma and in small tokamaks with a low heating power and a low magnetic field. The mixed B/gB transport model includes the ITB effect by having a cut-off in the Bohm term which is a function of flow shear and magnetic shear. The model can be expressed as follows [15]:

$$\chi_{\rm e} = 1.0\chi_{\rm gB} + 2.0\chi_{\rm B},$$
(3)

$$\chi_{\rm i} = 0.5\chi_{\rm gB} + 4.0\chi_{\rm B},\tag{4}$$

$$D_{\rm H} = D_{\rm Z} = (0.3 + 0.7\rho) \frac{\chi_{\rm e} \chi_{\rm i}}{\chi_{\rm e} + \chi_{\rm i}},$$
 (5)

where

$$\chi_{\rm gB} = 5 \times 10^{-6} \sqrt{T_{\rm e}} \left| \frac{\nabla T_{\rm e}}{R_{\rm m}^2} \right|,$$
 (6)

$$\chi_{\rm B} = \chi_{\rm B_0} \times \Theta\left(-0.14 + s - \frac{1.47\omega_{\rm E\times B}}{\gamma_{\rm ITG}}\right),$$
(7)

with

$$\chi_{\rm B_0} = 4 \times 10^{-5} R \left| \frac{\nabla (n_{\rm e} T_{\rm e})}{n_{\rm e} B_{\rm T}} \right| q^2 \left(\frac{T_{\rm e} (0.8 \rho_{\rm max}) - T_{\rm e} (\rho_{\rm max})}{T_{\rm e} (\rho_{\rm max})} \right), \tag{8}$$

where χ_e is the electron diffusivity, χ_i is the ion diffusivity, χ_{gB} is the gyro-Bohm contribution, χ_B is the Bohm contribution, D_H is the particle diffusivity, D_Z is the impurity diffusivity, ρ is the normalized minor radius, T_e is the local electron temperature in keV, B_T is the toroidal magnetic field, s is the magnetic shear, $\omega_{E\times B}$ is the shearing rate, γ_{TTG} is the linear growth rate, R is the major radius and n_e is the local electron density. The linear growth rate γ_{TTG} can be calculated as v_{th}/qR , where v_{th} is the electron thermal velocity. The original mixed B/gB model does not include the impurity transport. For the sake of simplicity, it is assumed in this work that the impurity transport is the same as the particle transport.

In this work, the $\omega_{E\times B}$ shearing rate is calculated according to the Hahm–Burrell model [29, 30]:

$$\omega_{E \times B} = \left| \frac{RB_{\theta}^2}{B_{\rm T}} \frac{\partial \left(E_r / RB_{\theta} \right)}{\partial \Psi} \right|,\tag{9}$$

where B_{θ} is the poloidal magnetic field, Ψ is the poloidal flux and E_r is the radial electric field, which can be calculated as follows:

$$E_r = \frac{1}{Zen_i} \frac{\partial p_i}{\partial r} - v_\theta B_{\rm T} + v_{\rm tor} B_\theta, \tag{10}$$

where $\partial p_i/\partial r$ is the pressure gradient, v_θ and v_{tor} are the poloidal and toroidal velocities, respectively, n_i is the ion density, Z is the ion charge number and e is the elementary charge. The calculation of toroidal velocity is discussed extensively in section 2.1. Note that the poloidal velocity is estimated using NCLASS.

2.3. The ETB model

In this study, the boundary condition of the plasma is set to be at the top of the pedestal [31], which is where the ETB is observed. The pedestal region is located at the steep gradient right near the edge of the plasma. It is assumed that the pressure gradient $(\partial p/\partial r)$ within this region is constant so the pedestal temperature $(T_{\rm ped})$ in keV unit can be calculated as follows [12]:

$$T_{\text{ped}} = \frac{1}{2kn_{\text{ped}}} \Delta \left| \frac{\partial p}{\partial r} \right|,$$
 (11)

Nucl. Fusion **50** (2010) 064009

B. Chatthong *et al*

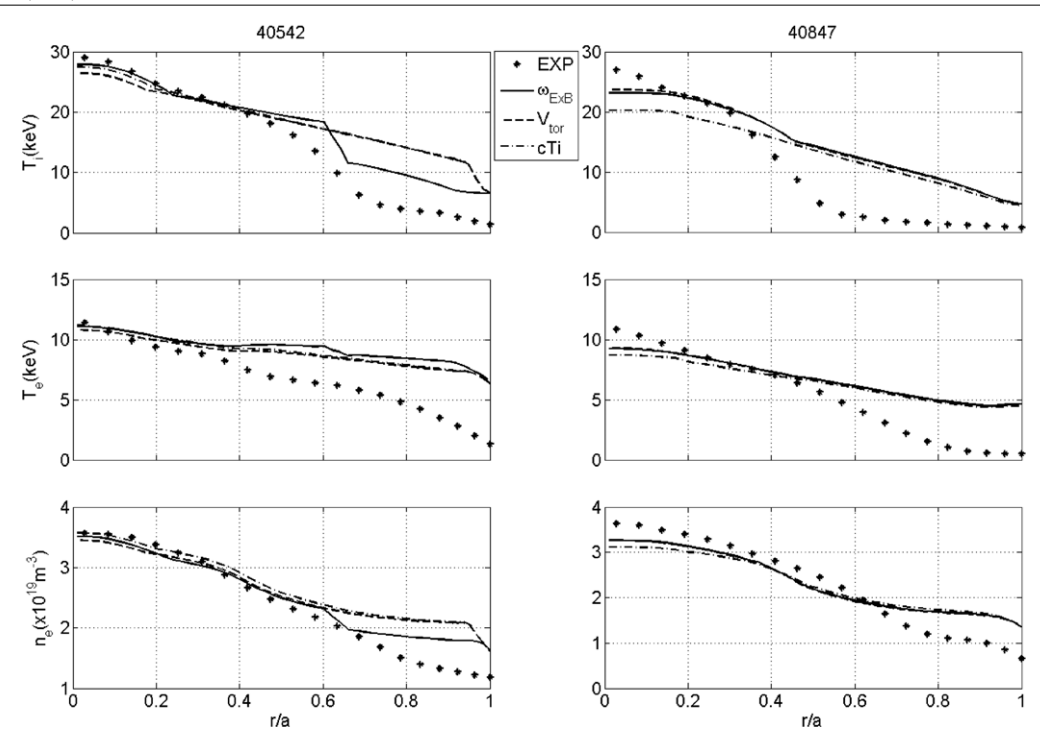


Figure 3. Ion temperature (top), electron temperature (middle) and electron density (bottom) profiles as a function of normalized minor radius for JET discharges 40542 at t=47 s (left) and 40847 at t=46 s (right). In each panel, the closed circles represent experimental data, the solid lines are the results of simulations using experimental $\omega_{E\times B}$, the dashed lines are the results of simulations using experimental V_{tor} and the dotted–dashed lines are the results of simulations using predicted toroidal velocity.

where $n_{\rm ped}({\rm m}^{-3})$ is the pedestal density, k is the Boltzmann constant and Δ is the pedestal width. So in order to calculate the pedestal temperature one must obtain pedestal density, pedestal width and pedestal gradient.

The pedestal pressure gradient scaling is limited by the ballooning mode instability [32]. It is based on the assumption that there exists a maximum normalized pressure gradient with a critical pressure gradient, α_c [12]:

$$\alpha_c(s, \delta, \kappa) = -\frac{2\mu_0 R q^2}{B_{\rm T}^2} \left(\frac{\partial p}{\partial r}\right)_{\rm c}.$$
 (12)

Here, κ is the elongation, μ_0 is the permeability of free space, R is the tokamak major radius, q is the safety factor and B_T is the vacuum toroidal magnetic field. Rewrite this relation and substitute pressure gradient into equation (11) to obtain

$$T_{\text{ped}} = \frac{\Delta}{2kn_{\text{ped}}} \frac{\alpha_c B_{\text{T}}^2}{2\mu_0 R q^2}.$$
 (13)

The pedestal width scaling model is based on magnetic and flow shear stabilization ($\Delta \propto \rho_i s^2$) [13]. There is an assumption that the transport barrier is formed in the region where the turbulence growth rate is balanced by a stabilizing $E_r \times B$ shearing rate. The scaling width is derived to be [10]

$$\Delta = C_1 \rho s^2 = C_1 \left(4.57 \times 10^{-3} \frac{\sqrt{A_{\rm H} T_{\rm ped}}}{B_{\rm T}} \right) s^2, \tag{14}$$

where C_1 is the constant of proportionality and $A_{\rm H}$ is the average hydrogenic mass. Combining this scaling with the

previous pressure gradient scaling, the final $T_{\rm ped}$ is obtained as follows:

$$T_{\text{ped}} = C_1^2 \left(\left(\frac{4.57 \times 10^{-3}}{4\mu_0 \left(1.6022 \times 10^{-16} \right)} \right)^2 \left(\frac{B_{\text{T}}^2}{q^4} \right) \times \left(\frac{A_H}{R^2} \right) \left(\frac{\alpha_c}{n_{\text{ped}}} \right)^2 s^4 \right).$$
 (15)

This result is used in the BALDUR code to calculate the pedestal temperature which is the boundary condition for the transport model and to eventually compute the plasma profiles. The constant C_1 is chosen to minimize the RMSE with 533 experimental data points from four large tokamaks obtained from the ITPA pedestal database and from [12], it is found to be 2.42. It is worth noting that this pedestal temperature model includes the effect of edge bootstrap current, which has an impact on magnetic shear and safety factor. This inclusion results in a non-linear behaviour in the pedestal temperature The scheme to deal with the approximation of magnetic shear and safety factor for pedestal prediction using the pedestal models has been completely described in [12]. Therefore, the values of magnetic shear and safety factor for the pedestal calculation are different from the values in the BALDUR code, which is based on a more appropriate calculation. The attempt to use self-consistent safety factor and magnetic shear for all calculations in the BALDUR code is under development. A preliminary result can be seen in [30]. In addition, there are several new approaches to estimate pedestal values, such as the pedestal scaling by Sugihara [16], which predicted the pedestal temperature of about 5.6 keV.

Nucl. Fusion **50** (2010) 064009

B. Chatthong *et al*

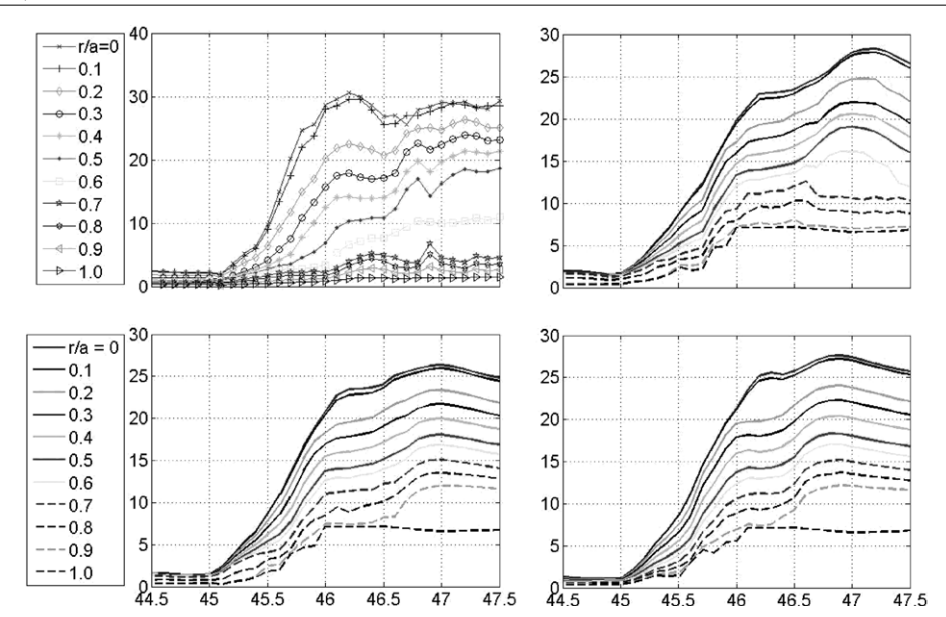


Figure 4. Time evolution of ion temperatures from JET 40542 discharge is plotted. The experimental result is shown at the top left, simulation result when experimental $\omega_{E\times B}$ is used is shown at the top right, simulation result when experimental V_{tor} is used is shown at the bottom left and simulation result when the empirical predicted V_{tor} model is used is shown at the bottom right. Each line represents different positions in the plasma from the centre (r/a=0) to the edge (r/a=1).

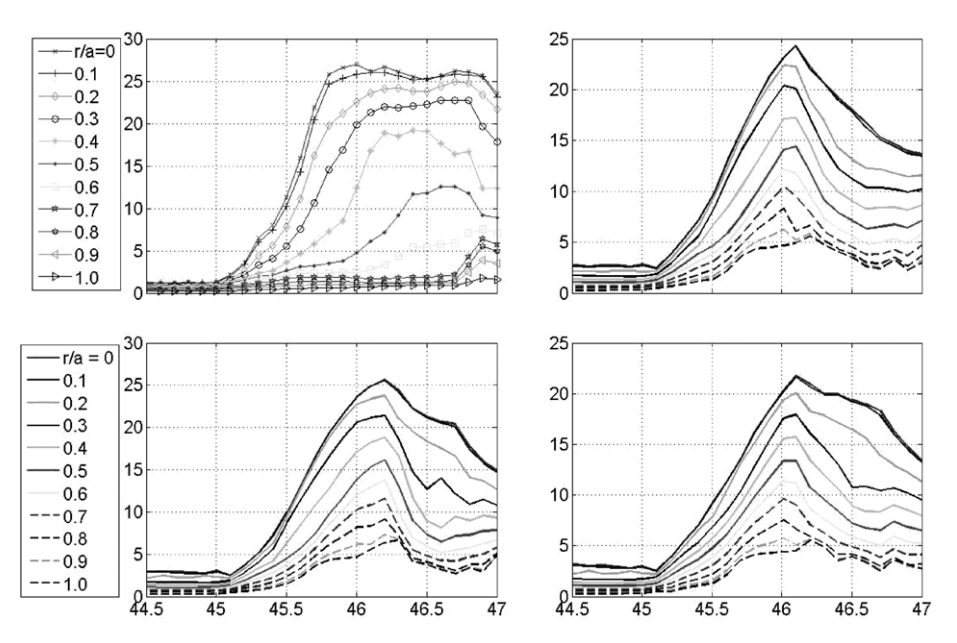


Figure 5. Time evolution of ion temperatures from JET 40847 discharge is plotted. The experimental result is shown at the top left, simulation result when experimental $\omega_{E\times B}$ is used is shown at the top right, simulation result when experimental V_{tor} is used is shown at the bottom left and simulation result when the empirical predicted V_{tor} model is used is shown at the bottom right. Each line represents different positions in the plasma from the centre (r/a=0) to the edge (r/a=1).

The pedestal density, $n_{\rm ped}$, is obtained by an empirical model which is based on the fact that $n_{\rm ped}$ is a fraction of line average density, $n_{\rm l}$, that can be taken from experimental data, as shown:

$$n_{\text{ped}} = 0.71 n_1.$$
 (16)

This pedestal density empirical model agrees with the data from the International Tokamak Physics Activity (ITPA) pedestal database with 12% RMSE [33].

3. Results and discussion

In this work, the simulations are carried out for 10 JET optimized shear discharges (40542, 40847, 46123, 46664, 51599, 51976, 52009, 53521, 53532 and 53537) using the BALDUR integrated predictive modelling code. These discharges are taken from the International Profile Database [34]. Table 2 summarizes the parameters for each discharge. These discharges are among the best results from JET with regards to the ITB formation that are available in the International Profile Database.

Nucl. Fusion **50** (2010) 064009

B. Chatthong *et al*

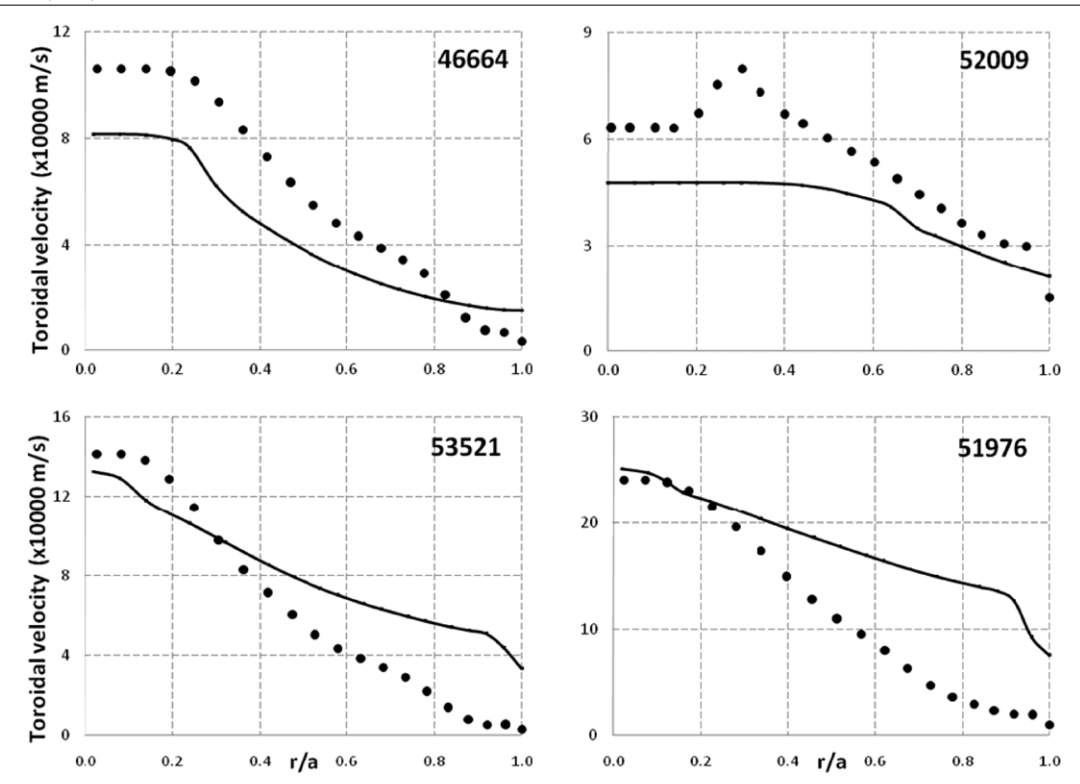


Figure 6. Toroidal velocity profiles are plotted as a function of normalized minor radius for JET discharges 46664, 52009, 53521 and 51976. In each panel, the closed circles represent experimental data and the solid curves are the toroidal velocity from simulations using the V_{tor} model.

Figure 3 illustrates the simulation results for the ion temperature, the electron temperature and the electron density as functions of normalized minor radius for JET optimized shear discharges 40542 at 47.0 s and 40847 at 46.0 s. In the experiment, for example discharge 40542, the plasma was initiated with a fast current ramp; 0.5 MW of ion cyclotron resonance heating (ICRH) was applied for pre-heating. Later, neutral beam injection (NBI) power was stepped up from 0 to 10 MW at 45.0 s and then to 18 MW at 45.4 s. Experimentally, the ITB was formed at 45.4s and persisted throughout the operation time. JET discharge 40847 was set up with a few differences from 40542; it started with initiated fast current ramp, and 1 MW of ICRH was used for pre-heating from 43.0 to 45.0 s. Then NBI was applied to 10 MW at 45.0 s and then to 18 MW at 45.4 s. ITB was experimentally found at 45.3 s and so on. In figure 3, by comparing the three BALDUR simulations for discharge 40542 during the diagnostic time (47 s), each line represents simulation using experimental $\omega_{E \times B}$, experimental V_{tor} or predicted V_{tor} using equation (2). The T_i plot showed that there were two ITBs formed: one was between r/a equal to 0.1 and 0.2, and another one was towards the edge of the plasma. It is found that the simulation using experimental $\omega_{E\times B}$ yielded somewhat different results from other BALDUR simulations. It can be seen that both temperature and density near the centre are in agreement with experimental data for JET discharges. However, the temperature and density at the boundary are significantly off. This may be explained by the fact that the boundary model (in this case the pedestal model) was developed for the standard type I ELMy H-mode. In addition, the low and intermediate mode numbers or peeling modes have not been considered.

Table 3. Summary of average RMS deviation and offset for T_i at the centre, edge and average for different constant C of toroidal velocity.

	RMSE (%)			RMSE (%)			(Offset (%)	
Constant	Centre	Edge	Avg	Centre	Edge	Avg			
C_{\min} C_{\min} C_{\max}	26.5 26.7 25.2	17.8 18.2 17.9	24.6 25.5 25.6	0.07 0.05 -0.02	-0.17 -0.17 -0.16	-0.11 -0.13 -0.16			

Table 4. RMSEs between experimental toroidal velocity and predicted toroidal velocity at the diagnostic time for each discharge.

JET	Time (s)	RMSE (%)
40542	47.0	45.4
40847	46.0	55.5
46123	46.5	50.0
46664	45.7	18.6
51599	46.0	41.7
51976	46.3	29.5
52009	21.6	25.2
53521	49.0	19.2
53532	46.5	41.4
53537	46.5	44.4
Average	;	37.1

This might not be appropriate for optimized shear plasmas. The new boundary model for optimized shear discharges should be developed. However, this development is beyond the scope of this paper.

The time evolutions for ion temperature at different plasma radii are shown in figures 4 and 5, for JET discharges 40542 and

Nucl. Fusion **50** (2010) 064009

B. Chatthong *et al*

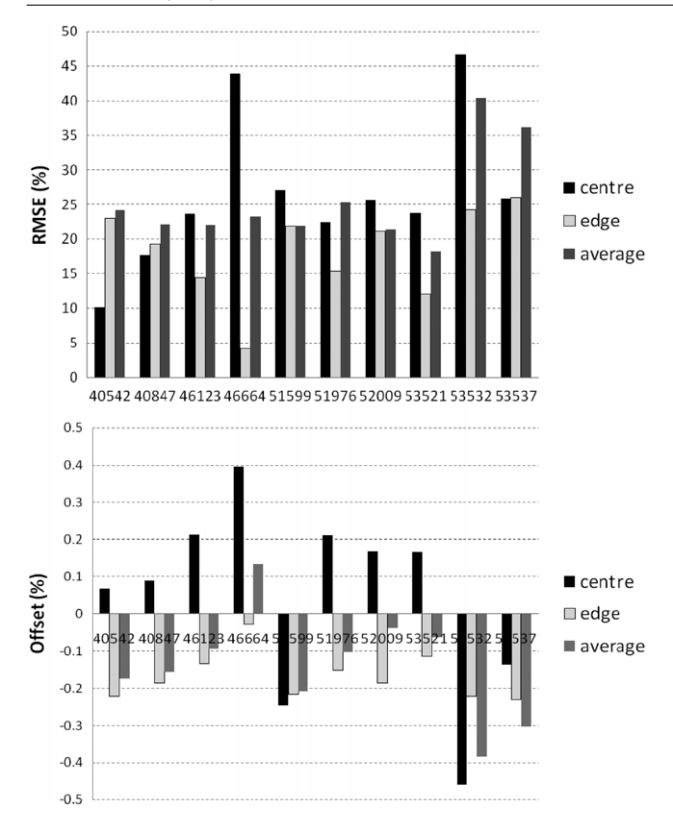


Figure 7. Summary of RMSE and offset results of ion temperature for 10 JET discharges at the centre, edge of the plasma and overall profile between the simulations using predicted toroidal velocity and experimental data.

40847, respectively. It can be seen that each simulation shows different agreement with experimental data. It can be noted in figure 4 that all simulations tend to under-predict the central ion temperature, but over-predict the pedestal temperature. However, in figure 5, the central ion temperature agrees with experimental data. For JET 40542 in figure 4, it can be seen that the simulation with the prediction of toroidal velocity shows the formation of ITB at a time and location close to experimental data. A comparison between toroidal velocity profiles from experiment and simulation is shown in figure 6 for JET discharges 46664, 52009, 53521 and 51976. It can be seen that the predicted toroidal velocity profiles are in the range of experimental data. The RMSEs between experimental data and simulation for each discharge are summarized in table 4.

To quantify the comparison between the predictions of ion temperatures and experimental data, the RMSE is computed. The RMSE and offset are calculated as follows:

RMSE(%) =
$$\sqrt{\frac{1}{N} \sum_{i=1}^{N} \left(\frac{T_{\exp_i} - T_{\text{mod } i}}{T_{\exp_0}} \right)^2} \times 100,$$
 (17)

Offset =
$$\frac{1}{N} \sum_{i=1}^{N} \left(\frac{T_{\exp_i} - T_{\text{mod } i}}{T_{\exp_0}} \right), \tag{18}$$

where N is the total number of data, T_{\exp_i} and $T_{\text{mod }i}$ are the ith experimental and model results of temperature and T_{\exp_0} is the experimental temperature at the centre of the tokamaks.

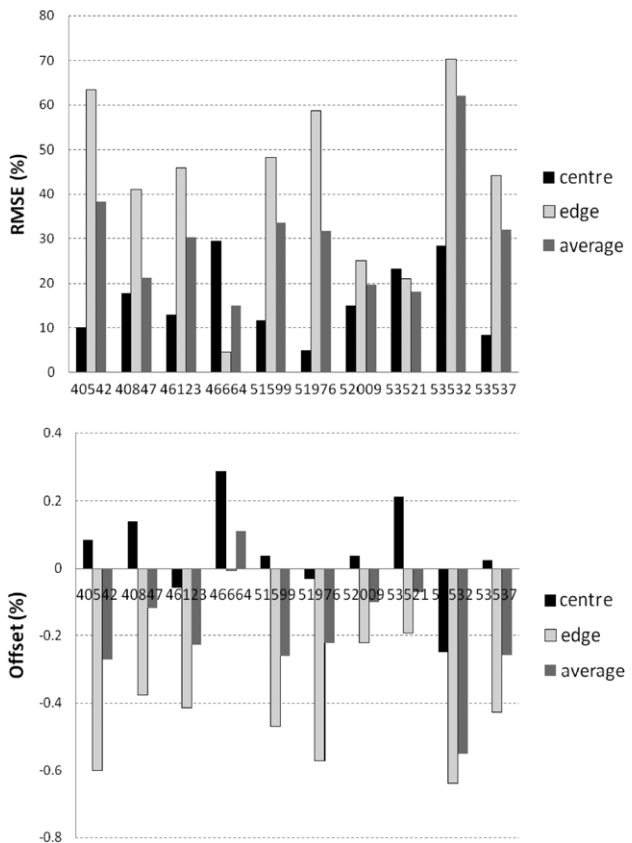


Figure 8. Summary of RMSE and offset results of electron temperature for 10 JET discharges at the centre, edge of the plasma and overall profile between the simulations using predicted toroidal velocity and experimental data.

In this experiment, there are a total of 5000 data points taken from the International Pedestal Database for the statistical analysis.

Table 3 summarizes the average RMSE and offset (equations (17) and (18)) for the BALDUR simulation of 10 JET optimized shear discharges with the prediction of toroidal velocity. The toroidal velocity in equation (2) is used with a different value of constant C. The statistics is given at the centre of the plasma, at the edge of the plasma and for the overall average. The RMS deviations range from 17.8% to 26.7%, while the offsets range from -0.17% to 0.07%. Comparing among the constant C values for toroidal velocity, the simulations using the lower bound of constant C yield the lowest RMS for edge and averages profiles. For the central profile, the upper bound of constant C yields the lowest RMS.

Figures 7–9 show the RMSE deviations and offsets of ion temperature, electron temperature and electron density, respectively, for each JET optimized shear discharge. These simulations are carried out using the predicted toroidal velocityfrom equation (2). It can be seen that the RMS deviations vary from discharge to discharge, and from profile to profile, with a minimum of about 4% and a maximum of about 47% for the ion temperature profiles, with a minimum of about 3% and a maximum of about 70% for the electron temperature profiles and with a minimum of about 5% and a maximum of about 35% for the electron density profiles.

Nucl. Fusion **50** (2010) 064009 B. Chatthong *et al*

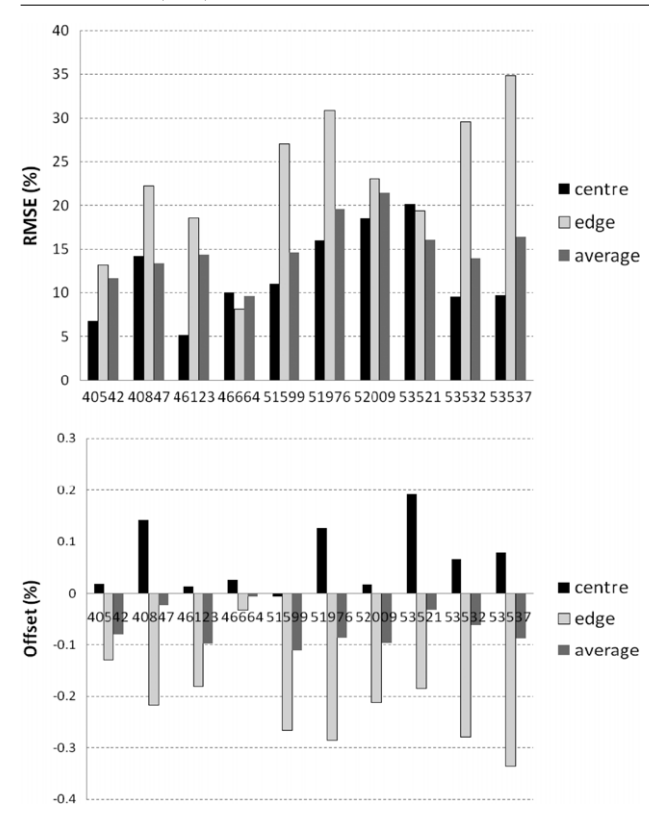


Figure 9. Summary of RMSE and offset results of electron density for 10 JET discharges at the centre, edge of the plasma and overall profile between the simulations using predicted toroidal velocity and experimental data.

4. Conclusion

An empirical model for predicting toroidal velocity in ITB H-mode plasmas is developed and implemented in the BALDUR integrated predictive modelling code, resulting in an improved predictive capability of the BALDUR code. The toroidal velocity is used by the transport code in BALDUR to calculate the shearing rate which is believed to be the cause of ITB formation. The core transport model used in this study is called mixed B/gB, which includes the effects of ITBs. The boundary is set to be at the top of the pedestal near the edge of the plasma with the boundary condition set by the ETB pedestal model, which is based on magnetic and flow shear stabilization combined with ballooning mode limit instability. It is found that the empirical toroidal velocity model

resulted in reasonable agreement between the predicted ion temperature and experimental results from 10 JET optimized shear discharges. It also successfully simulates formations of ITB inside the plasma.

Acknowledgments

This work is supported by the Commission on Higher Education (CHE) and the Thailand Research Fund (TRF) under Contract No RMU5180017. B Chatthong thanks the Royal Thai Scholarship and Mahidol University.

References

- [1] Aymar R. et al 2002 Plasma Phys. Control. Fusion 44 519
- [2] Hubbard A. 2000 Plasma Phys. Control. Fusion 42 A15
- [3] Connor J.W. et al 2004 Nucl. Fusion 44 R1
- [4] Burrell K.H. 1994 Plasma Phys. Control. Fusion 36 A291
- [5] Burrell K.H. 1997 Phys. Plasmas 4 1499
- [6] Tala T. et al 2007 Plasma Phys. Control. Fusion 49 B291
- [7] Rozhansky V. et al 2002 Nucl. Fusion 42 1110
- [8] Rogister A.L. et al 2002 Nucl. Fusion 42 1144
- [9] Eriksson A. et al 2007 Plasma Phys. Control. Fusion 49 1931
- [10] Tala T. et al 2009 Phys. Rev. Lett. 102 075001
- [11] Solomon W. et al 2008 Phys. Rev. Lett. 101 065004
- [12] Onjun T. et al 2002 Phys. Plasmas 9 5018
- [13] Sugihara M. et al 2000 Nucl. Fusion 40 1743
- [14] Tala T. et al 2001 Plasma Phys. Control. Fusion 43 507
- [15] Tala T. et al 2002 Plasma Phys. Control. Fusion 44 A495
- [16] Parail V.V. et al 1999 Nucl. Fusion 39 429
- [17] Parail V.V. 2002 Plasma Phys. Control. Fusion 44 A63
- [18] Tala T. et al 2005 Nucl. Fusion 45 1027
- [19] Tala T. et al 2006 Nucl. Fusion **46** 548
- [20] Kessel C.E. et al 2006 Proc. 21st Int. Conf. on Fusion Energy 2006 (Chengdu, China, 2006) (Vienna: IAEA) CD-ROM file IT/P1-7 and http://www-naweb.iaea.org/napc/physics/ FEC/FEC2006/html/index.htm
- [21] Singer C.E. et al 1988 Comput. Phys. Commun. 49 399
- [22] Onjun T. and Pianroj Y. 2009 Nucl. Fusion 49 075003
- [23] Hannum D. et al 2001 Phys. Plasmas 8 964
- [24] Onjun T. et al 2001 Phys. Plasmas 8 975
- [25] Erba M. et al 1997 Plasma Phys. Control. Fusion 39 261
- [26] Taroni A. et al 1994 Plasma Phys. Control. Fusion 36 1629
- [27] Erba M. et al 1995 Plasma Phys. Control. Fusion 37 1249
- [28] Erba M. et al 1998 Nucl. Fusion 38 1013
- [29] Pankin A.Y. et al 2005 Plasma Phys. Control Fusion 47 483
- [30] Zhu P. et al 2000 Phys. Plasmas 7 2898
- [31] Kritz A.H. et al 2004 Comput. Phys. Commun. 164 108 (http://w3.pppl.gov/NTCC)
- [32] Connor J. 1998 Plasma Phys. Control. Fusion 40 191
- [33] Bateman G. et al 2003 Plasma Phys. Control. Fusion 45 1939
- [34] Boucher et al 2000 Nucl. Fusion 40 1955

ITER Performance Study with the Presence of Internal Transport Barrier

Thawatchai Onjun

Plasma and Fusion Research Unit, Sirindhorn International Institute of Technology, Thammasat University,
Pathum Thani, Thailand

(Received: 5 September 2008 / Accepted: 11 April 2009)

Self-consistent modeling of the International Thermonuclear Experimental Reactor (ITER) has been carried out using the 1.5D BALDUR integrated predictive modeling code. In these simulations, the boundary is taken to be at the top of the pedestal, where the pedestal values are described using a theoretical-based pedestal model. This pedestal temperature model is based on magnetic and flow shear stabilization width scaling and ballooning mode pressure gradient model. The pedestal temperature model is used together with a Mixed B/gB core transport model, which can include the ITB effect. It is found that the formation of an ITB has a strong impact on both temperature profiles, especially near the center of the plasma. With the ITB effect is included, the central ion temperature increases significantly. The increase of central temperature results in a significant improvement of alpha power production and, consequently, fusion performance. It is observed that in most of the plasma core, the ion thermal diffusivity is smaller with an ITB included than in those without the ITB in the ITER simulations. This reduction in the diffusivity results in stronger gradients and, consequently, higher values of the central temperature.

Keywords: Plasma, Fusion, ITER, ITB, ETB, Pedestal

1. Introduction

International Thermonuclear Experimental Reactor (ITER) is an international collaborative effort with an aim to demonstrate the scientific and technological feasibility of nuclear fusion using the magnetic confinement fusion concept [1]. The goal of ITER is to produce plasmas with a sufficiently high energy density for a long enough time to achieve sustained high-performance fusion burning. Producing fusion reactions which satisfy such a condition inside a tokamak requires the ability to both heat and contain high-temperature plasmas. Due to the fact that high confinement mode (H-mode) discharges tokamaks generally provide excellent energy confinement and have acceptable particle transport rates for impurity control, many fusion experiments such as ITER are designed to operate in the H-mode regime. The improved performance of H-mode mainly results from the formation of the edge transport barrier (ETB) [2], called the pedestal. It is also known that performance of H-mode plasma can be further improved with the presence of a transport barrier inside plasma, called the internal transport barrier (ITB) [3]. The presence of ITB in H-mode plasma results a complicated scenario and yields an improve performance of that plasma.

The projections of ITER have been carried out in many scenarios using various integrated modeling codes [4-8]. For example, the BALDUR integrated predictive modeling code [9] was used to predict the performance of ITER for the standard H-mode scenario [4, 6-8]. The performance of ITER was evaluated in term of fusion Q. Note that fusion Q is the ratio of a fusion power with an applied heating power. A range of the performance is

predicted. It was found that the predicted performance of ITER using BALDUR code with the Mixed Bohm/gyroBohm (Mixed B/gB) transport code is relatively low compared to those using other transport codes [6-8]. It is worth noting that Mixed B/gB was developed using the JET plasma. In those previous works [6-8], the effect of ITB was not included in the simulations. As a result, it is interesting to explore the *H*-mode scenario of ITER when ITB is present.

In this work, the preliminary study of the ITER in the *H*-mode scenario with the presence of ITB is carried out. The *H*-mode is represented by the formation of ETB. The ETB is described by a pedestal model based on magnetic and flow shear stabilization, and ballooning mode instability. For the ITB, the ITB is formed by the suppression of core anomalous transport. This paper is organized as follows: brief descriptions for a BALDUR integrated predictive modeling code, anomalous transport models, and pedestal models are given in section 2. The ITER prediction using a BALDUR integrated predictive modeling code is described in section 3, while conclusion is given in section 4.

2. BALDUR Code

The BALDUR integrated predictive modeling code is used to compute the time evolution of plasma profiles including electron and ion temperatures, deuterium and tritium densities, helium and impurity densities, magnetic q, neutrals, and fast ions. These time-evolving profiles are computed in the BALDUR integrated predictive modeling code by combining the effects of many physical processes self-consistently, including the effects of transport, plasma

heating, particle influx, boundary conditions, the plasma equilibrium shape, and sawtooth oscillations. Fusion heating and helium ash accumulation are also computed self-consistently. The BALDUR simulations have been intensively compared against various plasma experiments, which yield an over all agreement within 10% relative RMS deviation [10, 11]. In BALDUR code, fusion heating power is determined by the nuclear reaction rates and a Fokker Planck package to compute the slowing down spectrum of fast alpha particles on each flux surface in the plasma. The fusion heating component of the BALDUR code also computes the rate of the production of thermal helium ions and the rate of the depletion of deuterium and tritium ions within the plasma core. The effect of sawtooth oscillation is also included, where a Porcelli sawtooth model [12] is used to determine a sawtooth crash and a modified Kadomtsev magnetic reconnection model [13] is used to describe the effects of sawtooth crash.

2.1 ITB model

In this work, the ITB is formed by the suppression of core anomalous transport due to $\omega_{\rm ExB}$ flow shear and magnetic shear. This effect is included in the anomalous core transport called "the Mixed Bohm/gyroBohm (Mixed B/gB) model [14]. This core transport model is an empirical model. It was originally a local transport model with Bohm scaling. A transport model is said to have "Bohm" scaling when the transport diffusivities are proportional to the gyro-radius times thermal velocity over a plasma linear dimension such as major radius. Transport diffusivities in models with Bohm scaling are also functions of the profile shapes (characterized by normalized gradients) and other plasma parameters such as magnetic q, which are all assumed to be held fixed in systematic scans in which only the gyro-radius is changed relative to plasma dimensions. The original JET model was subsequently extended to describe ion transport, and a gyroBohm term was added in order for simulations to be able to match data from smaller tokamaks as well as data from larger machines. A transport model is said to have "gyroBohm" scaling when the transport diffusivities are proportional to the square of the gyroradius times thermal velocity over the square of the plasma linear dimension. The Bohm contribution to the JET model usually dominates over most of the plasma. The gyroBohm contribution usually makes its largest contribution in the deep core of the plasma and plays a significant role only in smaller tokamaks with relatively low power and low magnetic field. To include the ITB effect, the Bohm contribution is modified. The Bohm/gyroBohm transport model with ITB effect included [15] can be written in the following way:

$$\chi_{e} = 1.0 \chi_{gR} + 2.0 \chi_{R} \tag{1}$$

$$\chi_i = 0.5 \chi_{gB} + 4.0 \chi_B + \chi_{neo}$$
 (2)

$$D_H = D_Z = \left[0.3 + 0.7\rho\right] \frac{\chi_e \chi_i}{\chi_e + \chi_i} \tag{3}$$

where

$$\chi_{gB} = 5 \times 10^{-6} \sqrt{T_e} \frac{\left| \nabla T_e \right|}{B_{\phi}^2} \tag{4}$$

$$\chi_B = 4 \times 10^{-5} R \left| \frac{\nabla (n_e T_e)}{n_e B_{\phi}} \right| q^2 \left(\frac{T_{e,0.8} - T_{e,1.0}}{T_{e,1.0}} \right)$$

$$\Theta\left(-0.14 + s - \frac{1.47\omega_{E\times B}}{\gamma_{ITG}}\right) . \tag{5}$$

The ω_{ExB} is the flow shearing rate and the value of γ_{ITG} ,

the ITG growth rate, is estimated as $v_{\rm ti}/qR$, in which $v_{\rm ti}$ is the ion thermal velocity. In, BALDUR code, the $\omega_{\rm ExB}$ shearing rate is calculated as follows:

$$\omega_{ExB} = \left| \frac{RB_{\theta}^2}{B_T} \frac{\partial (E_r / RB_{\theta})}{\partial \psi} \right|, \tag{6}$$

where R is the major radius, B_{θ} and B_{T} are the poloidal and toroidal magnetic fields, respectively, Ψ is the poloidal flux, and E_{r} is the radial electric field for the main plasma ions, which is calculated as follows:

$$E_r = \frac{1}{Zen_i} \frac{\partial p_i}{\partial r} - v_\theta B_T + v B_\theta, \qquad (7)$$

where $\partial p/\partial r$ is the pressure gradient, v_{θ} and v are the poloidal and toroidal velocities and, n_{i} is the ion density, Z is the ion charge number and e the elementary charge. Note that in this work, the toroidal velocity is taken directly from experiment.

2.2 ETB models

In the BALDUR code, a boundary condition is set at the top of the pedestal. As a result, the code requires both temperature and density at the top of the pedestal. A simple model for estimating pedestal temperature can be developed by using the values of pedestal width and pedestal pressure gradient [16]. In this work, the pedestal width is estimated using a magnetic and flow shear stabilization concept ($\Delta = C_w \rho s^2$) [17] and the pedestal gradient is estimated using first ballooning mode pressure gradient limit. The effect of bootstrap current and geometry are also considered. The pedestal temperature takes the following form:

$$T_{\text{ped}}(keV) = 0.323C_W^2 \left(\frac{B_T}{q^2}\right)^2 \left(\frac{M_i}{R^2}\right) \left(\frac{\alpha_c}{n_{\text{ped},19}}\right)^2 s^4$$
, (8)

where $n_{\text{ped},19}$ is the electron density at the top of the pedestal in units of 10^{19} m⁻³.

In general, the pedestal density (n_{ped}) in H-mode plasmas is a large fraction of line average density (n_1) . In the report by G. Bateman *et al.* [4], the pedestal density is taken to be

$$n_{ped} = 0.71 n_l.$$
 (9)

3. Simulations of ITER

The BALDUR integrated predictive transport modeling code is used to carry out the simulations of ITER with the designed parameters (R = 6.2 m, a = 2.0 m, $I_p = 15$ MA, $B_T = 5.3$ T, $\kappa_{95} = 1.70$, $\delta_{95} = 0.33$ and $n_1 =$ 1.0x10²⁰ m⁻³). In this work, the plasma current and density are gradually ramped up to the target values within 100 sec. The plasma current at the start up phase is 3 MA and is slowly increased to the target. It is found that the plasma reaches the H-mode phase at the time of 2 sec. It is worth noting that there are several physics that have not been included in these simulations, such as ELM crashes and neoclassical tearing modes. As a result, the simulation results are not appropriate to represent the dynamic of plasma in ITER. However, these simulations include enough physics to describe plasma when it reaches the steady state. The simulations still yield complex and interesting interactions within the plasma itself — such as the self plasma heating by the alpha particle and redistribution of heating power after sawtooth crash — still occurs and leads to interesting observation. Note that the sawtooth oscillation is considered during the time of 10 sec to 995 sec. For each simulation, an anomalous transport is calculated using the Mixed B/gB transport model, while the neoclassical transport is computed using the NCLASS module [18]. The boundary conditions are provided at the top of the pedestal by the pedestal model described above, which will be varied later to observe its sensitivity. It is assumed that the electron and ion pedestal temperatures are of the same values. In these simulations, the auxiliary heating power of 40 MW, which is a combination of 33 MW NBI heating power with 7 MW of RF heating power, is used.

A slow current ramp (reaching the target value in 100 sec) is used during the first stage of each simulation of the burning plasma experiments. The plasma density is also ramped up to the final plasma density during this stage; while the full heating is applied since the beginning. Note that the plasma density is ramping up and controlled at the target values by using gas puffing method. During this ramp, the plasma makes a transition from *L*-mode to *H*-mode. Since there is a strong heating at the beginning, all simulations enter the *H*-mode phase approximately

within 2 sec. In figure 1, the toroidal velocity and ω_{ExB} used in this work are shown. The toroidal velocity is taken from an optimized magnetic shear (OS) discharge in JET experiment, discharge 40542. The ω_{ExB} profile is calculated by Eqs. (6) and (7) by using the toroidal velocity from the top panel of figure 1.

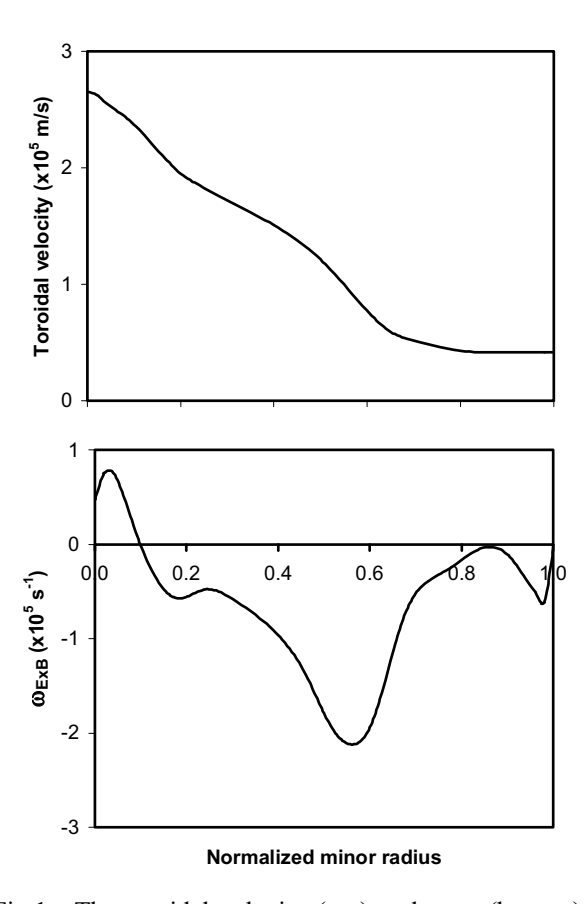


Fig.1 The toroidal velocity (top) and ω_{ExB} (bottom) profiles used in this work are plotted as a function of a normalized minor radius. Toroidal velocity profile is taken from JET experiment (discharge 40542), while the ω_{ExB} is calculated using Eqs. 6 and 7.

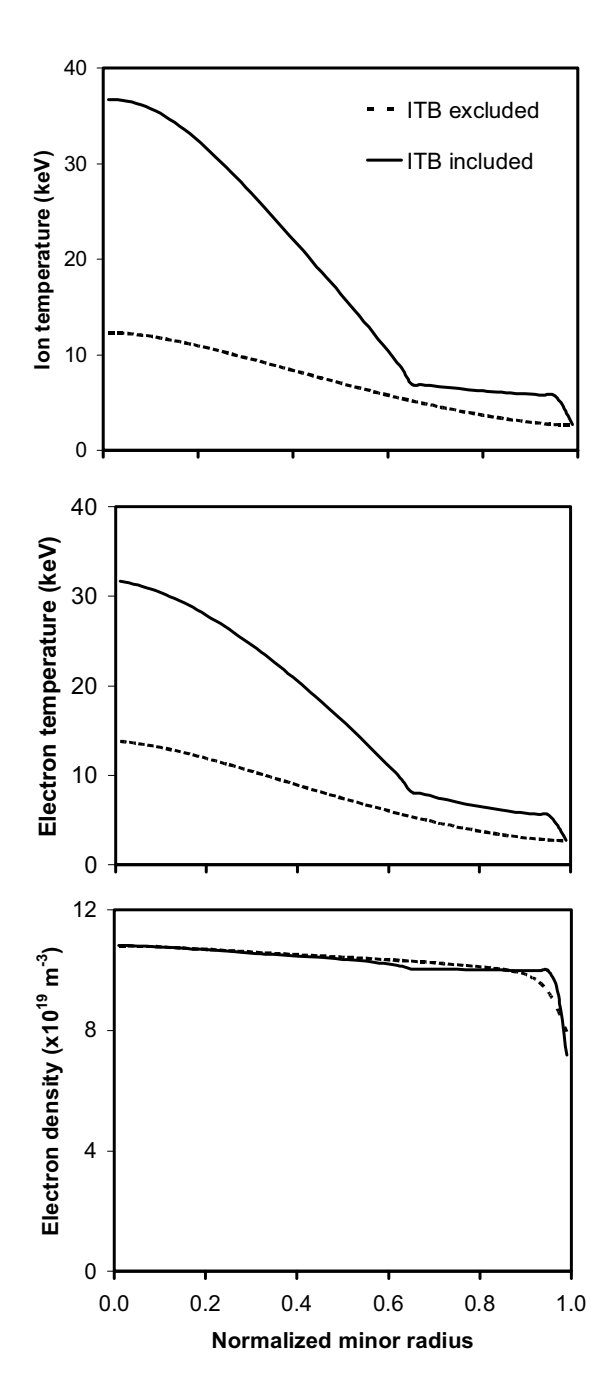


Fig.2 The profiles for ion (top) and electron (middle) temperatures and electron density (bottom) are plotted as a function of a normalized minor radius at time of 1000 sec. The simulations are carried out with and without the effect of ITB.

Figure 2 shows profiles for ion temperature (top), electron temperature (middle) and electron density (bottom) as a function of normalized minor radius at a time of 1000 sec. The simulations are carried out using Mixed B/gB model with the effects of ITB excluded and included. It can be seen that all ion and electron temperature profiles are peak. When the effects of ITB are included, the central temperature increases

significantly, where the edge remains the same. It is found that the pedestal is almost constant after the density reaches a target value. It is worth noting that the ion pedestal temperature is assumed to be the same with the electron temperature. Also, the effect of ELMs is not included in these simulations. For the electron density, the profile shape is a relatively small peak. It is also found that in both simulations, the electron density profile is almost the same, which means that the formation of ITB does not have an impact of density profile. In addition, it is found that the ITB effective region is up to $\rho = 0.6$. This ITB region results from the reduction of the transport in the region close to the plasma core, which can be seen in figure 3. It is worth mentioning that the safety factor profile in this ITER simulation is a monotonic profile with a flat profile near the plasma center, which is different from what observed in JET discharge 40542. This subject is beyond the scope this paper. It rather leaves this issue for future work.

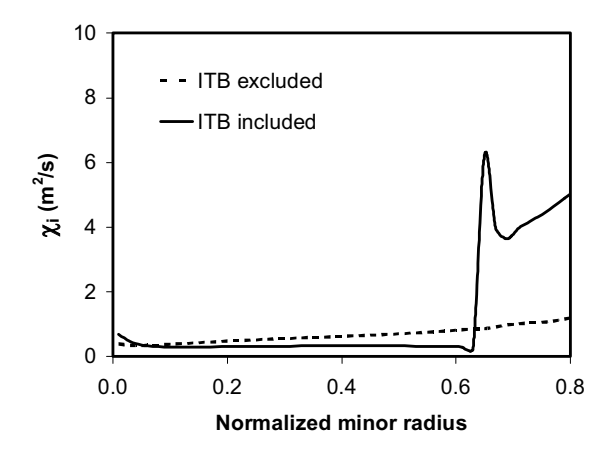


Fig. 3 The profile of total ion diffusivity is plotted as a function of normalized minor radius from the center up to a normalized radius of 0.8 at time of 1000 sec. The simulations are carried out with and without ITB effects.

The summary of central temperature and density is shown in Table 1. It can be seen that the central ion temperature increases significantly when the ITB effects are included. The central ion temperature in the simulation when ITB is included is about 36.7 keV, which is in effective range for fusion production. The central ion and electron temperatures increase 198% and 130%, respectively. This increase of central temperature will have a strong impact on the plasma stored energy and the nuclear fusion power production.

Figure 4 shows the plasma stored energy as a function of time between 900 sec to 1000 sec. It can be seen that the value of plasma stored energy is in the range

of 200 MJ for the simulation with ITB excluded; while the plasma stored energy increases to 450 MJ when ITB is included.

Table 1: The summary of central temperature and density at the time of 1000 sec.

Parameters	ITB excluded	ITB included
$T_{i,0}$ [keV]	12.3	36.7
$T_{\rm e,0}[{ m keV}]$	13.8	31.7
$n_{\rm e,0} [10^{19} \rm m^{-3}]$	10.8	10.8
$T_{\rm ped}$ [keV]	2.6	2.6
$n_{\rm e,ped} [10^{19} {\rm m}^{-3}]$	7.1	7.1

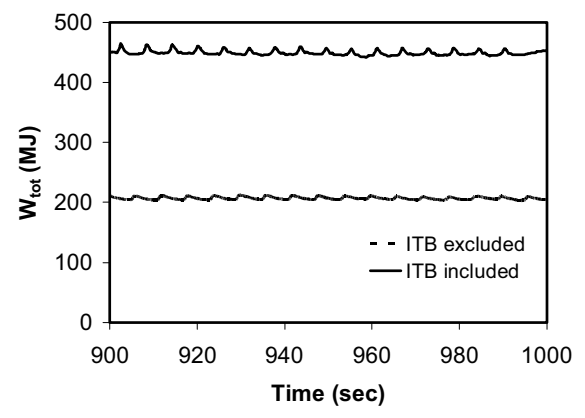


Fig.4 The plasma stored energy is plotted as a function of time for the simulation when ITB is excluded and included.

There are two types of auxiliary heating used in the ITER simulation. The total amount of neutral beam injection heating power, $P_{\rm NBI}$, is 33 MW. Another source of auxiliary heating is the RF heating. The total amount of RF heating power is 7 MW. For simplicity, the RF heating profiles are taken to be a parabolic shape, although it is recognized that the physics of RF heating might be more complicated in the ITER plasma. Note that Ohmic heating is small compared to other types of heating. The alpha heating power is also shown in figure 5. It is found that the alpha heating power is the main heating source of the plasma in the simulation with ITB. However, the alpha power heating is slightly higher than the NBI heating power in the simulation without ITB.

Figure 6 shows the alpha power production from the simulations when ITB is excluded and included. It can be seen that the alpha power from the simulation when ITB is included is much higher than that without ITB. The average of alpha power during the time of 900 sec to 1000 sec is summarized in Table 2. The fusion performance can be evaluated in term of Fusion Q, which can be calculated as

Fusion
$$Q = \frac{5 \times P_{\alpha,avg}}{P_{AUX}}$$
,

where $P_{\alpha,\text{avg}}$ is an average alpha power and P_{AUX} is an auxiliary heating power (equal to 40 MW for these simulations). It can be seen in Table 2 that the Fusion Q increases by 200% when ITB is included.

Table 2: The summary of average alpha power and corresponding fusion Q.

Parameters	ITB excluded	ITB included
P_{α} [MW]	26.3	124.9
Fusion Q	3.3	15.6

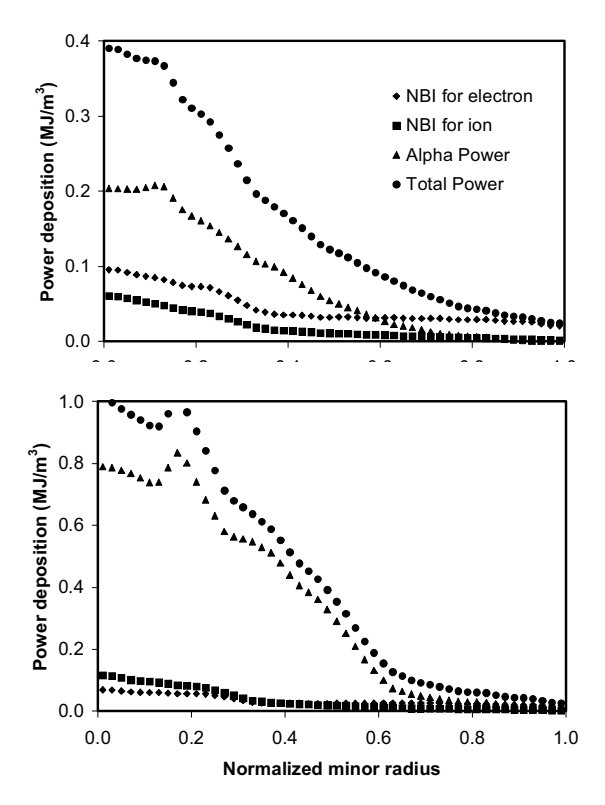


Fig.5 The power deposition profiles are shown as a function of normalized minor radius for the simulations when ITB is excluded (top) and included (bottom).

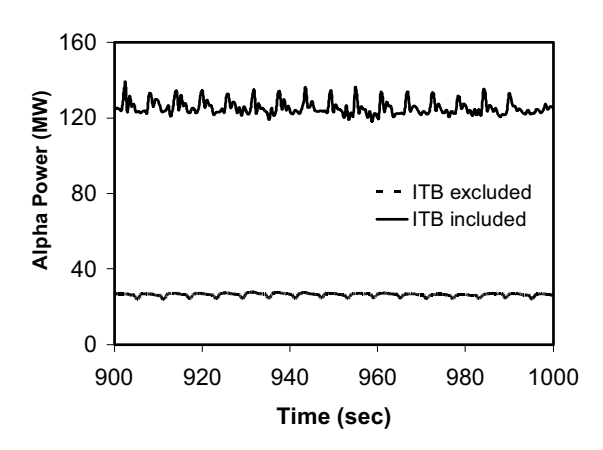


Fig.6 The alpha plasma production is plotted as a function of time for the simulation when ITB is excluded and included.

4. Conclusion

Self-consistent simulations of ITER have been carried out using BALDUR code, where the effects of both ETB and ITB are considered. The ETB condition is provided by the pedestal model based on magnetic and flow shear stabilization width scaling together with ballooning mode instability pressure gradient model; while the formation of ITB results from the suppression of transport by $E_r x B$ shear and magnetic shear. It is found that the formation of an ITB has a strong impact on both temperature profiles, especially near the center of the plasma. Because of the inclusion of the ITB effect, the central ion temperature increases more than a factor of two. The increase of central temperature results in a significant improvement of alpha power production and, consequently, fusion performance. In the simulation with ITB, it is observed the reduction of ion thermal transport in most of the plasma core, which results in stronger gradients and, consequently, higher values of the central temperature.

5. Acknowledgments

The author thanks Prof.Dr.A H Kritz, Dr.G Bateman, Dr.V Parail, Dr.A Pankin, Dr.S Suwanna, Dr.N Poolyarat, and Dr.R Picha for their helpful discussions and supports. This work is supported by Commission on Higher Education (CHE) and the Thailand Research Fund (TRF) under Contract No. RMU5180017.

6. References

- [1] R. Aymar *et al.*, Plasma Phys. Control. Fusion **44**, 519 (2002)
- [2] A. Hubbard, Plasma Phys. Control. Fusion **42**, A15 (2000)
- [3] J.W. Connor et al., Nucl. Fusion 44, R1 (2004)

- [4] G. Bateman *et al.*, Plasma Phys. Control. Fusion **45**, 1939 (2003)
- [5] T. Onjun et al., Phys. Plasmas 12, 082513 (2005)
- [6] T. Onjun *et al.*, J. of Physics: Conference Series 123, 012034 (2008)
- [7] K. Tharasrisuthi et al., Thammasat International Journal of Science and Technology 13, 45 (2008)
- [8] R. Picha *et al.*, Proc. of 35th EPS Conference on Plasma Physics, Hersonissos 9-13 June 2008 (2008)
- [9] C. E. Singer *et al.*, Comput. Phys. Commun. **49**, 399 (1988)
- [10] D. Hannum et al., Phys. Plasmas 8, 964 (2001)
- [11] T. Onjun et al., Phys. Plasmas 8, 975 (2001)
- [12] F. Porcelli *et al.*, Plasma Phys. Control. Fusion **38**, 2163 (1996)
- [13] G. Bateman et al., Phys. Plasmas 13, 072505 (2006)
- [14] M. Erba *et al.*, Plasma Phys. Control. Fusion **39**, 261 (1997)
- [15] T. J. J. Tala, et al., Phys. Control. Fusion 43, 507 (2001)
- [16] T. Onjun et al., Phys. Plasmas 9, 5018 (2002)
- [17] M. Sugihara et al., Nucl. Fusion 40, 1743 (2000)
- [18] W. A. Houlberg et al., Phys. Plasmas 4, 3231 (1997)

Simulations of ITER with combined effects of internal and edge transport **barriers**

T. Onjun and Y. Pianroj

Plasma and Fusion Research Unit, Sirindhorn International Institute of Technology, Thammasat University, Klongluang, Pathumthani, 12121, Thailand

E-mail: thawatchai@siit.tu.ac.th

Received 15 January 2009, accepted for publication 28 April 2009 Published 27 May 2009 Online at stacks.iop.org/NF/49/075003

Abstract

Predictive simulations of ITER with the presence of both an edge transport barrier (ETB) and an internal transport barrier (ITB) are carried out using the BALDUR integrated predictive modelling code. In these simulations, the boundary is taken at the top of the pedestal, where the pedestal values are described using theory-based pedestal models. These pedestal temperature models are based on three different pedestal width scalings: magnetic and flow shear stabilization ($\Delta \propto \rho_i s^2$), flow shear stabilization ($\Delta \propto \sqrt{\rho_i Rq}$) and normalized poloidal pressure $(\Delta \propto R\sqrt{\beta_{\theta,ped}})$. The pedestal width scalings are combined with a pedestal pressure gradient scaling based on the ballooning mode limit to predict the pedestal temperature. A version of the semi-empirical Mixed Bohm/gyroBohm (Mixed B/gB) core transport model that includes ITB effects is used to compute the evolution of plasma profiles. In this model, the anomalous transport in the core is stabilized by the influence of $E_r \times B$ flow shear and magnetic shear, which results in the formation of ITB. The combination of the Mixed B/gB core transport model with ITB effects, together with the pedestal model, is used to simulate the time evolution of plasma current, temperature, and density profiles for ITER standard type I ELMy H-mode discharges. It is found that ITER fusion performance using the BALDUR code with Mixed B/gB transport model without the presence of ITB is quite pessimistic (Fusion $Q \sim 3$). The presence of ITB is crucial and can result in a significant improvement, which is needed for achieving a target Fusion Q of 10. The improvement due to the presence of ITB is almost the same for all simulations with those three pedestal temperature models. This is caused by the predicted pedestal temperature from each pedestal temperature model varying just slightly. The presence of ITB has a strong impact on both temperature profiles, especially near the centre of the plasma, but has a small impact on electron, deuterium, tritium and carbon density profiles, except the helium density profile. The formation of ITB does not impact on the pedestal. It is also found that during a sawtooth crash, the temperature profiles drop significantly, but there is a small change in the density profiles. However, the sawtooth oscillation has no impact on the pedestal. When the auxiliary heating power is turned off, it is found that significant fusion power is sustained.

PACS numbers: 52.65.-y, 52.55.Fa, 52.25.Fi

Nom	enclature	I_p	plasma current (MA)
		$\dot{B_\phi}$	toroidal magnetic field (T)
Χe	electron thermal diffusivity (m ² s ⁻¹)	$B_{ heta}$	poloidal magnetic field (T)
χi	ion thermal diffusivity $(m^2 s^{-1})$	κ	elongation
$D_{ m H}$	particle diffusivity (m ² s ⁻¹)	δ	triangularity
D_z	impurity diffusivity (m ² s ⁻¹)	n_{e}	local electron density (m ⁻³)
χ_{gB}	gyro-Bohm contribution (m ² s ⁻¹)	q	safety factor
ХВ	Bohm contribution (m ² s ⁻¹)	S	magnetic shear
$\rho_{\rm i}$	ion gyro radius	$eta_{ heta, ext{ped}}$	normalized poloidal pressure
ρ	normalized minor radius	$\omega_{E \times B}$	flow shearing rate (s^{-1})
$T_{\rm e}$	local electron temperature (keV)	$\gamma_{ m ITG}$	ITG growth rate (s^{-1})
R	major radius (m)	$T_{ m ped}$	pedestal temperature (keV)
а	minor radius (m)	$\dot{M}_{ m i}$	hydrogenic mass (AMU)
	. ,	$lpha_{ m c}$	normalized critical pressure gradient
0029-5	515/09/075003+11\$30.00	1	© 2009 IAEA, Vienna Printed in the UK

1. Introduction

The concept of magnetic confinement fusion has long been explored to address the feasibility of nuclear fusion The International Thermonuclear Experimental energy. Reactor (ITER) is an international collaborative effort with the objective of demonstrating the scientific and technological feasibility of nuclear fusion [1]. The goal of ITER is to produce plasmas with a sufficiently high fusion energy density for a long enough time to achieve a sustained fusion burn. Producing a significant fusion reaction rate inside a tokamak requires the ability to heat and to contain high-temperature plasmas. Since the high confinement mode (H-mode) plasmas in tokamaks generally provide excellent energy confinement and have acceptable particle transport rates for impurity control, fusion experiments such as ITER are designed to operate in the H-mode regime. It is known that the improved performance of H-mode plasma results mainly from the formation of an edge transport barrier (ETB) [2], called the pedestal. The performance of an H-mode plasma can be further improved with the formation of a transport barrier inside the plasma, called an internal transport barrier (ITB) [3]. The presence of both ETB and ITB, results in a complicated scenario that yields higher plasma temperatures and, consequently, fusion power production.

In recent years, predictions of ITER performance in the standard type I ELMy H-mode scenario using integrated predictive modelling codes have been intensively studied [4-11]. For example, the BALDUR integrated predictive modelling code with Mixed Bohm/gyroBohm (Mixed B/gB) and MMM95 anomalous core transport models were used to predict the performance of ITER [4, 6–8]. The performance of ITER was evaluated in terms of the fusion power production and the Fusion Q, which is the ratio of fusion power (to neutrons and alpha particles) to the applied heating power. A wide range of performance is predicted, depending on the choice of plasma density, heating power, impurity concentration and assumptions about the core transport models employed in the simulations. In the recent work by Onjun et al [6, 7], the simulations of ITER were carried out with Mixed B/gB and MMM95 core transport model and different ETB models. It was found for all ETB models that the predicted performance of ITER with Mixed B/gB model is relatively low (Fusion $Q \sim 3$) compared with those simulations using MMM95 model (Fusion $Q \sim 10$). It is worth noting that the BALDUR simulations using Mixed B/gB and MMM95 models agree equally well with present-day experiments [12, 13]. In the ITER study using the JETTO code with Mixed B/gB model [5], an optimistic performance of ITER was found (Fusion $Q \sim 16$ with $T_{\rm ped} \sim 5\,{\rm keV}$). Access to second stability of ballooning mode instability for the plasma edge was obtained, and it was responsible for an increase in the pedestal temperature and, consequently, the central temperature and the fusion performance. In [9,10], the PTRANSP code with the GLF23 core transport model was used to simulate ITER performance. A wide range of performance was also found with the Fusion Q of 5-14. A recent report from the International Tokamak Physics Activity (ITPA) Profile Database group using the PTRANSP and ASTRA codes to investigate fusion performance in ITER was published in [11]. It was found that in the ELMy *H*-mode scenario, a wide range of Fusion *Q* was found (ranges from 5.5 to 20.1). Note that a pedestal temperature of 5.6 keV, predicted using the Sugihara model [14], was used in the PTRANSP simulations while the pedestal temperature of 1 keV was used in ASTRA simulations. It is worth noting that in those studies, the effects of ITBs were not included in the simulations. Consequently, this work is motivated by the need to explore ITER scenarios that include ITBs in type I ELMy *H*-mode discharges in order to improve its plasma performance.

It is widely known that the presence of ITBs usually results in an improved plasma performance, especially near central temperature and density. In general, the presence of ITBs results in a peaking of plasma profiles in the ITB region. The physics of ITBs can be found in [3]. There are several models attempting to describe the formation of ITBs [15–17]. An original Mixed B/gB model was modified to include the effect of ITBs by the suppression of anomalous core transport using $E_r \times B$ flow shear and magnetic shear. This model has been successfully reproduced in many JET experiments in various scenarios [16, 18–22].

In this paper, a study of ITER that includes the effects of ITBs together with the H-mode ETB is presented. These simulations are carried out using a BALDUR integrated predictive modelling code, where the ETB is described in terms of a pedestal model since the region considered in these simulations is up to the top of the pedestal. In this work, three best pedestal models in [22] are chosen. These pedestal models were developed by using the combination of the theoreticalbased pedestal width model together with pressure gradient limits imposed by a ballooning mode instability. are three choices of the pedestal width models considered: magnetic and flow shear stabilization ($\Delta \propto \rho_i s^2$) [24], flow shear stabilization ($\Delta \propto \sqrt{\rho_i Rq}$) [23] and normalized poloidal pressure ($\Delta \propto R\sqrt{\beta_{\theta,\mathrm{ped}}}$) [25]. These three pedestal temperature models yield similar agreement (with RMSE in the range of 30%) for predicting pedestal temperature when their predictions were compared against type I ELMy H-mode discharges from various tokamaks [23]. This pedestal module is taken from the NTCC library [26]. In simulations of discharges that contain an ITB, the ITB is formed by the suppression of core anomalous transport. The Mixed Bohm/gyro-Bohm with ITB effects [16] is used. The presence of both an ITB and an ETB results in complicated scenarios that yield improved performance compared with standard H-mode discharges.

This paper is organized as follows: brief descriptions of relevant components of the BALDUR code, the anomalous transport model and the pedestal models are presented in section 2; predictions of ITER performance using the BALDUR code are described in section 3 and a summary is given in section 4.

2. The BALDUR integrated predictive modelling code

The BALDUR integrated predictive modelling code [27] is used to compute the time evolution of plasma profiles including electron and ion temperatures, hydrogen and impurity densities, safety factor, neutrals and fast ions. These

time-evolving profiles are computed in the BALDUR code by combining the effects of many physical processes selfconsistently, including the effects of transport, plasma heating, particle influx, boundary conditions, the plasma equilibrium shape and sawtooth oscillations. Fusion heating and helium ash accumulation are also computed self-consistently. BALDUR simulations have been intensively compared against a variety of plasma experimental data, which yield an overall agreement with about a 10% relative RMS deviation [12, 13]. In the BALDUR code, fusion heating power is determined by the nuclear reaction rates together with a Fokker-Planck package used to compute the slowing down spectrum of fast alpha particles on each flux surface in the plasma. The fusion heating component of the BALDUR code also computes the rate of production of thermal helium ions and the rate of depletion of deuterium and tritium ions within the plasma core.

2.1. ITB model

In this work, an ITB is formed by the suppression of core anomalous transport due to $\omega_{E\times B}$ flow shear and magnetic shear. This effect is included in the Mixed Bohm/gyro-Bohm (Mixed B/gB) anomalous core transport model [16]. This core transport model is an empirical model. It was originally a local transport model with Bohm scaling. A transport model is said to have 'Bohm' scaling when the transport diffusivities are proportional to the gyro-radius times thermal velocity. Transport diffusivities in models with Bohm scaling are also functions of the profile shapes (characterized by normalized gradients) and other plasma parameters, such as magnetic q. These parameters are held fixed in systematic scans in which only the gyro-radius is changed relative to plasma dimensions. The original model was subsequently extended to describe ion transport, and a gyro-Bohm term was added in order to produce simulation results that match data from smaller tokamaks as well as data from larger machines. A transport model is said to have 'gyro-Bohm' scaling when the transport diffusivities are proportional to the square of the gyro-radius times thermal velocity divided by a plasma linear dimension such as the major radius. The Bohm contribution to the original model usually dominates over most of the plasma. The gyro-Bohm contribution usually makes its largest contribution in the deep core of the plasma and it plays a significant role only in smaller tokamaks with relatively low heating power and low magnetic field. To include the ITB effect, the Bohm contribution is modified by a cut-off that is a function of magnetic and flow shear. The Mixed B/gB transport model with ITB effect included [16] can be expressed as follows:

$$\chi_{\rm e} = 1.0\chi_{\rm gB} + 2.0\chi_{\rm B},$$
 (1)

$$\chi_{\rm i} = 0.5\chi_{\rm gB} + 4.0\chi_{\rm B} + \chi_{\rm neo},$$
 (2)

$$D_{\rm H} = [0.3 + 0.7\rho] \frac{\chi_{\rm e} \chi_{\rm i}}{\chi_{\rm e} + \chi_{\rm i}},$$
 (3)

$$D_{\rm Z} = D_{\rm H},\tag{4}$$

where

$$\chi_{\rm gB} = 5 \times 10^{-6} \sqrt{T_{\rm e}} \left| \frac{\nabla T_{\rm e}}{B_{\phi}^2} \right|,\tag{5}$$

$$\chi_{\rm B} = 4 \times 10^{-5} R \left| \frac{\nabla (n_{\rm e} T_{\rm e})}{n_{\rm e} B_{\phi}} \right| q^2 \left(\frac{T_{\rm e, 0.8} - T_{\rm e, 1.0}}{T_{\rm e, 1.0}} \right) \times \Theta \left(-0.14 + s - \frac{1.47 \omega_{E \times B}}{\gamma_{\rm TTG}} \right). \tag{6}$$

In these expressions, the χ_e is the electron diffusivity, χ_i is the ion diffusivity, D_H is the particle diffusivity, D_z is the impurity diffusivity, χ_{gB} is the gyro-Bohm contribution, χ_B is the Bohm contribution, ρ is normalized minor radius, T_e is the local electron temperature in keV, B_ϕ is the toroidal magnetic field, R is the major radius, n_e is the local electron density, q is the safety factor, s is the magnetic shear [r(dq/dr)/q], $\omega_{E\times B}$ is the flow shearing rate and the γ_{TTG} is the ITG growth rate, estimated as v_{ti}/qR , in which v_{ti} is the ion thermal velocity. The role of impurity transport is very complicated and crucial for burning plasma experiments since it controls impurity behaviour, such as helium ash accumulation. Since the original Mixed B/gB model does not include impurity transport, in this work, it is assumed that the impurity transport is equal to the particle transport.

In this work, the $\omega_{E\times B}$ shearing rate used for the formation of ITB is calculated as follows:

$$\omega_{E\times B} = \left| \frac{RB_{\theta}^2}{B_{\phi}} \frac{\partial (E_r/RB_{\theta})}{\partial \psi} \right|,\tag{7}$$

where R is the major radius, B_{θ} and B_{ϕ} are the poloidal and toroidal magnetic fields, respectively, Ψ is the poloidal flux and E_r is the radial electric field for the main plasma ions, which is calculated as follows:

$$E_r = \frac{1}{Zen_i} \frac{\partial p_i}{\partial r} - v_\theta B_{\rm T} + C_\phi v_\phi B_\theta, \tag{8}$$

where $\partial p_i/\partial r$ is the pressure gradient, v_θ and v_ϕ are the poloidal and toroidal velocities, respectively, C_ϕ is the constant for toroidal velocity effect (in most of simulations, $C_\phi=1$), and, n_i is the ion density, Z is the ion charge number and e the elementary charge. Note that in this work, the toroidal velocity is taken directly from one of the JET experiment.

2.2. ETB model

In the development of the pedestal temperature models described in [23], two ingredients are required: the pedestal width (Δ) and the pressure gradient $(\partial p/\partial r)$. If the pedestal density $(n_{\rm ped})$ is known, the temperature at the top of the pedestal $(T_{\rm ped})$ can be estimated as

$$T_{\text{ped}} = \frac{1}{2n_{\text{ped}}k} \left| \frac{\partial p}{\partial r} \Delta \right| = \frac{\Delta}{2kn_{\text{ped}}} \frac{\alpha_{\text{c}} B_{\phi}^2}{2\mu_0 R q^2}.$$
 (9)

where k is the Boltzmann constant, μ_0 is the permeability of free space, $\alpha_{\rm c}$ is the normalized critical pressure gradient, B_{ϕ} is the toroidal magnetic field, R is the major radius and q is the safety factor. In this work, three best pedestal temperature models in [23] are selected. These pedestal temperature models yield equally satisfactory agreement with the pedestal data from the ITPA Pedestal Database. These pedestal temperature models are based on either the magnetic and flow shear stabilization width scaling ($\Delta \propto \rho_i s^2$) [24], the flow shear stabilization width scaling ($\Delta \propto \sqrt{\rho_i R q}$) [23] or the

normalized poloidal pressure width scaling ($\Delta \propto R\sqrt{\beta_{\theta,\mathrm{ped}}}$) [25], where ρ_t is the ion gyro radius, s is the magnetic shear and $\beta_{\theta,\mathrm{ped}}$ is the normalized pedestal pressure. The pedestal pressure gradient calculation is normally complicated and requires a lot of details. For simplicity, the pedestal gradient is assumed to be uniform throughout the pedestal region and the pedestal gradient is limited by the first stability limit of infinite n ballooning mode, so that the normalized critical pressure gradient for the pedestal region is estimated by

$$\alpha_{\rm c} \equiv -\frac{2\mu_0 R q^2}{B_{\phi}^2} \left(\frac{\partial p}{\partial r}\right)_{\rm c} = 0.4s(1 + \kappa_{95}^2 (1 + 5\delta_{95}^2)),$$
 (10)

where κ_{95} is the elongation at the 95% flux surface and δ_{95} is the triangularity at the 95% flux surface. The further details of these pedestal temperature models can be obtained from [23]. It is worth noting that these pedestal temperature models were derived from different pedestal width scalings. The pedestal width constant in each model was chosen to minimize the RMS deviation with 533 experimental data points from four large tokamaks obtained from the International Tokamak Physics Activity (ITPA) pedestal database. So, in this work the pedestal models with the chosen width constant in [23] are used. These pedestal temperature models include the effect of edge bootstrap current, which has an impact on magnetic shear and safety factor. This inclusion results in a non-linear behaviour in the pedestal temperature model. The scheme to deal with the approximation of magnetic shear and safety factor for the pedestal prediction using the pedestal models was completely described in [23]. Therefore, the values of magnetic shear and safety factor for the pedestal calculation are different from the rest of both values in the BALDUR code, which is based on more appropriate calculation. The attempt to use self-consistent safety factor and magnetic shear for all calculations in the BALDUR code is underdevelopment. A preliminary result can be seen in [28]. In addition, there are several new approaches to estimate pedestal values; such as the pedestal scaling by Sugihara [14], which predicted the pedestal temperature about 5.6 keV.

The pedestal density is described by a simple empirical model. Since the pedestal density, $n_{\rm ped}$, is usually a large fraction of line average density, $n_{\rm l}$, the pedestal density can be calculated as

$$n_{\text{ped}} = 0.71 n_{\text{l}}.$$
 (11)

This pedestal density model agrees with the pedestal data obtained from the ITPA pedestal database with 12% RMSE [4]. In this work, it is assumed that the impurity consists of helium and carbon. The ratio of helium to electron density at the edge is 1%. The effective charge is about 1.4 at the edge of the plasma. With these conditions of the impurity, the densities of carbon and helium at the boundary are $1.3 \times 10^{18} \, \mathrm{m}^{-3}$ and $1.0 \times 10^{18} \, \mathrm{m}^{-3}$, respectively.

3. Simulation results and discussion

The BALDUR code is used to carry out simulations of ITER with the design parameters for full-current standard type I ELMy *H*-mode discharges ($R=6.2\,\mathrm{m},~a=2.0\,\mathrm{m},~I_\mathrm{p}=15\,\mathrm{MA},~B_\phi=5.3\,\mathrm{T},~\kappa_{95}=1.7,~\delta_{95}=0.33$ and $n_1=1.0\times10^{20}\,\mathrm{m}^{-3}$). In the simulations, the plasma current and

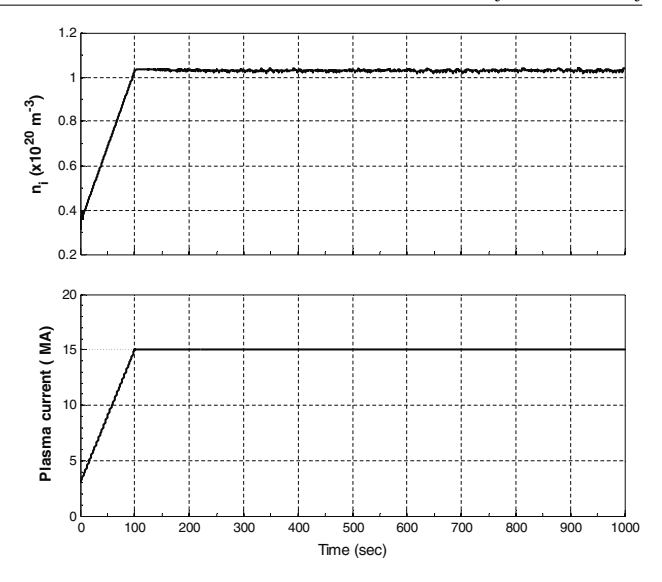


Figure 1. The time evolution of line average density (top) and plasma current (bottom) are shown.

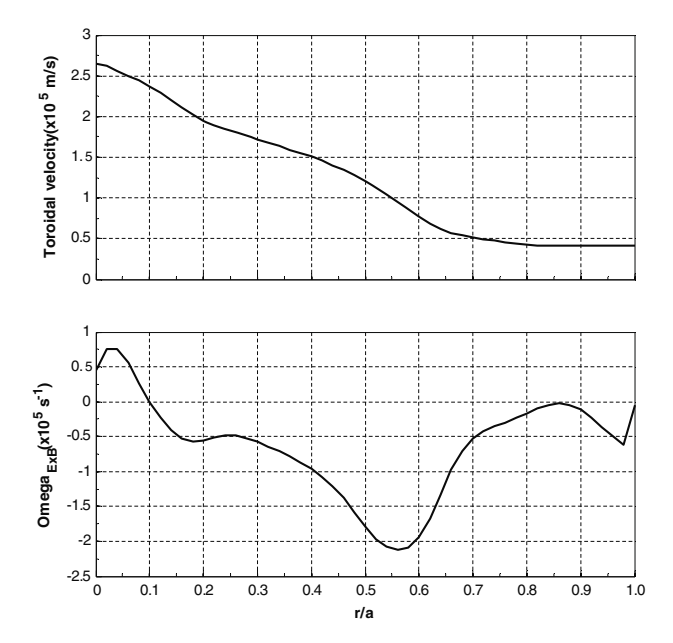


Figure 2. The toroidal velocity (top) and $\omega_{E\times B}$ (bottom) profiles used in this work are plotted as a function of a normalized minor radius. Toroidal velocity profile is taken from JET experiment (discharge 40542), while the $\omega_{E\times B}$ is calculated using equation (7).

density are slowly ramped up to the target values within the first $100 \, \text{s}$ of the simulation, shown in figure 1. The plasma current during the startup phase is initially $3 \, \text{MA}$ and is slowly increased at the rate of $0.12 \, \text{MA} \, \text{s}^{-1}$ to the target current. It is found, using the pedestal module [26], that the ITER plasma makes a transition to the H-mode phase at $4 \, \text{s}$ during this startup ramp. In this work, the threshold for the transition from L-mode to H-mode occurs when the plasma heating power exceeds the following empirical expression for the threshold power, taken from [29]:

$$P_{\text{L}\to\text{H}} \text{ (MW)} = 2.84 M_{\text{AMU}}^{-1} B_{\phi}^{0.82} n_{\text{e}.20}^{-0.58} R^{1.00} a^{0.81}.$$
 (12)

It is worth noting that there are several physical processes that have not been included in these simulations, such as

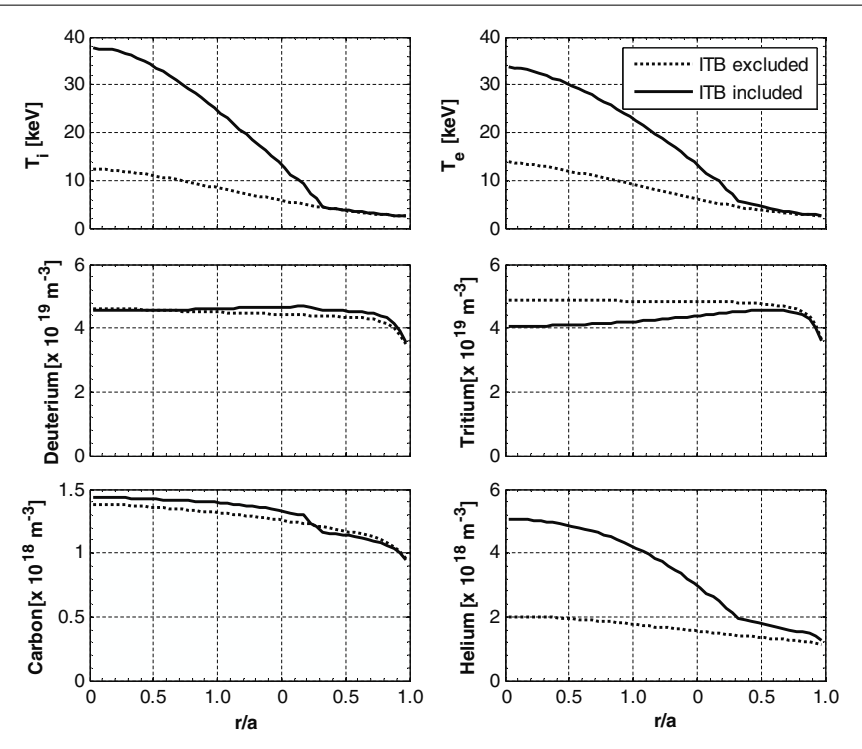


Figure 3. Profiles for ion temperature, electron temperature, deuterium density, tritium density, carbon density and helium density are plotted as a function of a normalized minor radius at the time before a sawtooth crash. The simulations are carried out with (solid) and without (dotted) ITB effects. The boundary condition is provided by the pedestal model based on magnetic and flow shear stabilization.

ELM crashes and neoclassical tearing modes. Consequently, the simulation results do not represent the complete dynamic behaviour of the ITER plasma. However, it is expected that these simulations include enough physics to describe the plasma when it reaches a quasi-steady state with sawtooth oscillations. The simulations yield complex and interesting interactions within the plasma itself—such as the self heating of the plasma by the production of fast alpha particles and redistribution of heating power after each sawtooth Sawtooth oscillations are also considered during these simulations. For each simulation, anomalous transport is calculated using the Mixed B/gB transport model with the effect of ITB included, while neoclassical transport is computed using the NCLASS module [30]. The boundary conditions are provided at the top of the pedestal by the pedestal model. In many experiments, it was found that ion pedestal temperature tends to be higher than the electron pedestal temperature, especially at low density plasma. Since the ITER plasma is a high density plasma, the ion pedestal temperature is expected to be not so different from the electron pedestal temperature. The ITER simulations using the JETTO code with sophisticated edge modelling in [5] indicated that the electron and ion temperatures at the top of the pedestal were found to be slightly different (4.4 keV for electron and 4.9 keV for ion). For simplicity, it is assumed in this work that the electron and ion pedestal temperatures have the same values. Note that this assumption for the ion and electron pedestal temperatures was employed in the BALDUR code to carry out the H-mode simulations for present-day experiments, which the agreement between simulations and experiments was in the range of 10% RMS deviation [4]. In these simulations, the total auxiliary heating power is 40 MW, which is composed of a combination of 33 MW NBI heating power together with 7 MW of RF heating power. As noted above, the Porcelli sawtooth model [31] is used to trigger sawtooth crashes and a modified Kadomtsev magnetic reconnection model [32] is used to compute the effects of each sawtooth crash. Note that during each sawtooth crash, it is assumed that 10% of magnetic flux is mixed to describe the effect of each sawtooth crash.

During the slow current ramp up phase (reaching the target value in $100\,\mathrm{s}$), the plasma density is also ramped up to the target plasma density while full auxiliary heating power is applied starting from the beginning of the simulations. In this work, the $\omega_{E\times B}$ shearing rate profile for initiating a formation of an ITB is calculated using equation (7); while the toroidal velocity is taken directly from one of the Joint European Torus (JET) experiment, discharge 40542. In figure 2, the toroidal velocity profile for an optimized magnetic shear (OS) discharge in JET experiment, discharge 40542 and the calculated $\omega_{E\times B}$ profile using equation (7) and the toroidal velocity from JET discharge 40542 are shown. It can be seen that the minimum value of calculated $\omega_{E\times B}$ shearing rate for ITER is located at $\rho=0.56$ with the value about $2.1\times10^5\,\mathrm{s}^{-1}$. Note that in [33], it suggests a simple estimation for toroidal velocity as

$$v_{\phi} (\text{m s}^{-1}) = 2.5 \times 10^4 T_{i} (\text{keV}).$$
 (13)

Since the average ion temperature near the plasma centre in ITER is expected to be around 10 keV, the expected range of the toroidal velocity in ITER is in the order of 10⁵ m s⁻¹, which is in the range of that used in this work. However, it is worth noting that there are two important factors for toroidal velocity: plasma density and NBI beam properties. In ITER

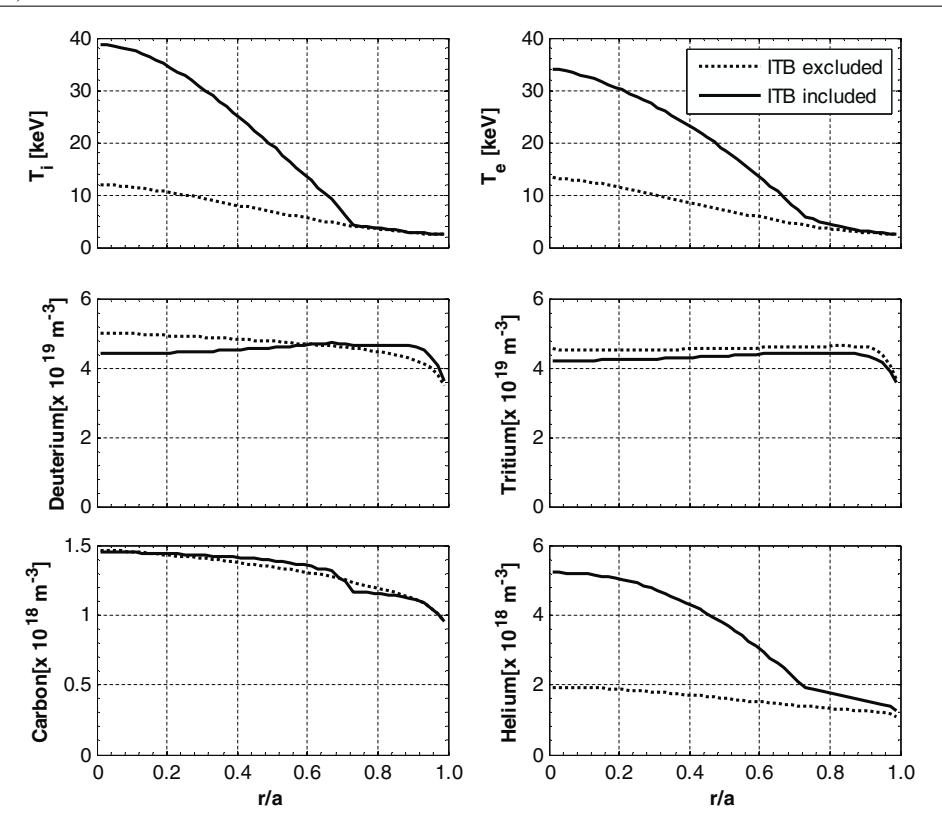


Figure 4. Profiles for ion temperature, electron temperature, deuterium density, tritium density, carbon density and helium density are plotted as a function of a normalized minor radius at the time before a sawtooth crash. The simulations are carried out with (solid) and without (dotted) ITB effects. The boundary condition is provided by the pedestal model based on flow shear stabilization.

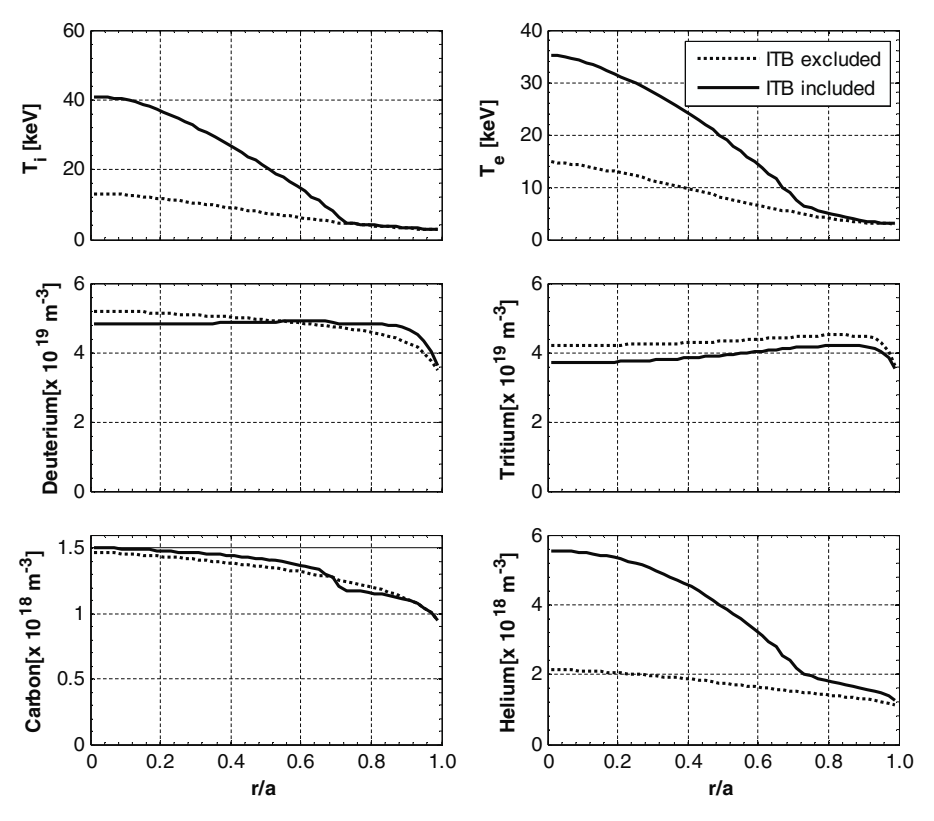


Figure 5. Profiles for ion temperature, electron temperature, deuterium density, tritium density, carbon density and helium density are plotted as a function of a normalized minor radius at the time before a sawtooth crash. The simulations are carried out with (solid) and without (dotted) ITB effects. The boundary condition is provided by the pedestal model based on normalized poloidal pressure.

Table 1. Summary of electron and ion temperatures, elec-	ctron density at the time before a sawtooth crash.
---	--

	$\Delta \propto ho s^2$		$\Delta \propto \sqrt{\rho R q}$		$\Delta \propto R \sqrt{eta_{ heta, ext{ped}}}$	
Parameters	ITB excluded	ITB included	ITB excluded	ITB included	ITB excluded	ITB included
$T_{i,0}$ (keV)	12.3	35.1	11.8	35.0	13.0	41.4
$T_{\rm e,0}~({\rm keV})$	13.8	33.2	13.3	33.7	14.7	34.0
$n_{\rm e,0}~(\times 10^{20}~{\rm m}^{-3})$	1.1	1.1	1.1	1.1	1.1	1.1
$T_{\rm ped}~({\rm keV})$	2.6	2.6	2.5	2.5	2.9	2.9
$n_{\rm e,ped} \ (\times 10^{20} \rm m^{-3})$	0.7	0.7	0.7	0.7	0.7	0.7

experiment, the plasma density in ITER is higher compared with that in the JET experiment (discharge 40542). Also, the 1 MeV neutral beams are planned for ITER, compared with the 100 keV beams in JET. As a result of these two effects, it may be more difficult to produce the magnitude of the toroidal velocity found in the JET experiment. The sensitivity of the toroidal velocity used will be shown later in section 3.1.

Figures 3–5 show the profiles for ion temperature, electron temperature, deuterium density, tritium density, carbon density and helium density as a function of normalized minor radius at a time before a sawtooth crash for simulations using the pedestal temperature model based on magnetic and flow shear stabilization, using the pedestal temperature model based on flow shear stabilization and using the pedestal temperature model based on normalized poloidal pedestal pressure, respectively. These results are shown for simulations that are carried out using the Mixed B/gB model with the effects of ITB excluded and included. It can be seen in all three figures that when the ITB effects are included in the simulations, the central temperatures for both ion and electron in all simulations increase significantly, while the temperatures near the plasma edge change just slightly. It is found in all simulations that the pedestal temperatures for both ion and electron remain almost constant after the plasma density reaches its target value. The constant pedestal temperature condition results from the constant electron density. For the deuterium density and tritium density, both profiles are nearly flat. The carbon and helium density profiles are peak, especially in the case of helium density in the simulation with ITB included. It can be seen that the helium profiles show the formation of ITB. It can be also seen that when the effect of ITB is included, deuterium, tritium and carbon densities change slightly, but the helium density increases significantly, especially near the plasma centre, which results from the formation of ITB. This result indicates the helium ash accumulation in the ITER plasma. It can be seen in figures 3-5 that the ITB effective region extends to a plasma radius of up to $\rho = 0.6$. This ITB region results from the reduction of transport in the region close to the plasma core. This suppression occurs due to the presence of $\omega_{E\times B}$ flow shear, which results in the formation of ITB. Note that the impurity transport is also included in all simulations in this work. It is assumed that particle transport is same as impurity transport. It is widely accepted that impurity transport is very complicated and different from particle transport. This is a very important issue and it needs special attention.

Summaries of the temperatures and densities at the centre and at the top of the pedestal predicted by these simulations are shown in table 1. It can be seen that the central ion temperature increases significantly when the ITB effects are included. For

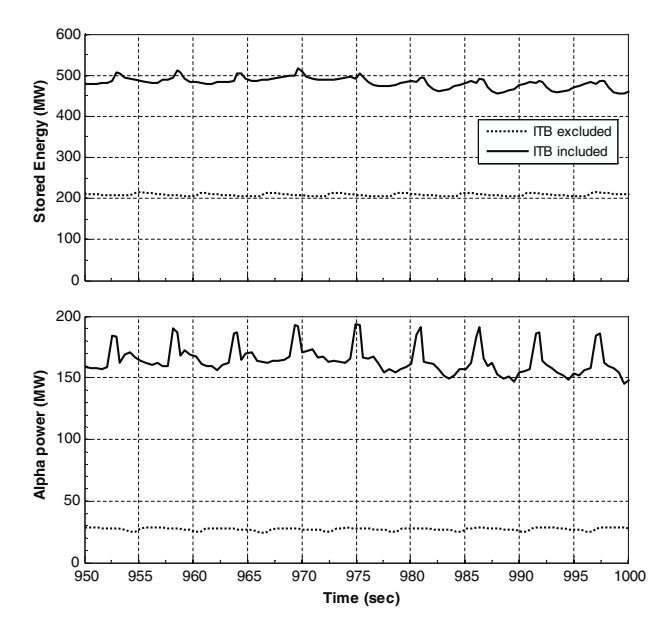


Figure 6. The plasma stored energy and alpha power production are plotted as a function of time for simulations with ITB effects excluded (dotted) and included (solid). These simulations are carried out using the pedestal temperature based on magnetic and flow shear stabilization.

example, the central ion temperatures in the ITB simulation range from 35.0 to 41.4 keV. The central ion and electron temperatures in the simulation using the pedestal temperature based on magnetic and flow shear stabilization increase by 190% and 140%, respectively, when simulations with ITB effects are compared with simulations without ITB effects. Note that the results for different pedestal temperature models yield the same range of improvement. This increase in central temperature has a strong impact on the total plasma stored energy and the nuclear fusion power production. It can be seen from table 1 that the pedestal temperature ranges from 2.5 to 2.9 keV, which is a minimum expected value for a pedestal in ITER. It is worth noting that these pedestal temperature models are based on the first stability limit of infinite-n ballooning modes. If the effect of access to second stability of ballooning modes is properly included, the predicted pedestal temperature should be significantly higher. In [5], access to second stability of ballooning mode was found, and consequently the pedestal temperature is close to 5 keV. When the Sugihara pedestal model [14] was used, a pedestal temperature of 5.6 keV was found. Therefore, the results obtained in this work can be considered as a minimum projection of ITER performance.

The total plasma stored energy in the simulation using the pedestal temperature based on magnetic and flow shear Nucl. Fusion 49 (2009) 075003 T. Onjun and Y. Pianroj **Table 2.** Summary of average of alpha power and Fusion Q during the last 50 s of the simulations (from 950 to 1000 s).

<u>, </u>	•	<u> </u>	
	$\Delta \propto \rho s^2$	$\Delta \propto \sqrt{\rho Ra}$	$\Delta \propto R_{\bullet}/\beta_{\theta, \text{ped}}$

	$\Delta \propto \rho s^2$		$\Delta \propto $	$\Delta \propto \sqrt{ ho Rq}$		$\Delta \propto R \sqrt{eta_{ heta, ext{ped}}}$	
Parameters	ITB	ITB	ITB	ITB	ITB	ITB	
	excluded	included	excluded	included	excluded	included	
$P_{\alpha,\text{avg}}$ (MW)	27.9	164.9	24.1	160.6	32.5	179.6	
Fusion Q_{avg}	3.4	20.6	3.0	20.1	4.1	22.4	

stabilization is shown as a function of time between 900 to 1000 s in figure 6. It can be seen that the value of plasma stored energy is in the range of 200 MJ for the simulation with no ITB, while the plasma stored energy increases to be close to 500 MJ in the simulation with ITB effects included. The time-dependence of the alpha power production is also shown in figure 6 from the simulations using the pedestal temperature based on magnetic and flow shear stabilization. It can be seen that the alpha power from the simulation with ITB effects included is much higher than that without an ITB. The average of alpha power during the time between 950 and 1000 s is summarized in table 2. The fusion performance can be evaluated in terms of the Fusion Q, which can be calculated as

Fusion
$$Q = \frac{5 \times P_{\alpha, \text{avg}}}{P_{\text{AUX}}}$$
,

where $P_{\alpha,\text{avg}}$ is a time-average of the alpha power and P_{AUX} is the auxiliary heating power (equal to 40 MW for these simulations). It can be seen in table 2 that the Fusion Q ranges from 20.1 to 22.4 when ITB effects are included. This means that the Fusion Q increases by 500%, 570% and 450% when ITB effects are included in the simulations using the pedestal temperature model based on magnetic and flow shear stabilization, flow stabilization and normalized poloidal pressure, respectively. The increasing alpha power results in the improved fusion performance that meets the requirement of ITER fusion performance, which is equal to 10. Remarking that in the ITER study using JETTO code with Mixed B/gB model [5], an optimistic performance of ITER (Fusion $Q \sim 16$) was found. When PTRANSP code with GLF23 core transport model was used to simulate ITER performance in [9, 10], a wide range of performance was also found with the Fusion Q of 5–14. In [11] that the ITER simulations yielded the Fusion Q ranging from 4.2 to 16.1. It can be seen that the results obtained in this work yield Fusion Q > 10 if an ITB can be sustained.

3.1. Effect of toroidal velocity

It can be seen in the previous section that the formation of ITB has a strong impact on the performance of ITER, in which Fusion Q can increase significantly when the ITB effects are included. The formation of ITB can result from the $\omega_{E\times B}$ shearing rate, which stabilizes anomalous transport in the plasma core. In this work, the profile of $\omega_{E\times B}$ shearing rate is computed using equation (7) by acquiring the value of toroidal velocity from the JET discharge 40542. In order to observe the impact of toroidal velocity, the value of the constant C_{ϕ} is varied. In figure 7, the ion temperature and electron density profiles before a sawtooth crash are shown for C_{ϕ} equalling to 0.1, 0.5 and 1.0. It can be seen that central

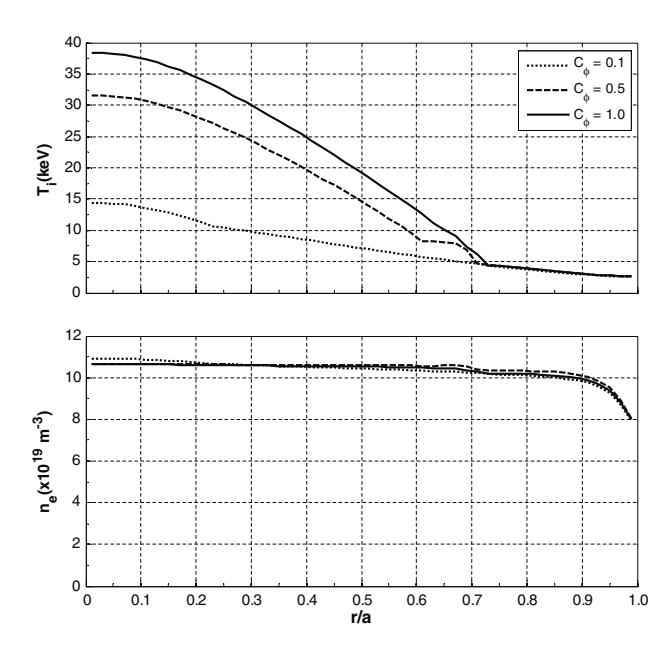


Figure 7. The ion temperature and electron density profiles are plotted at the time before a sawtooth crash for different values of the constant C_{ϕ} . These simulations are carried out using the pedestal temperature based on magnetic and flow shear stabilization.

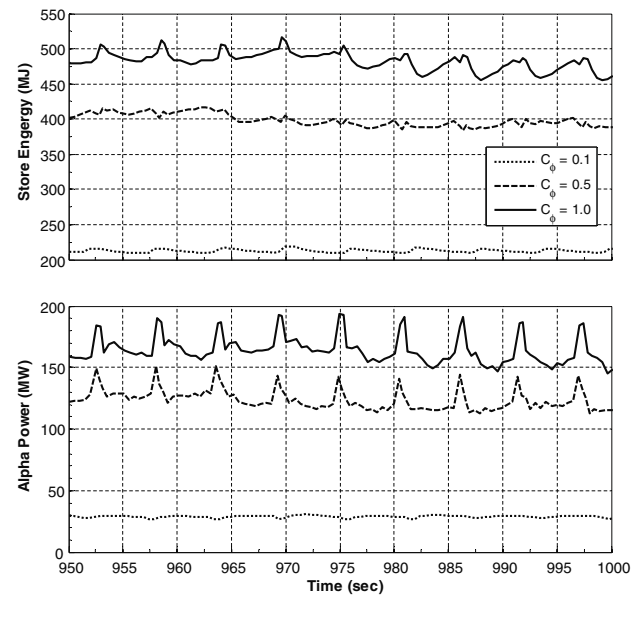


Figure 8. The plasma stored energy and alpha power production are plotted as a function of time for simulations with different values of the constant C_{ϕ} . These simulations are carried out using the pedestal temperature based on magnetic and flow shear stabilization.

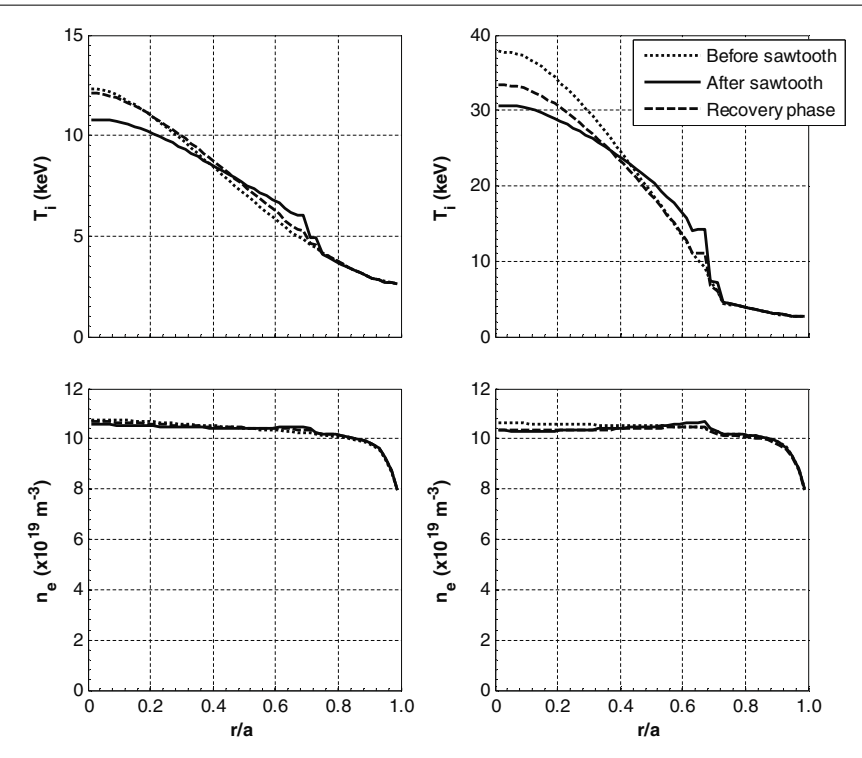


Figure 9. The ion temperature and electron density profiles during a sawtooth crash cycle are plotted for a simulation with ITB effects excluded (left) and included (right). These simulations are carried out using the pedestal temperature based on magnetic and flow shear stabilization.

ion temperature increases significantly with increasing of C_{ϕ} ; while the central electron density reminds almost the same (around $1.1 \times 10^{20} \, \mathrm{m}^{-3}$). In figure 8, the total plasma stored energy and alpha power is shown as a function of time between 900 and 1000 s. It is found that the average stored energy is about 220 MJ, 400 MJ and 480 MJ, as the value of C_{ϕ} equals to 0.1, 0.5 and 1.0, respectively. For the alpha power, the average alpha power is 30 MW, 130 MW and 160 MW, as the value of C_{ϕ} equals to 0.1, 0.5 and 1.0, respectively.

3.2. Effect of sawtooth crash

The effect of sawtooth oscillation is considered for all simulations in this work. The Porcelli sawtooth triggering model [30] is used to evaluate conditions of sawtooth crashes and a modified Kadomtsev magnetic reconnection model [31] is used to compute the effects of each sawtooth crash. Note that during each sawtooth crash, it is assumed that 10% of magnetic flux is mixed to describe the effect of sawtooth crash. It was found that this sawtooth model yield good agreement with the experimental data from various tokamaks [31].

In figure 9, the ion temperature and electron density profiles before, during and after a sawtooth crash are shown for the simulations using the Mixed B/gB model with the effects of ITB excluded and included. It can be seen that after a sawtooth crash, the central ion temperatures drop significantly; while the central electron density change slightly. It is found that the central ion temperature decreases about 46% and 26% during a sawtooth crash in the simulation with ITB and without ITB, respectively. Also, it can be seen that the sawtooth crash effective area is quite large, more than half of the plasma (normalized minor radius of 0.7, which is slightly larger than

the ITB affected area). With the time evolution during a sawtooth crash, it can be concluded that the sawtooth crash does not have an impact on the pedestal.

3.3. Test of self-sustaining heating

It is interesting to study the issue of self-sustained heating (ignition) in ITER since it is an ultimate goal of fusion study. Can the ITER plasma continue to produce a large amount of fusion power after all of auxiliary heatings are turned off? To answer this question, the BALDUR code is used to carry out simulation with the 40 MW auxiliary heating power until it reaches the quasi-steady state. In this work, the auxiliary heating is chosen to be off after 600 s. This means that after 600 s, the ITER plasma is heated by ohmic power and alpha power. In this simulation, the pedestal temperature is calculated using the pedestal temperature model based on magnetic and flow shear stabilization pedestal width scaling. It is found in the simulations that both stored energy and alpha power drop after heating power shutdown. However, the plasma recovers and is able to reach quasi-steady state after the shutdown of auxiliary heating in both simulations with and without ITB. This means that even though the auxiliary heating is shutdown, plasma can sustain itself by using alpha power. Note that ohmic power is small compared with alpha power. The average of alpha power after auxiliary heating turned off (during the time between 950 and 1000 s) is summarized in table 3. It can be seen that alpha power is in the range 27.3-28.5 MW for the simulations without ITB, and 116.7 to 138.3 MW for the simulations with ITB.

In figure 10, the profiles for ion temperature, electron temperature, deuterium density, tritium density, carbon density

Table 3. Summary of average of alpha power and Fusion Q during the last 50 s of the simulations (from 950 to 1000 s). The auxiliary heating is turned off after 600 s.

	$\Delta \propto \rho s^2$		$\Delta \propto \sqrt{ hoRq}$		$\Delta \propto R \sqrt{eta_{ heta, m ped}}$	
Parameters	ITB	ITB	ITB	ITB	ITB	ITB
	excluded	included	excluded	included	excluded	included
$P_{\alpha,\text{avg}}$ (MW)	27.3	116.7	28.5	118.8	28.4	138.3
Fusion Q_{avg}	∞	∞	∞	∞	∞	∞

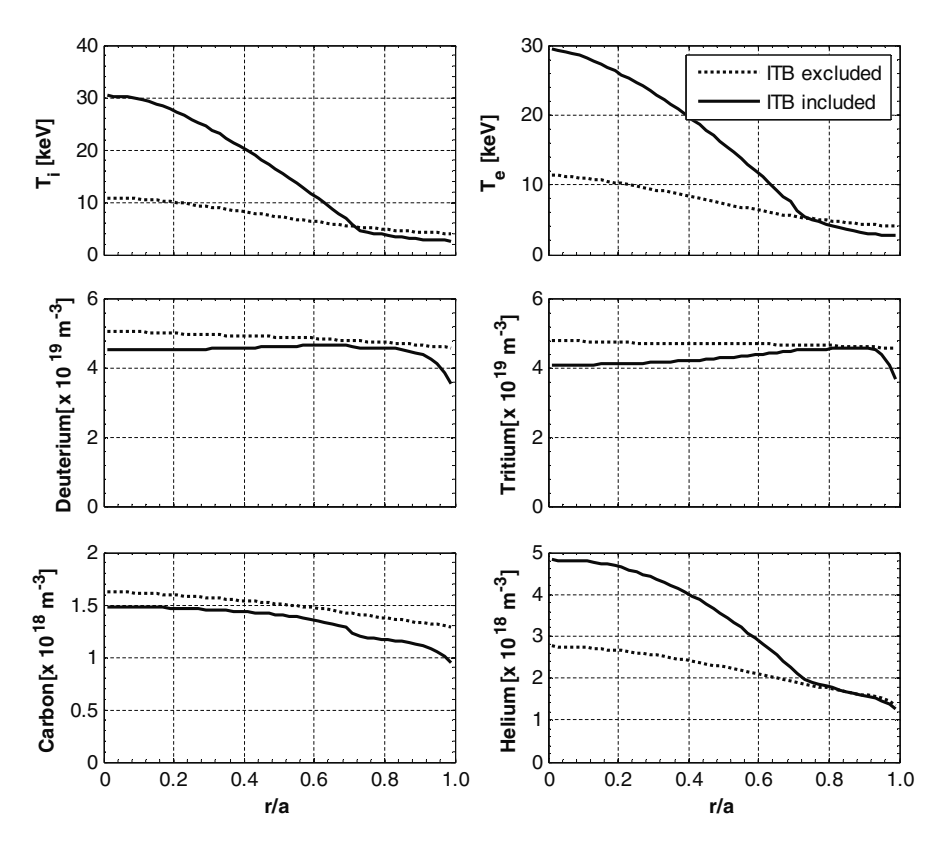


Figure 10. Profiles for ion temperature and electron density are plotted as a function of a normalized minor radius at the time before a sawtooth crash during the period that the auxiliary heating is turned off. The simulations are carried out without (dotted) and without (solid) ITB effects. The boundary condition is provided by the pedestal model based on magnetic and flow shear stabilization.

and helium density are plotted as a function of normalized minor radius at a time before a sawtooth crash after the auxiliary heating is shutdown for the simulations with and without ITB. These results are shown for simulations that are carried out using the pedestal temperature model based on magnetic and flow shear stabilization width scaling. By comparing figures 3 and 10 (same pedestal model), it can be seen that the central temperatures in the simulations either with or without ITB effects decrease if the auxiliary heating is turned off; while the density profiles change slightly. It can also be seen that the temperature and density at the top of the pedestal remains the same. Therefore, it can be concluded that the shutting down of the auxiliary heating has an impact on the central temperature (consequently, a reduction in plasma performance), but it does not have an impact on the pedestal values. This is not surprising since the pedestal value in this work is predicted using a pedestal model based on an infiniten ballooning mode limit, which is independent of the heating power. If a different-based pedestal model were used, such as a model based on peeling mode, the results might be different, such as the results shown in [34]. This discussion is beyond the scope of this paper.

4. Conclusions

Self-consistent simulations of ITER with the presence of both ETB and ITB are carried out using the BALDUR code. The combination of Mixed B/gB transport model together with three different pedestal models is used to simulate the time evolution of plasma current, temperature and density profiles for ITER standard type I ELMy H-mode discharges. It is found that ITER fusion performance using the BALDUR code with Mixed B/gB transport model without the presence of ITB is quite pessimistic (Fusion $Q \sim 3$). The presence of ITB is crucial and can result in a significant improvement, which is needed for achieving a target Fusion Q of 10. The improvement due to the presence of ITB is almost the same for all simulations with those three pedestal temperature models. This is caused by the predicted pedestal temperature from each pedestal temperature model varying just slightly. The presence

of ITB has a strong impact on both temperature profiles, especially near the centre of the plasma, but has small impact on electron, deuterium, tritium and carbon density profiles, except the helium density profile. The formation of ITB does not impact on the pedestal. It is also found that during a sawtooth crash, the temperature profiles drop significantly, but there is a small change in the density profiles. However, the sawtooth oscillation has no impact on the pedestal. When the auxiliary heating power is turned off, it is found that significant fusion power can be sustained.

Acknowledgments

The authors thank Professor Dr A.H. Kritz, Dr G. Bateman, Dr V. Parail, Dr A. Pankin, Dr S. Suwanna, Dr N. Poolyarat and Dr R. Picha for their helpful discussions and supports. This work is supported by the Commission on Higher Education (CHE) and the Thailand Research Fund (TRF) under Contract No RMU5180017.

References

- [1] Aymar R. et al 2002 Plasma Phys. Control. Fusion 44 519
- [2] Hubbard A. 2000 Plasma Phys. Control. Fusion 42 A15
- [3] Connor J.W. et al 2004 Nucl. Fusion 44 R1
- [4] Bateman G. et al 2003 Plasma Phys. Control. Fusion 45 1939
- [5] Onjun T. et al 2005 Phys. Plasmas 12 082513
- [6] Onjun T. et al 2008 J. Phys.: Conf. Ser. 123 012034

- [7] Tharasrisuthi K. et al 2008 Thammasat International J. Sci. Technol. 13 45
- [8] Picha R. et al 2008 Proc. 35th EPS Conf on Plasma Physics (Hersonissos, Crete, 9–13 June 2008)
- [9] Halpern, F.D. et al 2008 Phys. Plasmas 15 062505
- [10] Budny R.V. et al 2008 Nucl. Fusion 48 075005
- [11] Roach C.M. et al 2008 Nucl. Fusion 48 125001
- [12] Hannum D. et al 2001 Phys. Plasmas 8 964
- [13] Onjun T. et al 2001 Phys. Plasmas 8 975
- [14] Sugihara M. et al 2003 Plasma Phys. Control. Fusion 45 L55
- [15] Zhu P. et al 2000 Phys. Plasmas 7 2898
- [16] Tala T.J.J. et al 2001 Plasma Phys. Control. Fusion 43 507
- [17] Kinsey J.E. et al 2005 Phys. Plasmas 12 052503
- [18] Parail V.V. et al 1999 Nucl. Fusion 38 429
- [19] Parail V.V. 2002 Plasma Phys. Control. Fusion 44 A63
- [20] Tala T.J.J. et al 2002 Plasma Phys. Control. Fusion 44 A495
- [21] Tala T.V.V. et al 2005 Nucl. Fusion 45 1027
- [22] Tala T. et al 2006 Nucl. Fusion 46 548
- [23] Onjun T. et al 2002 Phys. Plasmas 9 5018
- [24] Sugihara M. et al 2000 Nucl. Fusion 40 1743
- [25] Osborne T.H. et al 1999 J. Nucl. Mater. 266-269 131
- [26] Kritz A. et al 2004 Comput. Phys. Commun. 164 108; http://w3.pppl.gov/NTCC
- [27] Singer C.E. et al 1988 Comput. Phys. Commun. 49 399
- [28] Onjun T. et al 2008 J. Phys.: Conf. Ser. 123 012014
- [29] Shimomura Y. et al 2000 Proc. 18th IAEA Conf. (Sorrento, Italy)
- [30] Houlberg W.A. et al 1997 Phys. Plasmas 4 3231
- [31] Porcelli F. et al 1996 Plasma Phys. Control. Fusion 38 2163
- [32] Bateman G. et al 2006 Phys. Plasmas 13 072505
- [33] Kessel C.E. et al 2006 Proc. 21st Fusion Energy Conference (Chengdu, China, 2006)
- [34] Onjun T. et al 2004 Phys. Plasmas 11 1469

=== TOKAMAKS ==

Pellet Injection into H-Mode ITER Plasma with the Presence of Internal Transport Barriers¹

P. Leekhaphan^a and T. Onjun^{b, c}

^a School of Bio-Chemical Engineering and Technology, Sirindhorn International Institute of Technology, Thammasat University, Klongluang, Pathum Thani, 12121 Thailand ^b School of Manufacturing Systems and Mechanical Engineering, Sirindhorn International Institute of Technology, Thammasat University, Klongluang, Pathum Thani, 12121 Thailand ^cThailand Center of Excellence in Physics, CHE, Ministry of Education, 328 Si Ayutthaya Rd., Ratchathewi, Bangkok, 10400 Thailand Received January 19, 2010

Abstract—The impacts of pellet injection into ITER type-1 ELMy H-mode plasma with the presence of internal transport barriers (ITBs) are investigated using self-consistent core-edge simulations of 1.5D BAL-DUR integrated predictive modeling code. In these simulations, the plasma core transport is predicted using a combination of a semi-empirical Mixed B/gB anomalous transport model, which can self-consistently predict the formation of ITBs, and the NCLASS neoclassical model. For simplicity, it is assumed that toroidal velocity for $\omega_{E \times B}$ calculation is proportional to local ion temperature. In addition, the boundary conditions are predicted using the pedestal temperature model based on magnetic and flow shear stabilization width scaling; while the density of each plasma species, including both hydrogenic and impurity species, at the boundary are assumed to be a large fraction of its line averaged density. For the pellet's behaviors in the hot plasma, the Neutral Gas Shielding (NGS) model by Milora—Foster is used. It was found that the injection of pellet could result in further improvement of fusion performance from that of the formation of ITB. However, the impact of pellet injection is quite complicated. It is also found that the pellets cannot penetrate into a deep core of the plasma. The injection of the pellet results in a formation of density peak in the region close to the plasma edge. The injection of pellet can result in an improved nuclear fusion performance depending on the properties of pellet (i.e., increase up to 5% with a speed of 1 km/s and radius of 2 mm). A sensitivity analysis is carried out to determine the impact of pellet parameters, which are: the pellet radius, the pellet velocity, and the frequency of injection. The increase in the pellet radius and frequency were found to greatly improve the performance and effectiveness of fuelling. However, changing the velocity is observed to exert small

DOI: 10.1134/S1063780X11030081

1. INTRODUCTION

Magnetically confined thermonuclear fusion concept, such as tokamak, has long been explored as an environmentally-friendly and cheap source of energy. However, its scientific and technological feasibility has not been demonstrated. Therefore, an international project called "the International Thermonuclear Experimental Reactor (ITER)" has been initiated [1]. Of its particular interest is the high-confinement mode (H-mode) operation due to its great enhancement of plasma performance. The plasma performance in H-mode plasma can be further improved by a formation of internal transport barriers (ITBs) [2] due to a steepening of the temperature gradient in the plasma core profiles. In addition, an effective reactant fuelling method must be developed for ITER since ITER is expected to be the first tokamak able to confine fusion

Extensive theoretical and experimental investigation of pellet injection in high-temperature plasma has been carried out in recent years [6-13]. Once a pellet is injected into the hot plasma, it is exposed to the

pulse for approximately 1 h. In general, the plasma ¹ The article is published in the original.

fuelling can be achieved either by conventional gas puffing or by pellet injections [3]. Although the conventional gas puffing is a simple and somewhat effective method for plasma fuelling, it relies solely on the thermal and particle transports, which are often hindered in the plasma core. On the other hand, the pellet injection relies on the high momentum of frozen hydrogenic pellets to penetrate into the hot plasma. Therefore, pellet injection is considered a more efficient and effective fuelling scheme [4, 5]. Besides, the fuelling aspect, pellet injection can also be used to increase the peaking of the density profile to increase the nuclear fusion reaction rate [5]. As a result, it is crucial to investigate the interactions of pellet and ITB in H-mode plasma, especially impacts on fuelling and fusion performance.

energy fluxes from the energetic particles, resulting in the ablation of the pellet. The rate is determined by the energy flux available and the flux required to remove the particles from the pellet surface, dissociate, ionize and accelerate them [12]. The review of the study of pellet injection can be found in [6]. Although pellet injection in ITB plasma offers the potential for improved performance, it was unclear whether the ITB would survive the injection of frozen pellets [14]. Therefore, several experiments were designed to study pellet injection in ITB plasma. The experimental investigation of pellet injection in JET plasma with ITB are described in [15, 16]. It was found that pellet injection from the low-field neither penetrates deeply into the plasma nor alters the ITB. On the other hand, pellet injection from the high-field side could fuel the core plasma, but the ITB is destroyed in the process. Garzotti et al. [14] attempted to simulate the same event using JETTO, TRB, and CUTIE codes, each yielding different results. As plasma parameters of JET and ITER are fundamentally different, the interaction between pellet injection and ITB in JET may not necessarily translate to ITER. A preliminary simulation result of pellet injection in ITER-like cases with ITB may be found in [17], where it was found that ITB formation depends strongly on pellet penetration depth, but the ITB itself is not destroyed as is the case for JET plasmas.

The present study aims to study the impacts of pellet injection in type-I ELMy H-mode ITER plasma with ITB via self-consistent simulations using BAL-DUR integrated predictive modeling code. Note that a similar study of pellet injection in non-ITB ITER plasma using BALDUR code was described by Wisitsorasak and Onjun in [13]. In this work, the Neutral Gas Shielding (NGS) model by Milora–Foster [18] is incorporated to describe the dynamics of pellet injection. It is worth mentioning that the NGS model is not a complete pellet model since several effects, such as ∇B drift effects, are not included. However, it is believe that the combination of core transport and pellet model is sufficient to provide an inside understanding of impacts of the pellet on plasma with the presence of ITB. A series of deuterium pellets with the radius and velocity of 2.0 mm and 1 km/s are injected into the tokamak with the frequency of 0.5 Hz during the time from 1200 to 1220 s. The plasma core transport is described by a combination of the NCLASS neoclassical transport model [19] and the modified Mixed Bohm/gyro-Bohm (Mixed B/gB) anomalous core transport model with ITB effects included [20]. It is assumed in these simulations that the toroidal velocity for the electric field (as well as $\omega_{\mathbf{E} \times \mathbf{B}}$) calculation is proportional to the local ion temperature. This toroidal velocity assumption was validated against 10 optimized shear discharges from JET and the predictions vield reasonable agreement [21]. Note that the notations used in this paper can be found in Table 1. The pedestal temperature is given by one of the best pedes-

tal temperature model in [22], where the pedestal width based on the flow shear and magnetic shear width scaling [23] and the infinite-n ballooning mode limit pressure gradient model are used together. The density of each hydrogenic and impurity species at the top of the pedestal is described by a simple model, called a dynamic boundary density model that assumes the proportionality between the pedestal density of each specie and its line averaged density. Using the conditions above, the temperature and density profiles are obtained from the simulations. It should be noted that the impurity species considered in this work are helium and beryllium. A parametric sensitivity analysis is also carried out to determine the impact of altering fundamental pellet parameters, i.e., the pellet radius, the pellet velocity, and the frequency of injec-

This paper is organized as follows: brief descriptions of relevant components of the BALDUR code, including the Milora—Foster pellet model, the ITB model, and the pedestal model, are given in Section 2; the predictions of ITER plasma profiles for standard type-I ELMy H-mode are presented and discussed in Section 3; the parametric sensitivity analysis is found in Section 4; and a summary is given in Section 5.

2. BALDUR INTEGRATED PREDICTIVE MODELING CODE

The BALDUR integrated predictive modeling code [24] is a 1.5-dimensional modeling code that solves time-dependent plasma profiles along the radial direction and the flux surfaces. Various physical processes are incorporated into the code to self-consistently solve for electron and ion temperatures, deuterium and tritium densities, helium and impurity densities, safety factor, neutrals, and fast ions. The models incorporated into the code include transport, plasma heating, helium influx, boundary conditions, plasma equilibrium shape, sawtooth oscillations, pedestal model, and internal transport barrier. In this study, the Milora-Foster pellet model is also included. Simulation results obtained from BALDUR code have previously been compared with experimental data, yielding an overall agreement of approximately 10% relative RMS deviation [25, 26].

2.1. NGS Pellet Model

In this work, The Neutral Gas Shielding (NGS) module developed by Milora and Foster [18] is used to describe the behavior of the pellet in the plasma. This pellet model assumes that frozen pellets are injected from the low-field side of a tokamak and are embedded in the homogeneous plasma with unlimited energy reservoir. Once the pellets are embedded in the plasma, energetic particle flux at the pellets' surface triggers the ablation process, whose rate depends on the flux. The ablation causes an expanding, spherically

Table 1. Notations used in this paper

Symbol	Units	Description	Symbol	Units	Description
\dot{r}_p		Pellet surface erosion rate	q		Safety factor
r_p	mm	Effective initial pellet radius	S		Magnetic shear
A_p		Ablatant atomic number	$\omega_{\mathbf{E} \times \mathbf{B}}$		Shearing rate
n_m	m ⁻³	Molecular density of solid hydrogen	$\gamma_{ ext{ITG}} \ W_{ ext{tot,avg}}$	MJ	Linear growth rate Averaged stored plasma energy
R	m	Major radius	E_r		Radial electric field
r	m	Minor radius	Ψ		Poloidal flux
ρ		Normalized minor radius	$V_{ m th}$	m/s	Electron thermal velocity
ρ_s		Ion gyro-radius	v_{θ}	m/s	Poloidal velocity
χ^{B}	m ² /s	Thermal transport coefficient with Bohm scaling	Z e		Ion charge number Elementary charge
χ^{gB}	m ² /s	Thermal transport coefficient with gyro-Bohm scaling	p_i	Pa Pa	Ion pressure Plasma pressure
χ^i	m ² /s	Ion thermal transport coefficient	I_p	MA	Plasma current
χ^e	m ² /s	Electron thermal transport coefficient	α_c		Normalized critical pressure gradient of ballooning mode
$D_{ m H}$	m ² /s	Hydrogenic particle transport coefficient	$Z_{ m eff, edge} \ P_{lpha, m avg}$	MW	Edge effective charge Averaged α-heating power
$D_{\rm Z}$	m ² /s	Impurity particle transport coefficient	$P_{lpha, ext{total}} \ P_{ m aux}$	MW MW	Total α-heating power Auxiliary heating power
B_{T}	Tesla	Vacuum toroidal magnetic field at R	n_1 n_{ped}	$\begin{array}{c} 10^{20} \mathrm{m}^{-3} \\ 10^{20} \mathrm{m}^{-3} \end{array}$	Line-averaged density Pedestal density
B_{Θ}	Tesla	Poloidal magnetic field	n_i	$10^{19}\mathrm{m}^{-3}$	Ion density
B_{ϕ}	Tesla	Toroidal magnetic field	n_e	$10^{19}\mathrm{m}^{-3}$	Electron density
δ_{95}		Plasma triangularity at 95% flux surface	n_D n_T	$10^{19} \mathrm{m}^{-3} \\ 10^{19} \mathrm{m}^{-3}$	Deuterium density Tritium density
κ_{95}		Plasma elongation at 95% flux surface	n_{He} n_{Be}	$ \begin{array}{c c} 10^{18} \text{ m}^{-3} \\ 10^{18} \text{ m}^{-3} \end{array} $	Helium density Beryllium density
T_i	keV	Ion temperature	Subscript	1 -	ı
T_e	keV	Electron temperature	0		Centre
a	m	Plasma minor radius	ped		Pedestal

symmetric neutral cloud that is subsequently ionized [27]. As the neutral cloud is bombarded by energetic particles such as background electrons and ions, and neutral particles from neutral beam injection (NBI) heating, the expressions that define the heat deposition in the cloud is integrated into the usual hydrodynamic conservation equations for mass, momentum, and energy [12]. A simplified expression for the pellet surface erosion rate (\dot{r}_p) is given by Houlberg et al. [28] as

$$\dot{r}_p \equiv \frac{dr_p}{dt} \propto \frac{n_e^{1/3} T_e^{5/3}}{A_p^{1/3} n_m r_p^{2/3}},\tag{1}$$

where r_p is the effective spherical pellet radius, n_m is the molecular density of solid hydrogen, A_p is the atomic mass number of the ablatant, n_e is the background plasma electron density, and T_e is the background electron density. The value of n_m can be calculated by the expression

$$n_m = 2.12 \times 10^{28} + 6.30 \times 10^{27} A_p - 8.66 \times 10^{26} A_p^2$$
. (2)

It is worth noting that the Milora—Foster pellet model tends to give lower ablation rate and, therefore, deeper penetration depth than that observed in experiment or contemporary theories.

2.2. ITB Model

Internal transport barrier is defined as the region in the core plasma where anomalous transport is reduced or quenched, resulting in the steepening of the central plasma profiles [2]. Although the physics of ITB formation is not fully understood, various models have been proposed to explain this phenomenon. In the present study, the ITB model based on the $\omega_{E\times B}$ shear and magnetic shear concept [29, 30] is incorporated into BALDUR code via the modification of the empirical Mixed B/gB core transport model [20].

Initially, the Mixed B/gB core transport model was a local transport model with Bohm scaling, where the transport fluxes depend entirely on local plasma properties and the transport diffusivities are proportional to the gyro-radius multiplied by thermal velocity over a plasma linear dimension such as major radius. The model was originally developed to describe electron transport for JET plasmas [31], and was later extended to describe the ion transport [32]. A gyro-Bohm term, with transport diffusivities that are proportional to the square of the gyro-radius multiplied by thermal velocity over the square of the plasma linear dimension, was added in order to improve predictions of plasmas in smaller and larger tokamaks [33]. For ITER, the Bohm term normally provides a larger contribution than the gyro-Bohm term, which normally exhibits a large contribution in the deep core of the plasma and plays a significant role only in smaller tokamaks with relatively low power and magnetic field.

In the ITB model described in [20], the conventional Bohm term is multiplied by a step function, which is set as zero when the condition is favorable for ITB formation. Hence, the Bohm term is effectively switched off. The expressions for the Bohm and gyro-Bohm terms are

$$\chi^{B} = \left\{ 4 \times 10^{-5} R \left| \frac{\nabla (n_{e} T_{e})}{n_{e} B_{T}} \right| q^{2} \left[\frac{T_{e, \rho=0.8} - T_{e, \rho=1.0}}{T_{e, \rho=1.0}} \right] \right\} \times \Theta \left(-0.14 + s - \frac{1.47 \omega_{E \times B}}{\gamma_{ITG}} \right),$$
(3)

$$\chi^{\rm gB} = 5 \times 10^{-6} \sqrt{T_e} \left| \frac{\nabla T_e}{B_{\rm r}^2} \right|,$$
(4)

respectively. Note that R is the major radius, B_T is the toroidal magnetic field, q is the safety factor, ρ is the normalized minor radius, s is the magnetic shear, γ_{ITG} is the linear growth rate, and $\omega_{E\times B}$ is the shearing rate. The value of γ_{ITG} is calculated by

$$\gamma_{\rm ITG} = \frac{V_{\rm th}}{aR},\tag{5}$$

where v_{th} is the electron thermal velocity. The value of $\omega_{E \times B}$ shearing rate is determined by the Hahm–Burrell model [34, 35] as

$$\omega_{\mathbf{E} \times \mathbf{B}} = \left| \frac{RB_{\theta}^{2}}{B_{T}} \frac{\partial \left(E_{r} / RB_{\theta} \right)}{\partial \Psi} \right|. \tag{6}$$

Here, B_{θ} is the poloidal magnetic field, ψ is the poloidal flux, and E_r is the radial electric field, which can be calculated by

$$E_r = \frac{1}{Zen_i} \frac{\partial p_i}{\partial r} - v_{\theta} B_{\mathsf{T}} + v_{\mathsf{tor}} B_{\theta}, \tag{7}$$

where $\partial p_i/\partial r$ is the pressure gradient, v_{θ} is the poloidal velocity, v_{tor} is the toroidal velocity, n_i is the ion density, Z is the ion charge number, and e is the elementary charge. The toroidal velocity is calculated by an empirical model that assumes proportionality between the toroidal velocity and the ion temperature [36]. The expression of v_{tor} is

$$v_{\text{tor}}[\text{m/s}] = 7.0719 \times 10^3 T_i \text{ [keV]}.$$
 (8)

Note that the constant in Eq. (8) is chosen to optimize the agreement between experimental toroidal velocity and ion temperature for two JET optimized shear discharges 40542 and 40847. From the Bohm and gyro-Bohm contribution terms, the ion (χ_i) and electron (χ_e) thermal diffusivities, and hydrogenic (D_H) and impurity (D_T) particle diffusivities can be calculated as

$$\chi_e = 1.0\chi^{gB} + 2.0\chi^B$$
, (9)

$$\chi_i = 0.5\chi^{gB} + 4.0\chi^{B}, \tag{10}$$

$$D_{\rm H} = D_{\rm Z} = (0.3 + 0.7 \rho) \frac{\chi_e \chi_i}{\chi_e + \chi_i} . \tag{11}$$

2.3. Pedestal Model

In the present work, the pedestal temperature model described in [22] is used. In this model, the temperature at the top of the pedestal can be estimated from the pedestal width (Δ) and the pressure gradient ($\partial p/\partial r$) as

$$T_{\text{ped}} = \frac{1}{2kn_{\text{ped}}} \left| \frac{\partial p}{\partial r} \Delta \right| = \frac{\Delta}{2k_{\text{b}}n_{\text{ped}}} \frac{\alpha_c B_{\text{T}}^2}{2\mu_0 R q^2},$$
 (12)

where k_b is the Boltzmann constant. The pedestal width can be calculated based on the magnetic and flow shear stabilization width scaling ($\Delta \propto \rho_s s^2$). As a result, one can calculate the pedestal temperature as

$$T_{\text{ped}} [\text{keV}] = 0.323 C_w^2 \left(\frac{B_T}{q^2}\right)^2 \left(\frac{A_H}{R^2}\right) \left(\frac{\alpha_c}{n_{\text{ped},19}}\right)^2 s^4.$$
 (13)

Note that the value of C_w was found to be 2.42 in [22].

These pedestal temperature models yield satisfactory agreement with the pedestal data from the ITPA Pedestal Database. The pedestal width constant in each model was chosen to minimize the RMS deviation with 533 experimental data points from four large tokamaks obtained from the International Tokamak Physics Activity (ITPA) pedestal database. In this study, the magnetic and flow shear stabilization width scaling with the pedestal with constant in [22] is used. As the pedestal pressure gradient calculation is normally complicated and requires detailed inputs, the pedestal gradient is assumed to be uniform throughout the pedestal region and the pedestal gradient is limited by the first stability limit of infinite *n* ballooning mode, so that the normalized critical pressure gradient for the pedestal region is estimated as

$$\alpha_{c} = -\frac{2\mu_{0}Rq^{2}}{B_{\phi}^{2}} \left(\frac{\partial p}{\partial r}\right)_{c} = 0.4s \left[1 + \kappa_{95}^{2} \left(1 + 5\delta_{95}^{2}\right)\right], \quad (14)$$

where κ_{95} is the elongation at the 95% flux surface, and δ_{95} is the triangularity at the 95% flux surface.

These pedestal temperature models include the effect of edge bootstrap current, which has an impact on magnetic shear and safety factor. This inclusion results in a nonlinear behavior in the pedestal temperature model. The scheme to deal with the approximation of magnetic shear and safety factor for the pedestal prediction using the pedestal models was completely described in [22]. Therefore, the values of magnetic shear and safety factor for the pedestal calculation are different from their values in other parts of the BALDUR code, which are based on a simpler calculation. The attempt to use a self-consistent safety factor and magnetic shear for all calculations in BAL-

DUR code is under development. A preliminary result can be seen in [37]. In addition, there are several new approaches to estimate the pedestal value, such as the pedestal scaling by M. Sugihara [38], which predicted the pedestal temperature of about 5.6 keV.

The pedestal density of a plasma species j is described by a simple empirical model that assumes proportionality between the pedestal density of that species $(n_{j, \text{ped}})$ and its line averaged density (\overline{n}_{j}) ,

$$n_{i,\text{ped}} = 0.71\overline{n}_i. \tag{15}$$

Hence, the pedestal electron density n_{ped} can be calculated by taking the summation of the product of density of each species and its charge (Z_i) ,

$$n_{\text{ped}} = \sum Z_j n_{j,\text{ped}}.$$
 (16)

The present pedestal model is modified from the empirical model developed in [38], which gives the pedestal density in term of the electron line average density (n_1) as

$$n_{\rm ped} = 0.71n_1. {(17)}$$

The model described in Eq. (16) was compared with the pedestal data obtained from the ITPA pedestal database with 12% RMSE [39]. Note that in this work, the edge effective charge ($Z_{\rm eff,\,edge}$) is determined from the pedestal density of each species. As a result, the edge effective charge is varied, depending on the plasma conditions.

3. SIMULATION RESULTS AND DISCUSSION

The simulations are carried out using the 1.5D BALDUR integrated predictive modeling code. Physical parameters are chosen to match those of type-I ELMy H-mode ITER discharges ($R = 6.2 \text{ m}, a = 2.0 \text{ m}, I_p = 15 \text{ MA}, B_T = 5.3 \text{ T}, \kappa_{95} = 1.7, \delta_{95} = 0.33,$ and $n_1 = 10^{20} \text{ m}^{-3}$). The total auxiliary heating power used is 40 MW. The heating power is delivered by a combination of NBI, which provides 33 MW, and RF heating. The plasma current and density are slowly ramped up to the target values within the first 100 s of the simulations. During the start-up phase, the initial plasma current is set at 3 MA, and the plasma current is slowly increased to the target value of 15 MA. The formation of ITB is introduced in the simulation via the modification of the anomalous transport, which is described by a modified Mixed B/gB core transport model [20]. The anomalous transport contribution is combined with the NCLASS neoclassical transport model [19] to describe the transport in the core plasma, whereas the dynamics of pellet injection is described by the Milora-Foster pellet model [18]. In this study, only the deuterium pellets are considered. It is assumed that four plasma species exist: deuterium, tritium, helium, and beryllium. The boundary condi-

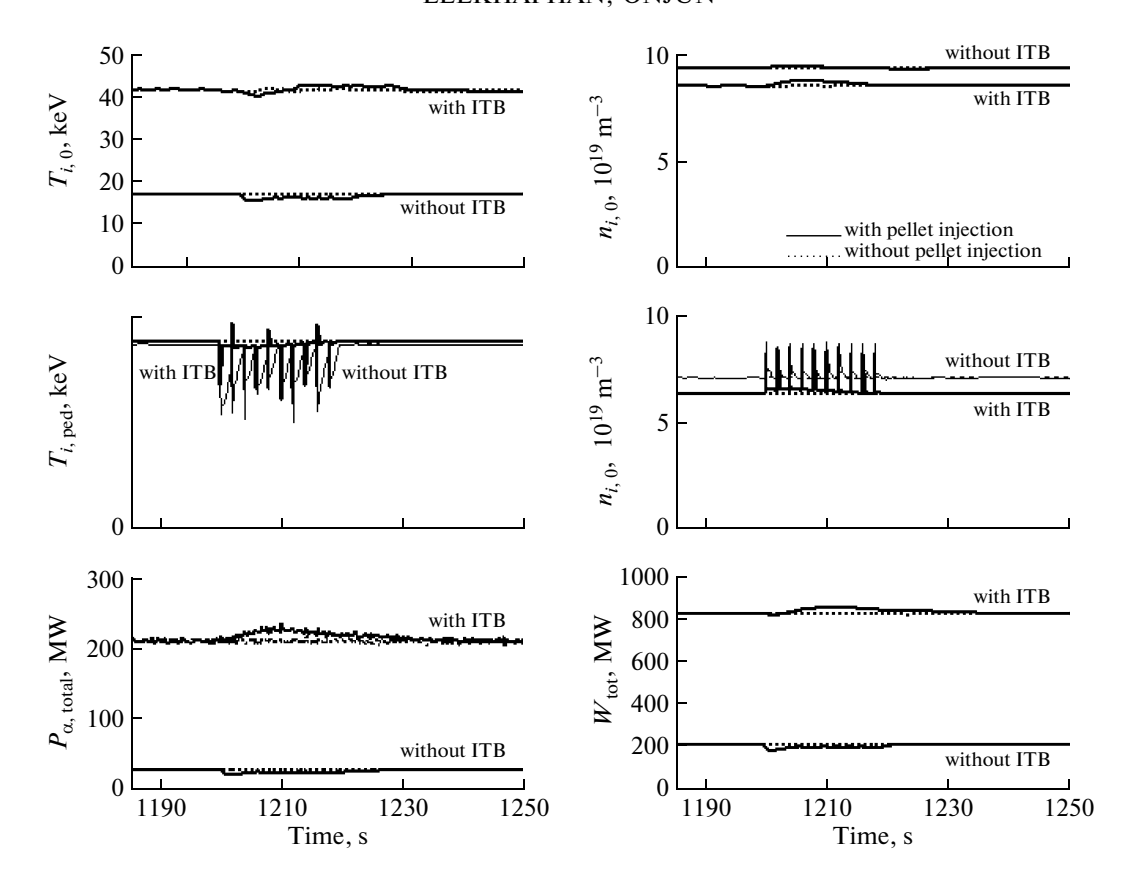


Fig. 1. Time evolution of the central ion temperature $(T_{i,\,0})$ and density $(n_{i,\,0})$, pedestal ion temperature $(T_{i,\,\text{ped}})$ and density $(n_{i,\,\text{ped}})$, total α -heating power $(P_{\alpha,\,\text{total}})$, and plasma stored energy (W_{tot}) . The values are obtained from simulations using the Mixed B/gB core transport model coupled with the Milora–Foster pellet ablation model, the pedestal model based on flow shear and magnetic shear stabilization width scaling, and, wherever applicable, the ITB model. The pellet velocity, radius, and injection frequency used are 1 km/s, 2 mm, and 0.5 Hz, respectively.

tion is provided at the top of the pedestal by the pedestal model developed in [22], with the pedestal width scaling based on flow shear and magnetic shear stabilization [23]. In the present BALDUR code, it is assumed that the ion and electron temperatures at the pedestal are equal. However, it has been observed in many experiments that ion temperature is higher than electron temperature at the pedestal in low density plasma. As ITER plasma is high density plasma, the assumption of temperature equality in BALDUR code is expected to be valid. Previous ITER simulations using the JETTO code in [40] gave electron and ion temperatures at the top of the pedestal of 4.4 and 4.9 keV, respectively. The assumption of equal ion and electron temperature employed by BALDUR code has been used to simulate present-day H-mode experiments, with 10% RMS deviation from the experimental data [39]. Although the present simulations do not represent the complete ITER plasma dynamics as they do not include several physical processes such as ELM crashes, neoclassical tearing modes and sawtooth crashes, it would be interesting to determine the

combined effects of ITB, ETB, transport, heating, and pellet injection included in the simulations.

In the present study, a series of deuterium pellets with radius of 2 mm are injected at the velocity of 1 km/s and the frequency of 0.5 Hz, from 1200 to 1220 s. Note that the pellet radius of 2 mm is considered as a small pellet. The expected pellet in ITER is in the range of 4 or 5 mm. The effect of varying the pellet parameters will be discussed in Section 4. In this section, the simulation results from 4 scenarios are presented: simulation without ITB and pellets, simulation with pellet but without ITB, simulation with ITB but without pellets, and simulation with both ITB and pellets. It is worth noting that when the pellet is not used, the plasma density is maintained by conventional gas puffing.

Figure 1 shows the time evolution of central ion temperature $(T_{i,\,0})$ and density $(n_{i,\,0})$, pedestal ion temperature $(T_{i,\,\mathrm{ped}})$ and density $(n_{i,\,\mathrm{ped}})$, total α -heating power $(P_{\alpha,\,\mathrm{total}})$ and plasma stored energy (W_{tot}) obtained from simulations for four scenarios of ITER described previously. It can be seen that the inclusion

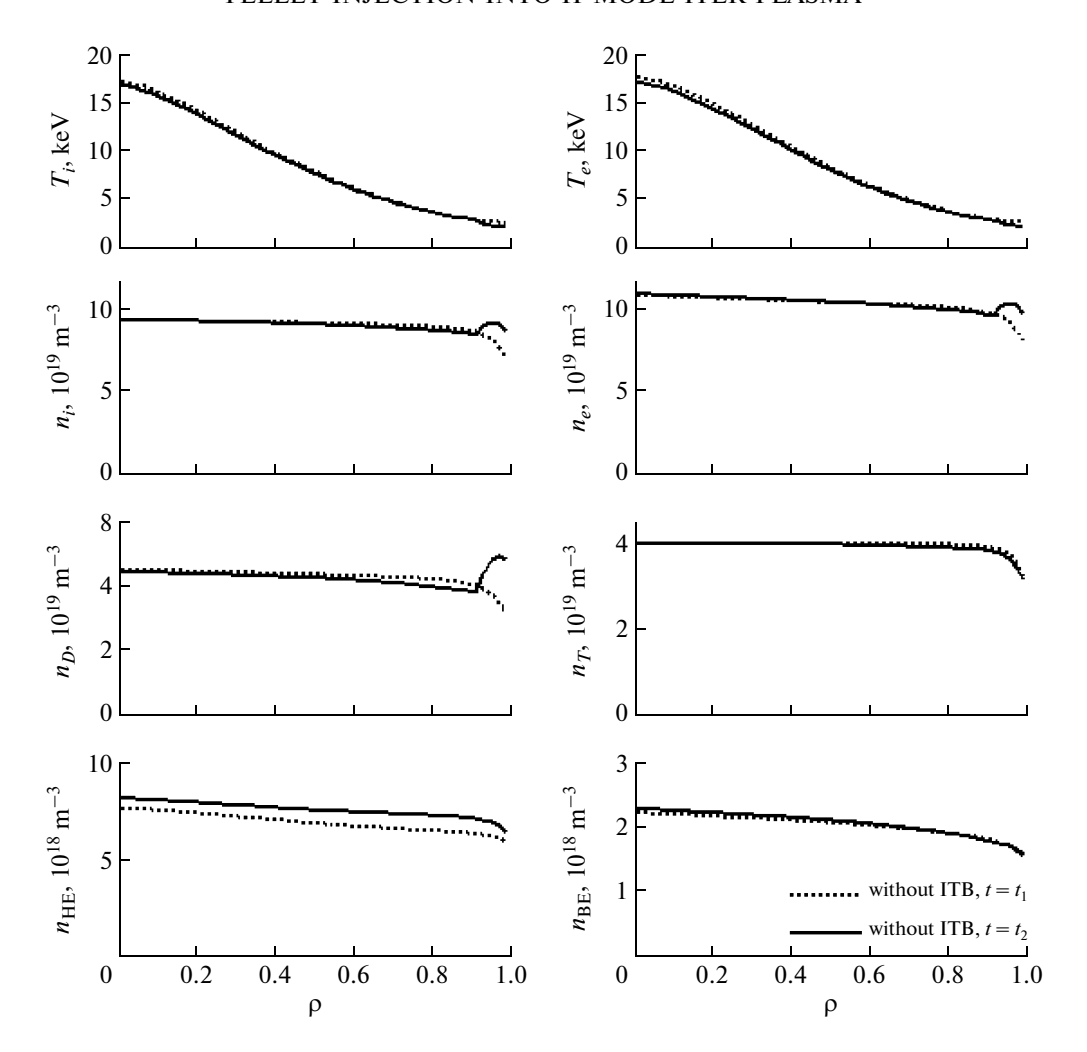


Fig. 2. Temperature and density profiles at the time before and after pellet injection obtained from simulations using the Mixed B/gB core transport model coupled with Milora—Foster pellet ablation model and pedestal model based on flow shear and magnetic shear stabilization width scaling. The formation of ITB is not included in this simulation. The pellet velocity, radius, and injection frequency used are 1 km/s, 2 mm, and 0.5 Hz, respectively.

of ITB brings about significant increase in $T_{i,0}$, leading to increased W_{tot} and $P_{\alpha,\,\mathrm{total}}$ as reported in the previous studied using BALDUR code by T. Onjun et al. [41]. On the contrary, the values of $n_{i,0}$ and $n_{i,ped}$ show a slight decrease, whereas the values of $T_{i, ped}$ show almost no change. It is worth mentioning here that the inclusion of ITB has a small impact on the electron pedestal density. As a result, the pedestal temperature reminds almost the same. Injection of deuterium pellets into non-ITB plasma causes the values of $T_{i,0}$, and thus $P_{\alpha, \text{ total}}$, to drop. The values of $T_{i, \text{ ped}}$ and $n_{i, \text{ ped}}$ spikes downward and upward, respectively, at the times that the pellets are injected, while the values of $n_{i,0}$ and n_1 remain almost unchanged. On the other hand, the injection of deuterium pellets into ITB plasma causes the $T_{i,0}$ to initially drop. The value later increases, resulting in improved $P_{\alpha, \text{total}}$. The initial drop in $T_{i,0}$ corresponds to the initial rise in the value

of $n_{i,\,0}$. Similarly, the values of $T_{i,\,\mathrm{ped}}$ and $n_{i,\,\mathrm{ped}}$ spikes downward and upward, respectively, at the times that the pellets are injected, although the recovery after each spike seems more efficient in ITB plasma. Apart from the time evolution of plasma properties, the plasma profiles as functions of normalized minor radius will be examined at times before $(t=t_1=1190~\mathrm{s})$ and during $(t=t_1=1210~\mathrm{s})$ pellet injection.

The profiles of the ion (T_i) and electron (T_e) temperatures, and ion (n_i) , electron (n_e) , deuterium (n_D) , tritium (n_T) , helium (n_{He}) and beryllium (n_{Be}) densities obtained from simulations without considering the effect of ITB are presented in Fig. 2. The values are obtained at times t_1 and t_2 . It can be seen that, when pellets are injected into the plasma, the ion and electron temperatures drop slightly at the edge. This is not surprising as energy is transferred to the pellet for ablation. As deuterium pellets are injected from the edge,

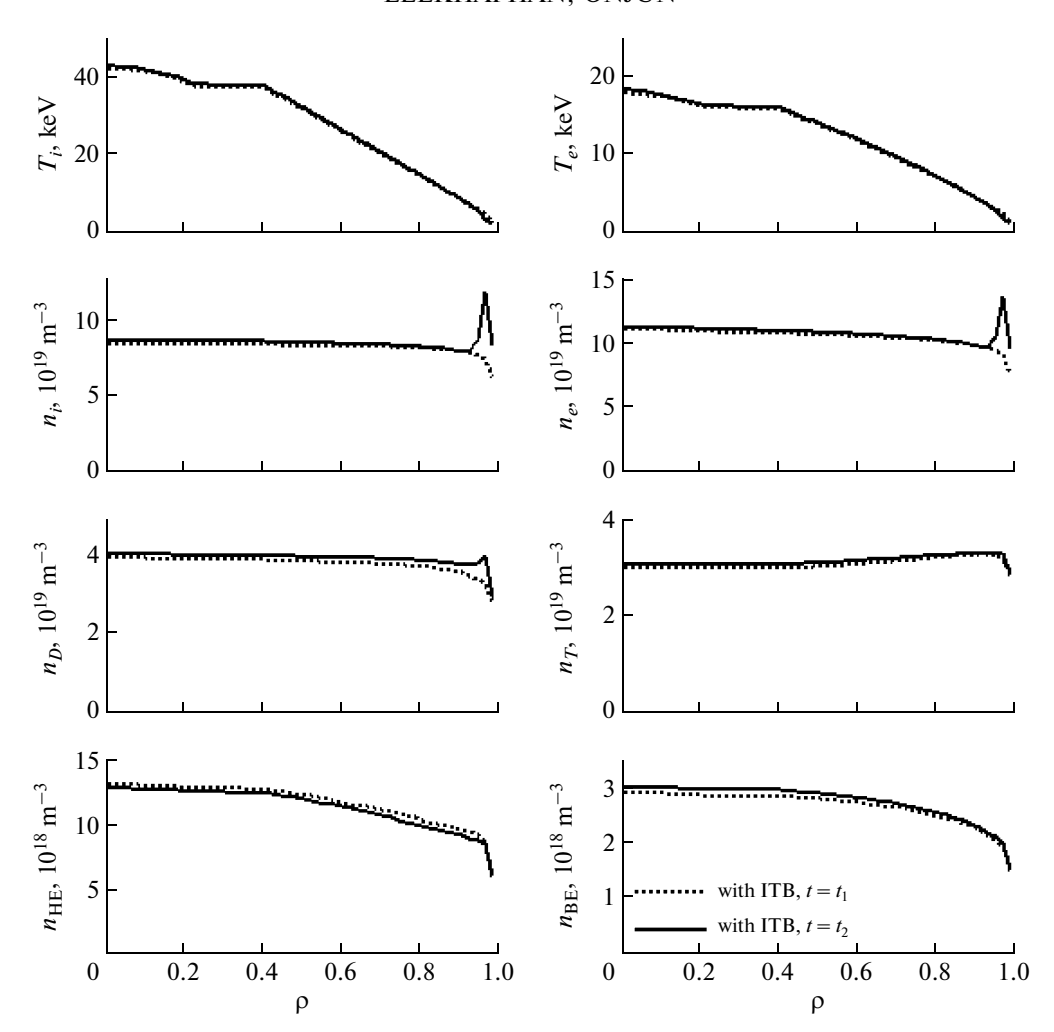


Fig. 3. Temperature and density profiles at the time before and after pellet injection obtained from simulations using the Mixed B/gB core transport model coupled with the Milora—Foster pellet ablation model and pedestal model based on flow shear and magnetic shear stabilization width scaling. The formation of ITB is included in this simulation. The pellet velocity, radius, and injection frequency used are 1 km/s, 2 mm, and 0.5 Hz, respectively.

the deuterium, ion, and electron densities at the edge would be expected to increase greatly during the injection. This is consistent with the simulation result. However, it is observed that the density of tritium at the edge decreases slightly, owing to slightly increased $D_{\rm H}$ upon pellet injection. Also, the density of helium rises significantly, whereas the density of beryllium shows a marginal increase. The behavior of the impurity species is consistent with the pellet injection simulation using MMM95 core transport model in [13].

The plasma profiles obtained from simulations with ITB are shown in Fig. 3. The formation of ITB brings about a significant increase in ion and electron temperatures, as well as the densities of helium and beryllium. However, the ion and deuterium densities show slight decreases, while the tritium density shows a larger drop. The electron temperature is almost unchanged when the ITB is included; this could be

due to the fact that the Bohm term, which is set to zero when ITB forms, contributes less to T_e than to T_i . Upon the injection of deuterium pellets into the ITB plasma, the edge ion and electron temperature decrease slightly, whereas the core values increase slightly. As is the case with a non-ITB plasma, the edge density of ion, electron and deuterium greatly increases due to the injection of deuterium pellets. The densities of tritium and beryllium increase marginally, while the helium density decreases slightly. It is worth mentioning that there is a flat temperature region between $\rho = 0.2$ to 0.4. This is probably due to the calculation of transport coefficient by Mixed B/gB model. This issue will be investigated further in the future work.

The summary of averaged ion and electron temperatures, deuterium and tritium densities, the stored plasma energy, α -heating power, and Q_{fusion} obtained

Table 2. Summary of averaged ion temperature, electron temperature, deuterium density and tritium density at the plasma center and at the top of the pedestal, as well as the stored plasma energy, α -heating power, and $Q_{\rm fusion}$, are shown before and during deuterium pellet injection. The values are obtained from simulations with and without including the effect of ITB. The pellet radius, velocity, and injection frequency used are 2.0 mm, 1.0 km/s, and 0.5 Hz, respectively

Parameters Without ITB With ITB $T_{i,0}$, keV Before 17.127 41.292 During 16.127 41.590 % change -5.840.72 $T_{e,0}$, keV Before 17.695 35.473 During 16.747 35.813 % change -5.360.96 D_0 , 10^{19} m⁻³ Before 4.343 3.951 4.399 4.062 During % change 1.29 2.81 T_0 , 10^{19} m⁻³ Before 4.005 2.925 During 3.900 2.988 % change -2.622.15 $T_{i, \text{ ped}}$, keV Before 2.574 2.610 During 2.201 2.533 -2.95% change -14.49 $T_{e. \text{ ped}}$, keV Before 2.597 2.662 During 2.330 2.591 % change -10.28-2.67 $n_{\rm D, ped}$, $10^{19} \, \rm m^{-3}$ Before 3.133 2.779 During 3.274 2.950 % change 4.50 6.15 $n_{\rm T, ped}$, $10^{19} \, \rm m^{-3}$ Before 3.174 2.778 During 3.154 2.836 % change -0.632.09 Before 212.7 $W_{\text{tot, avg}}$, MJ 818.3 196.3 During 837.8 % change -7.712.38 28.6 $P_{\alpha,\text{avg}}$, MW Before 211.0 During 24.2 222.5 % change -15.385.45 $Q_{\rm fusion}$ Before 3.58 26.38 During 3.03 27.81 % change -15.365.42

Table 3. Summary of averaged ion temperature, electron temperature, deuterium density, and tritium density at the plasma center and at the top of the pedestal, as well as the stored plasma energy, α -heating power, and $Q_{\rm fusion}$, are shown before and during deuterium pellet injection. The values are obtained from simulations with the pellet velocity and injection frequency of 1.0 km/s and 0.5 Hz, respectively. The pellet radii used are 1.5, 2.0, and 2.5 mm. The formation of ITB is included in these simulations

Paramet	orc .	Pelle	et radius (1	mm)
raiamet	CIS	1.5	2.0	2.5
$T_{i,0}$, keV	Before	41.292	41.292	41.292
	During	41.681	41.590	40.539
	% change	0.94	0.72	-1.82
$T_{e,0}$, keV	Before	35.473	35.473	35.473
	During	35.787	35.813	35.679
	% change	0.89	0.96	0.58
D_0 , 10^{19} m ⁻³	Before	3.951	3.951	3.951
	During	3.992	4.062	4.546
	% change	1.04	2.81	15.06
T_0 , 10^{19}m^{-3}	Before	2.925	2.925	2.925
	During	2.948	2.988	3.291
	% change	0.79	2.15	12.51
$T_{i, \text{ ped}}, \text{keV}$	Before	2.610	2.610	2.610
	During	2.586	2.533	2.493
	% change	-0.92	-2.95	-4.48
$T_{e, \text{ ped}}$, keV	Before	2.662	2.662	2.662
*	During	2.642	2.591	2.581
	% change	-0.75	-2.67	-3.04
$n_{\rm D, ped}$, $10^{19} \rm m^{-3}$	Before	2.779	2.779	2.779
•	During	2.854	2.950	3.423
	% change	2.70	6.15	23.17
$n_{\rm T, ped}$, $10^{19} \rm m^{-3}$	Before	2.778	2.778	2.778
•	During	2.778	2.836	3.237
	% change	0	2.09	16.52
$W_{\text{tot, avg}}$, MJ	Before	818.3	818.3	818.3
, 0	During	827.5	837.8	914.5
	% change	1.12	2.38	11.76
$P_{\alpha,\text{avg}}$, MW	Before	211.0	211.0	211.0
, 0	During	216.9	222.5	272.3
	% change	2.80	5.45	29.05
$Q_{ m fusion}$	Before	26.38	26.38	26.38
	During	27.11	27.81	34.04
	% change	2.77	5.42	29.04

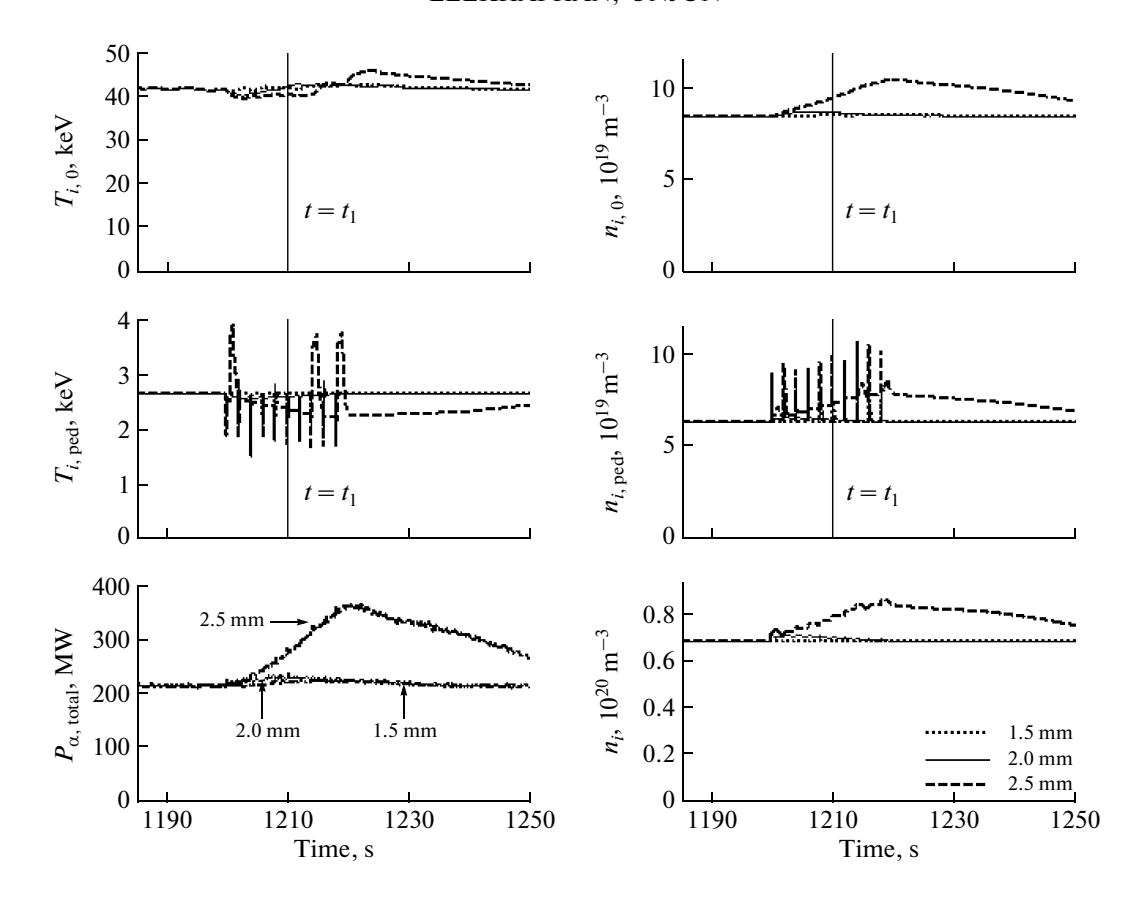


Fig. 4. Time evolution of the central ion temperature $(T_{i,\,0})$ and density $(n_{i,\,0})$, pedestal ion temperature $(T_{i,\,\text{ped}})$ and density $(n_{i,\,\text{ped}})$, total α -heating power $(P_{\alpha,\,\text{total}})$, and line-averaged density (n_{l}) . The values are obtained from simulations using the Mixed B/gB core transport model coupled with the ITB model, the Milora—Foster pellet ablation model, and the pedestal model based on flow shear and magnetic shear stabilization width scaling. The pellet velocity and injection frequency used are 1.0 km/s and 0.5 Hz, whereas the pellet radii of 1.5, 2.0, and 2.5 mm are used.

from simulations before and during the pellet injection is presented in Table 2. The values before pellet injection are averaged over the times 1190 to 1200 s, whereas the values obtained during pellet injection are averaged over the times 1200 to 1220 s. In this paper, $Q_{\rm fusion}$ is calculated by taking

$$Q_{\text{fusion}} = \frac{5 \times P_{\alpha,\text{avg}}}{P_{\text{aux}}}.$$
 (18)

It is obvious from Table 2 that the response of non-ITB and ITB plasma to deuterium pellet injection varies greatly. In non-ITB plasma, when deuterium pellets are injected, the central ion and electron temperatures and the central and pedestal tritium density drop, whereas the values increase in ITB plasma. The central and edge densities of deuterium increase in both cases, but the rise is more pronounced in an ITB plasma. Also, injection of pellets into a non-ITB plasma causes the averaged stored plasma energy, α -heating power, and $Q_{\rm fusion}$ to drop significantly, whereas injection in ITB plasma increase the values slightly. From this data, it can be said that injection of

deuterium pellets into ITB plasma improves the performance much more than injection into non-ITB plasma.

4. SENSITIVITY STUDY

In this section, the parametric sensitivity of BAL-DUR simulation results is investigated. The effects of varying the pellet parameters, i.e., the pellet radius, the pellet velocity, and the frequency of pellet injection, are studied and discussed in Sections 4.1 to 4.3, respectively. Note that in this section, only the cases with ITB will be considered.

4.1. Effects of Varying the Pellet Radius

The pellet radius is easily adjusted during the pellet shaping process. Therefore, the investigation of the effects of varying the pellet radius would be desirable, as it could offer a convenient method to improve the tokamak performance. The simulation results obtained using the pellet radius of 1.5, 2.0, and 2.5 mm are discussed in this section.

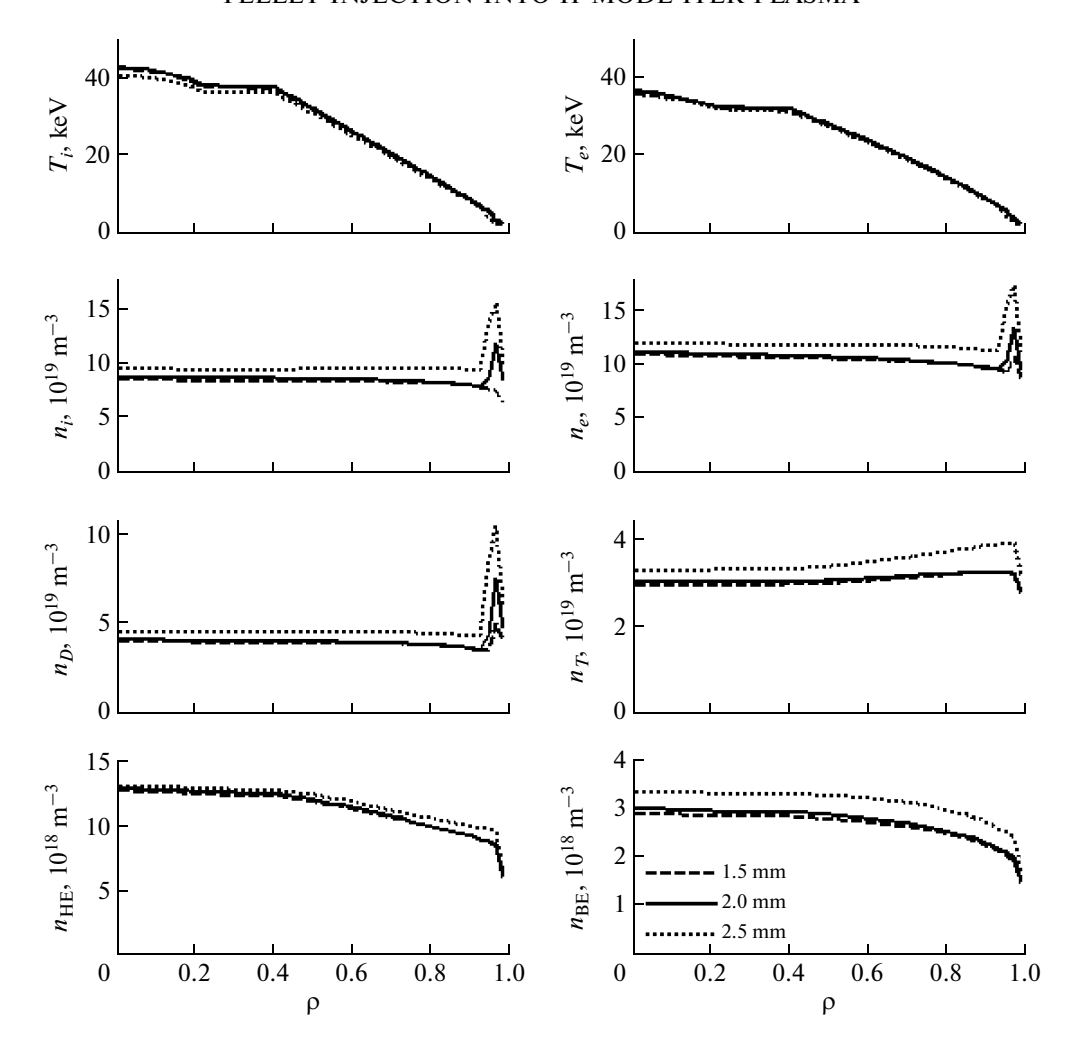


Fig. 5. Temperature and density profiles obtained from simulations using the Mixed B/gB core transport model coupled with the ITB model, the Milora—Foster pellet ablation model, and the pedestal model based on flow shear and magnetic shear stabilization width scaling. The values are taken at time t_1 (see Fig. 4). The pellet velocity and injection frequency used are 1.0 km/s and 0.5 Hz, whereas the pellet radii of 1.5, 2.0, and 2.5 mm are used.

The time evolution of the central and pedestal ion temperatures and densities, as well as total α -heating power and line-averaged density are presented in Fig. 4. It is found that, when larger pellet radius is used, the central and pedestal ion densities, as well as line-averaged density increase. The change observed is most pronounced when comparing the results between the pellet radius of 2.0 and 2.5 mm. This could be due to the fact that the transport is not fast enough to control the plasma density when excessive amount of deuterium is introduced. The increase in density leads to greatly increased total α -heating power, and hence, increased $T_{i,0}$. The results indicate that using pellets with larger radius may hold the key to improved performance and fuelling in ITER. Note that the structure of ITB is not altered, as the change in temperature is not significant.

The plasma profiles as functions of normalized minor radius at the time t_1 (see Fig. 4) can be found in Fig. 5. As the volume of the hydrogenic species injected into the plasma depends strongly on the pellet radius, it is expected that the density of ion, electron and deuterium would rise upon increasing the pellet radius, especially at the edge. This trend is observed in the simulation result. Also, the density of tritium, helium and beryllium are observed to increase. This could be due to increased line-averaged density, which causes the density of each species to rise. The summary of averaged ion and electron temperatures, deuterium and tritium densities, the stored plasma energy, α -heating power, and $Q_{\rm fusion}$ obtained from simulations before and during pellet injection is presented in Table 3. The values before pellet injection are averaged over the times 1190 to 1200 s, whereas the values obtained during pellet injection are averaged over the

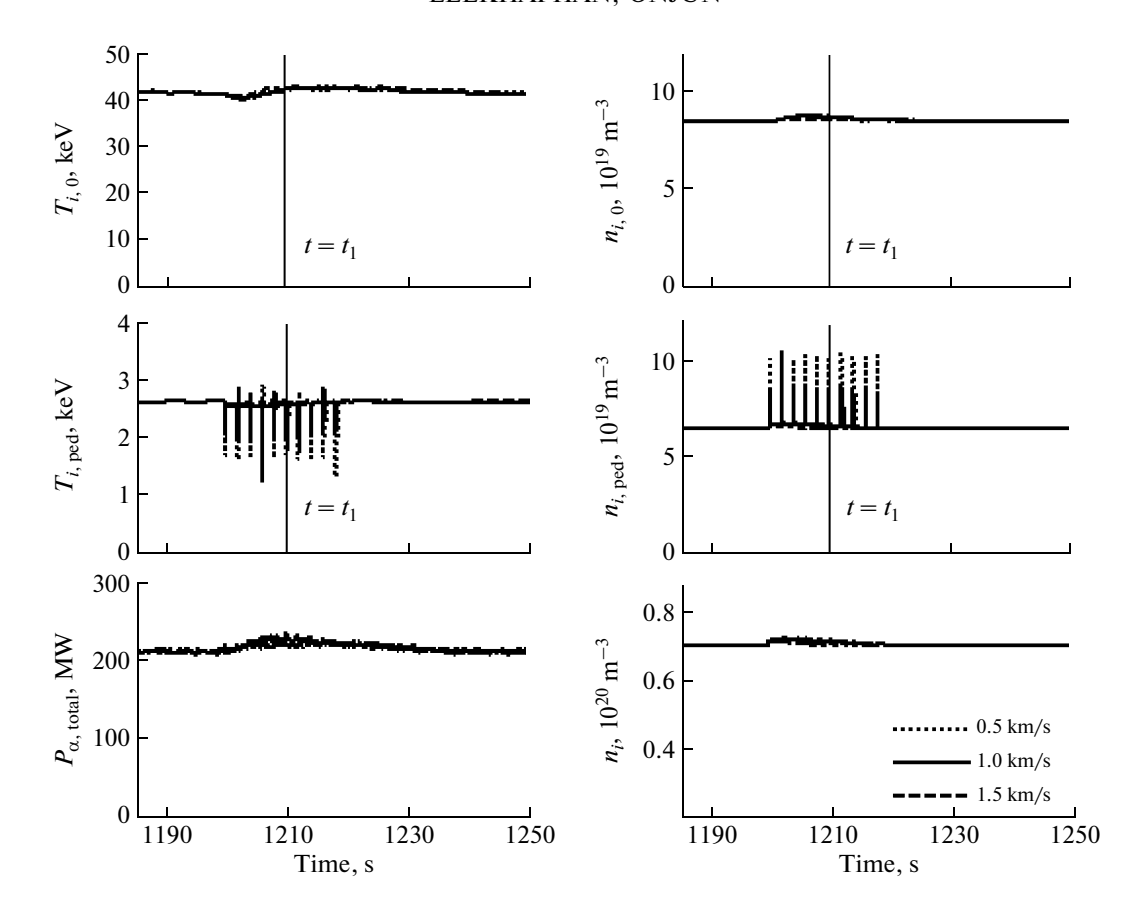


Fig. 6. Time evolution of the central ion temperature $(T_{i,\,0})$ and density $(n_{i,\,0})$, pedestal ion temperature $(T_{i,\,\text{ped}})$ and density $(n_{i,\,\text{ped}})$, total α -heating power $(P_{\alpha,\,\text{total}})$, and line-averaged density (n_{l}) . The values are obtained from simulations using the Mixed B/gB core transport model coupled with the ITB model, the Milora—Foster pellet ablation model, and the pedestal model based on flow shear and magnetic shear stabilization width scaling. The pellet radius and injection frequency used are 2.0 mm and 0.5 Hz, whereas the pellet velocities of 0.5, 1.0, and 1.5 km/s are used.

times 1200 to 1220 s. Upon increasing the pellet radius, the pedestal temperatures drop. This is not surprising since more energy is needed to ablate larger volume of solid hydrogen. Also, the pedestal deuterium and tritium densities increase. The core ion temperature decreases while the core electron temperature shows no conspicuous trend. The values of central deuterium and tritium densities also increase. It is observed that the values of the stored plasma energy, α -heating power, and $Q_{\rm fusion}$ increase greatly when the pellet radius is increased. The results indicate that using pellets with larger radius may hold the key to improved performance and fuelling in ITER. Note that the structure of ITB is not altered, as the change in the temperature is not significant.

4.2. Effects of Varying the Pellet Velocity

The pellet velocity is also one of the most easily varied parameters in pellet injection. Current pellet injection technology is capable of injecting pellets with the velocity of approximately 0.5 to 1.5 km/s [4]. Hence,

in this section, the effects of varying the pellet velocity on plasma properties are investigated. The pellet velocities considered are 0.5, 1.0, and 1.5 km/s.

The time evolution of the central and pedestal ion temperature and density, as well as total α -heating power and line-averaged density are presented in Fig. 6, whereas Fig. 7 shows the ion and electron temperatures and the ion, electron, deuterium, tritium, helium, and beryllium densities as functions of the normalized minor radius at time t_1 (see Fig. 6). The summary of the averaged ion and electron temperatures, deuterium and tritium densities, stored plasma energy, lpha-heating power, and $Q_{ ext{fusion}}$ obtained from simulations before and during pellet injection is presented in Table 4. The values before pellet injection are averaged over the times 1190 to 1200 s, whereas the values obtained during pellet injection are averaged over the times 1200 to 1220 s. It can be seen that varying the pellet velocity does not exert significant impact in the core plasma. However, it is observed that increasing the pellet velocity reduces the increase in pedestal ion temperature and density upon pellet

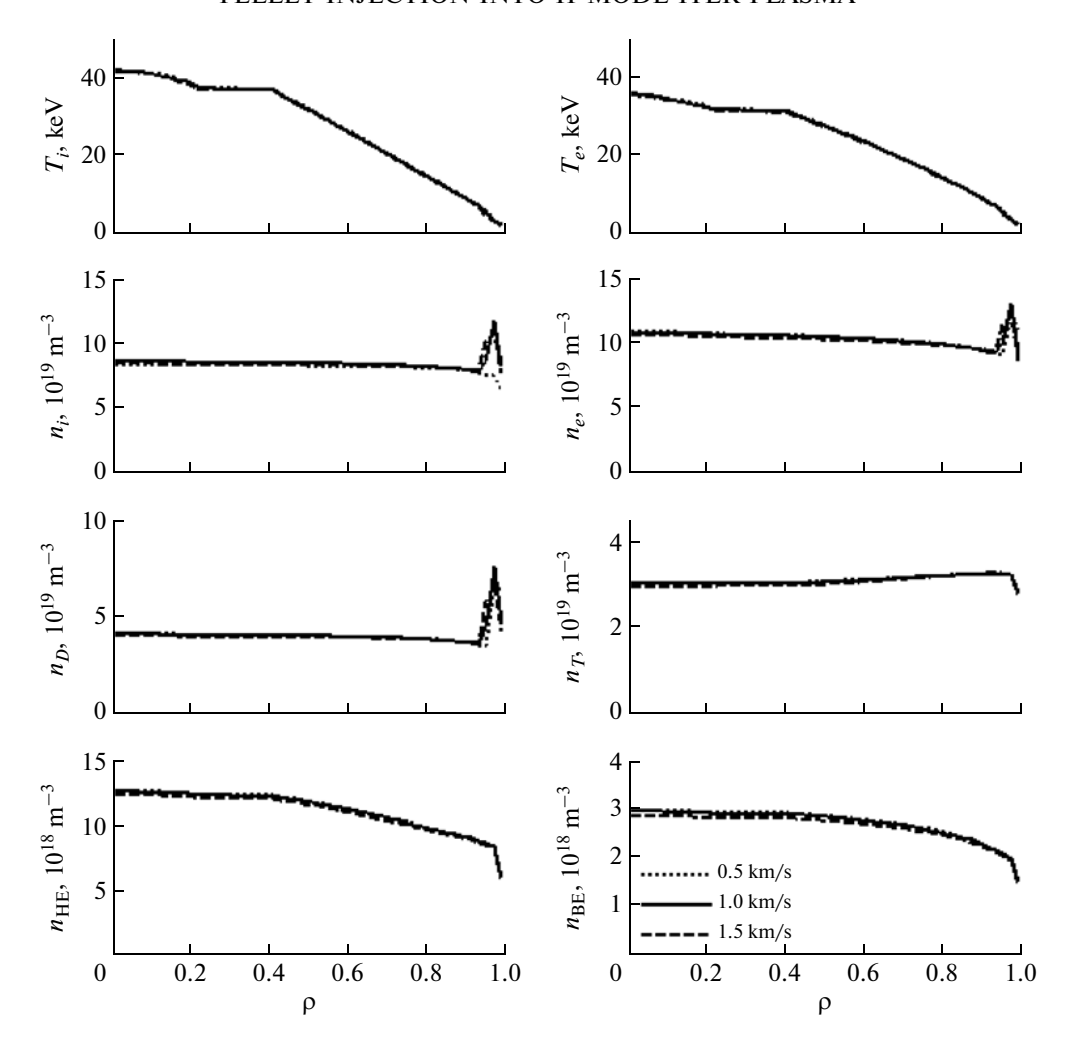


Fig. 7. Temperature and density profiles obtained from simulations using the Mixed B/gB core transport model coupled with the ITB model, the Milora—Foster pellet ablation model and the pedestal model based on flow shear and magnetic shear stabilization width scaling. The values are taken at time t_1 (see Fig. 6). The pellet radius and injection frequency used are 2.0 mm and 0.5 Hz, whereas the pellet velocities of 0.5, 1.0, and 1.5 km/s are used.

injection. Varying the pellet velocity does not alter the ITB structure. Since the effect of varying the pellet velocity is small, slower velocity can be used for easier operation.

4.3. Effects of Varying the Frequency of Pellet Injection

Similarly, the frequency of pellet injection can be easily varied during operation. The frequency of less than 1 up to 100 Hz is feasible in actual operation [4]. In this section, the pellet frequency of 0.25, 0.5, and 0.75 Hz, the pellet velocity of 1 km/s, and the pellet radius of 2 mm are used. Note that in this study, the simulations with pellet frequencies that are too large cannot be carried out.

The time evolution of the central and pedestal ion temperature and density, as well as total α -heating

power and line-averaged density are presented in Fig. 8, whereas Fig. 9 shows the ion and electron temperatures and the ion, electron, deuterium, tritium, helium, and beryllium densities as functions of normalized minor radius at time t_1 (see Fig. 8). The summary of averaged ion and electron temperatures, deuterium and tritium densities, the stored plasma energy, lpha-heating power and $Q_{
m fusion}$ obtained from simulations before and during pellet injection is presented in Table 5. The values before pellet injection are averaged over the times 1190 to 1200 s, whereas the values obtained during pellet injection are averaged over the times 1200 to 1220 s. It can be seen that the temperatures and helium density are unchanged upon varying the frequency. Similarly, the peak at the edge of n_i , n_e , and n_D profiles does not show significant increases. In general, the values of n_i , n_e , n_D , n_T , and n_{Be} increases slightly. The effect is most pronounced when the fre-

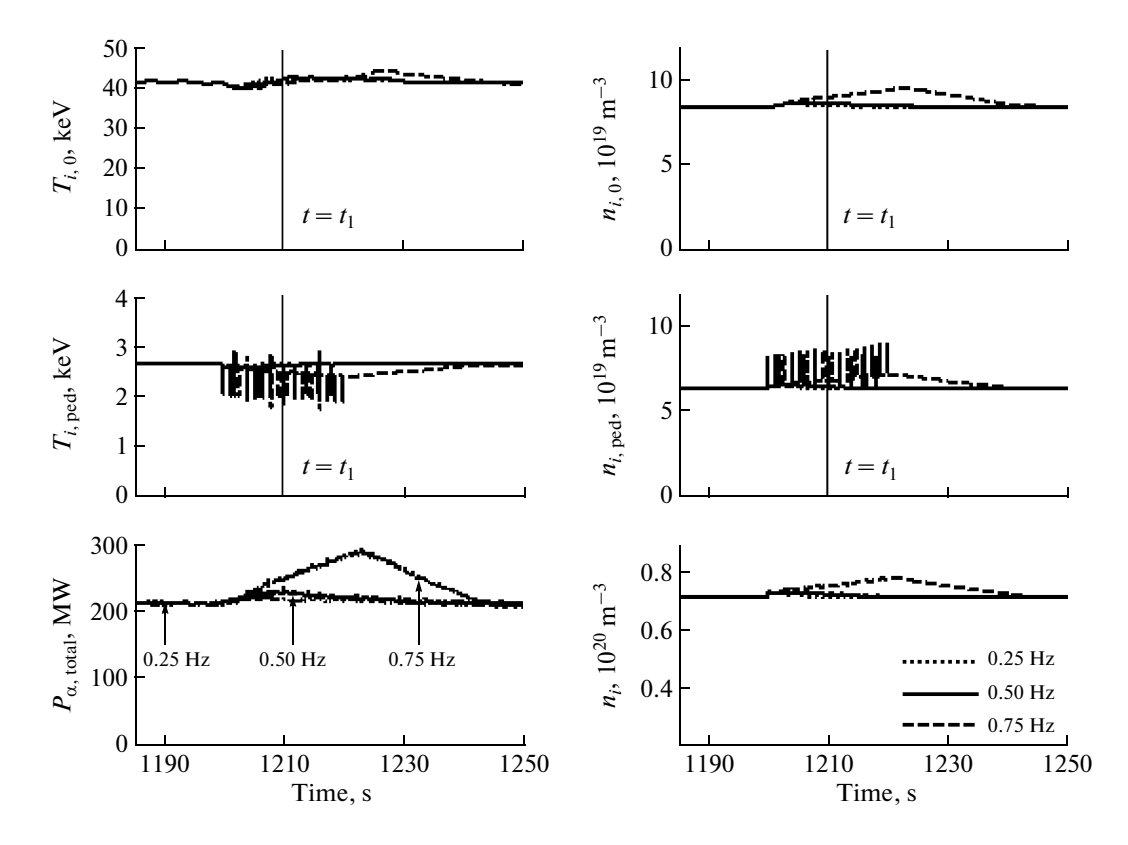


Fig. 8. Time evolution of the central ion temperature $(T_{i,\,0})$ and density $(n_{i,\,0})$, pedestal ion temperature $(T_{i,\,\text{ped}})$ and density $(n_{i,\,\text{ped}})$, total α -heating power $(P_{\alpha,\,\text{total}})$, and line-averaged density $(n_{\rm l})$. The values are obtained from simulations using the Mixed B/gB core transport model coupled with the ITB model, the Milora—Foster pellet ablation model, and the pedestal model based on flow shear and magnetic shear stabilization width scaling. The pellet radius and velocity used are 2.0 mm and 1.0 km/s, whereas the injection frequencies of 0.25, 0.50, and 0.75 Hz are used.

quency is switched from 0.50 to 0.75 Hz. This can be accounted for by considering the time evolution of n_1 in Fig. 8. The simulation with frequency of 0.75 Hz shows large increases in $n_{i,0}$, $P_{\alpha, \text{total}}$, and n_1 . The increase in density while the temperature is unchanged causes the fusion rate to rise, leading to increased $P_{\alpha, \text{total}}$. This effect is similar to the effect caused by increasing the pellet radius. Also, the ITB structure is not altered upon varying the frequency of pellet injection.

Hence, to improve the performance during fuelling, larger pellet radius or frequency may be considered.

5. CONCLUSIONS

The effects of pellets in type-I ELMy H-mode ITER discharges with ITB are investigated via simulations using 1.5D BALDUR integrated predictive modeling code. In these simulations, the ITB formation is described using a modified Mixed B/gB anomalous transport model. The simulations are carried out using a combination of the anomalous transport model with the ITB effect included, the NCLASS

neoclassical model, the pedestal temperature model based on the magnetic and flow shear stabilization pedestal width scaling, the dynamic density boundary model and the pellet model based on the Milora-Foster NGS pellet model. In the simulations, deuterium pellets are injected into ITER plasma with ITB. It is found that ITB and pellets interact in a complicated way that leads to different results from the case without ITB. Injection of pellets into ITB plasmas results in improved performance, whereas injection into non-ITB plasmas deteriorates it. The response of the plasma to pellet injection also depends sensitively on the pellet parameters, i.e., the pellet radius, the pellet velocity, and the frequency of injection, although these pellet parameters do not alter the structure of ITB. It can be concluded that injection of deuterium pellets from low-field side of the tokamak results in density peak at the edge. As the present code used is not capable of handling large perturbations introduced by larger pellets or more frequent injections, a further investigation of pellet injections into type-I ELMy Hmode ITER plasma with ITB from high-field side or medium-field side using a more robust code such as JETTO would be desirable.

Table 4. Summary of averaged ion temperature, electron temperature, deuterium density, and tritium density at the plasma center and at the top of the pedestal, as well as the stored plasma energy, α -heating power, and $Q_{\rm fusion}$, are shown before and during deuterium pellet injection. The values are obtained from simulations with the pellet radius and injection frequency of 2.0 mm and 0.5 Hz, respectively. The pellet velocities used are 0.5, 1.0, and 1.5 km/s. The formation of ITB is included in these simulations

Pellet velocity (km/s) **Parameters** 0.5 1.0 1.5 $T_{i,0}$, keV Before 41.292 41.292 41.292 During 41.604 41.590 41.816 0.72 % change 0.76 1.27 $T_{e,0}$, keV Before 35.473 35.473 35.473 35.812 35.813 35.911 During % change 0.96 0.96 1.23 D_0 , 10^{19} m⁻³ Before 3.951 3.951 3.951 4.062 During 4.064 4.024 % change 2.86 2.81 1.85 T_0 , 10^{19} m⁻³ Before 2.925 2.925 2.925 2.996 2.988 2.956 During % change 2.43 2.15 1.06 $T_{i, \text{ ped}}, \text{ keV}$ Before 2.610 2.610 2.610 2.500 2.533 2.566 During -4.21-2.95% change -1.69 $T_{e, \text{ped}}, \text{keV}$ Before 2.662 2.662 2.662 2.591 During 2.562 2.626 % change -3.76-2.67-1.35 $n_{\rm D, ped}$, $10^{19} \, \rm m^{-3}$ Before 2.779 2.779 2.779 During 3.042 2.950 2.883 6.15 3.74 % change 9.46 $n_{\rm T, ped}$, $10^{19} \, \rm m^{-3}$ Before 2.778 2.778 2.778 During 2.842 2.836 2.795 % change 2.30 2.09 0.61 $W_{\text{tot, avg}}$, MJ Before 818.3 818.3 818.3 During 839.4 837.8 830.7 % change 2.38 2.58 1.51 $P_{\alpha,\text{avg}}$, MW Before 211.0 211.0 211.0 During 223.5 222.5 218.8 % change 5.92 5.45 3.70 Before 26.38 26.38 26.38 $Q_{\rm fusion}$ 27.94 27.81 27.35 During % change 5.91 5.42 3.68

Table 5. Summary of averaged ion temperature, electron temperature, deuterium density and tritium density at the plasma center and at the top of the pedestal, as well as the stored plasma energy, α -heating power, and $Q_{\rm fusion}$, are shown before and during deuterium pellet injection. The values are obtained from simulations with the pellet radius and velocity of 2.0 mm and 1.0 km/s, respectively. The injection frequencies used are 0.25, 0.50, and 0.75 Hz. The formation of ITB is included in these simulations

Parameters		Frequency of pellet injection (Hz)		
		0.25	0.50	0.75
$T_{i,0}$, keV	Before	41.292	41.292	41.292
	During	41.574	41.590	41.040
	% change	0.68	0.72	-0.61
$T_{e,0}$, keV	Before	35.473	35.473	35.473
	During	35.743	35.813	35.719
	% change	0.76	0.96	0.69
D_0 , 10^{19} m ⁻³	Before	3.951	3.951	3.951
	During	4.006	4.062	4.280
	% change	1.39	2.81	8.33
T_0 , $10^{19} \mathrm{m}^{-3}$	Before	2.925	2.925	2.925
	During	2.958	2.988	3.135
	% change	1.13	2.15	7.18
$T_{i, \text{ ped}}, \text{keV}$	Before	2.610	2.610	2.610
	During	2.574	2.533	2.393
	% change	-1.38	-2.95	-8.31
$T_{e, \mathrm{ped}}, \mathrm{keV}$	Before	2.662	2.662	2.662
	During	2.628	2.591	2.459
	% change	-1.28	-2.67	-7.63
$n_{\rm D, ped}$, $10^{19} \rm m^{-3}$	Before	2.779	2.779	2.779
	During	2.862	2.950	3.192
	% change	2.99	6.15	14.86
$n_{\rm T, ped}$, $10^{19} \rm m^{-3}$	Before	2.778	2.778	2.778
	During	2.805	2.836	3.012
	% change	0.97	2.09	8.42
$W_{\text{tot, avg}}$, MJ	Before	818.3	818.3	818.3
	During	827.9	837.8	872.7
	% change	1.17	2.38	6.65
$P_{\alpha, \text{ avg}}, MW$	Before	211.0	211.0	211.0
	During	216.8	222.5	245.8
	% change	2.74	5.45	16.49
$Q_{ m fusion}$	Before	26.38	26.38	26.38
	During	27.10	27.81	30.73
	% change	2.73	5.42	16.49

PLASMA PHYSICS REPORTS Vol. 37 No. 4 2011

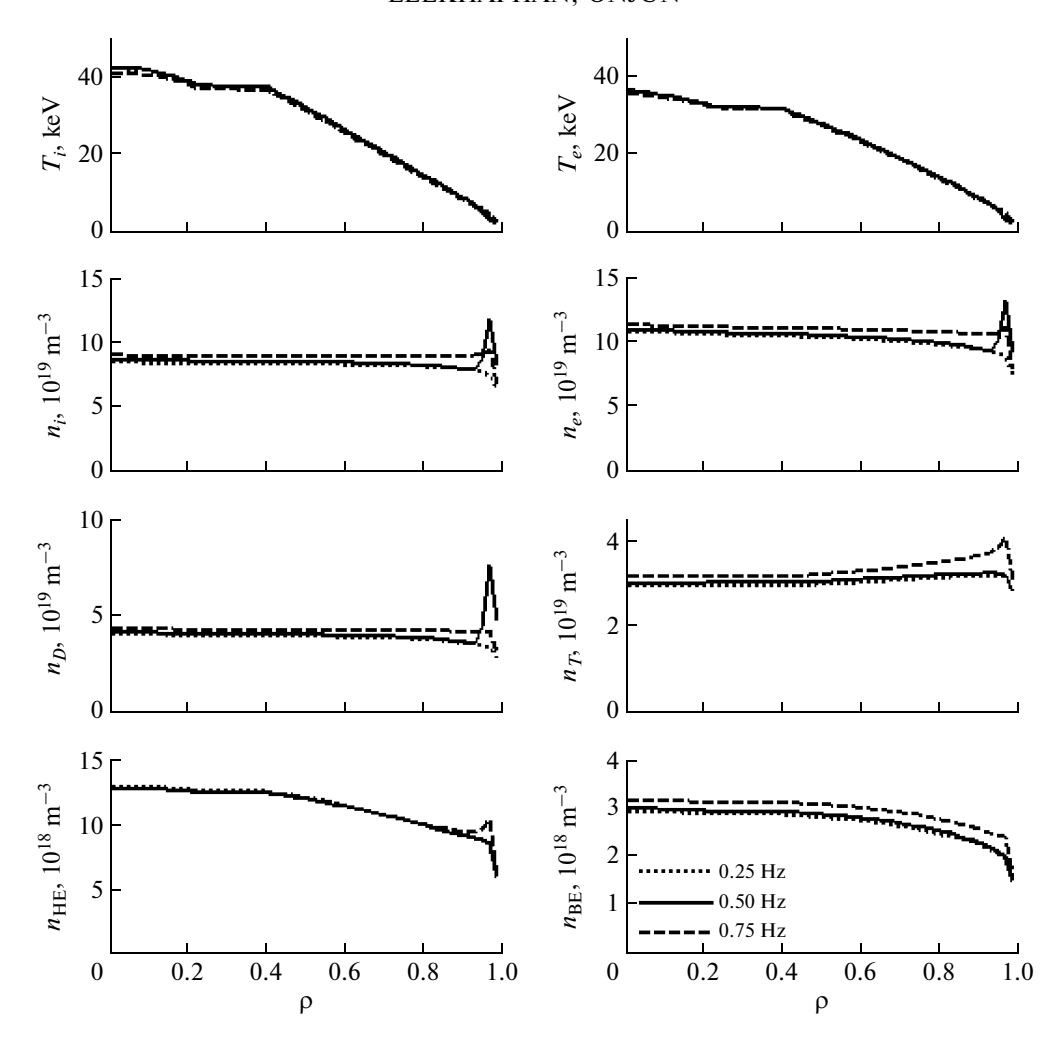


Fig. 9. Temperature and density profiles obtained from simulations using the Mixed B/gB core transport model coupled with the ITB model, the Milora–Foster pellet ablation model, and the pedestal model based on flow shear and magnetic shear stabilization width scaling. The values are taken at time t_1 (see Fig. 8). The pellet radius and velocity used are 2.0 mm and 1.0 km/s, whereas the injection frequencies of 0.25, 0.50, and 0.75 Hz are used.

ACKNOWLEDGMENTS

This work was supported by the National Research University Project of Thailand Office of Higher Education Commission and Thailand Toray Science Foundation.

REFERENCES

- 1. R. Aymar, P. Barabaschi, and Y. Shimomura, Plasma Phys. Controlled Fusion **44**, 519 (2002).
- 2. T. Tala, X. Garbet, and JET EFDA contributors, C. R. Physique 7, 622 (2006).
- H. Nakamura, J. Dietz, and P. Ladd, Vacuum 47, 969 (1996).
- B. V. Kuteev, Zh. Tekh. Fiz. 44 (9), 63 (1999) [Tech. Phys. 44, 1058 (1999)].
- Y. Yang, Y. Bao, L. Jiangang, et al., Nucl. Fusion 39, 1871 (1999).

- B. Pegourie, Plasma Phys. Controlled Fusion 49, R87 (2007).
- 7. E. Belonohy, O. J. W. F. Kardaun, T. Feher, et al., Nucl. Fusion **48**, 065009 (2008).
- 8. P. Gohil, T. E. Evans, J. R. Ferron, et al., Plasma Phys. Controlled Fusion **48**, A45 (2006).
- 9. V. Rozhansky, I. Senichenkov, I. Veselova, et al., Plasma Phys. Controlled Fusion **46**, 575 (2004).
- 10. L. R. Baylor, A. Geraud, W. A. Houlberg, et al., Nucl. Fusion **37**, 445 (1997).
- 11. L. L. Lengyel, R. Schneider, O. J. W. E. Kardaun, et al., Contrib. Plasma. Phys. 48, 623 (2008).
- 12. S. L. Milora, W. A. Houlberg, L. L. Lengyel, et al., Nucl. Fusion **35**, 657 (1995).
- 13. A. Wisitsorasak and T. Onjun, Fiz. Plazmy **37**, 3 (2011) [Plasma Phys. Rep. **37**, 1 (2011)].
- 14. L. Garzotti, X. Garbet, A. Thyagaraja, et al., in *Proceedings of the 31st EPS Conference on Plasma Physics, London, 2004*, ECA **28G**, Paper P-1.147 (2004).

- D. Frigione, C. Challis, M. de Baar, et al., in *Proceedings of the 30th EPS Conference on Controlled Fusion and Plasma Physics*, St. Petersburg, 2003, ECA 27A, Paper P-2.91 (2003).
- 16. L. Garzotti, C. Challis, M. de Baar, et al., *Proceedings* of the 30th EPS Conference on Controlled Fusion and Plasma Physics, St. Petersburg, 2003, ECA 27A, Paper P-2.92 (2003).
- 17. Y. Higashiyama, K. Yamazaki, J. Garcia, et al., Plasma Fusion Res. 3, 1048 (2008).
- 18. S. L. Milora, Rep. No. ORNL/TM-861631 (Oak Ridge National Laboratory, Oak Ridge, TN, 1983).
- W. A. Houlberg, K. C. Shaing, S. P. Hirshman, et al., Phys. Plasmas 4, 3231 (1997).
- 20. T. J. J. Tala, V. V. Parail, A. Becoulet, et al., Plasma Phys. Controlled Fusion **44**, A495 (2002).
- 21. B. Chatthong, T. Onjun, and W. Singhsomroje, submitted to Nucl. Fusion.
- 22. T. Onjun, G. Bateman, A. H. Kritz, et al., Phys. Plasmas **9**, 5018 (2002).
- M. Sugihara, Yu. Igitkhanov, G. Janeschitz, et al., Nucl. Fusion 40, 1743 (2000).
- C. E. Singer, D. E. Post, D. R. Mikkelsen, et al., Comput. Phys. Commun. 49, 399 (1988).
- D. Hannum, G. Bateman, J. Kinsey, et al., Phys. Plasmas 8, 964 (2001).
- T. Onjun, G. Bateman, A. H. Kritz, et al., Phys. Plasmas 8, 975 (2001).
- S. L. Milora and C. A. Foster, IEEE Trans. Plasma Sci. 6, 578 (1978).

- 28. W. A. Houlberg, S. E. Attenberger, L. R. Baylor, et al., Nucl. Fusion **32**, 1951 (1992).
- 29. T. J. J. Tala, J. A. Heikkinen, V. V. Parail, et al., Plasma Phys. Controlled Fusion **36**, 507 (2001).
- 30. M. Erba, A. Cherubini, V. V. Parail, et al., Plasma Phys. Controlled Fusion **39**, 261 (1997).
- 31. A. Taroni, M. Erba, E. Springmann, et al., Plasma Phys. Controlled Fusion **36**, 1629 (1994).
- 32. M. Erba, V. Parail, E. Springmann, et al., Plasma Phys. Cont. Fusion 37, 1249 (1995).
- 33. M. Erba, T. Aniel, V. Basiuk, et al., Plasma Phys. Controlled Fusion 38, 1013 (1998).
- 34. A. Y. Pankin, I. Voitsekhovitch, G. Bateman, et al., Plasma Phys. Control Fusion 47, 483 (2005).
- 35. P. Zhu, G. Bateman, A. H. Kritz, et al., Phys. Plasmas 7, 2898 (2000).
- 36. B. Chatthong and T. Onjun, Nucl. Fusion **50**, 064009 (2010).
- 37. T. Onjun, K. Tharasrisuthi, A. Y. Pankin, et al., J. Phys. Conf. Ser. **123**, 012034 (2008).
- 38. M. Sugihara, V. Mukhovatov, A. Polevoiet, et al., Plasma Phys. Controlled Fusion **45**, L55 (2003).
- 39. G. Bateman, T. Onjun, and A. H. Kritz, Plasma Phys. Controlled Fusion 45, 1939 (2003).
- 40. T. Onjun, G. Bateman, A. H. Kritz, et al., Phys. Plasmas **12**, 082513 (2005).
- 41. T. Onjun and Y. Pianroj, Nucl. Fusion **49**, 075003 (2009).